UNIVERSITÀ DEGLI STUDI FIRENZE

DOTTORATO DI RICERCA IN

SCIENZE DELLA TERRA

CICLO XXVI

COORDINATORE Prof. Rook Lorenzo

Integration between radar interferometric monitoring and hydrological modelling for the study of landslide evolution

Settore Scientifico Disciplinare GEO/05

Dottorando

Dott.ssa Ferrigno Federica

____

Tutore

Prof. Casagli Nicola

____

Coordinatore

Prof. Rook Lorenzo

____

Anni 2011/2013

TABLE OF CONTENTS

List of figures IV

List of tables IX

List of equations IX

Abstract X

Riassunto XII

Introduction 1

1. The radar monitoring systems: state-of-the-art 5

1.1 The remote sensing technique 5

1.2 The landing of a space technique: ground based SAR interferometry 10

1.3 The GBInSAR technique: general and principles 11

1.4 The GBInSAR approach applied on the landslide monitoring 12

2. Modelling: state-of-the-art 15

2.1 Introduction 15

2.2 Softwares and models 16

2.2.1 SHALSTAB, SHAllow Landslide STABility model 16

2.2.2 QDSLaM - Quasi-Dynamic Shallow Landsliding Model 17

2.2.3 SINMAP, Stability INdex MAPping 17

2.2.4 SEEP/W and SLOPE/W 18

2.2.5 TRIGRS – Transient Rainfall Infiltration and Grid based Regional Slope stability model 18

2.2.6 GEOtop-FS model 19

2.2.7 CI-SLAM - Connectivity Index-based Shallow LAndslide Model 20

2.2.8 HIRESSS - HIgh REsolution Slope Stability Simulator 21

2.3 Choice of the model 21

3. The Montaguto Earthflow: Case Study 23

3.1 Geological setting 23

3.2 Hydrogeological setting 28

3.3 Landslide description and history 29

3.4 GBInSAR Monitoring of the Montaguto earthflow 40

3.5 Others monitoring techniques 46

3.5.1 Laser scanning survey 46

3.5.3 Optical and thermal images 52

3.5.4 The Robotized Total Stations (RTSs) monitoring system 54

3.5.5 Geophysical and geognostic surveys 55

4. Interferometric Data Analisys 64

4.1 The monitoring activity 64

4.2 Data analysis 71
4.2.1 A Sector 74
4.2.2 B Sector 78
4.2.3 C Sector 82
4.2.4 D Sector 86
4.2.5 E Sector 89
4.3 The observational method as a support in stabilization works 96
4.3.1 The Observational Method 96
4.3.2 The coupled actions: OM and GBInSAR monitoring and stabilization works efficiency 98
4.3.3 The stabilization works 100
5. Hydrological and stability modelling of Montaguto landslide 104
5.1 Introduction 104
5.2 Climatic and hydrographical characteristic of the study area 106
5.3 The model 114
5.4 PCRaster® Software 114
5.5 The Slope hydrology model: STARWARS 120
5.6 The Slope hydrology model: PROBSTAB 122
5.7 Model implementation 124
5.8 The model run 128
6. Discussion 130
6.1 GBInSAR data results (Sectors A, B, C and D) 130
6.2 GBInSAR data results (E Sector) 132
6.3 Model results 135
6.4 Integration results 144
7. Conclusions 151
8. References 155
Acknowledgement 163
Appendices 165
Appendix 1: Geo-technical Survey Sample Points and Results 165
Appendix 2: Water balance calculation 166
Appendix 3: STARWARS PCRaster Script 169
Appendix 4: 183
Appendix 5: 185
Author's Resume 187

List of figures

Figure 1 - The electromagnetic spectrum. From http://en.wikipedia.org. 5

Figure 2 - SAR sensor acquisition geometries for ERS1/2 satellites. Background image from: esrl.noaa.gov. 8

Figure 3 - Comparison between the Foglio geologico n° 174 "Ariano Irpino" scale 1:100.000 (Servizio Geologico d'Italia, 1964) and the Appennino Foggiano geologyc map scale 1:200.000 (Crostella & Vezzani,1964). 25

Figure 4 - Geological setting of the study area. Legend: Unità di Altavilla: lithofacies arenaceus-sandy (UTAa) and lithofacies pelitic-silty (UTAb); Flysch di Faeto (FAE); Marne argillose del Toppo Capuana (TPC); alluvial deposits (b); colluvial deposits (b7); landslide deposit (a1). 27

Figure 5 - From the IGM Hydrologic map scale 1:100.000 (N° 174 Ariano di Puglia), edition 1890 (in red: the hydrografic lacuna. In blu: an hydrografic connection). 30

Figure 6 - IGM topographic map scale 1:25.000 (N°174 Ariano Irpino), edition 1955, in green and red, the new hydrographic network setting. 31

Figure 7 - Morphologic map of the erosion and instability phenomena active, presumably, in the 1955. 32

Figure 8 - Landslides reported in the "Carta geologica dell'Appennino Foggiano" scale 1:200.000 di Crostella & Vezzani (1964), based on the IGM topographic map scale 1:100.000, 1955 edition (Foglio n° 174 "Ariano Irpino") 33

Figure 9 - Topographic map IGM scale 1:50.000 (F° 420 Troia), 1984 edition. 34

Figure 10 - Morphologic map of the supposed landslide and erosional events in 1990. 35

Figure 11 - Morphologic Map of supposed erosional phenomena occurring during 1998, based on the ortophoto analisys IT2000 and on the Technical Regional Map (Campania Region) scale 1:5.000, edition 2000. 37

Figure 12 - Image of the landslide taken from the opposite slope, May 2006. 38

Figure 13 - Landslide image after the March 10th 2010 event, showing the flow reaching the round and railway.(from google earth 39

Figure 14 - Interruption of the main rail way network. 39

Figure 15 - GBInSAR monitoring system characteristics. 41

Figure 16 - Location of the GBInSAR monitoring system station. 42

Figure 17 - Interferogram covering a period spanning from 21.04 to 21.08 of 01/06/2010. Negative values indicate movement towards the instrument. 43

Figure 18 - Map of cumulated displacements (mm) recorded during the months of September 2010, December 2010, and March 2011. Negative values indicate movement towards the instrument. 43

Figure 19 - SAR interferogram (foot view zoom) refers to 4 minutes interval time of between 05:01 GMT (07:01 local time) and 05:06 GMT (07:06 local time) on 18th, May 2010 and location of the A, B, C and D monitored sectors. 45

Figure 20 - SAR interferogram related to 4 hours interval time, between 01:58 GMT (03:58 local time) and 05:57 GMT (07:57 local time) on August 1st, 2011 and the location of the "E Sector". 45

Figure 21 - Monitored sectors detection on the optical image based on the GB-InSAR monitoring system. 46

Figure 22 - Laser scanning observed area. 47

Figure 23 - Scans position location map. 48

Figure 24 - Total points cloud obtained from the combination of the low resolution scans. 48

Figure 25 - Total points cloud and reflectors location. 49

Figure 26 - Intensity coloured 3D points cloud realized from the scan position n°2. 50

Figure 27 - 3D points cloud generated from the combination of the scans realized from the position n°2,4 and 5. 50

Figure 28 - Terrain surface obtained through the points cloud elaboration. 51

Figure 29 - Contour lines (equidistance 1m) extracted from the DEM shown in the Figure 14. 51

Figure 30 - Overlaying of the contour lines to the digital terrain model. 52

Figure 31 - Thermal infrared image take on May, 5th 2010, from the GBInSAR location. 53

Figure 32 - Optical image of the Montaguto earthflow (acquisition time: 23/05/2010 – h 8.19 a.m.); and inside view of the GBInSAR installation point. 53

Figure 33 - Topography monitoring network of the Montaguto landslide in the period May to December 2010. The red, green and violet points indicate prisms position, while the squares indicate the Robotized Total Stations. (based on: Giordan *et al.*, 2013). 55

Figure 34 – Location of the surveys within the “A Sector”, continous core (A) and seismic refraction tomographies (B). (Modified from Amato and Dubbiosi, 2006; Guadagno 2010). 56

Figure 35 – Geological section obtained from the core surveys. (Modified from Amato and Dubbiosi, 2006). 56

Figure 36 – Subsoil seismic stratigraphy, (Guadagno, 2010). 57

Figure 37 – Location of the all surveys realized within the B Sector. (A, cone penetration tests and borehole; B and C, seismic tomography). 58

Figure 38 - Geolithological section obtained from the core surveys. (Modified from Amato and Dubbiosi, 2006). 58

Figure 39 - Subsoil seismic stratigraphy, (Guadagno, 2010). 59

Figure 40 – Location of the all surveys realized within the B Sector. (A, cone penetration tests and borehole in 2006; B borehole in 2010). 59

Figure 41 - Geolithological section obtained from the core surveys. (Modified from Amato and Dubbiosi, 2006). 60

Figure 42 - Location of the all surveys realized within the D Sector in 2010. 60

Figure 43 - Location of the all surveys realized within the E Sector. (A, cone penetration tests and borehole in 2006; B borehole in 2010). 61

Figure 44 – Geolithological section obtained from the core surveys. (Modified from Amato and Dubbiosi, 2006). 62

Figure 45 - Subsoil seismic stratigraphies, (Guadagno, 2010). 63

Figure 46 - Optical image showing the monitoring sectors location. 65

Figure 47- Monitored areas of interest detection on the 3D optical image and in the interferogram (time interval of approximately 4 minutes). 65

Figure 48- 2D SAR Interferogramma (foot zoom) relative to the time interval of about 4 minutes from 05.02 a.m. GMT (07.02 local time) and 05.06 a.m. GMT (07.06 local time) of 7th, May 2010. The color scale shows the displacements in millimeters along the radar line of sight (LOS = line-of-sight). 66

Figure 49- SAR interferogram acquired on May, 26th 2010, the maximum speed recorded is equal to 2.4 m/day, the show time interval of acquisition is 4 minutes, sufficiently to assess the landslide deformations occurred. 68

Figure 50 - Comparison between SAR interferograms with different time interval processing, acquired on July 26th, 2010. 69

Figure 51 - Comparison between SAR interferograms with different time interval processing, acquired on December 26th, 2010. 69

Figure 52 - Weekly and monthly cumulated maps, relative to the third week of March and the same month. ... 70

Figure 53 – Comparison between the monthly cumulated rainfall and the speed displacement recorded. ... 71

Figure 54 - Comparison between the monthly cumulated rainfall (2009-2012) and the displacement speed recorded, from May 2010. ... 73

Figure 55 - Interferogram (time interval of 4 minutes) of May, 21th 2010. The time is GMT (-2h compared to local time). The highest deformation of the "A Sector" was about 4.7 mm. ... 75

Figure 56 – Graph of the "A Sector" velocity and daily rainfall. ... 75

Figure 57 - Graph of the "A Sector" velocity and monthly rainfall. ... 76

Figure 58 - Comparison between the DTM and DSM of the "A Sector" and location of the area on the orthophotos (left). ... 77

Figure 59 – Cumulated displacement map of July 2010 and December 2012 (note the differences in scale) and location of the " A Sector ". ... 78

Figure 60 - Interferogram (time interval of 4 minutes) of June, 1st 2010. The time shown is GMT (-2h compared to local time). The deformation rate of the "B Sector" was about equal to 9.2 mm. ... 79

Figure 61 - Graph of the "B Sector" velocity and daily rainfall. ... 80

Figure 62 - Graph of the "B Sector" velocity and monthly rainfall. ... 80

Figure 63 - Comparison between the DTM and DSM of the "Sector B" and location of the area on orthophotos (left). ... 81

Figure 64 - Cumulated displacement map of July 2010, August 2010 and December 2012 (note the differences in scale) and location of the " B Sector ". ... 82

Figure 65 – Graph of the "C Sector" velocity and daily rainfall. ... 83

Figure 66 - Graph of the "C Sector" velocity and monthly rainfall. ... 83

Figure 67 - Interferogram (time interval of 4 minutes) of May, 29th 2010. The time shown is GMT (-2h compared to local time). The deformation rate of the "C Sector" was about equal to 6.2 mm. ... 84

Figure 68 - Comparison between the DTM and DSM of the "Sector C" and location of the area on orthophotos (left). ... 85

Figure 69 – Monthly cumulated displacement map of July 2010, May 2012 and December 2012 (note the differences in scale) and location of the " C Sector ". ... 85

Figure 70 – Graph of the "D Sector" velocity and daily rainfall ... 86

Figure 71 - Graph of the "D Sector" velocity and monthly rainfall. ... 87

Figure 72 - Interferograms (time interval of 4 minutes) referred to the days: a) 16 b) 17 c) 18 d) 21 (June 2010). The time shown is GMT (-2h compared to local time). The larger deformation of the "D Sector" was equal to 7.6 mm. ... 88

Figure 73 - Comparison between the DTM and DSM of the "D Sector" and location of the area on orthophotos (left) ... 88

Figure 74 - Comparison of the contour maps extrapolated from the monthly cumulated displacement maps, relative to "D Sector". ... 89

Figure 75 - Monthly cumulated displacement map of July 2010, May 2012 and December 2012 (note the differences in scale) and location of the " D Sector ". ... 89

Figure 76 – E sector limits and location. ... 90

Figure 77 – Interferograms of 4 hours referred to November, 24th 2010 (left) and del July, 28th 2011 (right). ... 91

Figure 78 – July 2011, weekly cumulated displacement maps (11th - 17th and 18th - 24th). ... 91

Figure 79 –July/August2011, weekly cumulated displacement maps (July, 25th – 31st and August, 1st - 7th). 92
Figure 80 - Graph of the "E Sector" velocity and daily rainfall. 93
Figure 81 - Graph of the "E Sector" velocity and monthly rainfall. 93
Figure 82 - Comparison between the DTM and DSM of the "E Sector" and location of the area on orthophotos (left). 94
Figure 83 - Comparison of the contour maps extrapolated from the monthly cumulated displacement maps, relative to "E Sector". 95
Figure 84 - Monthly cumulated displacement map of November 2010, March 2012 and December 2012 (note the differences in scale) and location of the "E Sector ". 95
Figure 85 – Monthly cumulated displacement map with deformation area location and relative variant design of the area. 100
Figure 86 – Landslide morphological characteristics and relative stabilization works description. 101
Figure 87 – Graph reporting the stabilization works evolution and the displacement velocity decrease from the emergency phase beginning and the end of the considered study period. 102
Figure 88: location of the meteorological station and of the unstable slope. 107
Figure 89: monthly average rainfall patterns relative to the years 2002-2012. 109
Figure 90: monthly average rainfall patterns comparison between the previous years (2002-2008) and last analysed four years (2009-2012). 110
Figure 91 - Monthly rainfall patterns comparison between the last analysed four years (2009-2012) the monthly average of the previous years (2002-2008). 110
Figure 92: graph of the monthly average evapotransipiration from 2009 to 2012. 112
Figure 93: comparison between the most relevant meteorological parameters (in blue the gross rainfalls, in red the net rainfalls and in green the evapotransipiration), all expressed in mm per month. 113
Figure 94: net and gross rainfall comparison 114
Figure 95 - A table defining relations between PCRaster map layers; using these conditions a NewMap is generated, on a cell by cell basis. 116
Figure 96 - Location attributes used to define the spatial characteristics of a PCRaster map. 117
Figure 97: Schematic representation of the model concept of the hydrological component STARWARS. The Perc(z)fluxes are defined by θE(z), the saturated lateral flow Qsat from the gradient *i* of the water level. 121
Figure 98: hydrological model component structure (after van Beek, 2002). 125
Figure 99 –Stability model component structure (after van Beek, 2002). 125
Figure 100 – Comparison between three optical images of the landslide medium-low part. a) May, 18th 2010; b) June, 15th 2011; c) September, 18th 2012. 131
Figure 101 - Histogram of landslide volumetric changes for different sectors. Negative values indicate erosion, positive values indicate deposition (modified from: Giordan *et al.*, 2013). 132
Figure 102 – Examples of damaged works, due to the E Sector deformation. 134
Figure 103 - Photos of some E Sector criticality: A and B) groundwater level rising in a dike test; C and D) streams and pools of water present landslide limit, E) fractures. 134
Figure 104 - Changes in the volumetric moisture content (VMC), for a quarter daily time steps (blue line) and a spin-up year (green line); compared with net monthly rainfall (violet bar) and total monthly rainfall (red bar) for each considered year. 136
Figure 105 – Overall yearly variation of the minimum safety factor. Location of an unstable area (blue circle) out of the landslide body (red square). The maps are obtained from daily time steps. 138

Figure 106 - Unstable time steps maps illustrating daily variations in slope stability. From yellow to red in shown the amount of unstable day. 139

Figure 107 - Minimum safety factor map relative to the pre-event time lapse, from January to March 2010. 140

Figure 108 - Landslide minimum safety factor map (2009) and safety factor values graph, corresponding to each pixel crossed from the line section. 141

Figure 109 – Landslide minimum safety factor map (2010) and safety factor values graph, corresponding to each pixel crossed from the line section. The graph also shows the overlying with the previous trend (2009). 142

Figure 110 – Landslide minimum safety factor map (2011) and safety factor values graph, corresponding to each pixel crossed from the line section. The graph also shows the overlying with the previous trends (2009 and 2010). 143

Figure 111 – Landslide minimum safety factor map (2011) and safety factor values graph, corresponding to each pixel crossed from the line section. The graph also shows the overlying with the previous trends (2009, 2010 and 2011). 143

Figure 112 – Overall data results representation, relative to the A sector and for the years 2010 and 2011. Monthly cumulated displacement map on the left (July 2010 – June 2011), minimum safety factor map in the centre, upper right displacement velocity graph and at lower left sector location on DTM. 145

Figure 113 - Overall data results representation, relative to the B sector and for the years 2010 and 2011. Monthly cumulated displacement map on the left (July 2010 – June 2011), minimum safety factor map in the centre, upper right displacement velocity graph and at lower left sector location on DTM. 146

Figure 114 - Overall data results representation, relative to the C sector and for the years 2010 and 2011. Monthly cumulated displacement map on the left (July 2010 – June 2011), minimum safety factor map in the centre, upper right displacement velocity graph and at lower left sector location on DTM. 147

Figure 115 - Overall data results representation, relative to the D sector and for the years 2010 and 2011. Monthly cumulated displacement map on the left (July 2010 – June 2011), minimum safety factor map in the centre, upper right displacement velocity graph and at lower left sector location on DTM. 148

Figure 116 - Overall data results representation, relative to the E sector and for the years 2010 and 2011. Daily interferogram and monthly cumulated displacement map on the left (July 2010 – June 2011), minimum safety factor map in the centre, upper right displacement velocity graph and at lower left sector location on DTM. 149

Figure 117 – Comparison between the monthly rainfall (expressed in mm) and the displacement velocity of the GBInSAR monitored sectors (in m/day and expressed in log scale). 150

List of tables

Table 1 - Table of IEEE (Institute of Electrical and Electronics Engineers) bands. ... 7

Table 1 - GBInSAR technical description ... 41

Table 1 - Description of the monitoring sectors relative to the corresponding landslide portion. ... 64

Table 2- Estimated velocity synthesis expressed in cm/h and m/day, corresponding to the monitoring sectors and their daily trend. The assessment of the trends variation is based on an increase or decrease in terms of displacement velocity equal to 10 cm/day, occurred in the previous 24 hours. ... 66

Table 3 - Estimated velocity synthesis expressed in cm/h and m/day, corresponding to the monitoring sectors and their daily trend. The change of the trends is assessed as considerable when is equal to the ±50% of the variation. ... 70

Table 4 – DTM and DSM characteristics. ... 74

Table 5 – Work phases outline. ... 101

Table 1: Main physiographic parameters of the examined basins. ... 106

Table 2: estimable runoff volumes (m^3) at a given period T for floods events ... 106

Table 3: Available meteorological parameters for the Savignano Irpino meteorological station ... 108

Table 4: List of data types, domains for default cell representation, without legends. ... 119

Table 5: Model input and output of the coupled hillslope model for hydrology (STARWARS) and stability (PROBSTAB) [based on: van Beek, 2002] ... 126

Table 6: Data, Type and Use ... 127

List of equations

Equation 1: Extraterrestrial Solar Radiation ... 111

Equation 2: Hargreaves Equation for Evapotransipiration ... 111

Equation 3: Soil Moisture Storage equation ... 111

Equation 4: Net precipitation equation. ... 113

Equation 5: Safety Factor ... 122

Equation 6: Variable Performance ... 123

Equation 7: Mean Factor Safety ... 123

Equation 8: Cumulative Variance of Safety Factor ... 123

Equation 9: Z score assuming normal distribution ... 124

Abstract

This thesis has been carried out in the working enviroment of the SAR.net 2 project, funded by the National Civil Protection Department. It represents the main outcome of three years-long activity at the Earth Sciences Department of the University of Firenze (Centre of Competence of the Italian Civil Protection for geo-hazards) and at the at the Department of Physical Geography of Utrecht University. The main objective of this PhD program was:

- to discuss the behavior of a continuous creep component in clayey o silty-clayey soils by means of an hydrological and stability model;
- the use of GBInSAR data analysis for the study of landslide evolution;
- the validation of the stabilization works effectiveness through the coupled action of the GBInSAR and Observational Method;
- the integration between interferometry analysis the and the model performances;

To achieve these objectives, the landslide of Montaguto (AV) was selected as a case study, basing its features. It is one of the largest earth flows in Europe, subject to medium-slow deformation velocity and shows wide character of persistence over time that make it perfectly suited for the performance of the main activities in assessment and management of geological risk:

- Monitoring: measure through time the surface displacement fields induced by the event. This type of information is of great value endangered by movement and where the investigated phenomenon is going to threat valuable elements at risk.
- Modelling: application of hydrological and stability model, in order to simulate the hydraulic response of a landslide it was necessary to represent the physical nature of component hydrological processes in a relatively simple manner.
- Integration: validation of the results obtained from the interferometric data analysis by the comparison the evidence shown by the model, taking into account the influence of the works on the landslide equilibrium, and the single event scale landslide nature. Since, the scale of interest on the model is usually defined by larger natural or administrative entities (e.g. catchments and provinces) and by periods covering many years, this limit represent the main thesis challenges.

The results exhibit a general decrease in terms of displacement trend, referable to the whole landslide system, even when the meteorological condition report substantial rain supply.

Using of real time monitoring with new technologies allowed us to accomplish a 3 years of daily activity, which are still carrying out.

Meanwhile the GBInSAR approach has been proved to be very useful during the emergency phase supporting in the fast definition of the landslide toe excavation, and to guarantee the safety of the involved personnel, as well.

Through the daily monitoring activities was also possible to enrich the study using of the observational method. This phase allowed us to establish the efficiency of the works and to direct the possible project variations.

Finally, the efficiency of the undertaken activities can be evaluated by observing the time history of the velocity recorded at critical points.

Among the successes of this work certainly we highlight the effective integrated monitoring system, obtained by analyzing the results of the monitoring campaign, and by the comparison between the capabilities of the hydrological and stability model.

The awareness of having, at least in part, achieved the goal was represented by a clear correspondence in terms of temporal-space evolution and distribution of the most unstable areas, observed between the developed models and the measurements obtained through monitoring campaigns, despite the presence of the stabilization works which have continuously disrupted the landslide environment.

Riassunto

Questa tesi è stata svolta nell’ambito del progetto SAR.net2, finanziato dal Dipartimento di Protezione Civile Nazionale. Costituisce il risultato principale di tre anni di attività di ricerca condotte presso il Dipartimento di Scienze della Terra dell'Università degli Studi di Firenze (Centro di Competenza della Protezione Civile Italiana per il rischio idrogeologico), e per un periodo di circa quattro mesi, presso il Dipartimento di Geografia Fisica dell'Università di Utrecht.

Gli obiettivi principali di questo dottorato sono stati:

- lo studio del comportamento di un processo di deformazione lento e continuo che coinvolge terreni argillosi e limoso-argillosi per mezzo di un modello idrologico e stabilità;
- l'utilizzo e l’analisi dei dati GBInSAR per lo studio dell'evoluzione di una frana;
- la validazione dell’efficacia dei lavori di stabilizzazione, mediante la combinazione dell’applicazione del Metodo Osservazionale e la tecnica di monitoraggio GBInSAR;
- l'integrazione tra le analisi dei dati interferometrici e le prestazioni del modello applicato.

Per il conseguimento di tali obiettivi, è stata selezionata come caso di studio la frana di Montaguto (AV), grazie alle sue caratteristiche. Costituisce una delle più grandi colate di terra d’Europa, soggetta a velocità di deformazione medio-lente e presenta forti caratteri di persistenza nel tempo che la rendono perfettamente adatta allo svolgimento delle due principali attività in campo di valutazione e gestione del rischio idrogeologico :

- Monitoraggio: misurare in tempo quasi-reale (ogni 4 minuti) gli spostamenti superficiali occorsi. Questo tipo di informazione è di grande valore laddove il fenomeno indagato mostri tassi di deformazioni tali da minacciare gli elementi a rischio coinvolti.

- Modellazione: applicazione di un modello combinato idrologico e di stabilità, con il fine di simulare la risposta idraulica di una frana e rappresentandone la natura fisica dei processi idrologici e le condizioni di stabilità in modo relativamente semplice.

- Integrazione: validazione dal confronto tra i risultati ottenuti dall'analisi dei dati interferometrici e quelli indicati dal modello, tenendo conto dell'influenza che le opere realizzate hanno avuto sull’equilibrio del versante soggetto a frana. Dal momento che,

l’oggetto indagato è a scala di singolo evento e che invece il modello viene solitamente eseguito su eventi a larga scala (ad esempio bacini e regioni) e su intervalli di tempo che ricoprono molti anni, la principale sfida di questa tesi è rappresentata proprio dalla’ipotesi di dimostrare la possibile compatibilità dei due metodi.

I risultati mostrano una generale diminuzione in termini tendenziali di spostamento, riferibili a tutto il sistema frana, anche quando le condizioni meteorologiche riportano sostanziali e maggiori apporti di pioggia.

L’utilizzo di un sistema di monitoraggio in tempo reale con le nuove tecnologie ci ha permesso di eseguire 3 anni di attività quotidiana, che si stanno tutt’ora ancora svolgendo .

Allo stesso modo, l'approccio GBInSAR ha dimostrato di essere molto utile durante la fase di emergenza, come supporto nella rapida definizione delle operazioni di scavo del piede della frana, e contestualmente, come garanzia della sicurezza del personale coinvolto.

Attraverso le quotidiane attività di monitoraggio è stato anche possibile approfondire lo studio dell’evoluzione della frana applicando il metodo osservazionale. Questa fase ha permesso di stabilire l'efficienza delle opere e di dirigere le possibili varianti di progetto.

L’osservazione dell'evoluzione temporale delle velocità registrata per ciascun settore monitorato, evidenzia la riuscita di tali attività.

Tra i successi di questo lavoro si evidenzia certamente l’integrazione dei dati ottenuti del sistema di monitoraggio e dall’esecuzione del modello idrologico e stabilità.

La consapevolezza di avere, almeno in parte, raggiunto l'obiettivo è rappresentata dalla netta corrispondenza in termini di evoluzione spazio-temporale delle zone maggiormente instabili osservate tra il modello sviluppato e le misure ottenute attraverso campagne di monitoraggio, tenendo sempre in considerazione gli elementi di disturbo provocati dall’esecuzione dei lavori di stabilizzazione.

Introduction

Landslides cause thousands of casualties and billions of dollars in property damage annually (Spiker & Gori 2003). To reduce hazards from landslides, mechanisms controlling their movement must be understood. Knowledge of landslide kinematics is the most basic requirement for this understanding, and also assists characterization of landslide boundary geometry, positions of landslide elements driving and resisting motion, and variations in material properties, landslide thickness, and pore-water pressures. The movement of even simple, single blocks of sliding rock often is temporally complex, and most landslides also have spatially complex movement. Short-term and long-term temporal features of a landslide's kinematics generally are documented from in-situ monitoring using extensometers, crack meters, inclinometers, laser or sonar range finders, GPS receivers, etc. at specific locations on a landslide. Such monitoring efforts are spatially discontinuous, costly, and labour intensive. Surface manifestations of temporal and spatial variations in a landslide's kinematics can be mapped to provide a more spatially continuous kinematic characterization, but such mapping also is costly and labour intensive to perform and requires sufficient movement (generally decimetres to meters) to be effective. Additionally, these traditional approaches for documenting landslide kinematics require access to the landslide, careful selection of proper monitoring equipment and locations for point monitoring, and weeks-months for initial site evaluations, planning, permit acquisitions, equipment installation, mapping activities, and, most importantly, sufficient landslide movement to permit the mapping and monitoring methods to be effective.

Interferometric ground-based InSAR (GB-InSAR) surveying can overcome many of the limitations inherent in traditional kinematic studies by providing autonomous, rapid acquisitions (minutes) of kinematic data at long distances (up to 4 km) and across large areas (several km2) from remote locations with displacement accuracy on the order of mm or better (e.g., Tarchi et al. 2003a, b). These surveys can be performed in any weather and lighting conditions and do not require access to the landslide for any reason, including for installation of manmade reflectors. Furthermore, kinematic data can be reduced in near real time, permitting GB-InSAR to be used for monitoring of critical slope failures and issuing of alarms when selected movement characteristics are observed. GBInSAR has a major role to

play for studying geohazard-related events at different stages, such as detection, mapping, monitoring, hazard zonation, modelling and prediction.
GB-InSAR is now commonly used by prominent mining groups internationally and by civil protection authorities in developed trees, which were in leaf during our surveys.

This thesis has been carried out in the working environment of the SAR.net 2 project, funded by the National Civil Protection Department. It represents the main outcome of three years-long activity at the Earth Sciences Department of the University of Firenze (Centre of Competence of the Italian Civil Protection for geo-hazards) and at the at the Department of Physical Geography of Utrecht University. The main objective of this PhD program was:

- to discuss the behaviour of a continuous creep component in clayey o silty-clayey soils by means of an hydrological and stability model;
- the use of GBInSAR data analysis for the study of landslide evolution;
- the validation of the stabilization works effectiveness through the coupled action of the GBInSAR and Observational Method;
- the integration between interferometry analysis the and the model performances;

On March 10th, 2010, due to the heavy rainfall occurred in the previous days, the Montaguto (Southern Italy, Avellino province) earthflow reactivated, involving the road SS 90 “Delle Puglie”, as already happened in May 2005 and in September 2009, and reaching the Caserta-Foggia railway. A monitoring activity using GBInSAR technology began, in order to investigate the landslide kinematics, and to plan urgent safety measures for risk mitigation and to design stabilization works.
To achieve these objectives, the landslide of Montaguto (AV) was selected as a case study, basing its features. It is one of the largest earth flows in Europe, subject to medium-slow deformation velocity and shows wide character of persistence over time that make it perfectly suited for the performance of the main activities in assessment and management of geological risk:

- Monitoring: measure through time the surface displacement fields induced by the event. This type of information is of great value endangered by movement and where the investigated phenomenon is going to threat valuable elements at risk.

- Modelling: application of hydrological and stability model, in order to simulate the hydraulic response of a landslide it was necessary to represent the physical nature of component hydrological processes in a relatively simple manner.
- Integration: validation of the results obtained from the interferometric data analysis by the comparison the evidence shown by the model, taking into account the influence of the works on the landslide equilibrium, and the single event scale landslide nature. Since, the scale of interest on the model is usually defined by larger natural or administrative entities (e.g. catchments and provinces) and by periods covering many years, this limit represent the main thesis challenges.

Besides the *Introduction*, this thesis includes a total of nine chapters, structured as follows:

Chapter 2 describes the basic principle of radar monitoring systems, as remote sensing and ground based; and reviews the current status of interferometric processing techniques (both single pairs and multi-interferograms) and their applications for geohazard investigations.

Chapter 3 describes the contribution of modelling in rainfall induced landslides and/or landslide prediction, giving an overview on the most suitable different kinds of models and defining the reason of the model choice;

Chapter 4 describes the case study: the Montaguto earthflow; a detailed description about the geological, hydrological and geotechnical setting is presented. Furthermore the GBInSAR monitoring system characteristics are illustrated;

Chapter 5 mainly deals with discussions regarding the interferometric data analysis, with the detailed examination of the monitored sectors;

Chapter 6 describes the hydrological and stability model features, it’s implementation and the model run;

Chapter 7 summarizes the main finding of this thesis and relative results discuss;

Chapter 8 the main references of this work are listed in alphabetical order.

1. The radar monitoring systems: state-of-the-art

1.1 The remote sensing technique

The word Radar is the acronym of Radio Detection and Ranging. Radar is an active instrument, which measures the echo of scattering objects, surfaces and volumes illuminated by an electromagnetic wave internally generated belonging to the microwave portion of the electromagnetic spectrum, Figure 1.

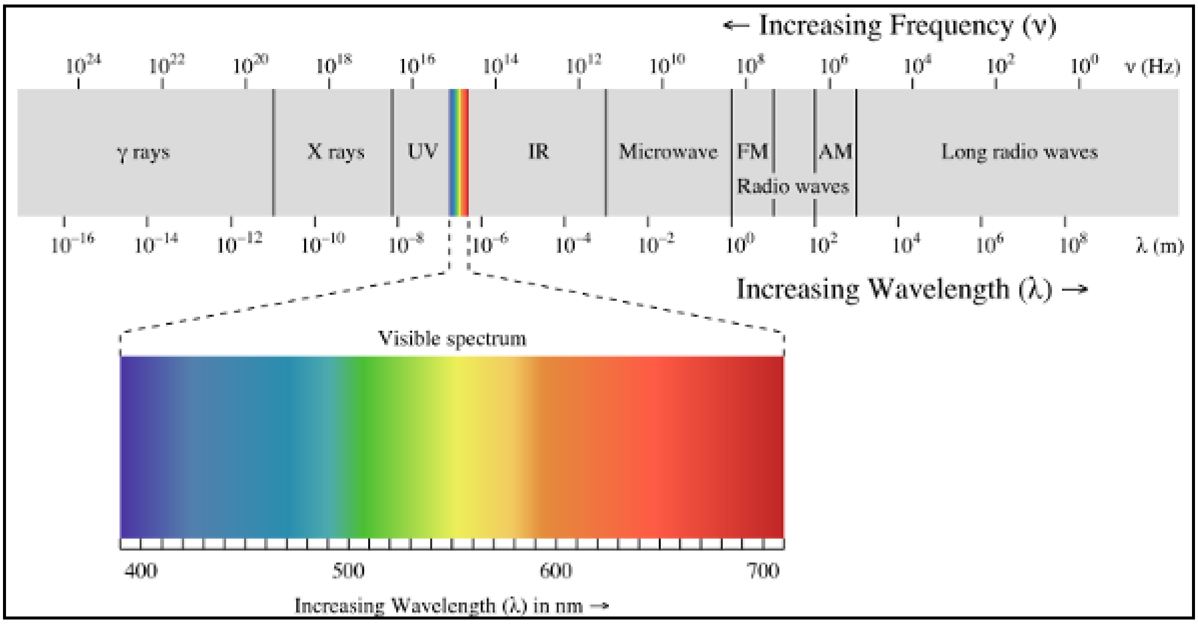

Figure 1 - The electromagnetic spectrum. From http://en.wikipedia.org.

It was born just before the second world war for detecting and ranging target for non-civilian scopes. In this case the requested spatial resolution was not so challenging for the technology available that time. The resolution of radar sensor in the direction parallel to the flight of the satellite (*azimuth* direction) depends on the width of the radar beam (b), which depends on the employed wavelength (λ) and on the physical (i.e., real) length L of the transmitting antenna:

$$b = \lambda/L$$

The azimuth resolution ($R_{azimuth}$) for a real aperture radar system is given by:

$$R_{azimuth} = R^* b$$

Where:

R is the distance between the sensor and the target.

Real aperture radars, hosted by satellite platforms do not provide suitable resolution. For instance, given a beam width of 10 milliradians, at a distance of 800 kilometres, the azimuth resolution will be 8 km.

For such systems, azimuth resolution can be improved increasing the length of the physical antenna used to illuminate the target scene or by using a shorter wavelength. Decrease of the wavelength leads to a higher cloud and atmosphere impact on the capability of imaging radars. On the other hand, to obtain a finer resolution (in the order of few meters), it would be necessary a physical antenna some kilometres long.

Synthetic aperture radar (SAR) technique was invented to overcome resolution restrictions encountered in radar observations from space and generally to improve the spatial resolution of radar images. The SAR is an active micro- wave device capable of recording the electromagnetic echo backscattered from the Earth surface and of arranging it in a 2D image map, whose dimensions are the sensor-target distance (slant range or Line of Sight direction, LOS) and the platform flight direction (azimuth).

SAR system achieves fine azimuth by using a small antenna and “long” wavelengths (in the order of few cm, see Table 1). Moreover, retrieved information is independent of the sensor to target distance. SAR is usually implemented by exploiting the forward motion of the aircraft or spacecraft. A single beam antenna, few meters long, is used. From different position, the antenna repeatedly illuminates a target scene. Individual echoes, received successively at the different antenna positions, are recorded, stored, combined and then processed together, simulating a “*synthetic aperture*”, to provide a much finer azimuth resolution.

SAR sensors emit signals with a specific central frequency, the so-called operating frequency, which characterizes signal propagation and penetration features. Hence sensors work at specific bands of the microwave domain, corresponding to different wavelengths (λ). The most commonly used bands in spaceborne radar applications (Table 1) are C-band (5-6 GHz, ~5,6 cm wavelength) and X-band (8-12 GHz, ~3,1 cm wavelength) and L-band (1-2 GHz ~23 cm wavelength).

Image resolution of SAR images depends on the sensor used and its acquisition mode. Pixel dimension ranges from 20x5m for ERS1/2 or Envisat satellites, up to 1m for the new X-band satellites (TerraSAR-X and Cosmo Sky-Med).

Table 1 - Table of IEEE (Institute of Electrical and Electronics Engineers) bands.

Band	Frequency range	Band	Frequency range
L	**1 – 2 GHz**	Q	30 – 50 GHz
S	2 – 4 GHz	U	40 – 60 GHz
C	**4 – 8 GHz**	V	50 – 75 GHz
X	**8 – 12 GHz**	E	60 – 90 GHz
K_u	**12 – 18 GHz**	W	75 – 110 GHz
K	18 – 26 GHz	F	90 – 140 GHz
K_a	26 – 40 GHz	D	110 – 170 GHz

The family of satellites, carrying platform hosting the SAR sensors, orbits the Earth, at an altitude ranging from 500 to 800km above the Earth's surface, following sun-synchronous, near-polar orbits, slightly inclined with respect of Earth meridians. The angle between north-south direction and the satellite orbit varies slightly, depending on the satellite, but in general lies in the range of 10 degrees. The direction along the trajectory of the satellite is called *azimuth.* The direction perpendicular to azimuth is called *ground range* or *across-track*. The *slant-range* represents the direction along the sequence of rays from the radar to each reflecting point in the illuminated scene. The 'sensor to target' direction, inclined of an angle 'θ' with respect to the vertical, is referred to as *Line Of Sight* (LOS). 'θ' is also called the off-nadir angle (or *look angle*) and it varies accordingly to satellite employed (θ usually ranges from 23° to 34°). In Figure 2 geometry acquisition of ESA's European Remote Sensing (ERS) satellites is shown as representative example.

The combination between the Earth's rotation movement and the polar orbits of all SAR satellites, allows the sensor to scan along predetermined paths and to gather information of the same target from two opposite acquisition geometries: ascending and descending. When satellites travel from the North Pole towards the South Pole this direction is referred to as a descending orbit. Conversely, when the satellite is travelling from the South Pole towards the North Pole, it is said to be in an ascending orbit.

SAR sensors are mounted on their platforms with the direction of transmission at 90° to the flight direction. For example, ERS1/2 satellites were right-looking satellites, meaning that the radar antenna transmits and receives pulses microwaves only on the right side only of the satellite. This side-looking viewing geometry is typical of imaging radar systems (both airborne and spaceborne).

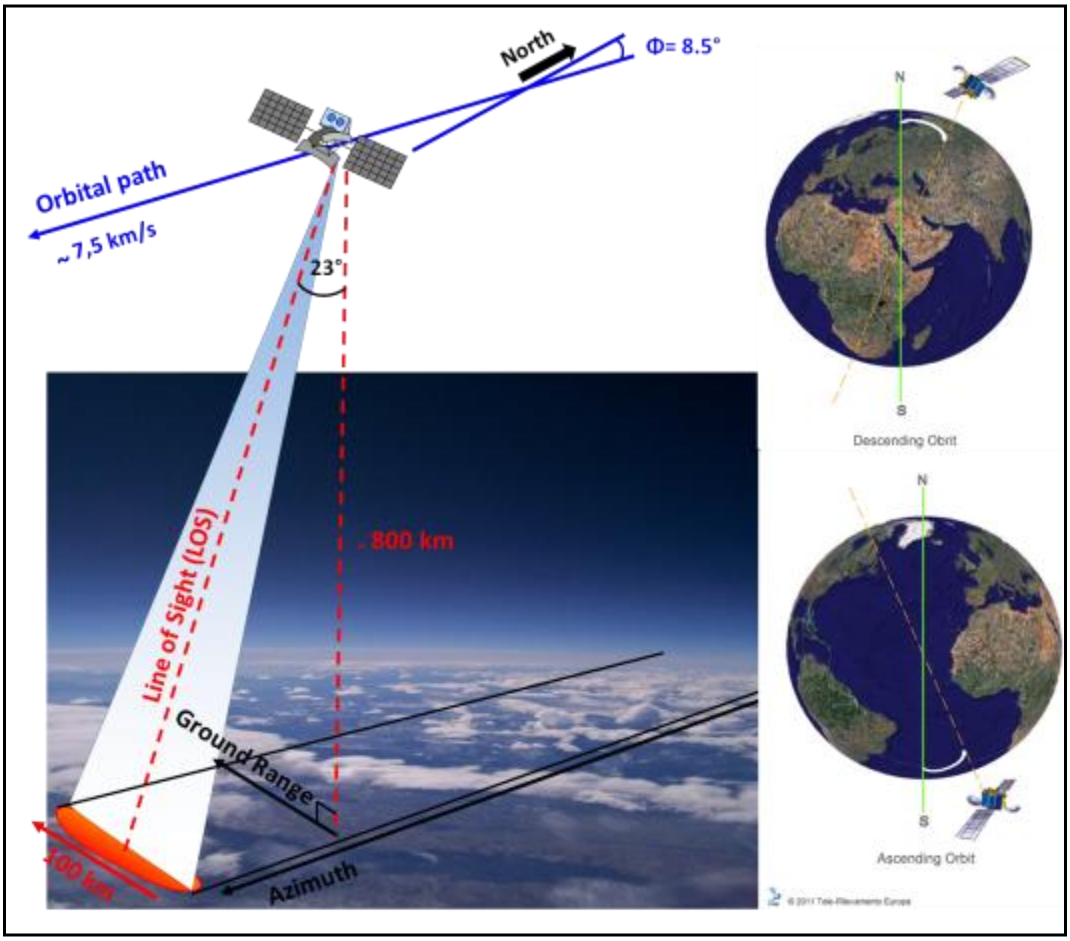

Figure 2 - SAR sensor acquisition geometries for ERS1/2 satellites. Background image from: esrl.noaa.gov.

As the satellite circumnavigates the Earth, SAR sensor emits a stream of radar signals toward the Earth's surface along the radar beam's LOS. The microwave beam is transmitted obliquely at right angles to the direction of flight, illuminating a *swath*. Radar signals are transmitted in pulses. The data for a SAR image are collected by a receiving antenna, which records the signal corresponding to each pulse, backscattered by the earth's surface back to the satellite. SAR processing is the transformation of raw SAR signal data into a spatial image.

With respect to optical sensors SAR offers several unique opportunities, but also presents considerable data processing and interpretation difficulties. Being an active system, SAR is independent of sun illumination. Moreover, microwaves can penetrate clouds, and, to some extent (up to several cm, depending on the operating frequency) even soil, vegetated canopies, and snow.

Thanks to the development of this peculiar technique, the radar observations have been successfully refined, offering the opportunity of a microwave vision of several natural media. Nowadays SAR instruments can produce microwave images of the earth from space with resolution comparable to or better than optical systems and these images of natural media disclosed the potentials of microwave remote sensing in the study of the earth surfaces. The unique feature of this radar is that it uses the forward motion of the spacecraft to synthesize a much longer antenna, which in turn, provides a high ground resolution. The satellite SEASAT launched in 1978 was the first satellite with an imaging SAR system used as a scientific sensor and it opened the road to the following missions: ERS, Radarsat, ENVISAT, JERS and the recent TerraSARX and Cosmo-SkyMED. The measurement and interpretation of backscattered signal is used to extract physical information from its scattering properties. Since a SAR system is coherent, i.e. transmits and receive complex signals with high frequency and phase stability, it is possible to use SAR images in an interferometric mode. The top benefit from microwave observations is their independence from clouds and sunlight but this capability can weaken by using interferometric techniques. Among the several applications of SAR images aimed at the earth surface monitoring, in the last decades interferometry has been playing a main role. In particular, it allows the detection, with high precision, of the displacement component along the sensor–target line of sight.

The feasibility and the effectiveness of radar interferometry from satellite for monitoring ground displacements at a regional scale due to subsidence (Ferretti *et al.*, 2001), earthquakes and volcanoes (Zebker *et al.*, 1994 , Sang-Ho, 2007 and Massonnet *et al.* 1993 (a)) and landslides (Lanari *et al.*, 2004 ; Crosetto *et al.*, 2005) or glacier motion (Goldenstein *et al.*, 1993 ; Kenyi and Kaufmann, 2003) have been well demonstrated. The use of Differential Interferometry based on SAR images (DInSAR) was first developed for spaceborne application but the majority of the applications investigated from space can be extended to observations based on the use of a ground-based microwave interferometer to whom this chapter is dedicated. Despite Ground based differential interferometry (GBInSAR) was born later, in the last years it became more and more diffused, in particular for monitoring landslides and slopes.

After this introduction the first following sections of this chapter resume SAR and Interferometry techniques basics, taking largely profit from some educational sources from literature (Rosen 2000; Massonnet, 2003a; Askne, 2004, Ferretti, 2007). The following sections are devoted GBInSAR and to a case study as example of application of the technique.

1.2 The landing of a space technique: ground based SAR interferometry

It is possible to acquire SAR images through a portable SAR to be installed in stable area. The motion for synthesizing the SAR image is obtained through a linear rail where a microwave transceiver moves regularly. Ground-based radar installations are usually at their best when monitoring small scale phenomena like buildings, small urban area or single hillsides, while imaging from satellite radar is able to monitor a very large area. As for satellite cases GBSAR radar images acquired at different dates can be fruitful for interferometry when the decorrelation among different images is maintained low. In ground based observations with respect to satellite sensors there is the necessity of finding a site with good visibility and from where the component of the displacement along the LOS is the major part. Recent papers have been issued about the feasibility of airborne (Reigber *et al.*, 2003), or Ground Based radar interferometry based on portable instrumentation as a tool for monitoring buildings or structures (Tarchi *et al.* 1997), landslides (Tarchi *et al.*, 2003b), (Leva *et al.* 2003), glaciers (Luzi *et al.* 2007). On the other hand satellite observations are sometimes not fully satisfactory because of a lengthy repeat pass time or of changes on observational geometry. Satellite, airborne and ground based radar interferometry are derived from the same physical principles but they are often characterized by specific problems mainly due to the difference of the geometry of the observation.

The Joint Research Center (JRC) has been a pioneer of the GB-SAR technology and here the first prototype was born. The first paper about a GB SAR interferometry experiment dates back to 1999 (Tarchi *et al.*, 1999), reporting a demonstration test on dam financed by the EC JRC in Ispra and the used equipment was composed of a radar sensor based on Vectorial Network Analyser (VNA), a coherent transmitting and receiving set-up, a mechanical guide, a PC based data acquisition and a control unit.

After some years a specific system, known as GBInSAR LiSA, reached an operative state and became available to the market by Ellegi-LiSALab company which on June 2003 obtained an exclusive licence to commercially exploit this technology from JRC. The use of VNA to realize a scatterometer, i.e. a coherent calibrated radar for RCS measurement, has been frequently used by researchers (e.g. Strozzi *et al.*, 1998) as it easily makes a powerful tool for coherent radar measurements available. The basic and simplest schematic of the radiofrequency set-up used for radar measurements is shown in Figure 4 together with a simple scheme of the GBSAR acquisition.

1.3 The GBInSAR technique: general and principles

The differential interferometry GBInSAR allows , through the comparison between the phases of the signal of two temporally separate acquisitions , but acquired from the same place and with the same parameters , to derive for the various pixels forming the scenario observed the displacement , along the direction of line of sight (LOS) system , which occurred during the delay period.

The final product can be traced to displacement maps (or deformation maps) generally with the following characteristics :

• The displacements measured , relative to the time interval between two acquisitions , refer to the component of the displacement actual projected lingo the direction of the line of sight (LOS)

• the spatial resolution of the maps of deformation is equal to that of immaini sar departure;

• The measurement precision of the movements usually reaches values of precision less than a millimetre.

Compared to interferometry by plane or by satellite the GB- InSAR (Tarchi *et al.* , 1999; Rudolph *et al.* , 1999; Tarchi *et al.* , 2003; Luzi *et al.* , 2004) offers several advantages , including:

• the high sampling frequency , generally 5-15 minutes (depending on the length of the track and by the technical aspects of radio frequency) , which allows a continuous monitoring and the possibility of obtaining a large number of SAR images ;

• possibility to easily vary the parameters of the radar (sampling interval , length of the track , the wavelength of the signal , polarization etc. .) Depending on the characteristics of the case studied ;

• a sampling frequently used to monitor landslides also relatively fast without incurring the risk of the phase ambiguity problem ;

• or a reduced sampling frequency allows to repeat several times the acquisitions made in the various positions of the sensor before they are focused , giving the possibility of making an average between the various measures and thus reduce the noise ;

• possibility to compare this technique with the traditional methods of monitoring landslides (strain gauges , inclinometers , GPS and levelling terrain);

• indirect approach , therefore without the need to directly access the site , with consequent reduction of costs and time related to direct surveys , and particularly useful for the study of dangerous places and are difficult to access ;

• allows a measure that is extensive and range, allowing you to avoid spatial interpolation between the acquired data and to obtain a continuous measurement in time and , theoretically, in space. Freeing herself from the risk of incorrect positioning of the instruments and to monitor only the phenomena of a local or in general from any inability to obtain data of good quality from a given point , (Massonet D. & Feigl KL , 1998);

• measuring system for quick installation , accurate , versatile , provides the data in real time, and potentially with a good geometric resolution , is able to operate in all conditions of visibility and atmospheric; latter aspect is particularly important if one considers the movement of landslides that often is associated with the rains.

The main limitations of interferometry are that this allows to measure only the component of displacements projected along the line of sight of the instrument. In addition, the radar interferometric fail to provide good results in areas that are too vegetated or characterized by very rapid movements or chaotic.

1.4 The GBInSAR approach applied on the landslide monitoring

The reduction of landslide hazards needs a detailed description of mass movements which generally cannot be achieved by means of geodetic or global positioning system (GPS) measurements. In addition, the proposed GB-SAR interferometer does not require the direct inspection of the landslide area. This is of great importance when the access to the landslide area is dangerous.

An example of how to benefit from the use of GBInSAR in Geosciences, is its employ as a monitoring tool for instable slopes, a well consolidated application largely reported in literature (Leva *et al.* 2003, Pieraccini *et al.*, 2003, Tarchi *et al.*, 2003a), see *Appendix 5*. The investigation and interpretation of the patterns of movement associated with landslides have been undertaken by using a wide range of techniques, including the use of survey markers: extensometers, inclinometers, analogue and digital photogrammetry, both terrestrial and aerial. In general, they suffer from serious shortcomings in terms of spatial resolution.

The GBInSAR technique applied to the monitoring of landslides, guarantees at low cost, multi-temporal deformation maps (almost) in real time, constitutes a valuable and versatile tool for rapid mapping, functional both in case of rapid alert (early warning) in emergency conditions, both as a scientific-technological support during the emergency phases management, in accordance with the provisions of the DPCM on 27/02/2004.

2. Modelling: state-of-the-art

2.1 Introduction

Soil slips and debris flows are among the most dangerous landslides (Jakob and Hungr, 2005): the threat they pose to human activities and life is mainly due to the high velocity that they can reach during the run out and to the nearly total absence of premonitory signals. These movements are usually triggered by heavy rainfall and therefore they have the same extemporaneous character. Moreover, small and apparently harmless debris flows, triggered by small zones of unstable slopes, can group from different sources in channels greatly increasing mass displacement and destructive powers reaching velocities up to 20m\s. There are several examples that show the destructive power and the extemporaneous character of shallow landslides. Some Italian regions are under continuous threat and every year are hit by these phenomena that usually cause damage to infrastructures and occasionally even human casualties (Tofani *et al.*, 2006).

Effective management of the hazard associated with shallow landsliding requires information on both the location of potentially unstable hillslopes and the conditions that cause slope instability. The need for spatial assessment of landslide hazard, along with the widespread use of Geographical Information Systems (GISs), has led to the proliferation of mathematical, GIS-based models (e.g. Montgomery and Dietrich, 1994; Pack *et al.*, 1998; Borga *et al.*, 2002a; Tarolli and Tarboton, 2006; Baum *et al.*, 2008) that can be applied over broad regions to assist forecasting, planning, and risk mitigation. Such models couple a hydrologic model, for the analysis of the pore-water pressure regime, with an infinite slope stability model, for the computation of the factor of safety (i.e. the ratio of retaining to driving forces within the slope) at each point of a landscape.

Despite the large number of studies, publications and applications available nowadays, the prediction of shallow landslides over large areas in real or near real time remains a very complex task (Baum and Godt, 2010). This is mainly due to: the necessary simplifications introduced in hydrological and geotechnical models (Crosta and Frattini, 2003; Baum *et al.*, 2010), the errors introduced by rainfall predictions (Jakob *et al.,* 2012), the consequences of the uncertainties in the knowledge of morphometric, mechanical and hydrological parameters of soils (Segoni *et al.*, 2012) and the extremely high computational effort required to operate on a basin scale (Baum *et al.*, 2010).

2.2 Softwares and models

Distributed slope stability models apply algorithms and equations to every cell of an extended area. Usually the analysed area is divided into pixels, and sometimes it is necessary to apply the model equations at different depths to each of them. As a consequence, the computation can be extremely time consuming depending on the thickness of the soil, the extension of the studied area, the spatial and temporal resolution and the complexity of the equation. Many softwares have been developed to handle this large amount of computations to apply stability models to large areas and to visualize the results. It is usually possible to find two different software approaches: plug-in oriented and stand-alone. Plug-in oriented codes are routines or add-ons that work on an existent software that provides a platform; this approach usually discharges all the file management and logical operations on the platform software and in some cases even part or all calculations are entrusted to the host software computational engine. Stand-alone software has a file management system and a dedicated and optimized computing routine which is developed in a universal programming language (C++, Fortran, Basic, etc.).
In the next sections different models are listed and briefly described.

2.2.1 SHALSTAB, SHAllow Landslide STABility model

SHALSTAB, SHAllow Landslide STABility model, is a popular distributed slope stability analysis software (Dietrich *et al.*, 1998). It has a physical core based on a distributed steady state description of the hydrological fluxes coupled with an infinite slope analysis. The basic tool is a grid-based model, a combination of C++ programs and ARC/INFOAML scripts intended to be used within an ESRI-ArcGIS software environment. This model has been classified as spatially predictive because it is not suited to forecast the timing of landslide triggering (Simoni *et al.*, 2008).

2.2.2 QDSLaM - Quasi-Dynamic Shallow Landsliding Model

Borga *et al.* (2002b) relaxed the hydrological steady-state assumption used in SHALSTAB by using a modified version of the quasi-dynamic wetness index developed by Barling *et al.* (1994). This model, called Quasi-Dynamic Shallow Landsliding Model – QDSLaM, permits us to describe the transient nature of lateral subsurface flow (Grayson *et al.*, 1997). However, research in the last decade has shown that the establishment of hydrological connectivity (the condition by which disparate regions on the hillslope are linked via subsurface water flow, Stieglitz *et al.*, 2003) is a necessary condition for lateral subsurface flow to occur at a point (e.g. Spence and Woo, 2003; Buttle *et al.*, 2004; Graham *et al.*, 2010; Spence, 2010). Lack of or only intermittent connectivity of subsurface flow systems invalidates the assumptions built into the TWI theory (i.e. the variable – and continuum – contributing area concept originally proposed by Hewlett and Hibbert, 1967). Both field (e.g. Freer *et al.*, 2002; Tromp van Meerveld and McDonnell, 2006) and numerical (e.g. Hopp and McDonnell, 2009; Lanni *et al.*, 2012) studies have shown that subsurface topography (and therefore soil-depth variability) has a strong impact in controlling the connectivity of saturated zones at the soil–bedrock interface, and in determining timing and position of shallow landslide initiation (Lanni *et al.*, 2012). However, despite these evidences, most shallow landslide models do not include a connectivity component for subsurface flow modelling.

2.2.3 SINMAP, Stability INdex MAPping

SINMAP, Stability INdex MAPping, and SINMAP 2 are other add-on tools for the ESRI-ArcGIS software. These have their theoretical basis in the infinite slope stability model with groundwater pore pressures obtained from a topographically based steady state model of hydrology (Pack *et al.*, 1998, 2001). The input information (slope and specific catchment area) is obtained from the analysis of digital elevation models (DEM). These parameters can be adjusted and calibrated with an interactive visual procedure that adjusts them based upon observed landslides. SINMAP allows an uncertainty of the variables through the specification of lower and upper bounds that define uniform probability distributions. Between these boundaries the parameters are assumed to vary at random with respect to the probability distribution. Other softwares have a more complex approach to the hydrological modelling of the groundwater flow and require longer computational time.

2.2.4 SEEP/W and SLOPE/W

For example, SEEP/W (Geo-Slope, 2003a) is a stand-alone finite element software that resolves the Richards equations to account for transient groundwater flow within a slope. This software analyses groundwater seepage and excess pore-water pressure dissipation within porous materials and can model both saturated and unsaturated flow (Krahn, 2004). SEEP/W is very efficient in resolving saturated-unsaturated and time dependent problems and in combination with the software SLOPE/W (Geo-Slope, 2003b) it performs the slope stability analysis adopting the limit equilibrium method. This software works very well for single slope stability analysis (Tofani *et al.*, 2006) but is not suited to be applied to a distributed analysis.

2.2.5 TRIGRS – Transient Rainfall Infiltration and Grid based Regional Slope stability model

The Transient Rainfall Infiltration and Grid-Based Regional Slope-Stability Model (TRIGRS) is a Fortran program for computing transient pore-pressure changes, and attendant changes in the factor of safety, due to rainfall infiltration. The original version (Baum and others, 2002) was based on the method outlined by Iverson (2000), with implementation of complex storm histories, an impermeable basal boundary at finite depth, and a simple runoff routing scheme. In version 2, we have retained the features of the original version. We have, however, expanded the model to address infiltration into a partially unsaturated surface layer above the water table by using an analytical solution of the Richards equation for vertical infiltration (given by Srivastava and Yeh, 1991). The analytical transient flow model is one-dimensional and represents the vertical infiltration in homogeneous isotropic materials that occurs during a storm. To improve usability, we have implemented property zones to simplify model input and have made numerous small changes. The program operates on a gridded elevation model of a map area and accepts input from a series of ASCII text files. Infiltration, hydraulic properties, and slope stability input parameters are allowed to vary over the grid area thus making it possible to analyse complex storm sequences over geologically complex terrain. The optional routing scheme achieves mass balance between rainfall input, infiltration, and runoff over the entire grid by allowing excess water to flow to downslope cells that are receiving less direct precipitation than they are able to absorb. The program saves output to a series of text files that can be imported to GIS software for display or further analysis.

Analyses using TRIGRS are applicable to areas that are prone to shallow precipitation-induced landslides and that satisfy other model assumptions reasonably well. These assumptions include a well-documented initial water table and steady background flux, and relatively isotropic, homogeneous hydrologic properties. The soil-water characteristic curves are approximated by an exponential function. However, we have not evaluated the magnitude of such possible errors. Model results are very sensitive to the initial conditions, particularly the steady component of the flow field and initial depth of the water table. Consequently, the model may produce questionable results where the initial water table depth is poorly estimated.

The TRIGRS program runs from the command line or in a simple input/output window with relatively little user interaction. The user controls an analysis by means of an initialization file that contains the names of all other input and output files as well as other parameters needed to run the program. The following discussion will briefly describe system requirements for running the program, installation, and features and limitations of the program, and will provide a detailed description of the initialization file. An included tutorial helps familiarize the user with program features and operation.

2.2.6 GEOtop-FS model

GEOtop-FS is one of the most advanced models for distributed slope stability and was recently proposed by Simoni (2008). This model uses the hydrological distributed model GEOtop (Rigon *et al.*, 2006) to compute pore pressure distribution by an approximate solution of the Richards equation and an infinite slope stability analysis to compute the distributed factor of safety. The approximate solution of Richards equation used by the software works in saturated soil conditions. The factor of safety of GEOtop-FS is computed in a probabilistic approach assigning statistical distributions to soil parameters instead of a single deterministic value and analysing the error propagation. Apip *et al.* (2010) proposed a model that combines a satellite real time estimate of rainfall intensity, a one-dimensional physically based distributed hydrological model based on grid-cell kinematic wave rainfall–runoff model (Kojima and Takara, 2003) and a geotechnical stability model based on a infinite slope and on Mohr–Coulomb law. The hydrological model simulates three lateral flow mechanisms: subsurface flow through capillary pores; subsurface flow through noncapillary pores; surface flow on the soil layer.

2.2.7 CI-SLAM - Connectivity Index-based Shallow LAndslide Model

Connectivity Index-based Shallow LAndslide Model (CI-SLAM) includes the concept of hydrological connectivity in the description of the subsurface flow processes while keeping the simplicity of the topographic index approach needed to conduct large scale analysis. In this model framework, hydrological connectivity is related to the spatial variability of soil depth across the investigated catchments and the initial soil moisture conditions. Vertical rainwater infiltration into unsaturated soil is simulated by using the concept of drainable porosity (i.e. the volume of stored soil-water removed/added per unit area per unit decline/growth of water table level; Hilberts *et al.*, 2005; Cordano and Rigon, 2008). This allows simulation of pore-water pressure dynamics under the assumption of quasi-steady state hydraulic equilibrium and to estimate the time for development of saturated conditions at the soil/bedrock interface.

The model incorporates the computation of a characteristic time for describing the connection of these “patches” of saturation. Specifically, it is assumed that an element (x,y) in a hillslope connects (hydrologically) with its own upslope contributing area A(x,y) when the water table forms a continuous surface throughout A(x,y). Once hydrological connectivity is established, the dynamic topographic index developed by Lanni *et al.* (2011) is used to describe the transient subsurface flow converging to the element in (x,y). The hydrological module is then coupled with the infinite slope stability equation to derive CI-SLAM, a shallow landslide model which is able to (a) account for the (positive) effect of the unsaturated zone storage on slope stability, and (b) reproduce pre-storm unsaturated soil conditions. This implicitly helps reducing the fraction of catchment area which is categorized as unconditionally unstable (i.e. failing even under dry soil moisture conditions), improving the confidence in model results (Keijsers *et al.*, 2011).

2.2.8 HIRESSS - HIgh REsolution Slope Stability Simulator

The landslide prediction model used in the forecasting chain is the HIgh REsolution Slope Stability Simulator (HIRESSS) (Rossi *et al.*, 2013). The HIRESSS code is a physically based distributed slope stability simulator for analysing shallow landslide triggering in real time, on large areas, using parallel computational techniques. The physical model proposed is composed of two parts: hydrological and geotechnical. The hydrological one receives the rainfall data from the downscaled COSMO-LM model as dynamical input and computes the pressure head as perturbation to the geotechnical stability model, which provides results in factor of safety (FS) terms. The hydrological model is based on an analytical solution of an approximated form of Richards equation under the wet condition hypothesis and it is introduced as a modelled form of hydraulic diffusivity to improve the hydrological response. The geotechnical stability model is based on an infinite slope model and it takes into account the increase in strength and cohesion due to matric suction in unsaturated soils, where the pressure head is negative. The soil mass variation on partially saturated soil caused by water infiltration is also modelled. HIRESSS computes the factor of safety at each selected time step (and not only at the end of the rainfall event) and at different depths within the soil layer. In addition to rainfall, the model input data are constituted by slope gradient, geotechnical and hydrological parameters and soil thickness (Rossi *et al.*, 2013).

2.3 Choice of the model

Models are classically defined as a representation of reality, not real because models represent those perceptions of human kind of the object/subject being modelled. Models of the landscape are almost always representations in miniature even thought the representation is physical (an analogue model) or in mathematical equations (Kassenberg 2002).

By itself physically based geomorphic models are powerful to assess the influence of specific parameters to the phenomenon being modelling. However they cannot in general give precise predictions. Because geomorphic landscape models are based on quantitative representations of processes, this model are, in part, quantitatively testable. The deterministic nature of the model makes it suitable to assess scenario; the uncertainty involved looming upon the prediction, an inevitable compromise to be made.

Crosta and Frattini (2003) compare several distributed models that simulate debris flow event, and conclude that the ideal method for modelling debris flow is through physically based mathematical models, because they explicitly incorporate the dynamic variables that are crucial in the mobilization and motion of debris flow. They conclude that the ideal means of modelling a debris flow is by coupling the infinite slope satiability model with the hydrological models able to simulate water table heights in steady or quasi-steady condition with groundwater flow parallel to the slope.

Owing to aforesaid reason supporting the capabilities, was decided to utilize a deterministic dynamic model for this study. The flexibility and the adaptability of the Van Beek's model (STARWARS and PROBSTAB, see Chapter 6) makes it the most ideal choice, considering our case study is represented by a relative slow earthflow. So also was the fact that the model was scripted in an environment modelling language (PCRaster) that had an easy learn curve, but with ample controls to script necessary adaptation; this software is distributed for free by the Utrecht University.

3. The Montaguto Earthflow: Case Study

3.1 Geological setting

The earthflow developed along the left-bank slope of the Cervaro valley, following the local morphology, and spanning a total length of almost 3 km, this sector occupies the slope bounded on the north by the ridge “La Montagna” and on the southern side by the valley bottom, with an elevation drop of about 430 m. The morphology and hydrography occur quite articulated with a strong structural control in fact, while the high sector of the slope (up to 630m shares-640 m AMSL) presents a general exposure to W-SW, with hydrographic and secondary ridges oriented in the general direction SW-NE, the lower middle of the slope occurs exposed to the south with the hydrographic network and secondary ridges oriented in the general direction SSENNW.

The topographical map of the IGM shows that, over the decades, the hydrographic network of the upper slope pertains alternately to Torrente Tre Confini, which flows into the stream Cervaro approximately 1 km upstream of the study area, or to the Fosso Nocelle, which develops in the left bank of the landslide system and, in part, flows into the landslide. From the point of view of structural geology the area fall within the northern part of the tectonics structure, defined in 1964 "Syncline Pliocene Wipers" by Crostella & Vezzani (1964) and by the Geological Survey of Italy (1964), Figure 4.1. The tectonic structure develops along the Vella river, at the height of the of the La Montagna relief.

This structure, interpreted (Crostella & Vezzani, 1964) as a large syncline fold with axis oriented NW-SE having aligned clay-sandy deposits of Pliocene age of Training Wipers, indicated by the letters Pa, Ps and Pp shown in the Foglio Geologico N°174 "Ariano Irpino "(SGd'I, 1964). Along the fold sides the chalcky-clastic, marl and clay sequences of Miocene age pertaining to the flysch of Faeto (Crostella & Vezzani, 1964), are indicated by the abbreviation BCD (Training Daunia) in geological Sheet No. 174 "Ariano Irpinia "(SGd'I, 1964). On the western flank of the synclinal structure, north of the river Cervaro, along the low Vallone Tre Confini, clayey-marly sequences Toppo Capuana Fomation (Miocene) are reported (Crostella & Vezzani, 1964) and indicated under the symbol *i* ("undifferentiated complex") in the Foglio Geologico N°174 "Ariano Irpino" (SGd'I, 1964).

The outcropping stratigraphic units are mainly three: the Flysch Faeto, the Marne and the clay of the Toppo Capuana, the Altavilla Unit, and the Cervaro river alluvial deposits. (Figure 3)

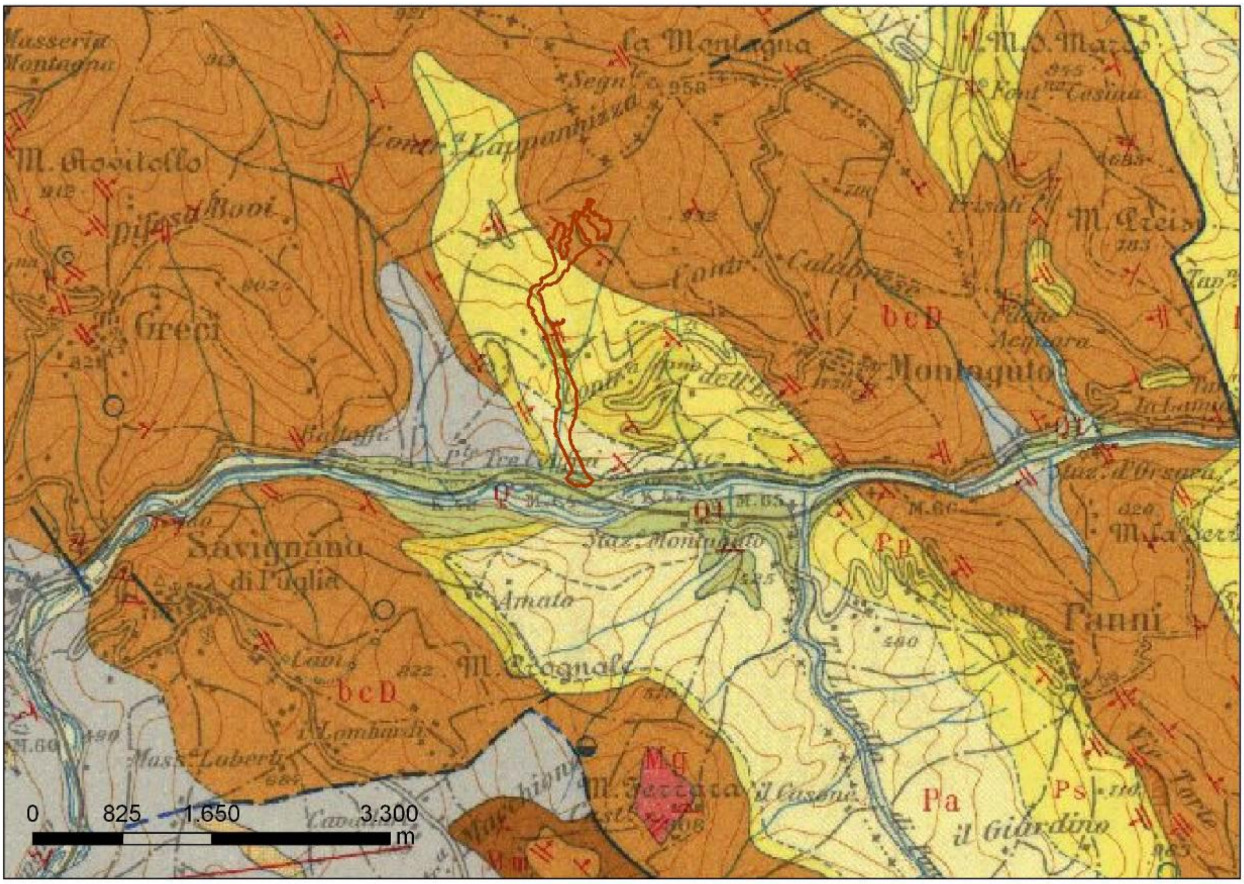

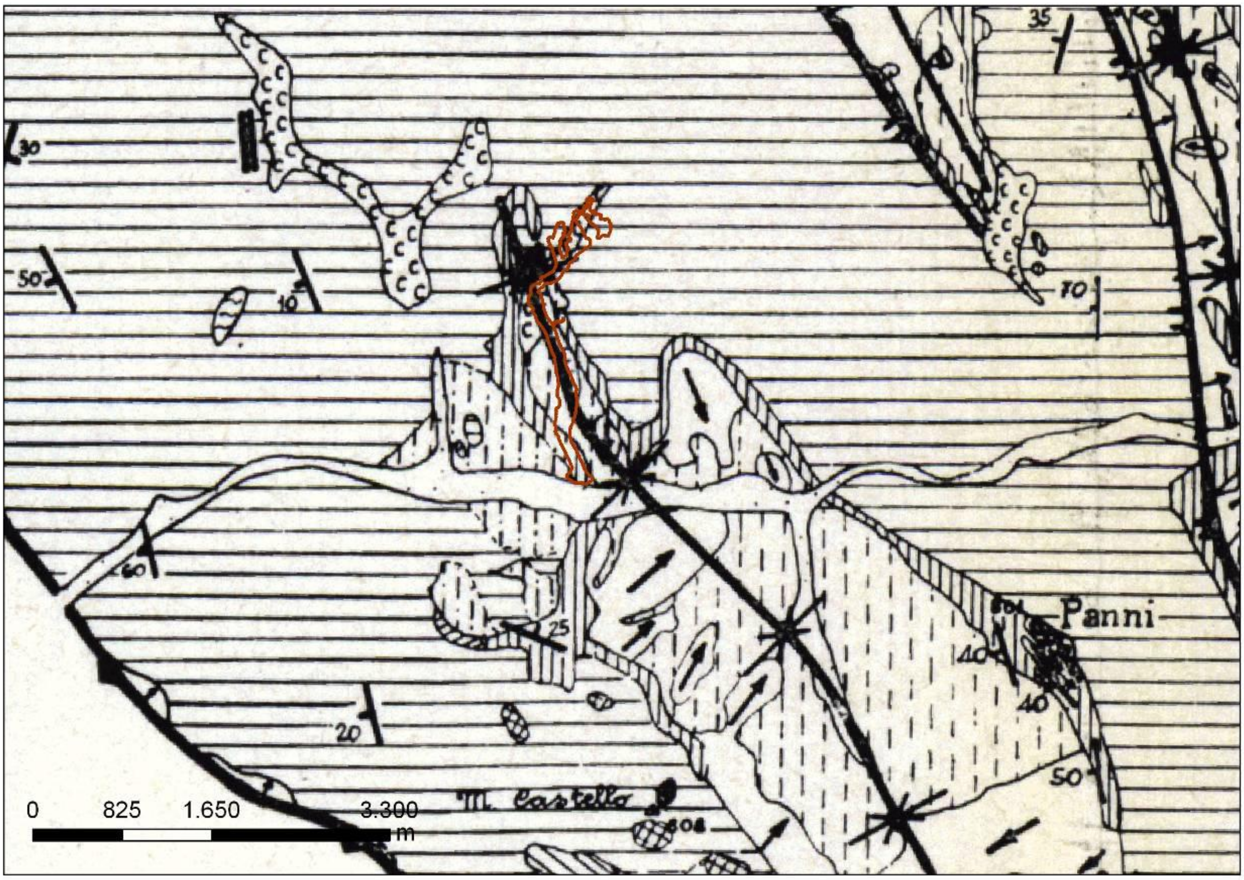

Figure 3 - Comparison between the Foglio geologico n° 174 "Ariano Irpino" scale 1:100.000 (Servizio Geologico d'Italia, 1964) and the Appennino Foggiano geologyc map scale 1:200.000 (Crostella & Vezzani,1964).

The Flysch Faeto formation constits of two main lithofacies. The limestone-marl lithofacies consists of an alternation of turbidite limestones, calcilutites and whitish marls intercalated with greenish clays and bioclastic calcirudites. Well expositions occur along the top ridge between the mountains and Acqua S.Giovanni village, where a sequence, consisting of benches and graded layers and laminates calcirudites and bioclastic limestones with subordinate intercalations of marly clay and yellowish-white marl, outcrops. The chaotic and extremely fractured arrangement of the pelit layers is prevalently due to the tectonic contest. We can find this formation also along the road between State Road 90 and Montaguto and along the downstream portion of the pond of 525m a.s.l..

The clayey-marly-limestone lithofacies consists of alternations of marl, clayey marl and greenish clays, marly limestones and subordinate, calcilutites and limestones. It is present in a intermediate band of the slope, between 650m and 700m a.s.l. , in correspondence with the bending the elbow of the landslide body. The overall thickness outcropping is about 200-300 m. Succession is attributable to Miocene (upper Burdigalian - lower Messinian).

The formation of Clayey-Marl of the Toppo Capuana (Crostella and Vezzani, 1964) consists of marly clays and clayey marl, sometimes silty, with rare levels of calcilutites; the deposition may be occurred in a basin environment. The formation has a lower boundary gradually and partially heteropic lateral-vertical with FAE. The sequence occurs along the Tre Confini valley lower part and, apparently, also in its upper part. The thickness outcropping is about 100-150m; age is attributable to the upper Miocene.

The Altavilla Unit includes arenaceous-pelitic succession (Messinian), they unconformably overlay the Faeto and Toppo Capuana Units. Two distinct lithofacies were detected: a sandstone-sandy lithofacies in the basal position and a pelitic lithofacies in the upper position. The arenaceous - sandy lithofacies (UTAA) outcrops along the ridge currently bordering the landslide. It is a succession of sandstone and sandy-pelitic, form poorly to medium cemented, medium-fine grained sometimes reddened, with lenses of well-rounded cemented pebbles. Furthermore, the lithofacies is recovers in layers and tables affected by a high degree of fracturing along the State Road 90 in Puglia and the Montaguto village. A small sandstone outcrops at the foot of the scarp develops at an altitude of 525m a.s.l..

The pelitic lithofacies is generally sub outcrops along the landslide where it is tectonically underlying the Flysch Faeto, while is well exposed (

Figure 4) along the landslide scarp. Geological surveys evidenced the lithofacies consist of sandy-silty clays and grayish clays.

The alluvial deposits of the T. Cervaro are characterized by gravel and gravel sandy locally cemented (Late Pleistocene- Holocene), reporting to flooding both the right and left of the T. Cervaro. The thickness of the deposits has been rated not more than 15 m. There are also, widely distributed along the valley bottom, the recent torrential alluvial deposits (Holocene and Present), consisting of gravel and gravel-sandy, with lenses of sand and silt. These soils were mapped with the abbreviation **b**.

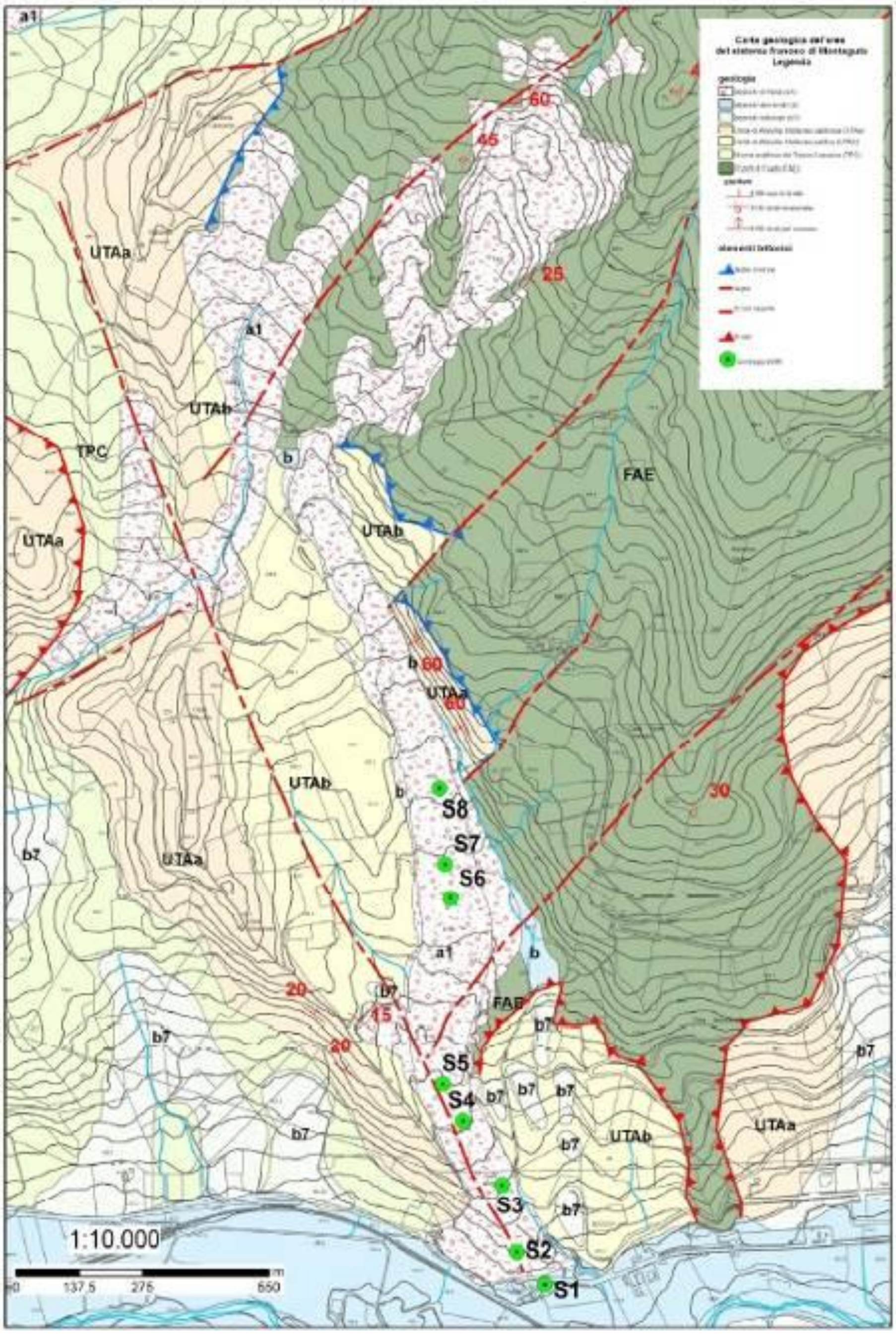

Figure 4 - Geological setting of the study area. Legend: Unità di Altavilla: lithofacies arenaceus-sandy (UTAa) and lithofacies pelitic-silty (UTAb); Flysch di Faeto (FAE); Marne argillose del Toppo Capuana (TPC); alluvial deposits (b); colluvial deposits (b7); landslide deposit (a1).

The area has been the subject of studies stratigraphic-structural, which have totally reinterpreted the stratigraphy and local tectonic, recognizing complex compressive structural systems, consisting of east-verging folds and thrust-reverse faults back-verging (middle Pliocene), and Quaternary tensile tectonic structures. These newer structures have entirely disjointed the original syncline structural setting, influencing strongly both shallow and deep water circulation and the morphodynamic evolution of the Montaguto sector. In particular, there is a family of thrust faults in eastern convergence, consisting of some different features as the overlap of the Flysch Faeto on the Marne clay Topcpo Capuana and Altavilla Unit.

3.2 Hydrogeological setting

After the main reactivation occurred in March 2010, hydrogeological and geotechnical surveys were carried out.

Those in-depth analysis had allow to realize a detailed hydrological setting of the area. Considering the several lithotipes detected seven hydrogeological complex can be defined:

- *Detritus complex*: limited and confined areas located to the east of landslide, the complex has a permeability variable from medium to low. The complex due to his reduced extension doesn't assume a lot of importance with reference to the landslide evolution;

- *Alluvial complex*: located along the Cervaro river bank, close the landslide, the complex
  has a permeability ranging between medium and high. In fact, it represents an hydrogeological aquifer location, quite important in terms of productivity with a ground-water level at an average deep between 2 to 4 meters. The aquifer is in direct fluid communication with the river Cervaro. In relation to the hydrological period, it may be an element of draining water circulation, or, conversely, a supply area. However this aquifer doesn't affect the landslide area;

- Silty-clay complex: its outcrops corresponding to the Villamaina clay formation UVM3, they are located in both the right and the left bank of the landslide and are relatively extended. The degree of permeability change from low and very low. This complex, hosting a discontinuous and very low productivity sub-shallow flap, is not important from an hydrological point of view;

- sandstone-conglomerate complex: corresponding to the members of the UVM1 and UVM2 (Villamaina Formation), it outcrops in both right and left landslide, the complex has a mixed permeability with predominantly low degree. The reduced relative permeability makes the complex waterproof.

- clay-limestone-marly complex: their lithotypes outcrop to the east of the landslide body (sequences FAE1c of Faeto Unit outcrop zone). The complex has a fracture permeability with variable degree of permeability between low and medium. From the hydrogeological point of view complex assumes a reduced importance of being home of little flapproduction located in the most shallow layer of alteration.

- Complex limestone-clay : outcropping in both the right and in the left of the landslide (FAE1b), is characterized by a fracturing permeability . The permeability degree varies between medium and high. Similarly to the clay-limestone-marl complex , these one can be one of the less productive among those, with a water circulation, usually localized in the most superficial altered portion . Nevertheless, it should be noted that where the fractures frequency increases, and especially where their opening increases too, groundwater flow tends to be widen, with discontinuous levels and characterized by very different hydraulic loads . In this case, the complex can supplies some important springs as, for example the Caraventa and Del Ponte springs, with an annual flow generally higher than 7.0 l/s.

- Clay complex: outcropping in a small area east of the landslide (FAE1a zone), permeable porosity, very low permeability degree.

Thank to the hydrogeological survey many springs, close to the landslide area were found. The springs abundance was higher in the area located to the north and east of the landslide body. The surveyed springs are all predominantly attributable to undefined limit permeability and more rarely, to the superimposed permeability threshold.

In the area of the main scarp of the landslide an high number of springs were identified with a total substantial flow rate, its value in may is around 2.0 l/s. The springs are supplied from the calcareous-clayey complex. The outflows are channelled within the landslide body.

3.3 Landslide description and history

The first historical information related to instability phenomena along the road up to Montaguto are dated back to 1763, when Borboni realized the first stabilization works. (Il Mattino, ediz. Avellino del 20.7.2009; Vincenzo Grasso - Montaguto e la lezione dei Borboni), There are reports about the royal road and the Cervaro River involvement by the presence of a lobe of deposit.

The IGM hydrographic chart (scale 1:100.000, edition 1890 “174 ° F Ariano di Puglia”) shows, at the time, the hydrographic network of the current landslide system of Montaguto (Fosso Montagna) was developed up to an altitude of 956 m a.s.l. of the "the Mountain" relief (Figure 5) capturing on the way to the valley also the Fosso Nocelle, and therefore, presumably, it was the site of an intense sediment transport due to the substantial hydraulic discharge was flowing into it.

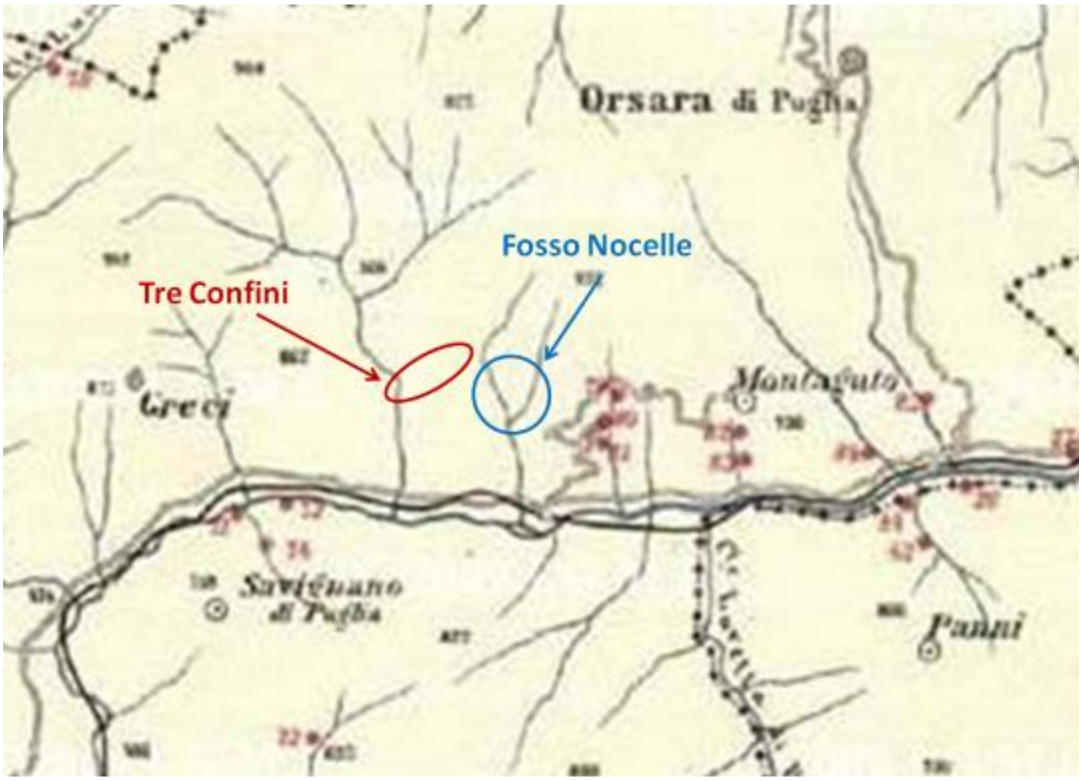

Figure 5 - From the IGM Hydrologic map scale 1:100.000 (N° 174 Ariano di Puglia), edition 1890 (in red: the hydrografic lacuna. In blu: an hydrografic connection).

The connection between the Fosso Nocelle and Fosso Montagna doesn't appear so clear looking at the IGM Topographic map, scale 1:25.000 edition 1955 (174 ° F Ariano Irpino) showing water coming from Fosso Mountain was probably drained to the west, in the Tre Confini stream basin (Figure 6).

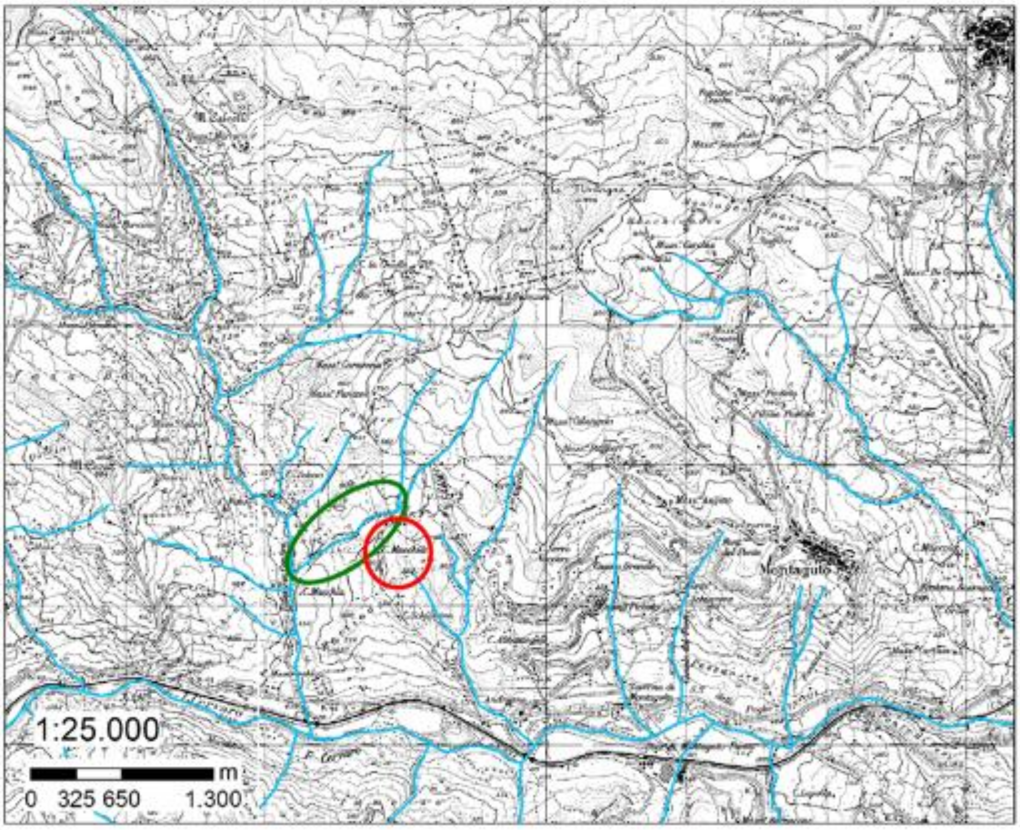

Figure 6 - IGM topographic map scale 1:25.000 (N°174 Ariano Irpino), edition 1955, in green and red, the new hydrographic network setting.

The comparison between the Figure 7 and the"Geological Map of the Apennines Foggiano" 1:200,000 by Crostella & Vezzani (1964), Figure 8, and the Figure 4.6 shows that during the elapsed time until 1964, a landslide has developed from 860m a.s.l.. to an altitude of about 500m a.s.l. along the Fosso Montagna towards the confluence with the Fosso Nocelle, pre-existing deposit were so covered. Evidences collected in the study area reveal the landslide development Figure 4.8, should correspond to the two-year period between the 1957 – 1958.

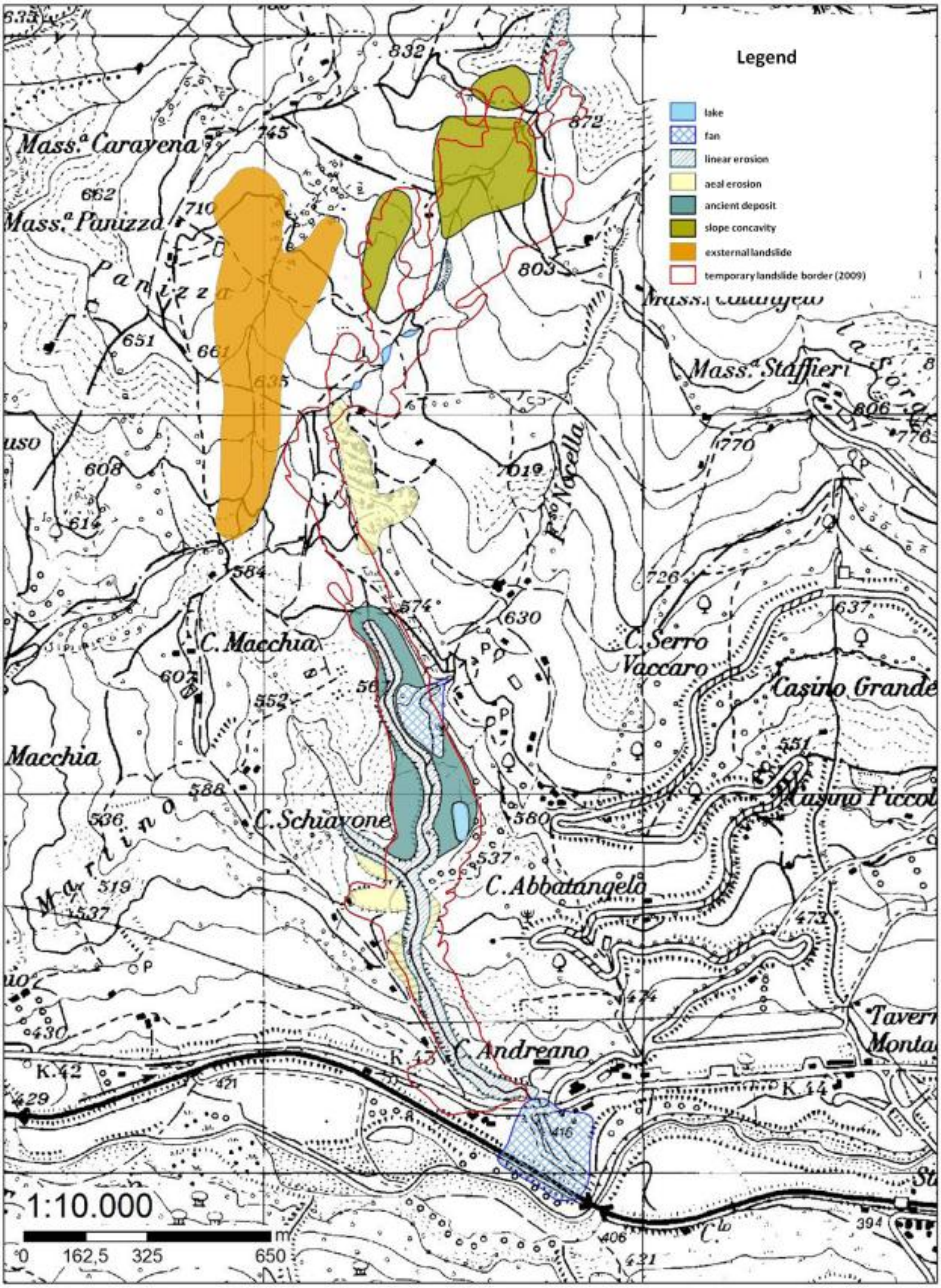

Figure 7 - Morphologic map of the erosion and instability phenomena active, presumably, in the 1955.

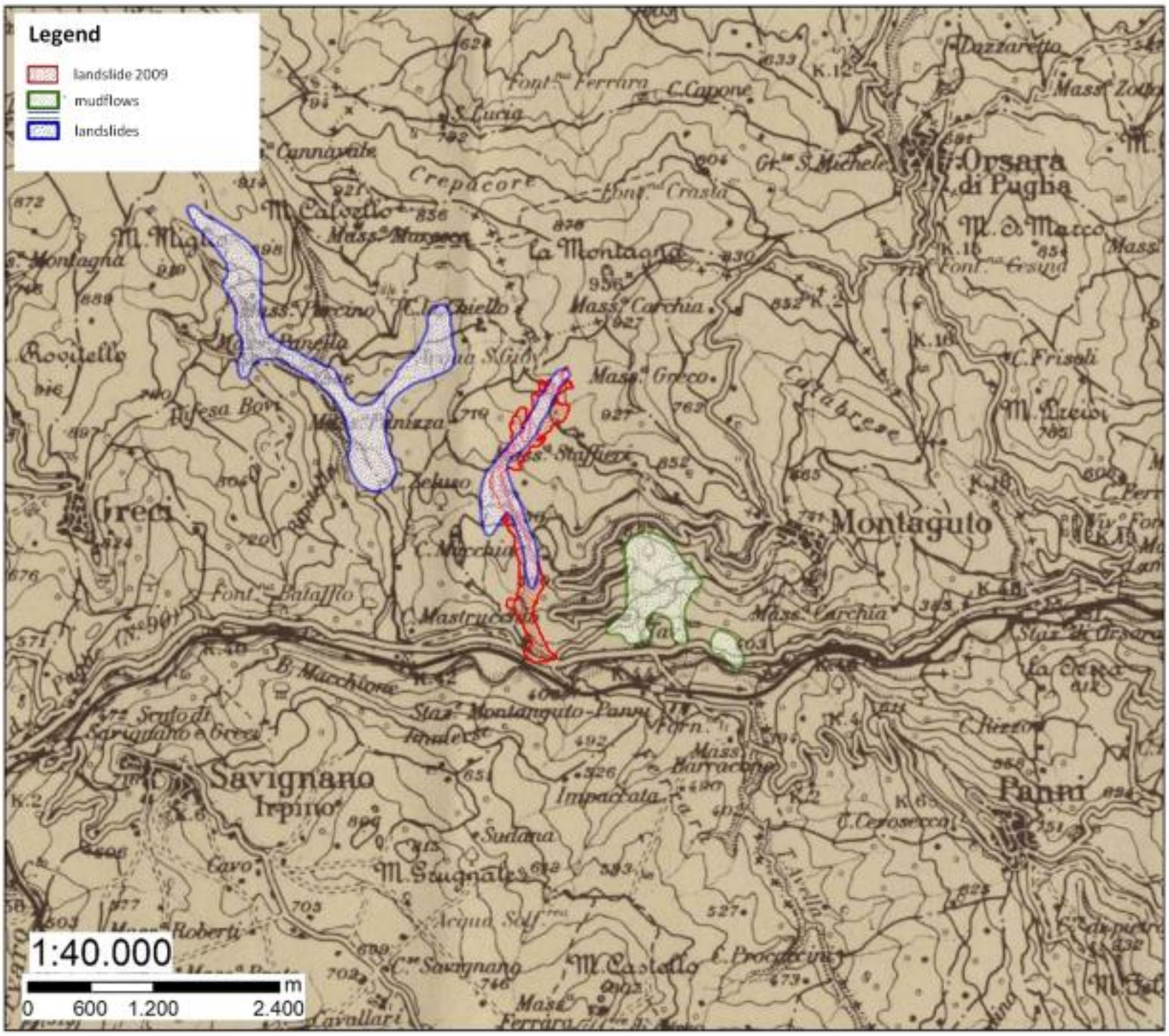

Figure 8 - Landslides reported in the “Carta geologica dell’Appennino Foggiano” scale 1:200.000 di Crostella & Vezzani (1964), based on the IGM topographic map scale 1:100.000, 1955 edition (Foglio n° 174 “Ariano Irpino”.

After an initial paroxysmal phase, the landslide was continuously slowly developing until at least the 1980, when it began a dormancy phase or limited activity during which, as documented by the IGM cartography of 1980 (

Figure 9), there was the restoration of the confluence between the Fosso Montagna river and the Fosso Nocelle, even if the connection with the Tre Confini creek was still saved.

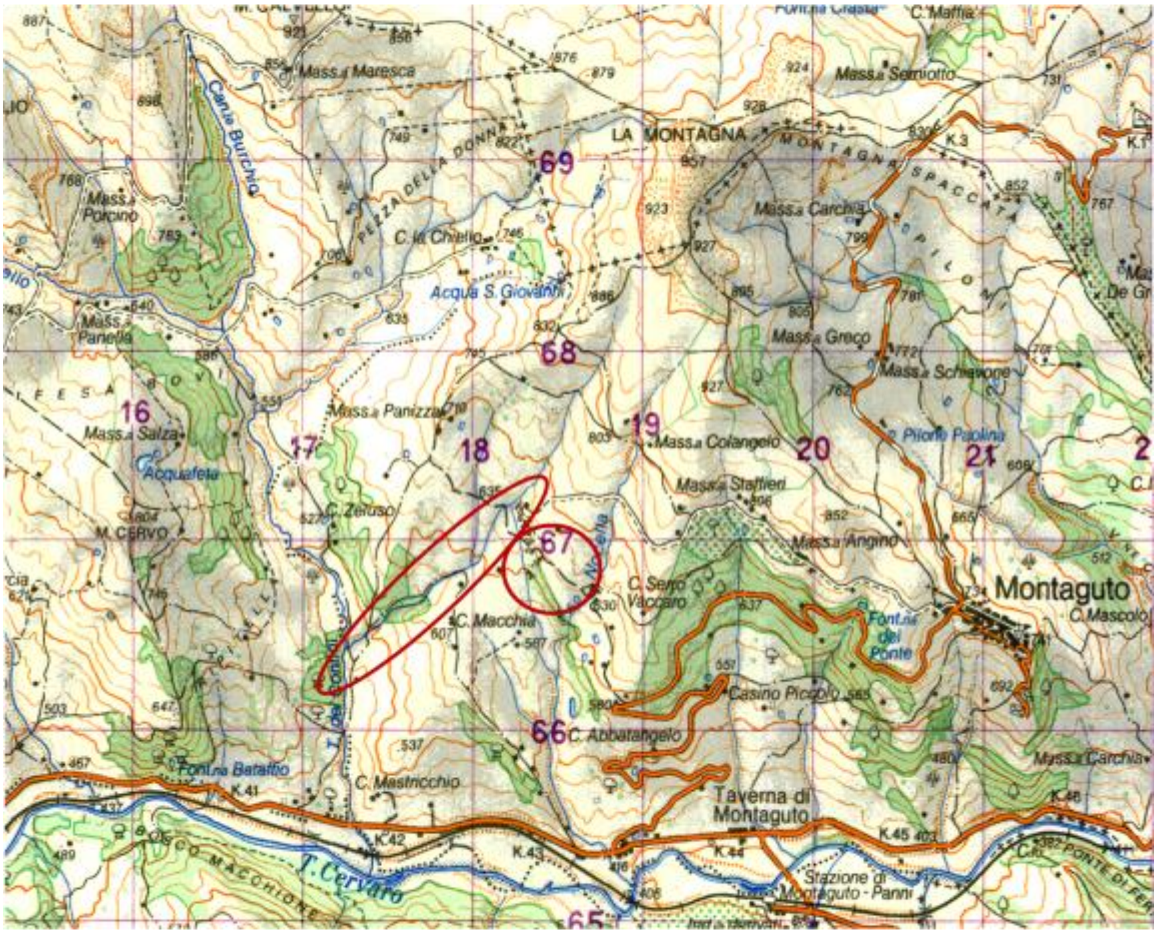

Figure 9 - Topographic map IGM scale 1:50.000 (F° 420 Troia), 1984 edition.

During the next decade the landslide preserved its quiescent/low activity, as documented by the morphology observed in the early '90s, Figure 10, when the evolution of an external landslide interrupts presumably the hydraulic connection between the Fosso Montagna and the Tre Confini, channeling a greater supply of water within the Fosso Nocelle.

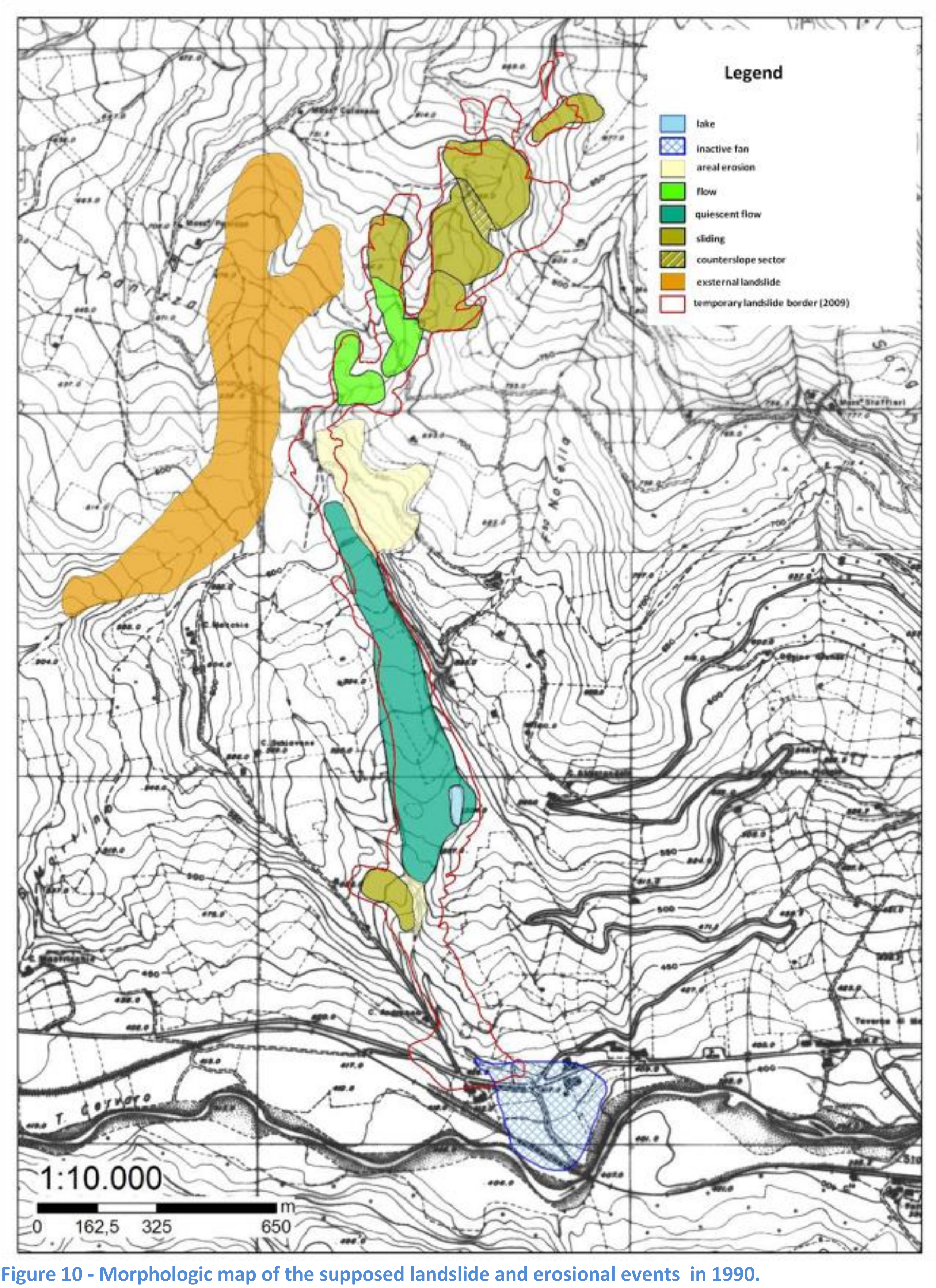

Figure 10 - Morphologic map of the supposed landslide and erosional events in 1990.

In the upper sector the landslide system consists in slow and large rotational sliding, with deep sliding surfaces (between 10m and 20m), and in a wide counter slope zone around 760m a.s.l. in altitude, downstream it’ possible to identify the flow channel up to an altitude of 650m a.s.l.. Further down a large area of erosion is observed on the left bank, while the quiescent flow deposit develops from an altitude of 630m a.s.l. to a height of 500m a.s.l.. Downstream a areal erosion phenomena develops due to the Fosso Nocelle riverbed deepening, causing a sliding process on the right bank, from the 525m a.s.l. altitude.

The IT2000 orthophotos and the Regional Technical Map of Campania, referring to 1998, document the morphological evolution of the described landslide system occurred in the 1990. In particular, the small landslide outside the landslide system continues its development towards the Tre Confini valley and, in the upstream sector of the Fosso Montagna, where creep processes keep slowly growing with the merging of the flow channel, which evolves until the altitude of 650 m a.s.l.. In this sector the connection between the two sections of the hydrographic network is stabilized (Fosso Nocelle and Fosso Montagna) and an increase of the processes of erosion occurred.

Finally, the quiescent deposit is weakly affected by the hydrographic network of the Fosso Nocelle, while, in the downstream sector around 500m a.s.l., an increasing of a gully erosion phenomena in pelitic deposits dell'UTAb occurred, Figure 11.

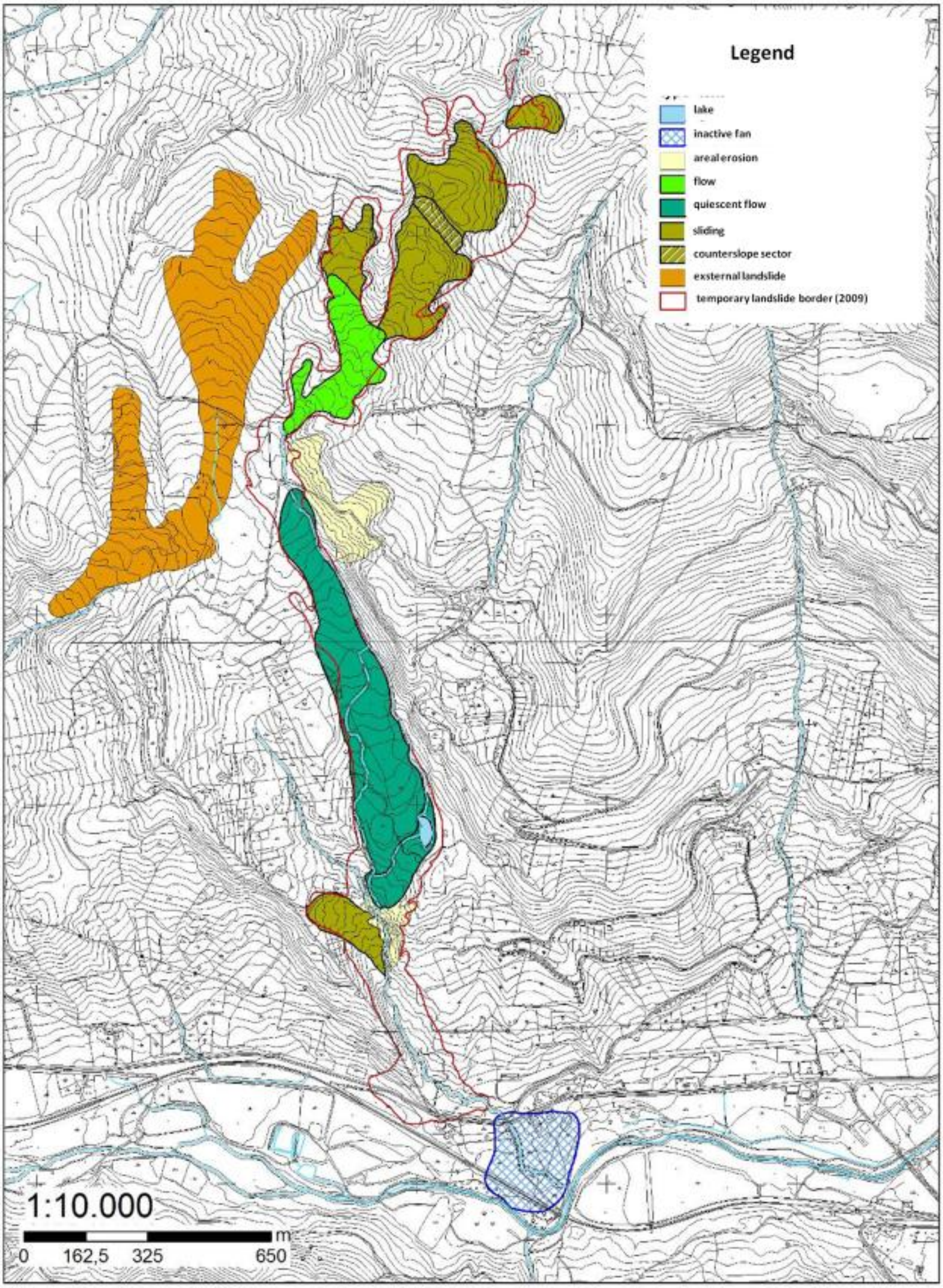

Figure 11 - Morphologic Map of supposed erosional phenomena occurring during 1998, based on the ortophoto analisys IT2000 and on the Technical Regional Map (Campania Region) scale 1:5.000, edition 2000.

This morphological condition is almost unchanged preserved, at least until October 2002. In 2003 and 2004 occurred minor landslide reactivations, the active part (between elevation 830 and 460 m a.s.l.) of the landslide has covered the deposits of the inactive pre-existing landslide.

Others main events occurred during the first months of the 2006, until the May 12th 2006 when the landslide, has continued to advance towards the bottom reaching and interrupting the highway, Figure 12.

Figure 12 - Image of the landslide taken from the opposite slope, May 2006.

The same dynamic occurred also in 2009. But On March 10th, 2010 due to the heavy rainfall, the flow reactivated with a higher intensity and in the following weeks it destroyed road and railway stretches, Figure 13 and *Appendix 4.*

Figure 13 - Landslide image after the March 10th 2010 event, showing the flow reaching the round and railway, (from Google Earth).

In this case, although there were no causalities, the damage to the infrastructures caused the completely interruption of the transports through the only two ways of connecting between the region of Campania and Puglia.

Figure 14 - Interruption of the main rail way network.

3.4 GBInSAR Monitoring of the Montaguto earthflow

The monitoring activity was carried out through the integration of different techniques. The Department of Earth Sciences of the University of Florence was responsible for the management, together with the ELLEGI S.r.l., of the installation of a ground-based real-time monitoring system (based on SAR interferometry technique GB-InSAR LISAlab); and in the same time had the task to project and plan the emergency and stabilization works, executed by the INGEO S.r.l..

The GBInSAR LISAlab provides displacement measurements over areas up to few square kilometres with sub-millimetre precision and high temporal frequency of acquisition (up to ten scans per hour).

The monitoring is performed through the production of interferograms, which are obtained using pairs of averaged sequential images.

Depending on the method of installation and from the distance between the sensor and the observed scene, different properties of SAR images acquired with the technique GBInSAR LiSALab, and in particular the value of spatial resolution exist. The resolutions in range (distance) and azimuth (direction parallel to the movement of the sensor) are given by the following two relations:

$$\Delta r = \frac{c}{2B} \qquad \Delta r_x = \frac{cR}{2Lf_c}$$

the longitudinal dimension (azimuth) of the resolution cell is effected in inverse proportion by the total extent of the covered stretch along the antennas track (L) and the central frequency of the transmitted signal (fc), while the transmitted frequency band width (B) affects only the second dimension (range), always in inverse proportion, (Figure 15)

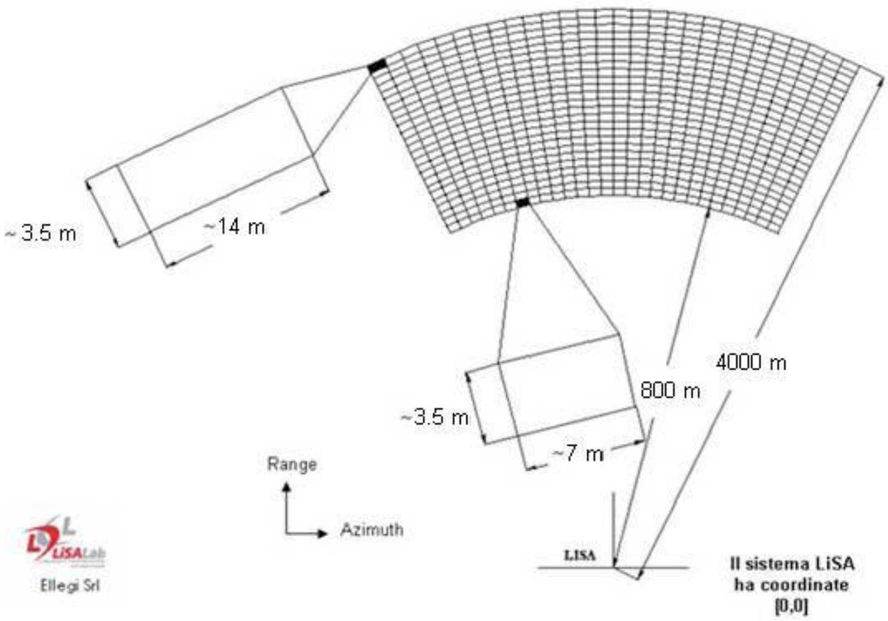

Figure 15 - GBInSAR monitoring system characteristics.

In according to the selected parameters, the theoretical resolution in range in this case is approximately 3.5 m, while the azimuth one, varies between about 3 m and 14 m. The radar images were processed on a spatial window in the direction that range in size ranging from 800 m to 4000 m and in azimuth direction from -1600 m to 1600 m, Table 2.

Table 2 - GBInSAR technical description

Minimum observed area distance	800 m
Maximum observed area distance	4000 m
Displacement estimate accuracy	0.5-0.7 mm
Theoretical resolution in range (constant)	~ 3.5 m
Theoretical resolution in azimut a 800 m	~ 3 m
Theoretical resolution in azimut a 2000 m	~ 7 m
Theoretical resolution in azimut a 4000 m	~ 14 m
Scan time interval	3.5 min

Given the phase difference of the backscattered signal in different times, it is possible to estimate the displacement. The use of GB-InSAR as a landslide monitoring technique is well documented in the last decade, with applications in different risk scenarios (Tarchi *et al.* 2003; Canuti *et al.* 2003; Casagli *et al.* 2009; 2010). In some cases, the system was used for controlling slope movements, threatening one or more lifelines (Casagli *et al.* 2008; Gigli *et* *al.* 2011), as in the Montaguto site. However, the velocity of this landslide at the beginning of the reactivation was high in comparison with the usual resolution power of the GBInSAR systems: in this sense, the Montaguto case history represents a very interesting benchmark for the application of this technique.

On April 29th, the apparatus was installed on the opposite stable slope located at the distance of about 4 km, in order to measure the component of the movement along the line-of-sight of the radar, Figure 16. From the installation site, the lower part of the landslide is visible and a very clear image of the toe can be obtained where, during the emergency phase the highest displacement velocity was reached.

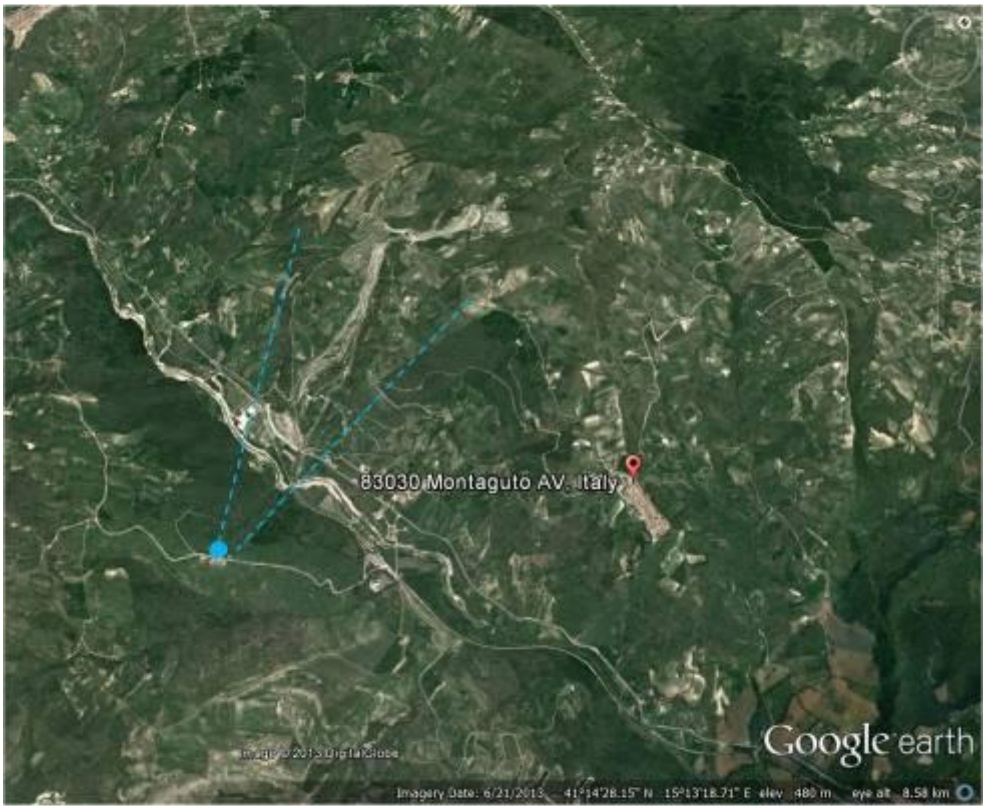

Figure 16 - Location of the GBInSAR monitoring system station.

The GB-InSAR system has been continuously acquiring images since the 29th of April 2010, and produces multi-temporal deformation maps (Figure 17), cumulated displacement maps (Figure 18) and time series of displacements.

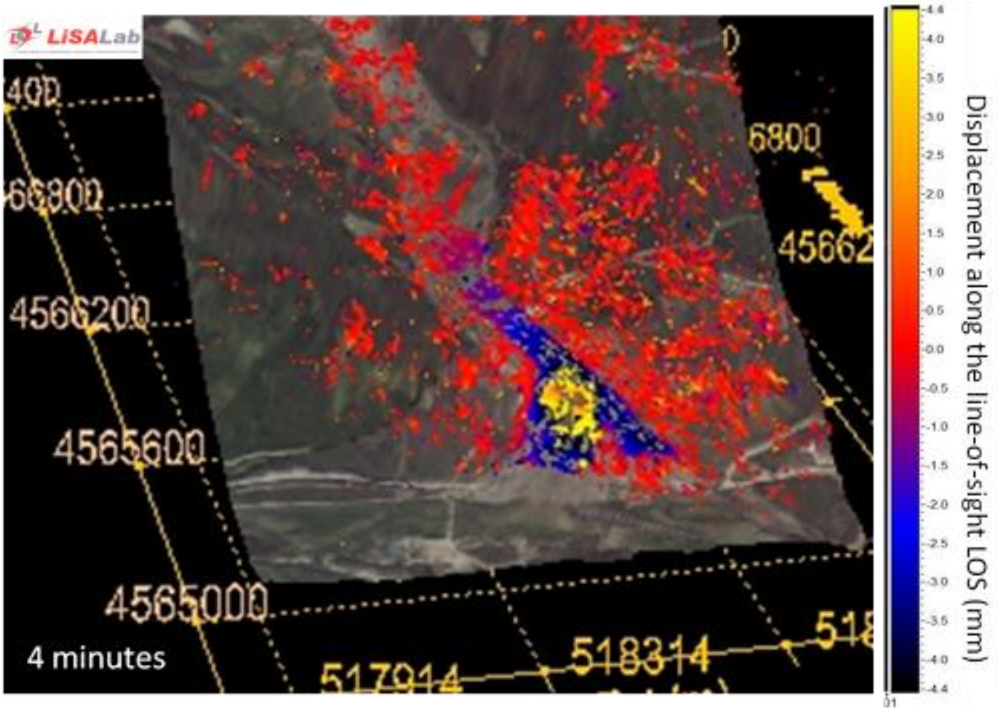

Figure 17 - Interferogram covering a period spanning from 21.04 to 21.08 of 01/06/2010. Negative values indicate movement towards the instrument.

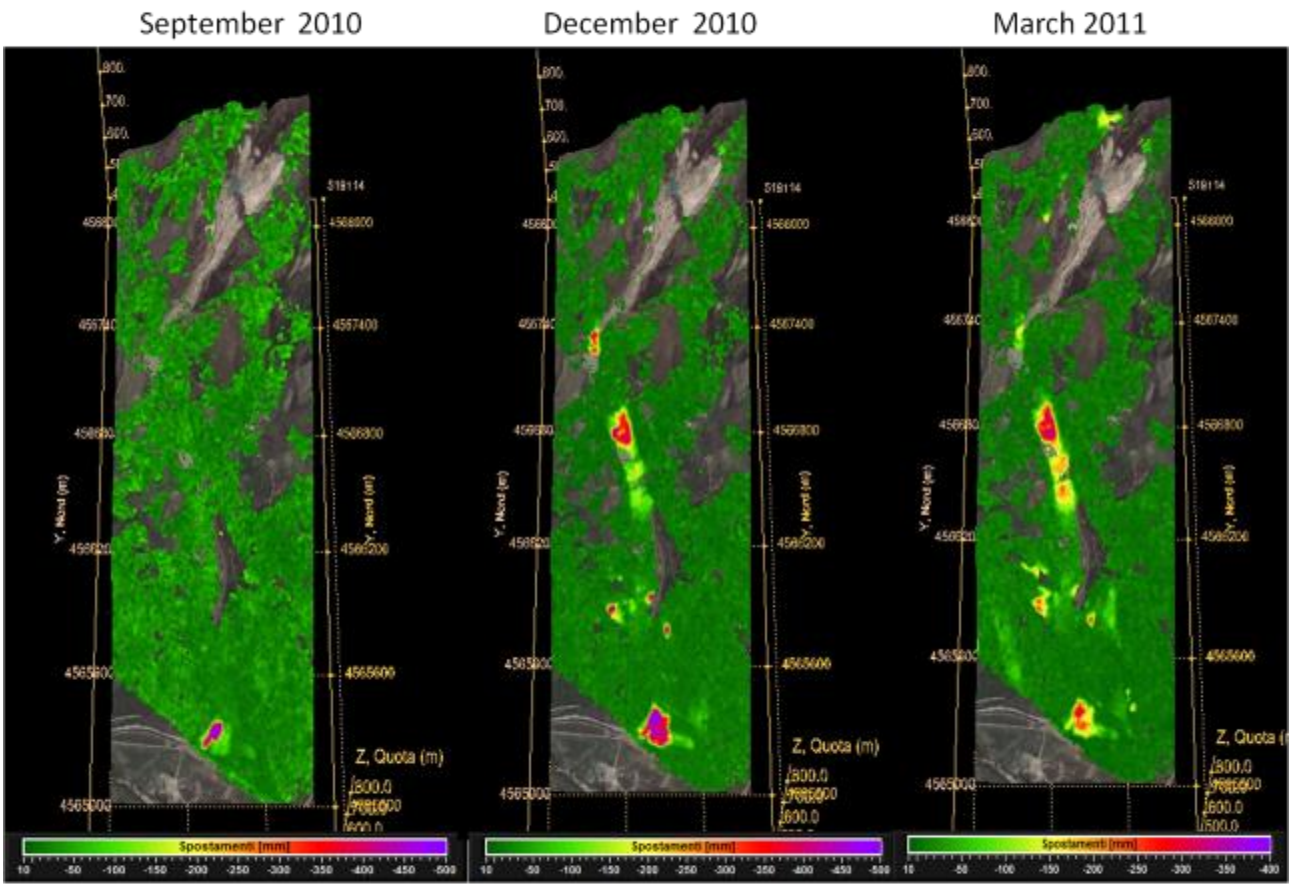

Figure 18 - Map of cumulated displacements (mm) recorded during the months of September 2010, December 2010, and March 2011. Negative values indicate movement towards the instrument.

The system was adapted to the landslide features, and the revisiting time lapse was reduced to 3,5 minutes, in order to assure the correct detection of the movement and a real time monitoring.

The displacement rate reached, in fact, values of about one meter per day (maximum recorded velocity 2.9 m/day on June 1st, 2010), also with significant intraday variations.

In the framework of this landslide velocity pattern, the Civil Protection Department started with large earth-moving works at the toe with the operational support of the Army. Thanks to these activities it was possible to re-open the railway on June 7th, 2010 and the road SS 90 on July 10th, 2010.

The GBInSAR system became a key element in the work planning, reporting on a daily basis interferometric data that drove the interventions, and also suggesting when to stop in case of abrupt accelerations.

This first emergency phase ended in July, when the displacement rate decreased, thanks to the works and to the dry season.

Since a daily bulletin was extremely necessary to realize, a suitable and an easiest as possible way to report the interferograms interpretation was identified.

Based on the first interferograms analysis, the recognition of sectors characterized by different displacement speed, was soon possible.

In Figure 19 is shown, as example, the interferogm relative to the 18th May, 2010, in which four different sectors are distinguishable :

- the portion located at the landslide bottom, corresponding to the monitored central area, which has been identify as “A Sector”
- the landslide toe upper part, named “B Sector”;
- the left landsliede toe side, named “C Sector”;
- the right landsliede toe side, named “D Sector”;
- the area approximately located between 530 m and the elbow portion of the landslide (610 m), sub sequentially identified (Figure 20) (see Chapter 5), called “E Sector”.

The Figure 21 highlights the optical image of the GBInSAR monitoring system landslide view, with the location of the monitored sectors.

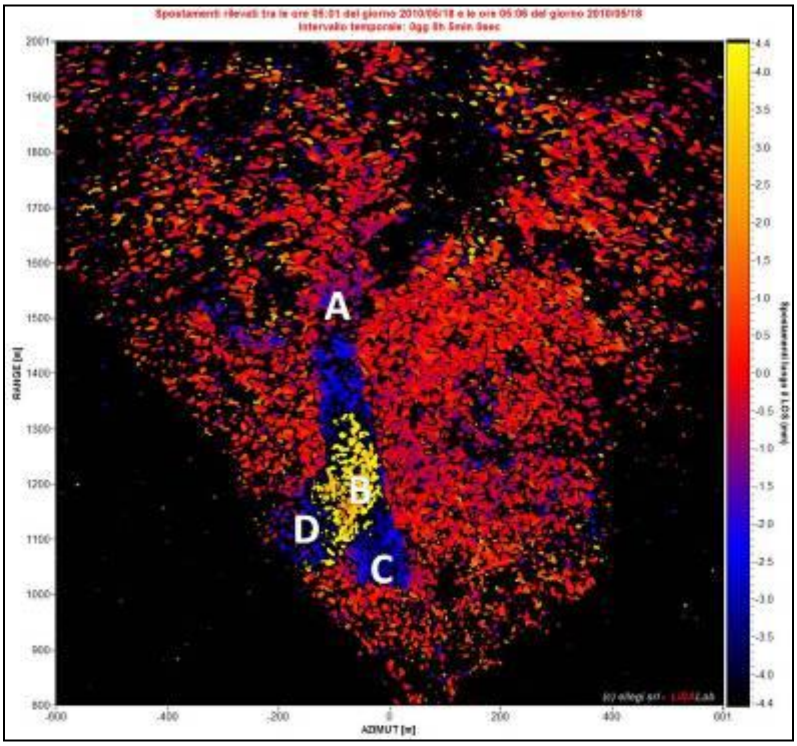

Figure 19 - SAR interferogram (foot view zoom) refers to 4 minutes interval time of between 05:01 GMT (07:01 local time) and 05:06 GMT (07:06 local time) on 18th, May 2010 and location of the A, B, C and D monitored sectors.

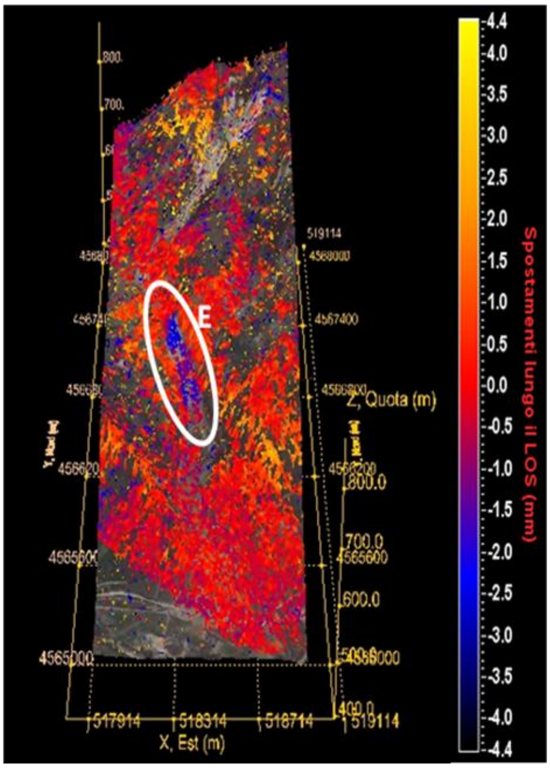

Figure 20 - SAR interferogram related to 4 hours interval time, between 01:58 GMT (03:58 local time) and 05:57 GMT (07:57 local time) on August 1st, 2011 and the location of the "E Sector".

Figure 21 - Monitored sectors detection on the optical image based on the GB-InSAR monitoring system.

3.5 Others monitoring techniques

The real-time monitoring is based on the production and interpretation of interferograms, or of georeferenced deformation maps, related to defined time laps, which allow to estimate the displacement rate. These products were initially geo-referenced using the digital terrain model (DTM) realized thought the application of the LIDAR technique. Due to the substantial change in the topographic profile occurred during the landslide activity months others monitoring techniques or surveys where required, these are listed below:

- laser scanning survey (DST-UNIFI);
- using of optical and thermal images (DST-UNIFI);
- robotized total stations (RTSs) monitoring system (CNR-IRPI Torino);
- geophysical and geognostic surveys (UNI SANNIO).

3.5.1 Laser scanning survey

A detailed survey of the most critical portion was performed to obtain an updated topographic setting, supporting the monitoring activity. This operation was carried out on

January 2011, 26th and 27th together with the beginning of the design work of the landslide foot. The result was, however, also used for design purposes and for the suitable works location.

Overall, the topographic survey was then performed to obtain the following results:

1. reconstruction of a detailed 3D model of the study area;
2. georeferenced map realization for the works location;
3. volumes calculation.

The scan has involved an area of approximately 55,000 m^2

Figure 22). The environment is characterized by the presence of significant morphological roughness elements and anthropogenic disturbance as all the man at work on the landslide foot. In order to minimize the shadow zones, the acquisition plan was carried out from 7 different positions, 3 from the road, and 4 on the landslide body (Figure 23).

Figure 22 - Laser scanning observed area.

Figure 23 - Scans position location map.

For each scan location were made low resolution overview scans, shooting and high-resolution optical scans, to achieve a suitable resolution. In this way over 10 million points were obtained.

Figure 24 shows the total points cloud obtained from the union of low-resolution points cloud related to each scan position.

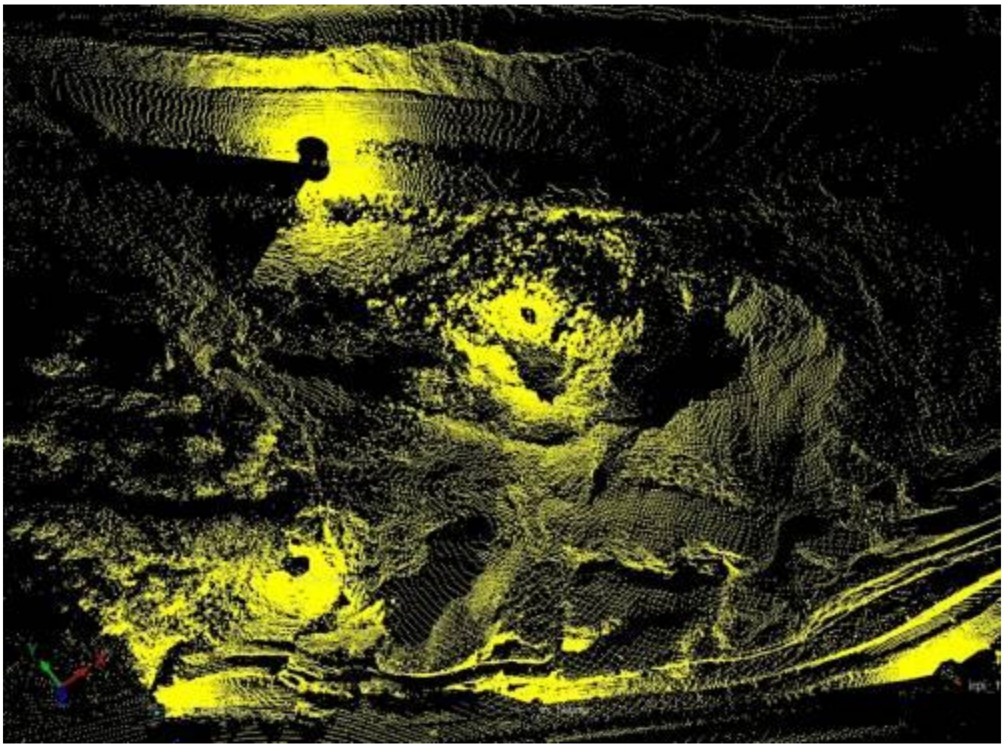

Figure 24 - Total points cloud obtained from the combination of the low resolution scans.

To allow the reconstruction of the global points cloud, the installation of 14 reflectors into the observed area was necessary; their localization was carried out using an high definition GPS survey (
Figure 25).

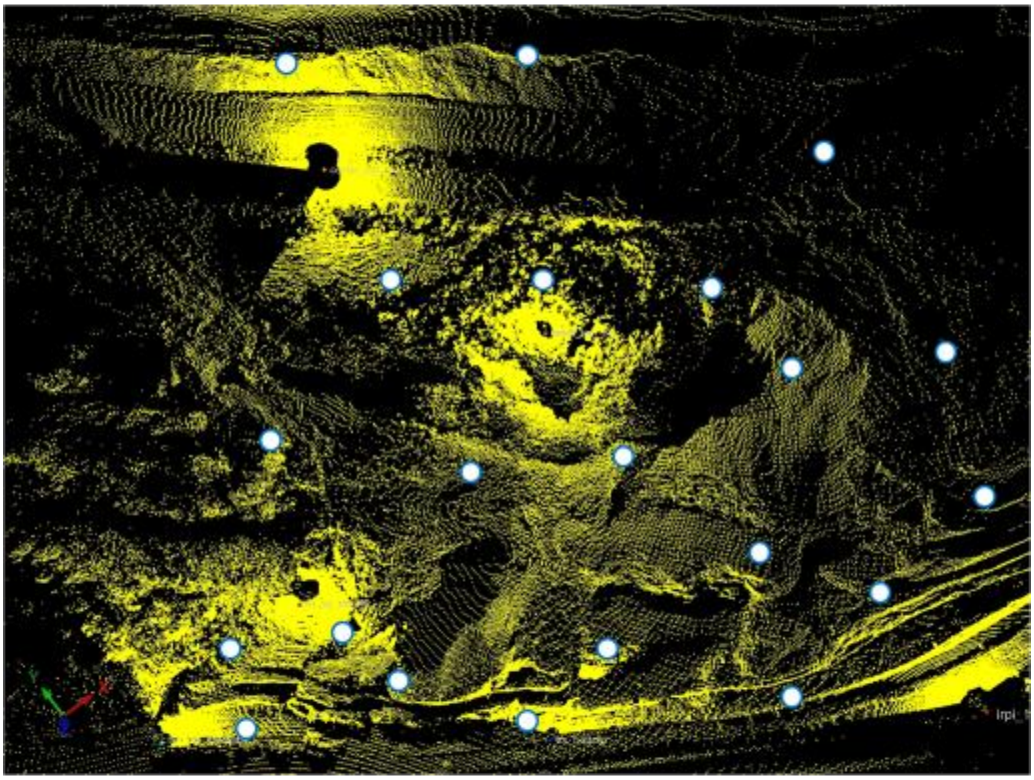

Figure 25 - Total points cloud and reflectors location.

The raw data coming from each scan position where laid out on the base of e common cartographic system. The area along the landslide banks is poorly vegetated, however, in addition to create limited shadow zones, it represents e disturbing element for the interpretation phase. To avoid it the vegetative component was deleted manually or using automatic algorithms.

Thanks to the high resolution the points cloud from the seven scans, the entire study area covering, corresponding with the D monitoring sector, was realized. (Figure 26 e Figure 27)

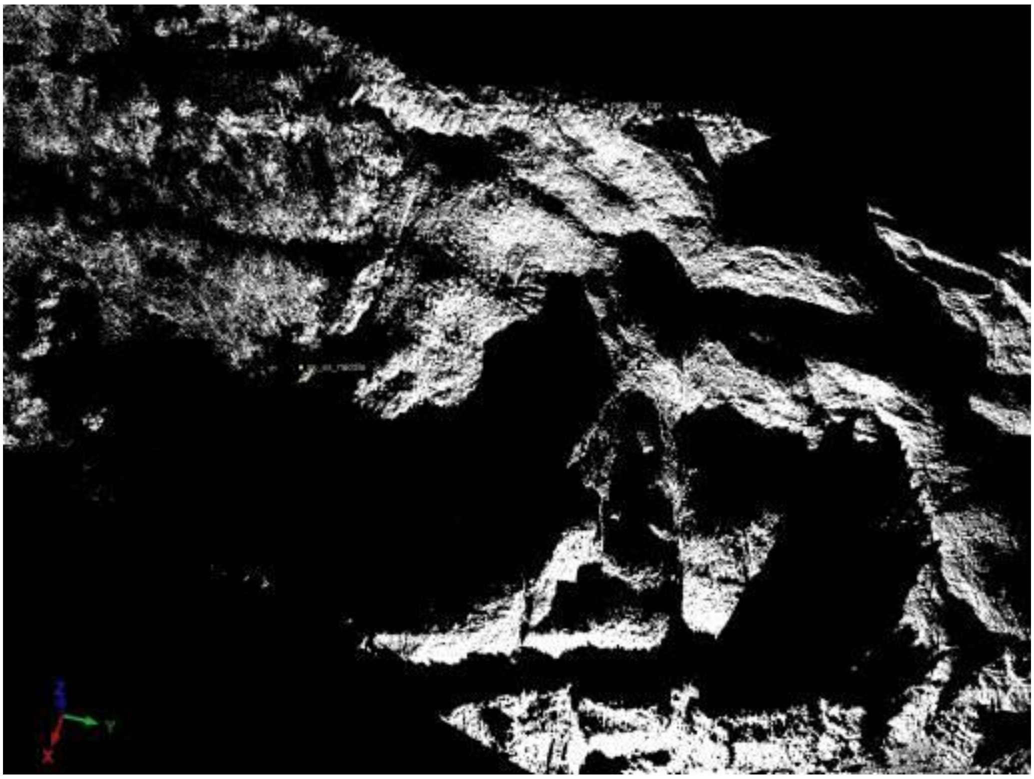

Figure 26 - Intensity coloured 3D points cloud realized from the scan position n°2.

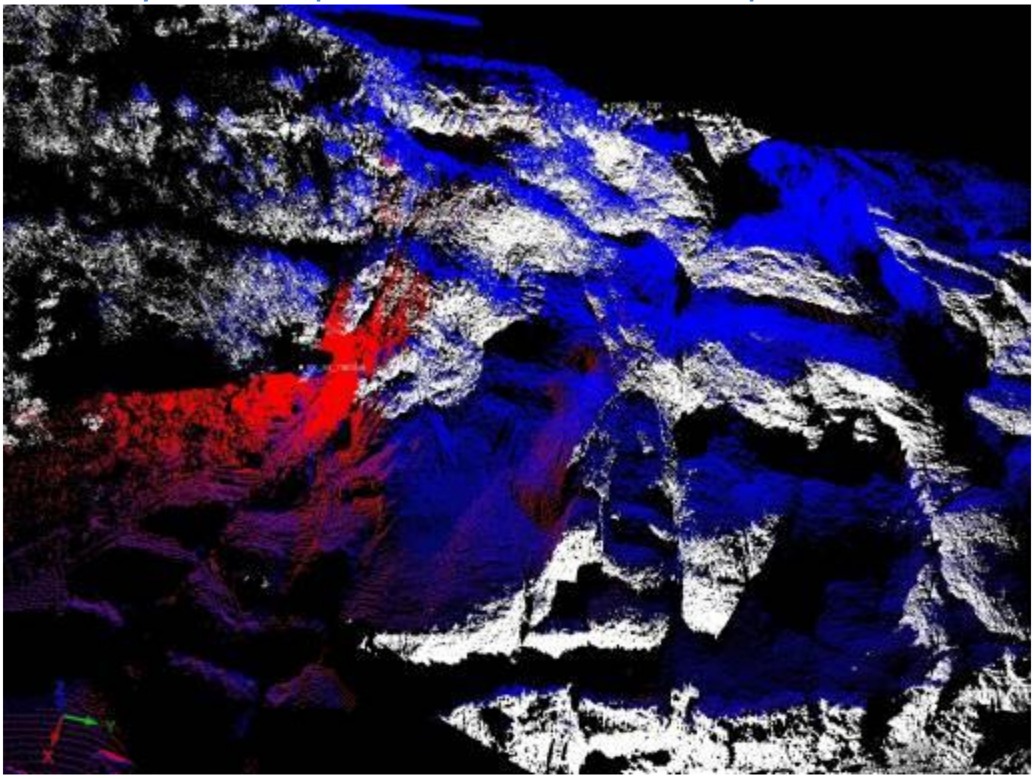

Figure 27 - 3D points cloud generated from the combination of the scans realized from the position n°2,4 and 5.

The obtained 3D model is reported in Figure 28 and its relative contour lines with equidistance 1.0 m in Figure 29. Figure 30 shows the overlaying of the contour lines to the digital terrain model.

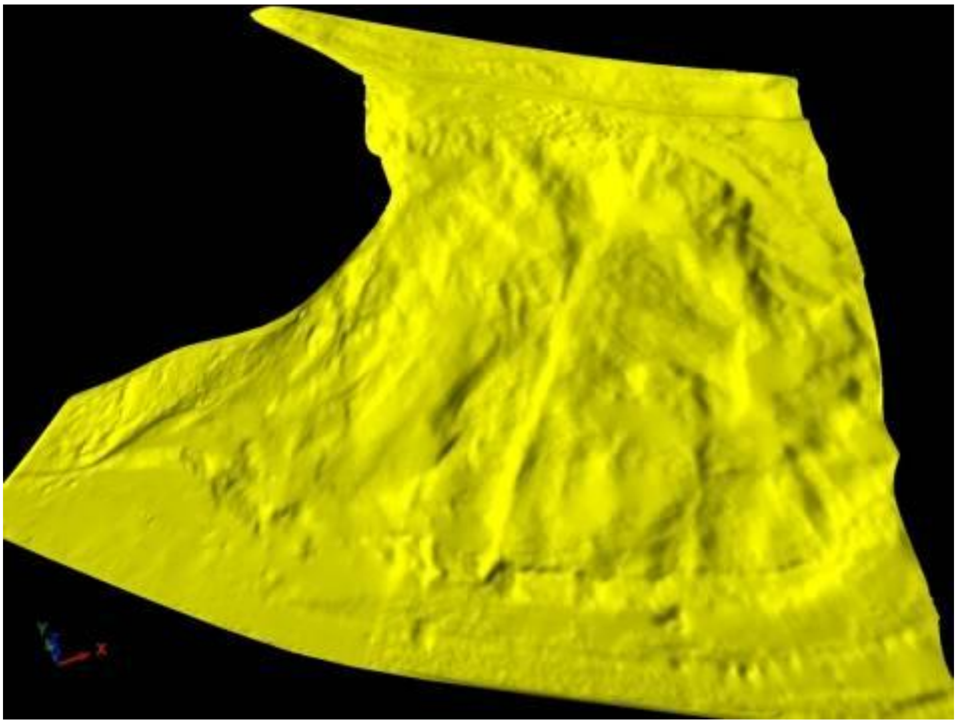

Figure 28 - Terrain surface obtained through the points cloud elaboration.

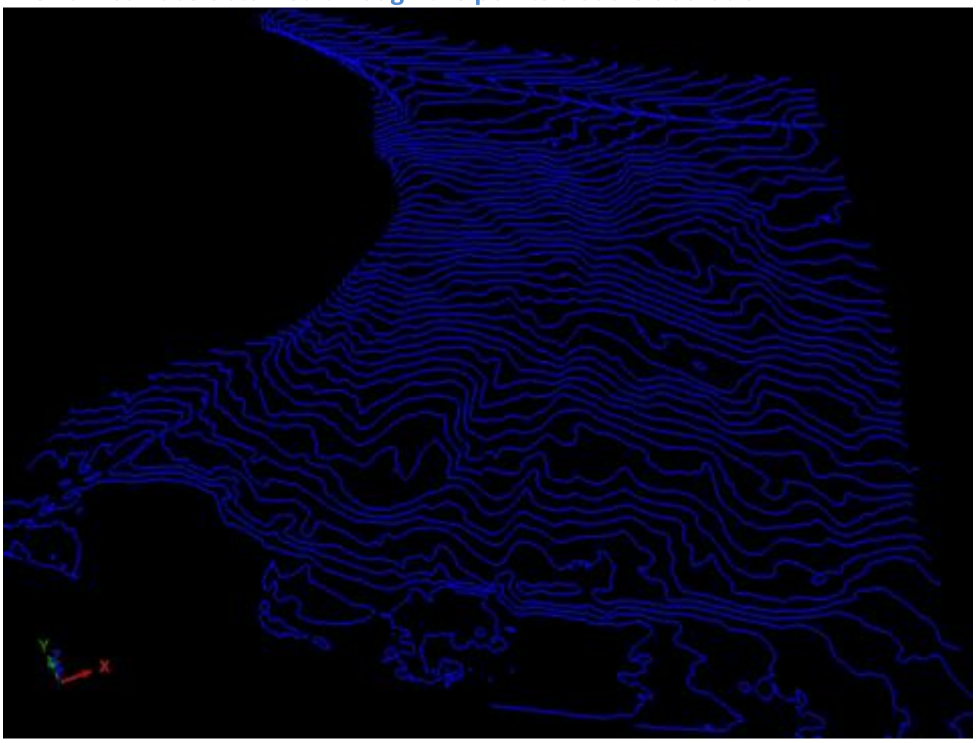

Figure 29 - Contour lines (equidistance 1m) extracted from the DEM shown in the Figure 14.

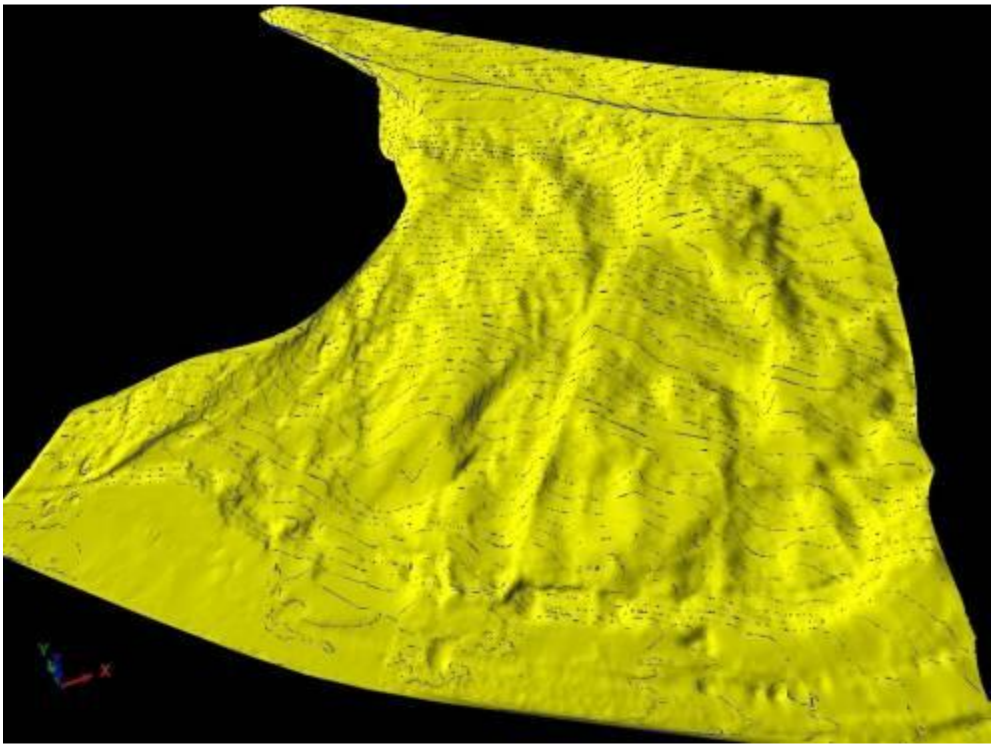

Figure 30 - Overlaying of the contour lines to the digital terrain model.

3.5.3 Optical and thermal images

During the emergency phase the GBInSAR instrument was partnered with a webcam (for a visual calibration of SAR images), and with a thermal infrared camera during the first weeks. Latter, thanks to the thermal infrared properties and the ability to detect different temperature zones, allowed a very accurate control of water flow paths and drainage directions, providing useful data for the earth-moving works. The Figure 31 points out the location of the wettest zones within the landslide toe, represented by the low temperature areas (darker shades).

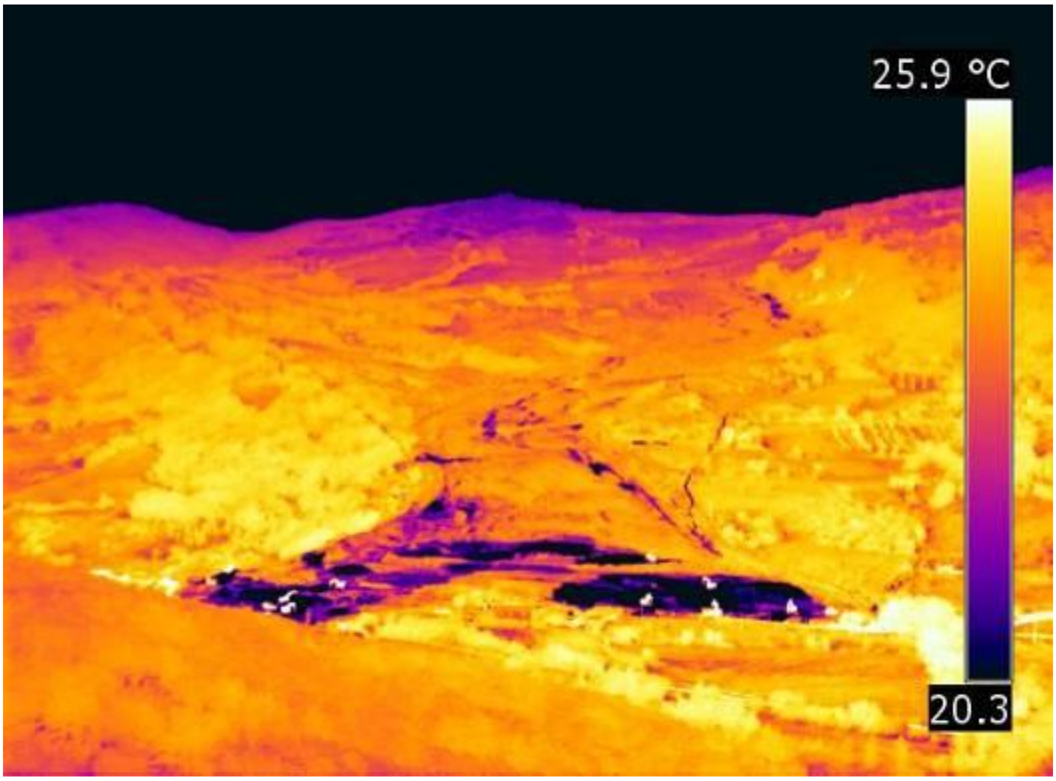

Figure 31 - Thermal infrared image take on May, 5th 2010, from the GBInSAR location.

The webcam, installed into the monitoring station, acquires continuously an optical image of the landslide toe every 15 minutes; starting from the April, 29th 2010. (Figure 32).

Figure 32 - Optical image of the Montaguto earthflow (acquisition time: 23/05/2010 – h 8.19 a.m.); and inside view of the GBInSAR installation point.

3.5.4 The Robotized Total Stations (RTSs) monitoring system

Three RTSs were installed as well by the CNR-IRPI of Turin, on the stable ground along the western side of the Montaguto landslide. The first station (RTS-1) was installed on the west side of the landslide source area at an elevation of 750 m on 29 April 2010 to monitor the area not covered by the GB-InSAR system. A total of 19 benchmarks (optical prisms) were installed primarily in the landslide crown area, with one reference benchmark located at stable terrain outside the landslide. The optical prisms were located at distances ranging from 116 to 430 m from RTS-1. At the location of RTS-1. The second monitoring station (RTS-2) was installed on 9 June 2010 near the boundary between sector A and sectors B1 at an elevation of 670 m. RTS-2 measured 15 benchmarks inside the landslide deposit at distances ranging from 148 to 1008 m from the station. The third monitoring station (RTS-3) was installed on 30 April 2010 at an elevation of 410 m. This station monitored surface movements in sector C and provided near real-time information to the local authorities who were responsible for the safety of the workers on or near the active landslide. RTS-3 monitored 18 benchmarks inside the landslide deposit and two prisms in stable terrain outside of the landslide deposit at distances between 62 and 230 m from the station. (Figure 33). The RTSs monitoring results were reported in a daily (currently weekly) bulletin as well.

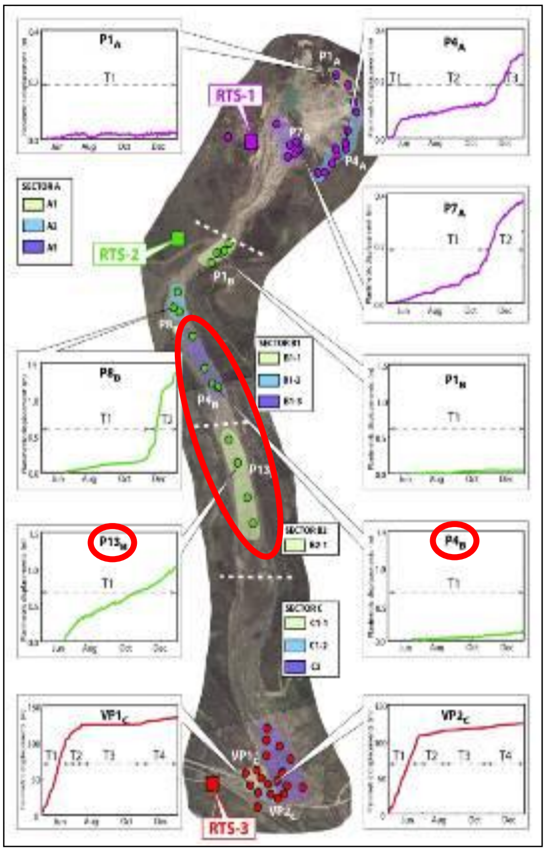

Figure 33 - Topography monitoring network of the Montaguto landslide in the period May to December 2010. The red, green and violet points indicate prisms position, while the squares indicate the Robotized Total Stations. (based on: Giordan *et al.*, 2013)

3.5.5 Geophysical and geognostic surveys

Many of geotechnical surveys were carried out during the years from 2006 and 2010:

- 2 geognostic survay : 60 m depth – n°4 samples – n° 2 SPT (Amato e Dubbiosi, 2006);
- 7 geognostic survey : 30 m depth – n°4 samples – n° 2 SPT (Amato e Dubbiosi, 2006);
- 9 geognostic survey : 20-30 m depth – n°4 samples taken for each – n° 10 SPT (Guadagno 2010);
- 7 seismic refraction tomographies: 120 m length (Guadagno, 2010).

In order to illustrate the results of the surveys, considering their distribution within the more critical landslide areas, a description for the monitored sector is here reported.

The *Appendix 1* contains the surveys location maps, and their detailed results. In the area of the A Sectors, corresponding to the landslide toe, many geotechnical surveys have been carried out: two continuous core surveys (S4 and S5, Figure 34 A) and four static penetration tests (CPT - Cone Penetration Test - 6, 7, 8, 9 Figure 34 A) in 2010 (Guadagno, 2010) and seismic refraction tomographies (S1b, S2b and S3b, Figure 34 B).

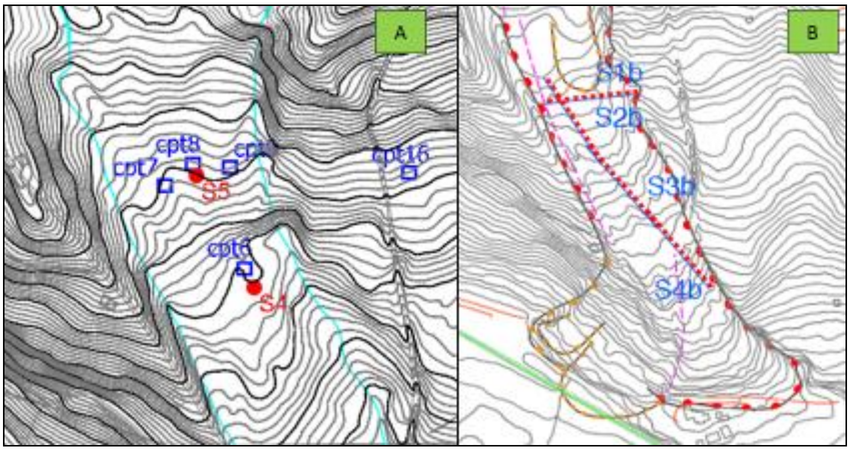

Figure 34 – Location of the surveys within the "A Sector", continous core (A) and seismic refraction tomographies (B). (Modified from Amato and Dubbiosi, 2006; Guadagno 2010).

With regard to the two surveys, these have reached a depth of 40 m and 30 m from ground level and, respectively, the water table was measured at 3.5 and 2.0 m depth. From the evidence obtained from the surveys and penetration tests a geolithological section was realized; from which it appears that landslide deposit reaches a depth of 23 m below ground level and it lays on the local substrate (Figure 59).

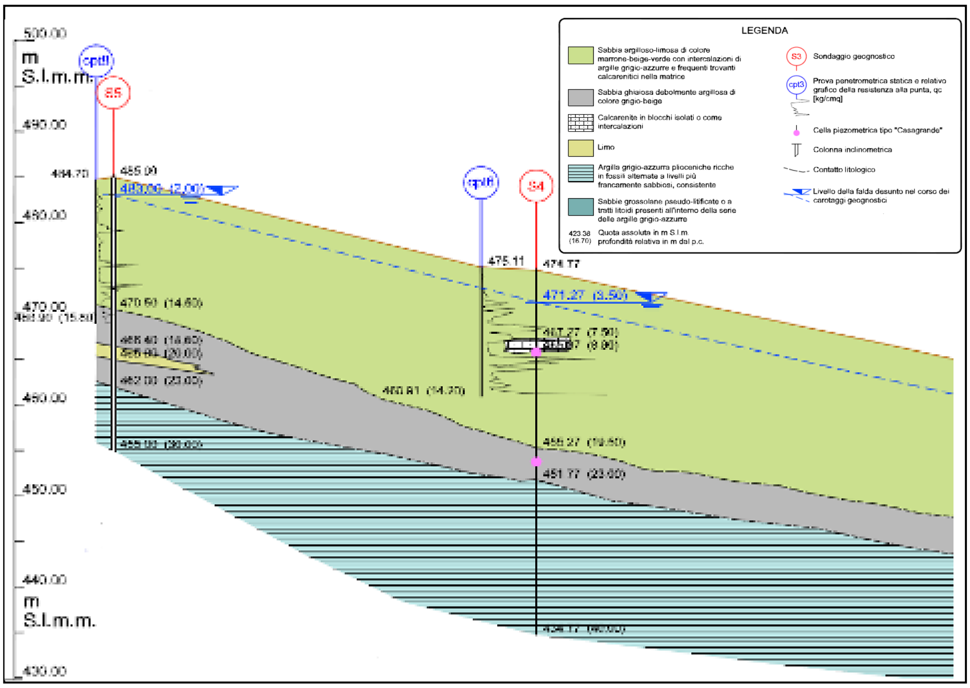

Figure 35 – Geological section obtained from the core surveys. (Modified from Amato and Dubbiosi, 2006).

With regard to seismic refraction tomography, Figure 36 shows the seismostratigraphic interpretation derived from the S2b and S3b: the results differ from those obtained in the core surveys, in fact, the S4 survey, slightly shifted to the east, was located at roughly half the tomography S2b. From the tomography it is possible to detect the deposit landslide depth at about 5 m while from core survey it results at 23 m depth: this may indicate that from 2006 to 2010 the portion of the soil involved in the landslide in this area has declined, probably due to the sliding of the material downwards.

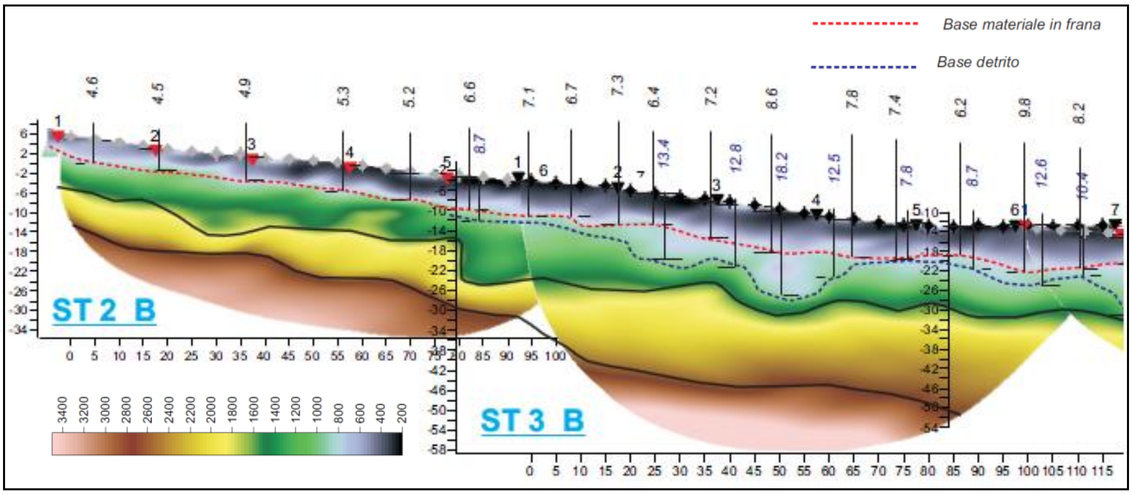

Figure 36 – Subsoil seismic stratigraphy, (Guadagno, 2010).

In the area of the B Sector in 2006 a continuously cored borehole (S3, Figure 37 A) and three static penetration tests (CPT - Cone Penetration Test - 3, 4, 5, see Appendix A and detailed in Figure 37 A) (Amato and Dubbiosi, 2006), have been made. While in 2010 a survey and a seismic tomography have been carried out (S7 and S4b, Figure 37 B and C).

The S3 borehole has reached a depth of 30 m (with flap measured at 4.8 m) and the S7 24 m from ground level; the landslide deposit thickness it is, respectively, 17m to 22.3 m. From the evidence obtained from the survey and from the penetration tests of 2006 a geolithological section was realized, extended from the previous sector (Figure 38).

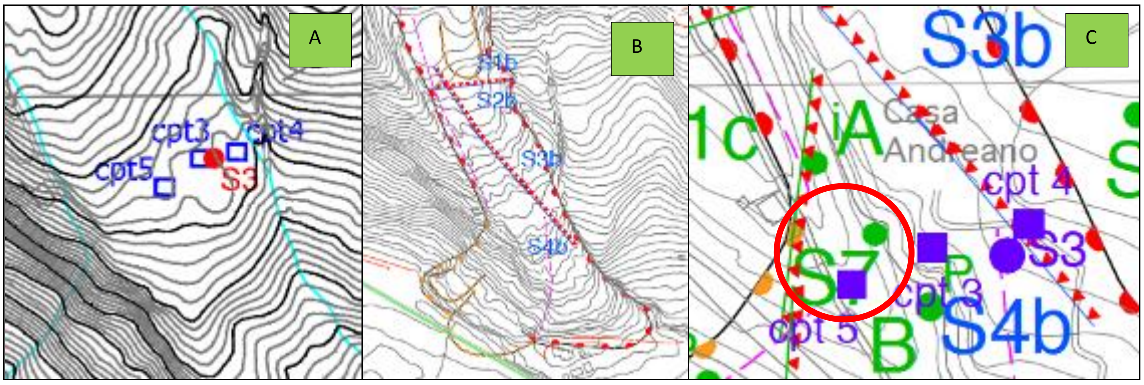

Figure 37 – Location of the all surveys realized within the B Sector. (A, cone penetration tests and borehole; B and C, seismic tomography).

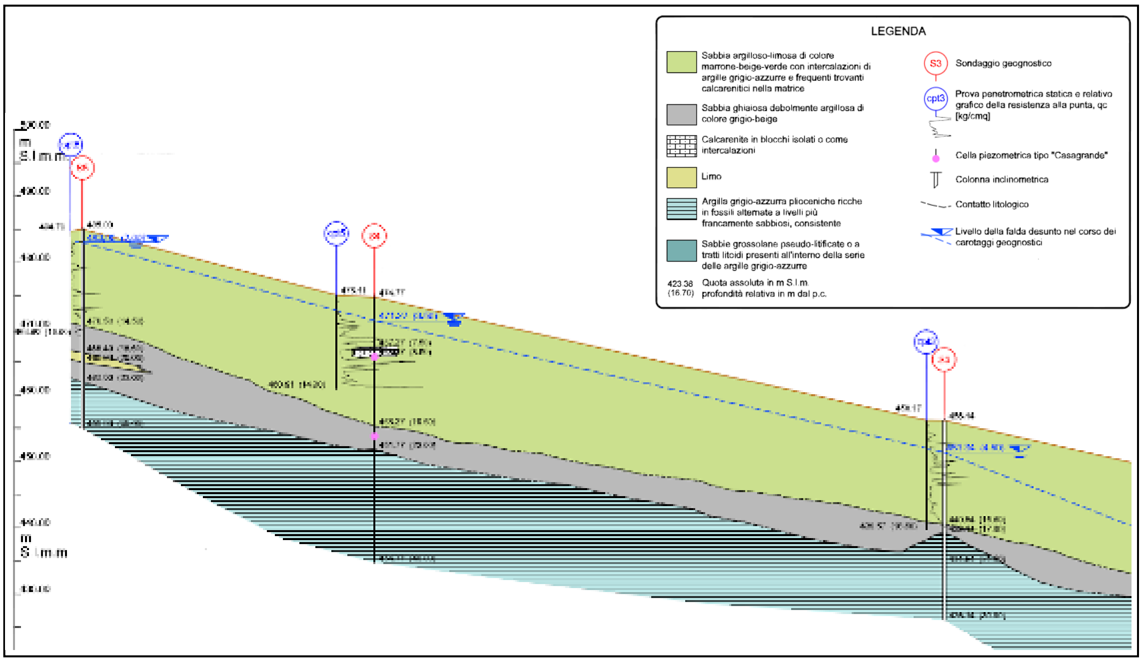

Figure 38 - Geolithological section obtained from the core surveys. (Modified from Amato and Dubbiosi, 2006).

The seismostratigraphic interpretation was assembled to those shown for the "A Sector". As in the previous case, the thickness of the landslide material in 2010 is less thick than in 2006, in fact the survey S3 coincides roughly with the final part of the tomography. However, if for the first the landslide thickness is 17 m, for the second the maximum depth reached is about 11 m (Figure 39). The material is probably slipped down as well.

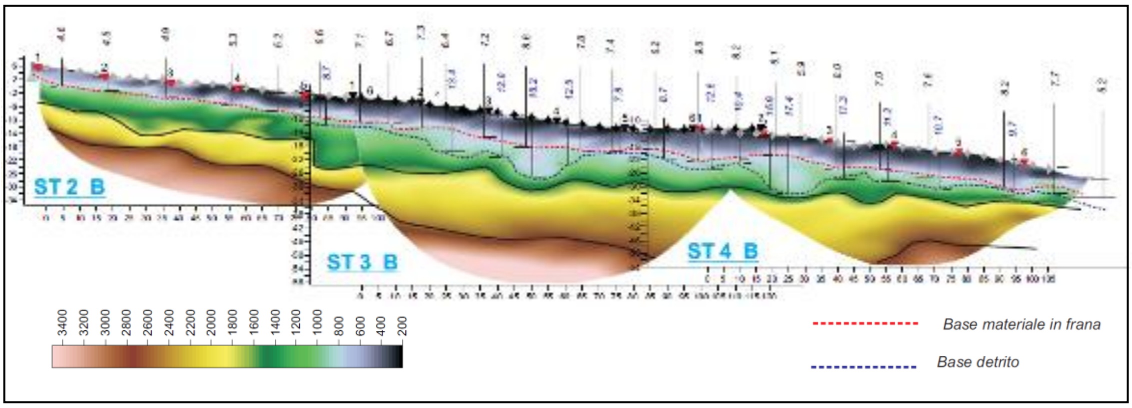

Figure 39 - Subsoil seismic stratigraphy, (Guadagno, 2010).

In the area of the C Sector a continuously cored borehole (S2, Figure 40 A) and a static penetration test (CPT - Cone Penetration Test - 2, Figure 40 A) have been made (Amato and Dubibosi, 2006).

Further survey have been carried out in 2010 (NS6, Figure 40 B).

The survey S2 has reached a depth of 60 m below ground level (water table was found at 18 m), the survey NS6 was stopped at 30 m: the thickness obtained is respectively of 22.7 and of 15.4 m depth. Figure 41 shows the geolithological section realized basing on the 2006 data, extended from the areas previously discussed.

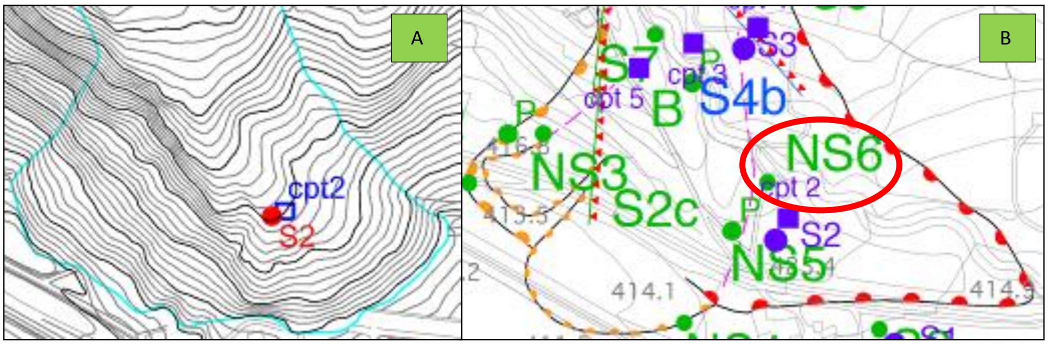

Figure 40 – Location of the all surveys realized within the B Sector. (A, cone penetration tests and borehole in 2006; B borehole in 2010).

For this sector it is not possible to make a clear correlation between the landslide material in the in 2006 and 2010, as the S2 survey was carried out at a height less than the NS6. However it can be deduced, based on the interferometric analysis, that also in this case the thickness of the overlapping is reduced because of its downward shift, due to the events occurred over the years (2009 and 2010).

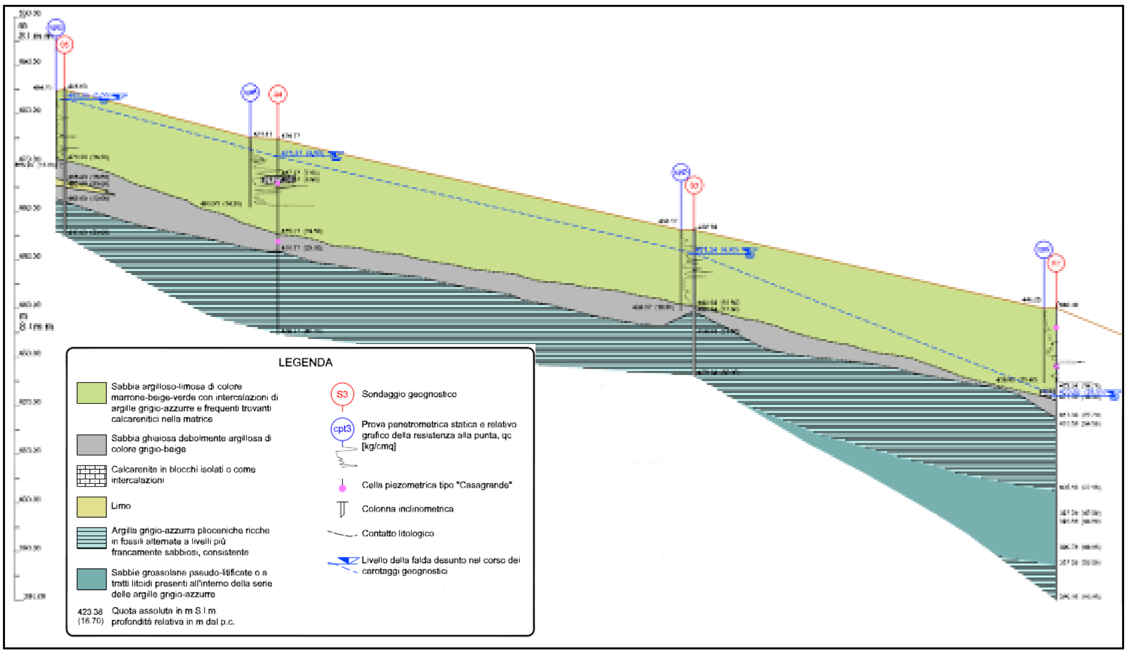

Figure 41 - Geolithological section obtained from the core surveys. (Modified from Amato and Dubbiosi, 2006).

In correspondence of the D Sector, and in particular within its bottom, in 2010 several boreholes were realized: NS1, NS2, NS3, NS4, NS5 (Figure 42). The depth reached by the various surveys and the landslide deposits thickness are listed as follows:

- NS1: depth of 10 m; landslide thickness of 2.3 m;
- NS2: depth of 20 m; landslide thickness of 3.2 m;
- NS3: depth of 24 m; landslide thickness of 4.8 m;
- NS4: depth of 10 m, the thickness was all attributed to eluvio-colluvium and/or slope deposit;
- NS5: depth of 20 m; landslide thickness of 7 m.

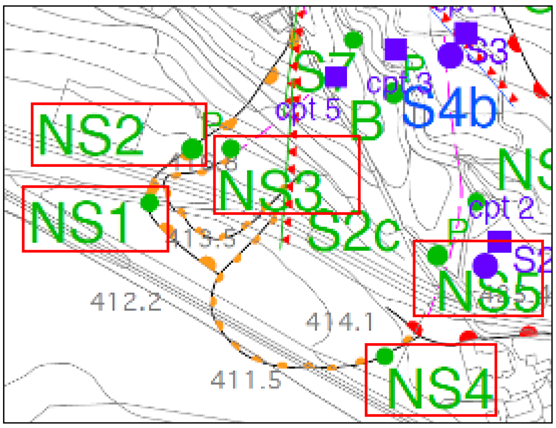

Figure 42 - Location of the all surveys realized within the D Sector in 2010.

Since no geological surveys were carried out before 2010, for the "D Sector" is not possible to have a correlation between landslide thickness evolution. However, knowing that this foot area was interested by high deformations rate, and part of material had reached the road infrastructure, probably a change in terms of landslide deposit amount have occurred.

In the landslide portion coinciding with the "E Sector" two continuous core have been carried out (S7 and S8 , Figure 43A) and four static penetration tests (CPT - Cone Penetration Test - 12 , 13, 14 , 15, see Appendix a and detailed in Figure 43A), Amato and Dubbiosi, 2006). In 2010, three seismic tomography were realized (S4 , S5 and S2, Figure 43B) .
The S7 and S8 surveys both have reached a depth of 40 m: in S7 the landslide thickness is 24.4 m (with flap measured at 15.2 m) , while in the S8 the thickness is 16.8 m (with a flap 10.2 m). A From the survey's results a geolithological section was obtained.

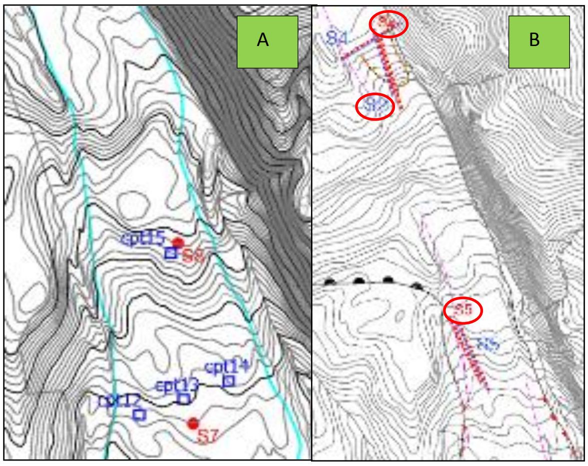

Figure 43 - Location of the all surveys realized within the E Sector. (A, cone penetration tests and borehole in 2006; B borehole in 2010).

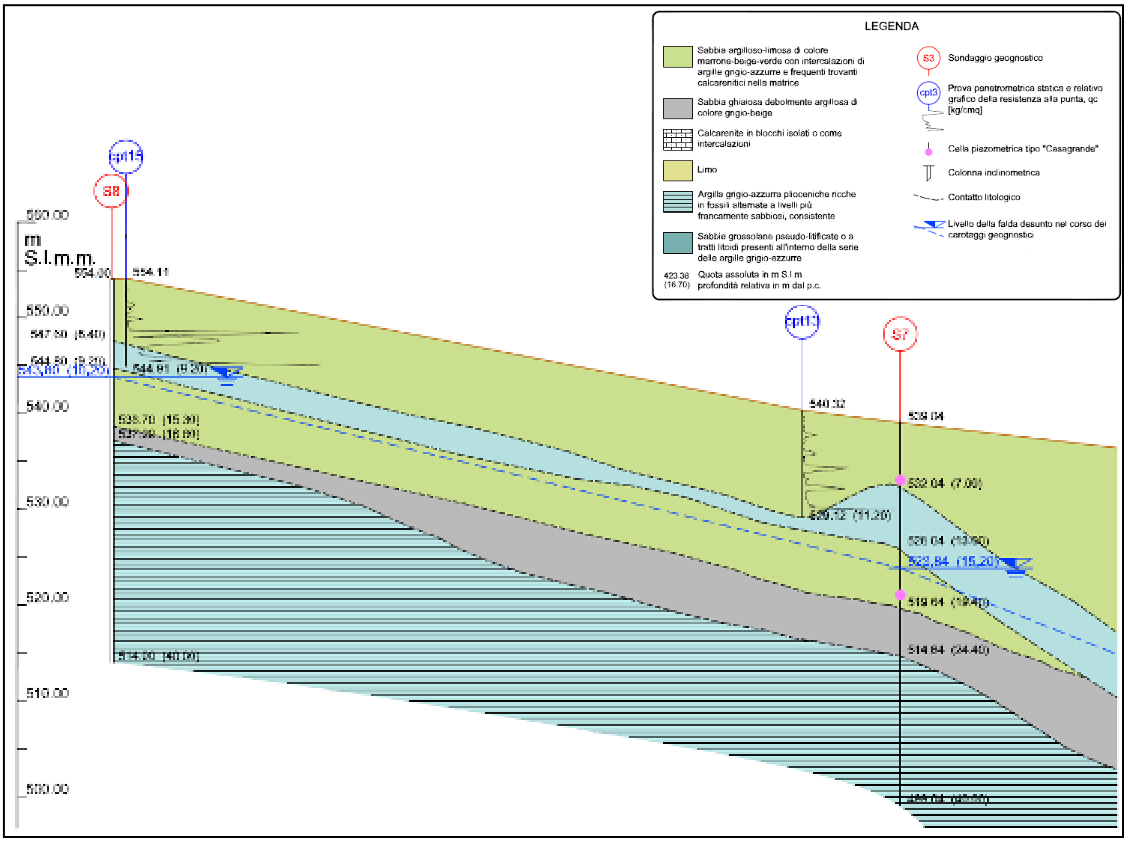

Figure 44 – Geolithological section obtained from the core surveys. (Modified from Amato and Dubbiosi, 2006).

The sismostratigrafics interpretations are shown in Figure 45: S2 was performed in the same position, starting slightly upstream from S4. The two interpretations provide about the same information regarding the landslide body depth, testifying that in about two months the masses involved have remained almost unchanged in terms of quantity. Instead, tomography performed in August also highlights an area subjected to high water circulation. The sismostratigraphy obtained from S5 indicates that even in the lower part of the "E Sector" the landslide thickness is comparable to the upper part .

A correlation between the survey S8 and S5 tomography shows that: the first is moved towards the east, in the most central area, compared to the second, the thickness in the centre is higher than that detectable by the tomography located more laterally. The difference between the two figures can be attributed to two concurrent factors, the first is that the thickness of the material at the centre of the area is greater than the other, and that from 2006 to 2010 there has been a downstream translation of the material and a lowering of the surface.

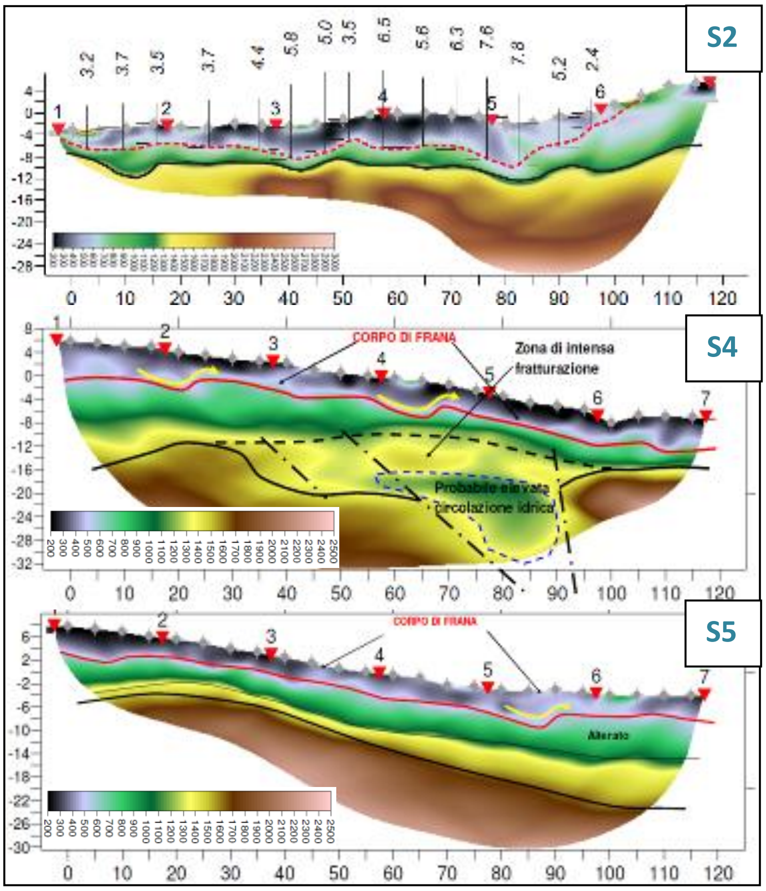

Figure 45 - Subsoil seismic stratigraphies, (Guadagno, 2010).

4. Interferometric Data Analisys

4.1 The monitoring activity

The real-time monitoring is realized through the production of interferograms, or of deformation maps, relative to predetermined time intervals (initially every 4 minutes), which allow the estimation of the sectors observed movement speed. The monitoring activities, from April, 29th 2010 to September, 2nd 2012, have been coordinated through the preparation of a daily bulletin, which refers to the deformations occurring within 24 hours of the issuance of the bulletin itself, and which includes:

• Table with the description of the areas monitored (Table 3);

• optical image taken from the radar station (Figure 46);

• interferogram (global view) with the monitored areas location (Figure 47);

• interferogram (foot zoom view) (Figure 48);

• Speed Chart displacement estimated for each sector, expressed in cm/h and cm/day (Table 2).

Table 3 - Description of the monitoring sectors relative to the corresponding landslide portion.

<table>
<tr><th colspan="2">Sectors</th><th>Description</th></tr>
<tr><td>Landslide</td><td>A</td><td>Landslide bottom portion (central part of the monitored area).</td></tr>
<tr><td rowspan="3">Landslide foot</td><td>B</td><td>Upper part of the landslide toe</td></tr>
<tr><td>C</td><td>landslide foot left side (affected by the slope reprofiling works).</td></tr>
<tr><td>D</td><td>landslide foot right side (affected by the slope reprofiling works).</td></tr>
</table>

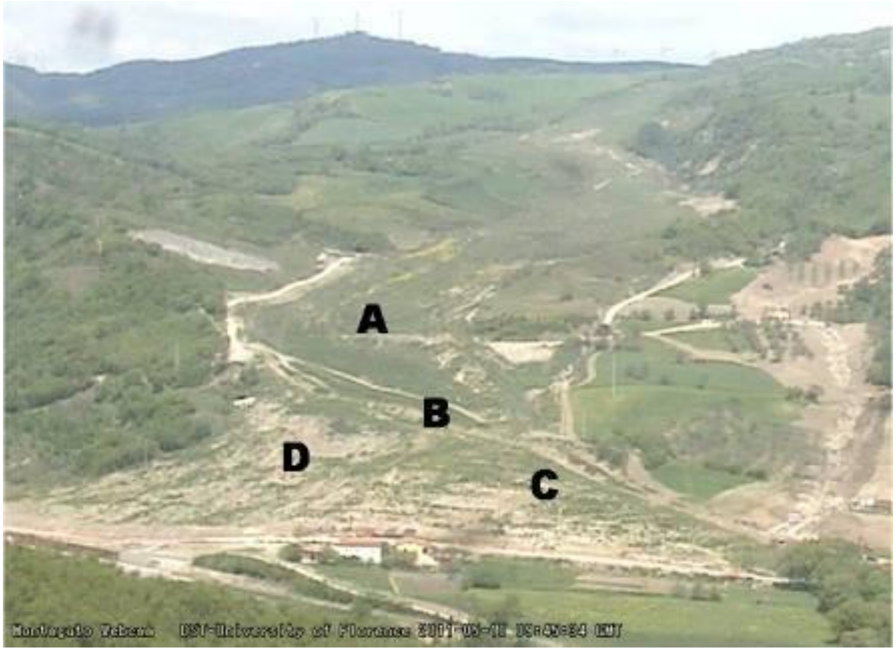

Figure 46 - Optical image showing the monitoring sectors location.

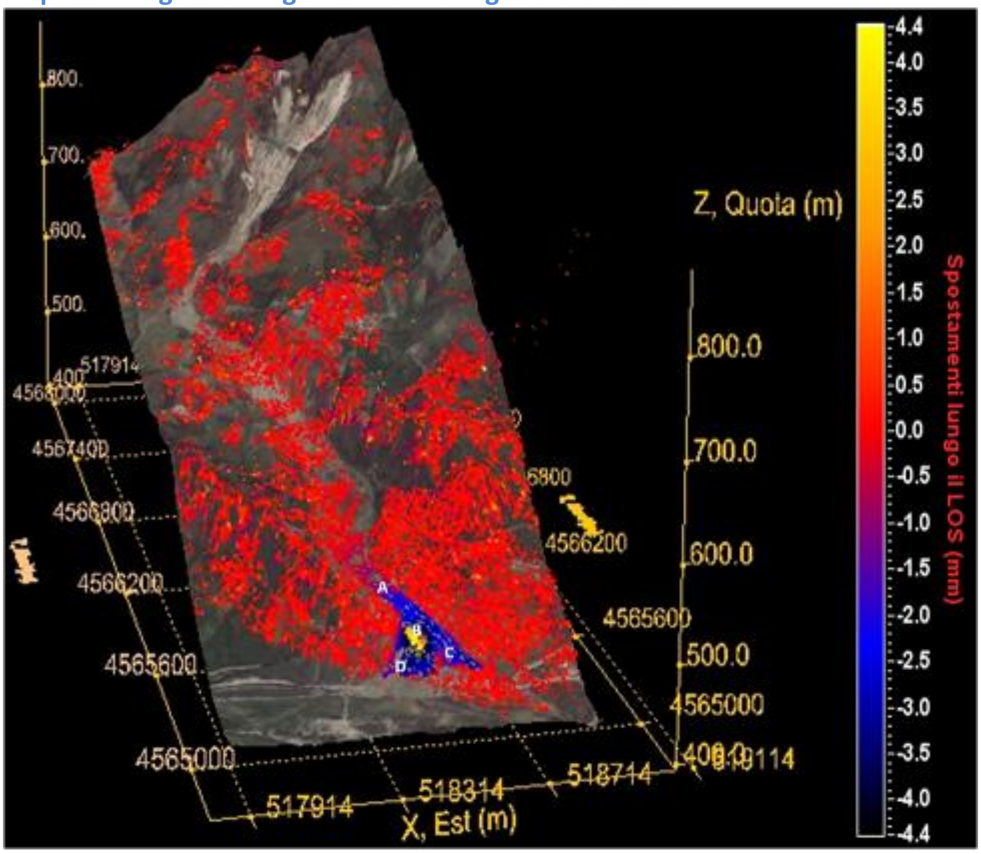

Figure 47- Monitored areas of interest detection on the 3D optical image and in the interferogram (time interval of approximately 4 minutes).

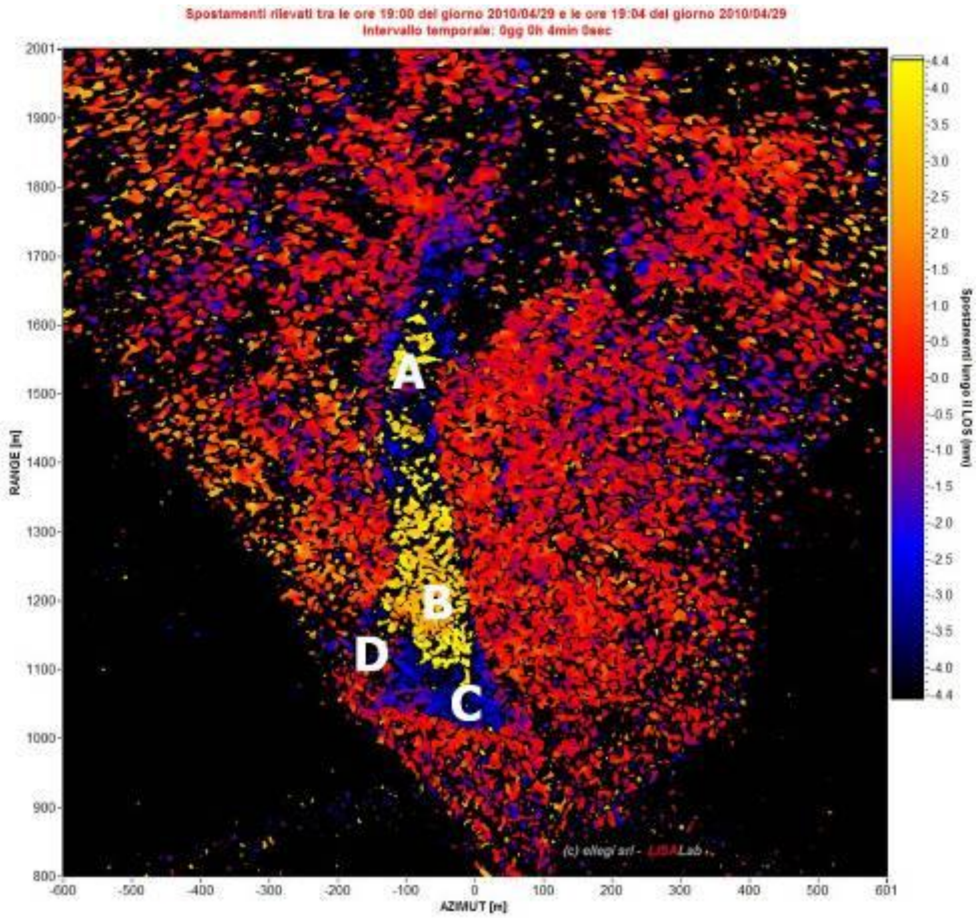

Figure 48- 2D SAR Interferogramma (foot zoom) relative to the time interval of about 4 minutes from 05.02 a.m. GMT (07.02 local time) and 05.06 a.m. GMT (07.06 local time) of 7th, May 2010. The color scale shows the displacements in millimeters along the radar line of sight (LOS = line-of-sight).

Table 4- Estimated velocity synthesis expressed in cm/h and m/day, corresponding to the monitoring sectors and their daily trend. The assessment of the trends variation is based on an increase or decrease in terms of displacement velocity equal to 10 cm/day, occurred in the previous 24 hours.

Sector	Displacement velocity		daily *Trend*
	cm/h	m/day	
A	**2.3**	**0.5**	**Stable**
B	**8.1**	**2.0**	**Stable**
C	**5.7**	**1.4**	**Stable**
D	**5.6**	**1.3**	**Stable**

Since the monitoring activities beginning the methodology used in the bulletins preparation, in particular for the phases concerning the interpretation of the interferograms, has been subjected to many variations induced by changes in the landslide displacement velocity.

During the early monitoring stages, the emission of the bulletins was based on the observation and interpretation of interferograms only related to an time interval equal to 4 minutes. This procedure was chosen due to the high displacement velocity deformation, which reached values of about one meter per day (the highest speed recorded was 2.9 m/day on June 1st, 2010), in such cases a very short time interval allowed, in a very clear and unambiguous way, to discriminate the occurred displacement speed variations (Figure 49).

Since approximately July 2010, the deformation rate began to decrease, this variation made it necessary to include interferograms processed on a wider time interval, from 4 minutes to 4 hours. Similarly, over the next few months, for the same reason, further interferograms processing with an time interval of 24 hours were introduced. The figures 5, 6 and 7 represent the evolution of the interferograms time lapse variation just described, with reference to the relative periods and flow speed recorded. Figure 50 shows the three different time interval of processing acquired on July, 26th 2010, pointing out that the 4 minutes time lapse was not enough to detect the displacement rate, which was reaching at that time a maximum speed equal to 3×10^{-2} m/day.

Figure 51 exhibits the landslide evolution in terms of decrease in the displacement rate after five months, the interferogram refer to the day December, 26th 2010, when the maximum speed reached was equal to 4×10^{-3} m/day. This velocity was too low to be able to discriminate the displacement variations using the 4 minutes or 4 hours time interval; accordingly the interferogram with a time interval of 24 hours seemed to be more suitable.

Since March 2011, with the aim of making the monitoring activities even more comprehensive, and to get advantage from the interferometric data, useful to the landslide analysis and the study, interferograms with a longer time interval were processed. Consequently, weekly and monthly deformation cumulated maps were available as well, referred to the entire acquisition period (Figure 52).

The sectors, though slowly, were keeping a deformation rate; from December 2010, even the area located between the A Sector and the elbow area, this zone was later defined as E Sector (see section 5.2.5).

The distinction of the different landslide areas, characterized by different deformation trend, in the Montaguto earthflow case is easily understandable. As occurs with the others similar earthflows, they are improperly considered as a single landslide, but the various geomorphological characteristics derive from multiple activation events.

In the case study, volumetric analysis and topographical measurements have shown the activation of the different surfaces at different times and with different deformation rates characteristic (Giordan *et al*, 2013). It follows that the landslide assessment, depending on the requirements and from the earthflow behaviour, seems to be more complex, for example for the determination of its activity status (Reichenbach *et al*, 1998), for the evaluation of the reactivation frequency (Guzzetti *et al*, 2005, 2006), statistical computing of the area (Guzzetti *et al*, 2002; Malamud *et al*, 2004) and landslide volume (Guzzetti *et al*, 2009).

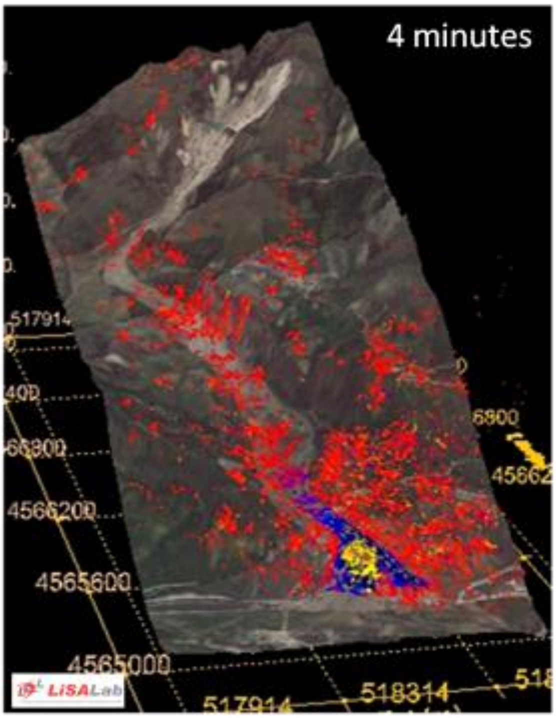

Figure 49- SAR interferogram acquired on May, 26th 2010, the maximum speed recorded is equal to 2.4 m/day, the show time interval of acquisition is 4 minutes, sufficiently to assess the landslide deformations occurred.

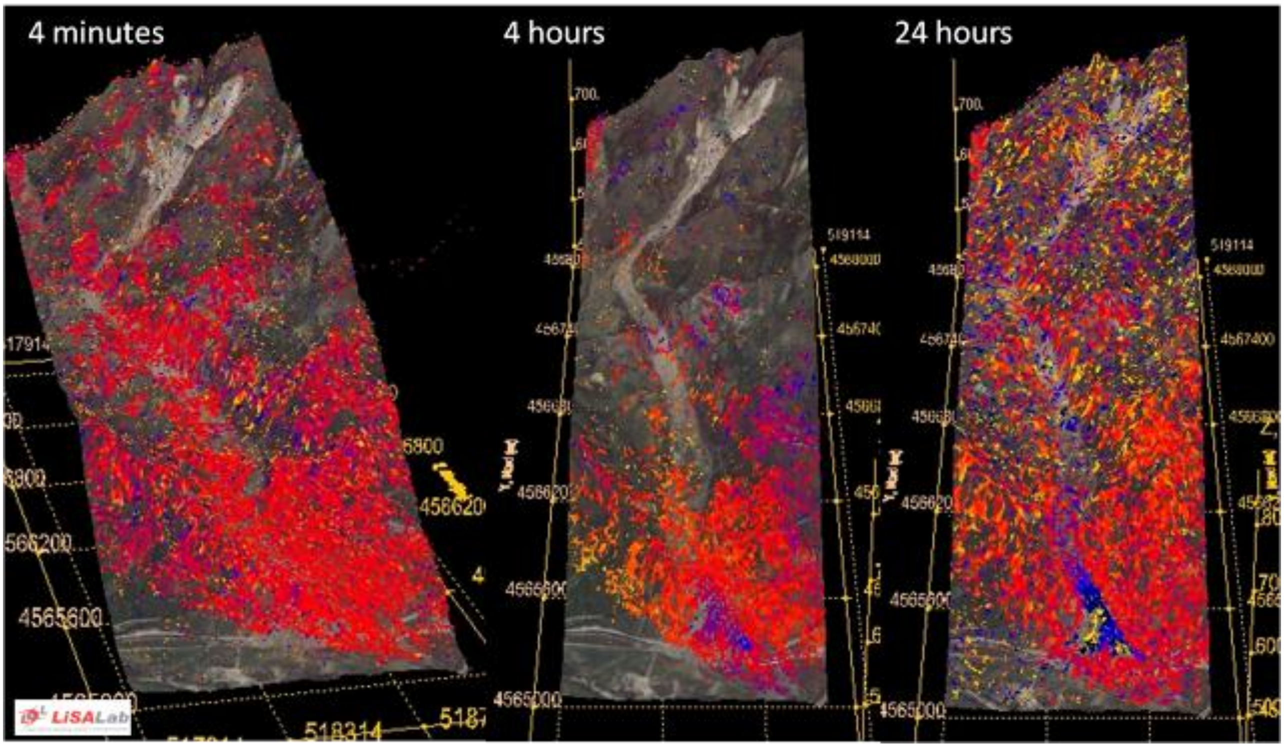

Figure 50 - Comparison between SAR interferograms with different time interval processing, acquired on July 26th, 2010.

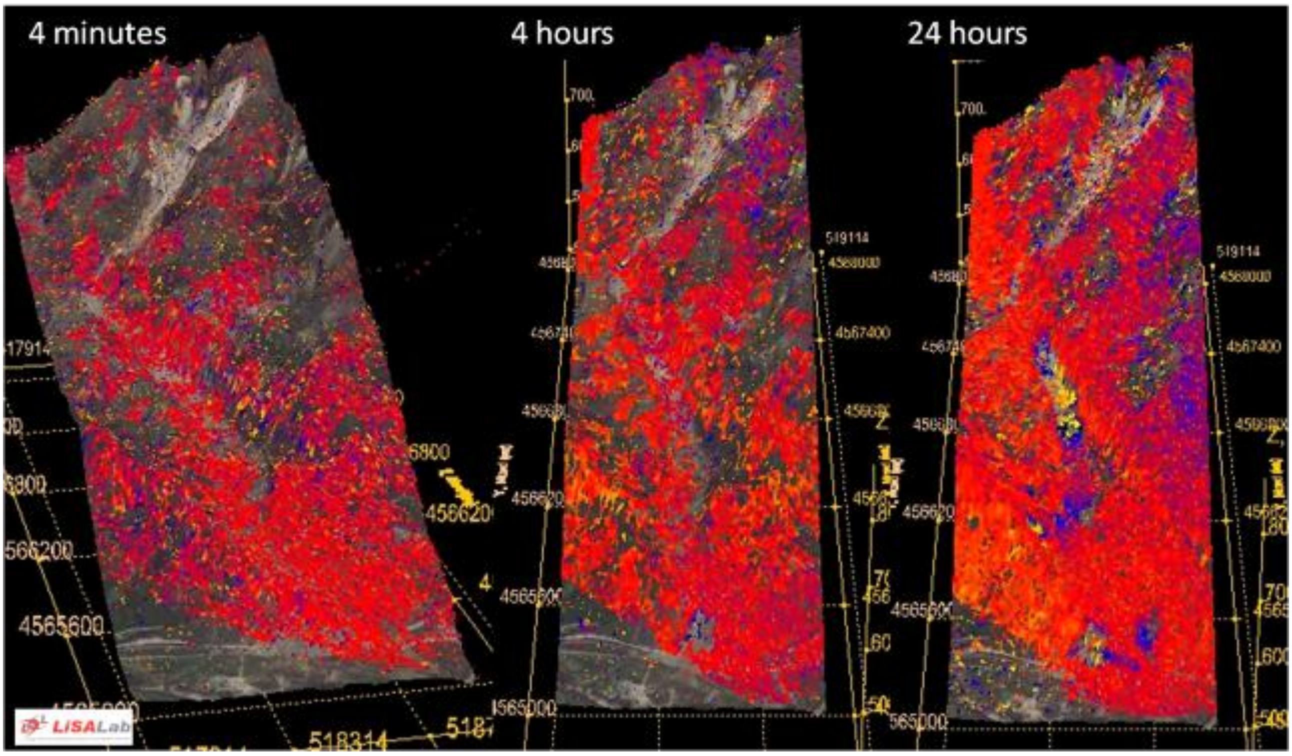

Figure 51 - Comparison between SAR interferograms with different time interval processing, acquired on December 26th, 2010.

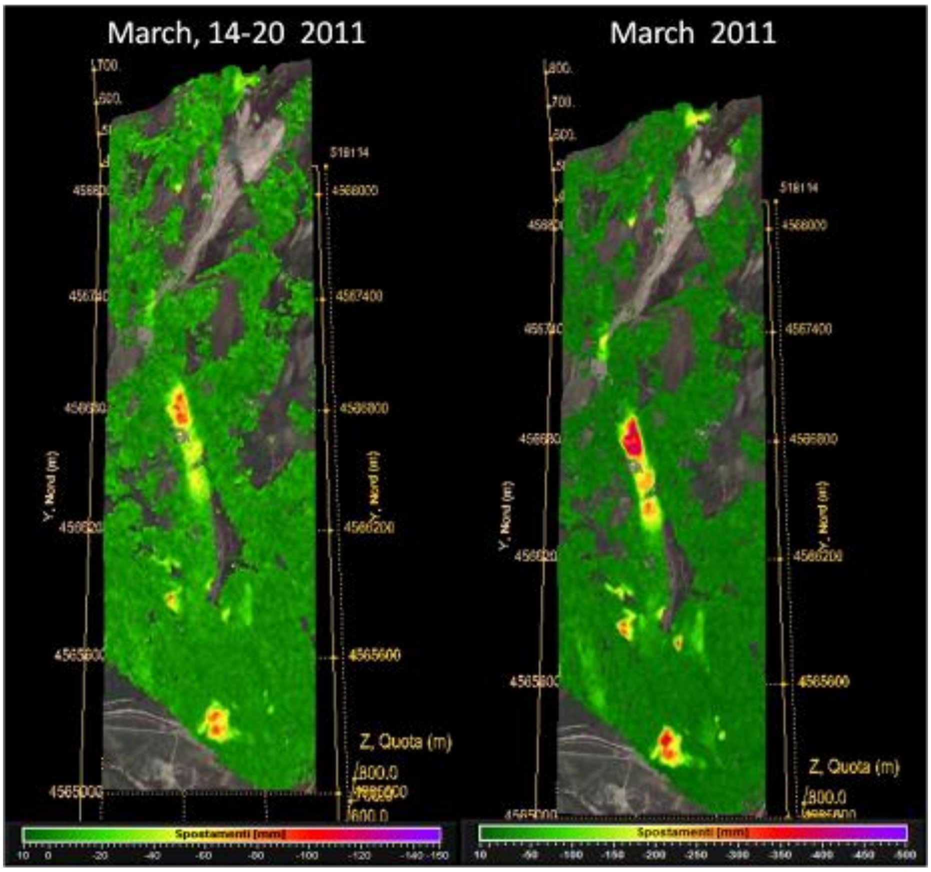

Figure 52 - Weekly and monthly cumulated maps, relative to the third week of March and the same month.

From September 2nd, 2012 the frequency of the bulletins issue has been changed, it has switched from a daily to a single weekly operating mode; providing however a daily monitoring. This change was considered appropriate in response to the observation and to the analysis of the all monitored sectors, which demonstrating that their displacement speeds were stable and equal to very low values (0.01 m/ day).

The issue of the weekly bulletin takes place every Monday, and two variations were applied: the insertion of the graph showing the weekly velocity trend, and the speed table, which estimates displacements relative to variation occurred during the week (Table 5).

Table 5 - Estimated velocity synthesis expressed in cm/h and m/day, corresponding to the monitoring sectors and their daily trend. The change of the trends is assessed as considerable when is equal to the ±50% of the variation.

Sector	**Maximun dayly speed (cm/h)**	**Maximun dayly speed (m/day)**	**Weekly *trend***
A	**<0.01**	**<0.01**	Stable
B	**0.01**	**<0.01**	Stable
C	**0.01**	**<0.01**	Stable
D	**0.01**	**<0.01**	Stable

E	**0.01**	**<0.01**	Stable

4.2 Data analysis

Basing on the data analysis and interpretation, provided by the monitoring system, it was possible to detect and define a daily evolution of the observed phenomena, in terms of decrease in the deformation rate, and increase as well. In this way, as said previously, we proceeded to the introduction of the use of deformation maps refer to time intervals longer than 4 minutes.

Whereas said, it is important to note how the deformation processes and movement speeds are been gradually decreasing. Figure 53 illustrates the evolution of the deformation speed, the graph compares the cumulative monthly rainfall (rain gauge of Savignano Irpino, AV), with the monthly cumulated displacement of the five monitored areas (A, B, C, D and E).

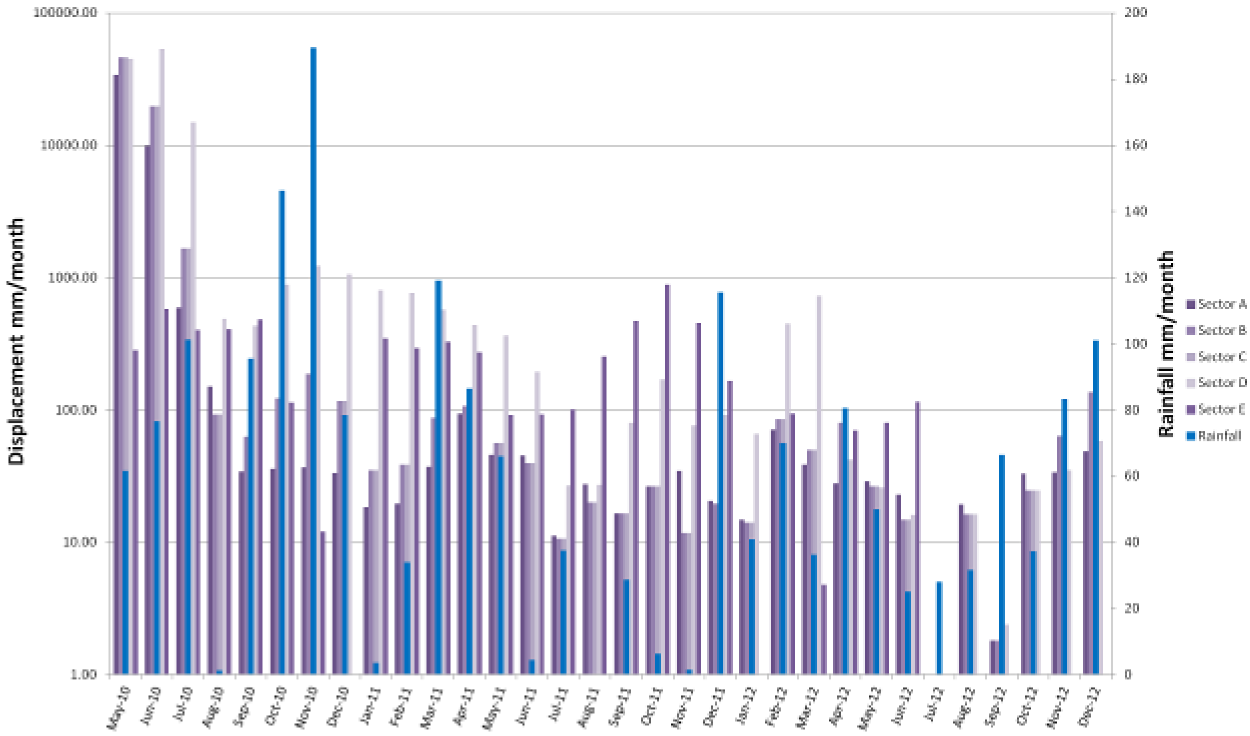

Figure 53 – Comparison between the monthly cumulated rainfall and the speed displacement recorded.

The graph shows that the "B Sector" was recorded the highest deformation rate in terms of cm/day, and the "D Sector" showed high strains because, although smaller than "B Sector" were more long-drawn-out. The "C Sector" recorded displacement rate contained than the previous sectors, while the “A Sector” was characterized by movements still minors. Except for the D, the deformation rate of the others sectors located into the landslide foot, have suffered an abrupt decrease from July 2010. The date correspond with the beginning of the repair works and the realization of some engineering works.

The choice to include in the graph also the cumulative monthly rainfall, aims to highlight the difference, in terms of quantity, of the rain occurred from 2009 to 2012. In particular, between January 2010 and December 2010 have been reached 1099.6 mm of rain, while between January 2011 and December 2011 the total rainfall was 502.4 mm, respectively the maximum and minimum yearly amount of the studied period. Also equally between January and March 2012 mm of rainfall achieved were 290, and the movements recorded were extremely low, below the cm per day.

In order to validate this hypothesis, the graph in Figure 54 shows the same deformation rate compared with the cumulated monthly rainfall from July 2009.

Given the correlation between the meteorological events and reactivations of the instability, it is interesting to note that the period that corresponds to episodes of reactivation of the landslide has recorded a quantity of rains minor compared to the period in which, on the contrary, the landslide has started to slowly move on towards the valley.

This data demonstrates the effectiveness and the impact that stabilization works have achieved.

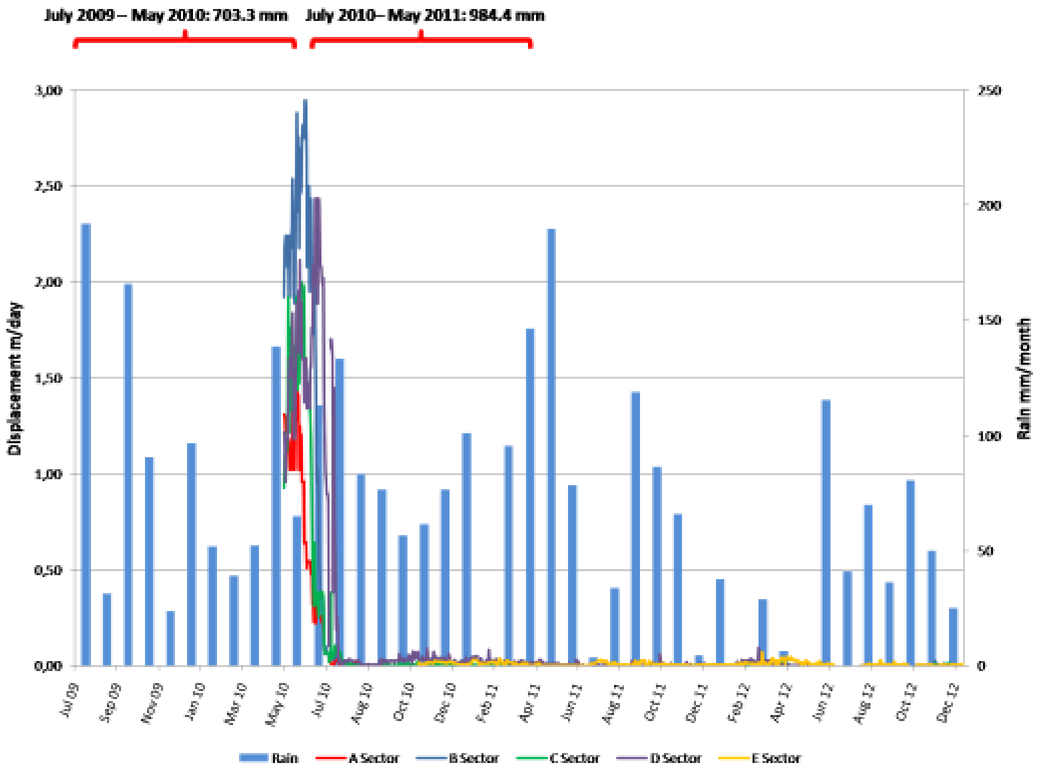

Figure 54 - Comparison between the monthly cumulated rainfall (2009-2012) and the displacement speed recorded, from May 2010.

From July 2009 to May 2010 rainfall total were equal to 703.3 mm, related with the high deformation occurred in May 2010. During the period July 2010 - May 2011 the total rainfall ware equal to 984.4 mm, while the deformation rate was minimal in the areas A, B and C, however minor, except short periods, even in the “Sector D". The difference of rainfall occurred, in terms of quantity, during the year 2010 - 2011 would think of an increase in deformation: instead, since a high decrease occurred, the hypothesis that the stabilization works have had a positive influence can be supported.

Comparing to the landslide foot sectors, the "E Sector" showed low deformation, but these were continued for almost the entire considered time, causing several problems to the works design. For this reason, part of the results discussion obtained from the monitoring system GBInSAR , will primarily focus on the "E Sector".

In the next sections five different areas characteristics and behaviour will be analyzed. The comparison of the landslide surface topography, thanks to hillshade derived from a DTM (Digital Terrain Model) and a DSM (Digital Surface Model) refers to two different periods, will described too: the first indicates the ground surface proportion, while the second represents the top of the soil, including buildings, infrastructure and vegetation. To limit the problems caused by the interpretation of different angles of illumination, the two hillshade were produced by illuminating the digital topography from the same direction (315 ° N) and from the same height (45 °). Despite the diversity of the data shown between the two models (clearly visible to the outside of the landslide due to the presence of vegetation) is still possible to make comparisons of the landslide surface, since this is devoid of any infrastructure and vegetation is primarily herbaceous and therefore very low, with no tall trees; so these two models can be compared. In particular, the DSM and DTM were drawn from two flights LiDAR (Light Detection and Ranging), respectively, in April 2010 and June 2011 , Table 6 shows the characteristics of the two models.

Table 6 – DTM and DSM characteristics.

	DSM	DTM
Source	LiDAR - April 2010	LiDAR - June 2011
Resolution	6 - 7 pt m^{-2}	1 $\times$ 1 m
Precision	<0.2 m	<0.2 m

4.2.1 A Sector

The area called "A Sector" is located in the landslide bottom, between 470 and 490 m a.s.l. From the GBInSAR acquisitions, it appears that the maximum landslide deformation took place on May, 21th 2010 (Figure 55): the greater apparent displacement is 4.7 mm in 4 minutes, corresponding to 1.5 m/day. The days in which the higher apparent displacement were recorded during the same month.

Figure 56 shows the relationship between the daily deformation and the daily cumulated rainfall, from July 2010, the deformations suffered a sharp decline. Instead Figure 57, is referred to the monthly rainfall: from the landslide reactivation, the month with the highest number of precipitation was not May, it follows that the deformation decrease is directly correlated with the start of work and the dry season.

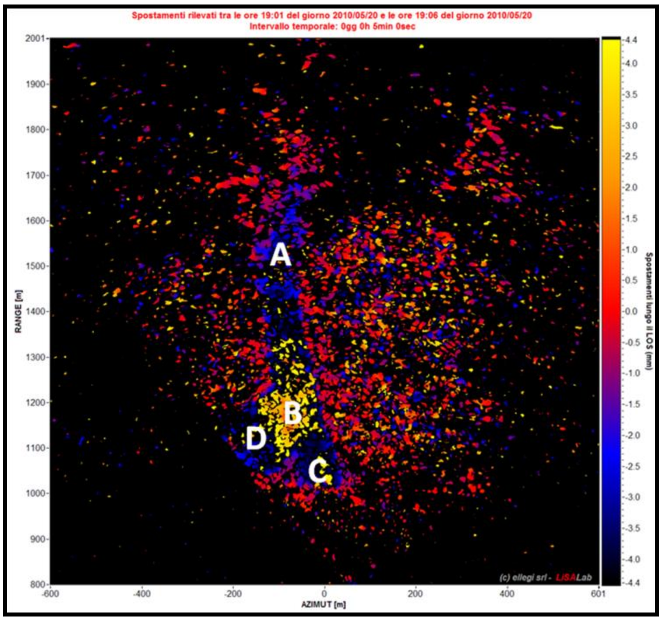

Figure 55 - Interferogram (time interval of 4 minutes) of May, 21th 2010. The time is GMT (-2h compared to local time). The highest deformation of the "A Sector" was about 4.7 mm.

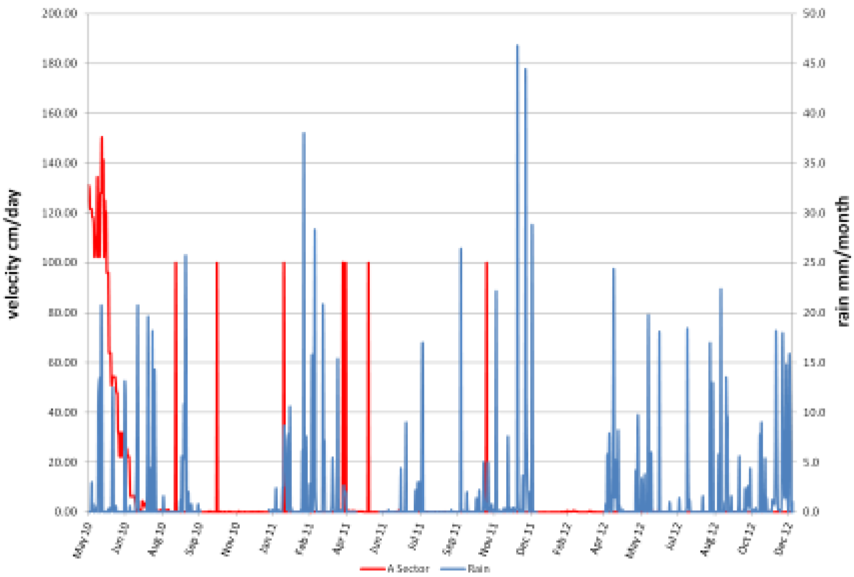

Figure 56 – Graph of the "A Sector" velocity and daily rainfall.

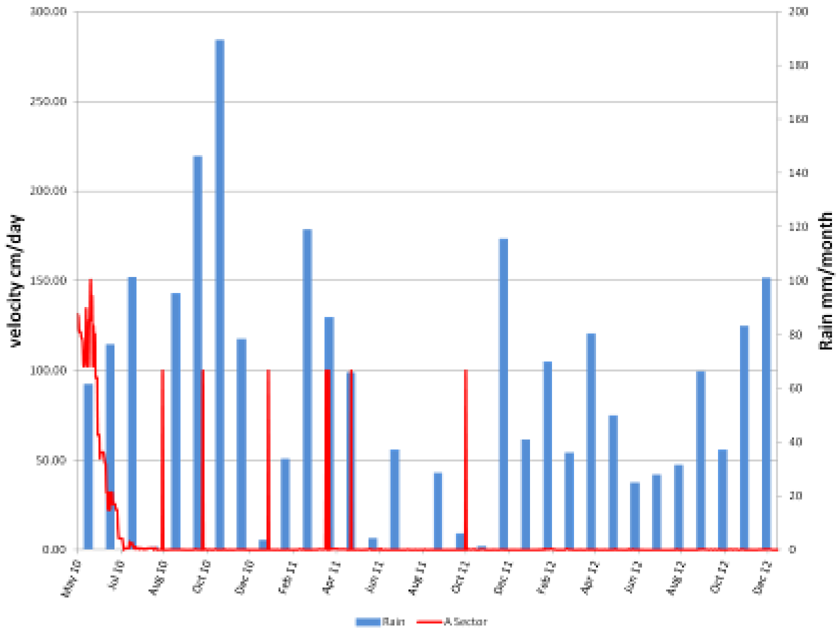

Figure 57 - Graph of the "A Sector" velocity and monthly rainfall.

With respect to the time period July 2010-December 2012 (Figure 62B), in order to better appreciate the minor variations, it shown how the apparent displacement decreases further since September 2010.

In order to detect the variation of the surface topography in the years a comparison between the DTM (April 2010) and DSM (June 2011) is exhibited in Figure 58.

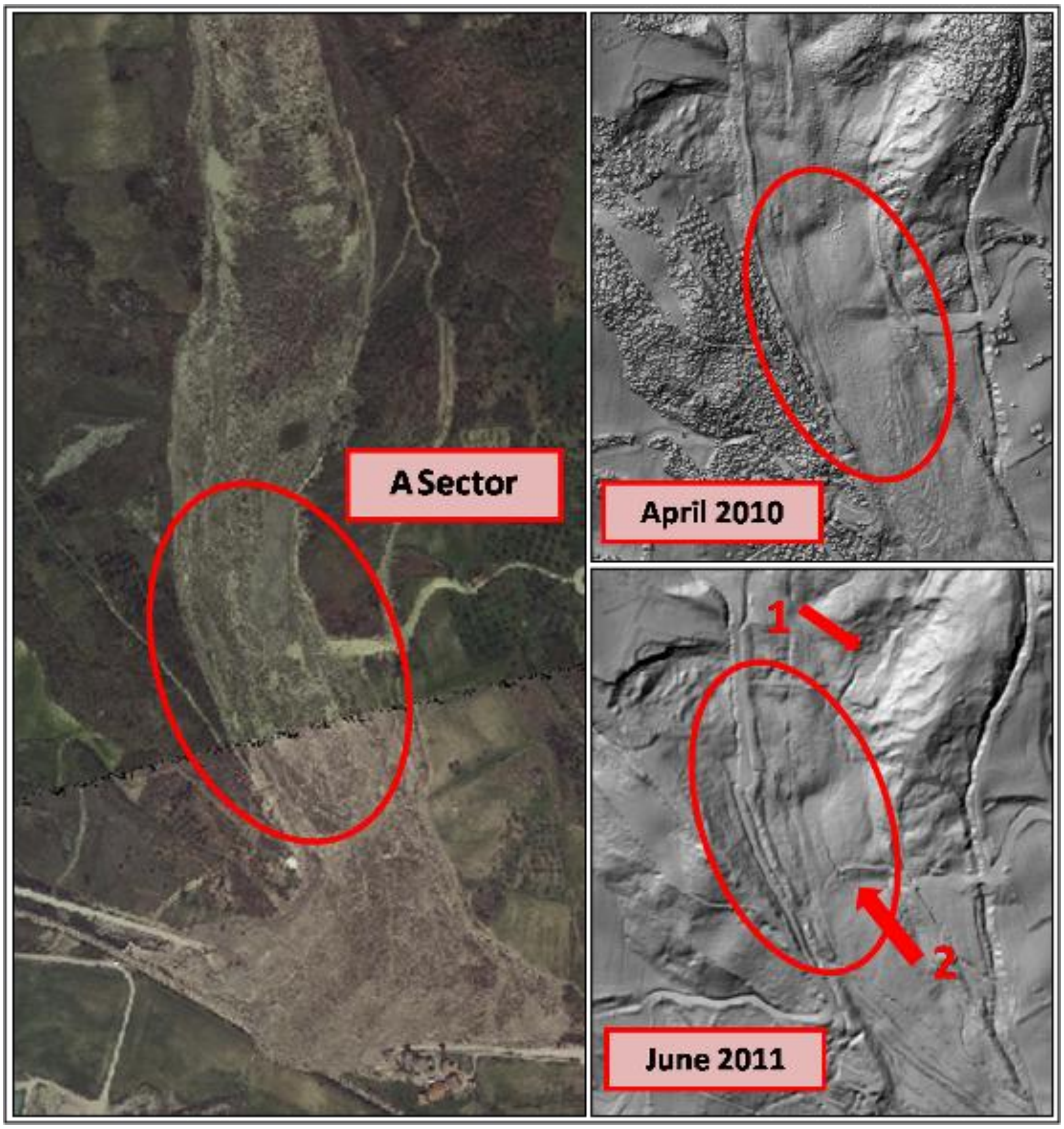

Figure 58 - Comparison between the DTM and DSM of the "A Sector" and location of the area on the orthophotos (left).

The two main variations detected consist of: a larger incision in the upper lobe of the area of interest, which is, however, due to the "Laghetto delle rane" drainage (identified by arrow 1), and the higher visibility of an access road to the landslide (arrow 2), due to anthropogenic work. Overall, the morphology of the sector kept on his shape, with the exception of the more uniform surface, indicating a redistribution of material, probably for both natural and human action.

Figure 59 shows the comparison between the first monthly cumulated displacement map (July 2010) and those relative to December 2012: taking into account the differences in scale, we see that the deformation is decreased significantly.

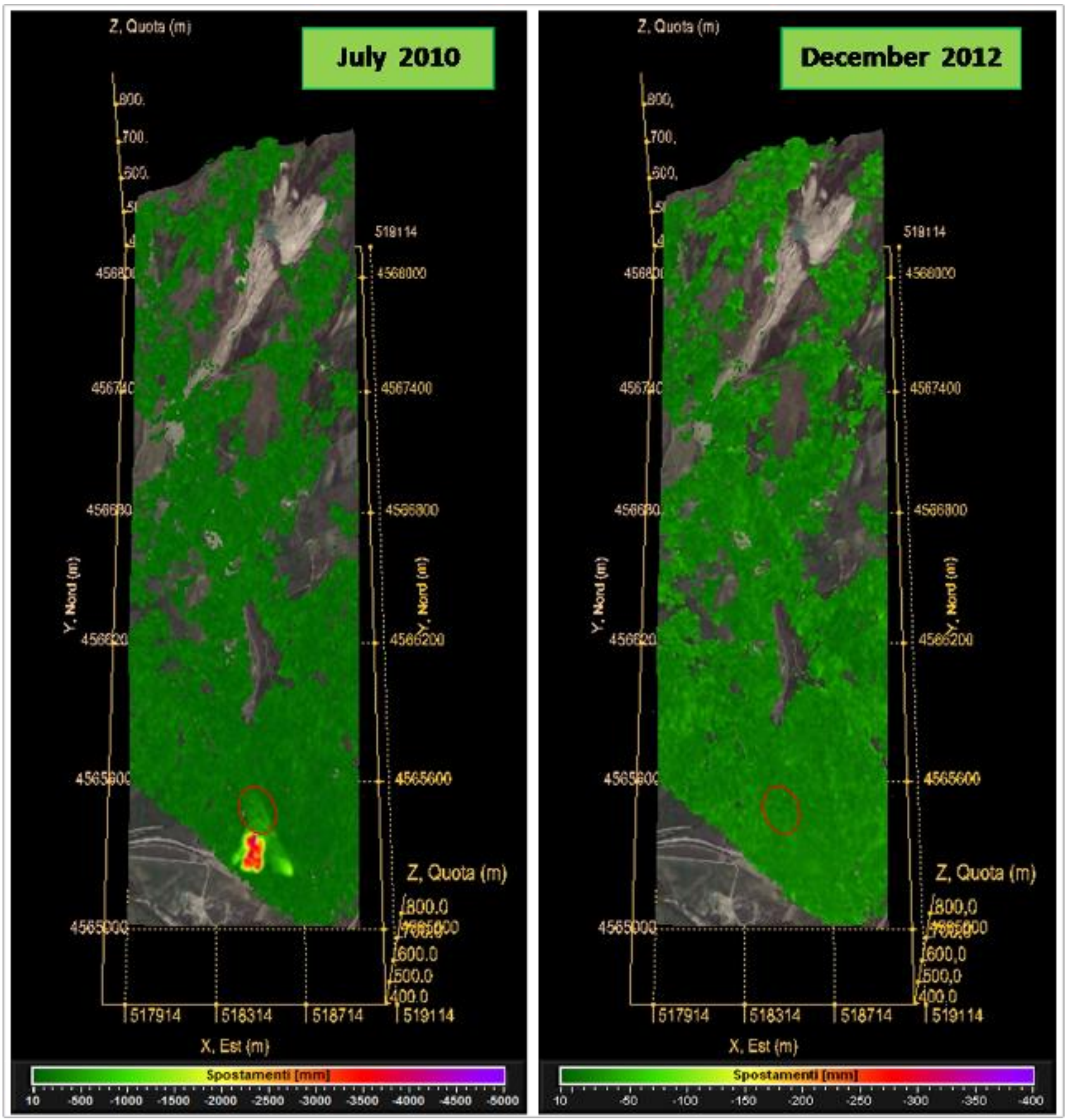

Figure 59 – Cumulated displacement map of July 2010 and December 2012 (note the differences in scale) and location of the " A Sector ".

4.2.2 B Sector

The maximum deformation occurred on June, 1st 2010, Figure 60 shows the interferogram on the short-term: the highest apparent displacement reached was equal to 9.2 mm in 4 minutes, corresponding to 2,94 m/day.

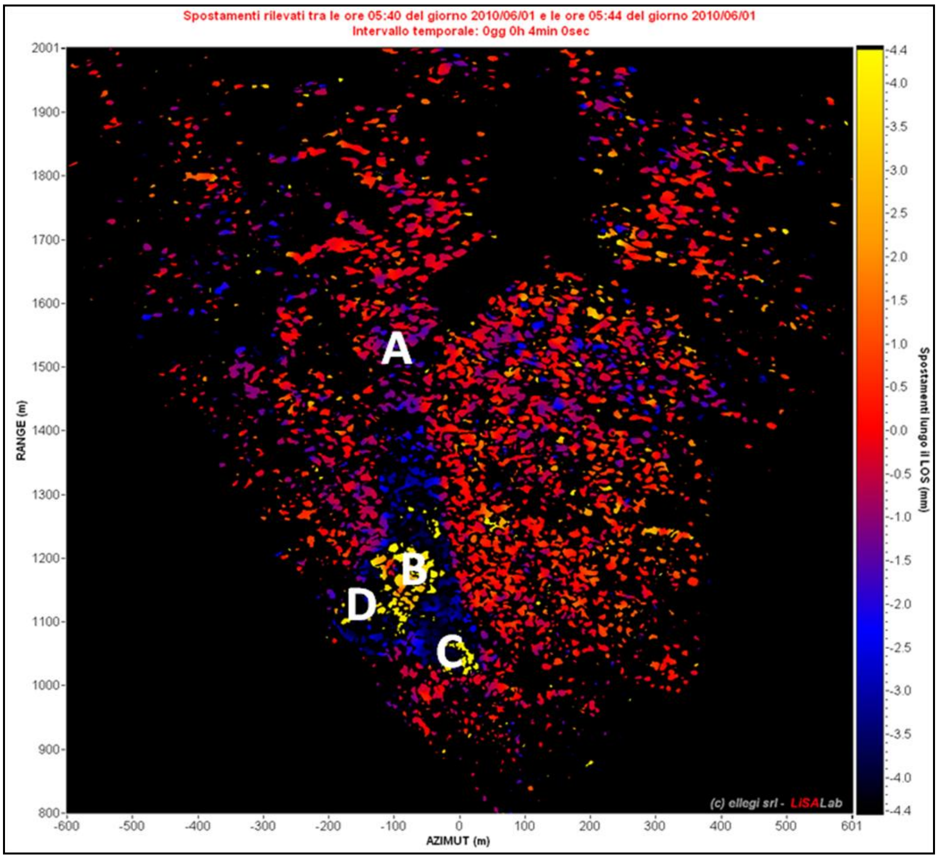

Figure 60 - Interferogram (time interval of 4 minutes) of June, 1st 2010. The time shown is GMT (-2h compared to local time). The deformation rate of the "B Sector" was about equal to 9.2 mm.

This value is the highest recorded data during the entire recording period and among the all sectors. Figure 61 shows the relationship between the daily deformation and the daily cumulated rainfall: as for the "A Sector" from July 2010, the deformations suffered a sharp decline. Taking into account also the Figure 62, which refers to the monthly rainfall, the deformation decrease is directly correlated with the start of work in the area as well.

The apparent displacement decreases further since August 2010, the deformation rate becomes very low, with exception of occasionally increases, due to the work for the Rio Nocella water deviation and the subsequent drainage of the "Laghetto delle Rane."

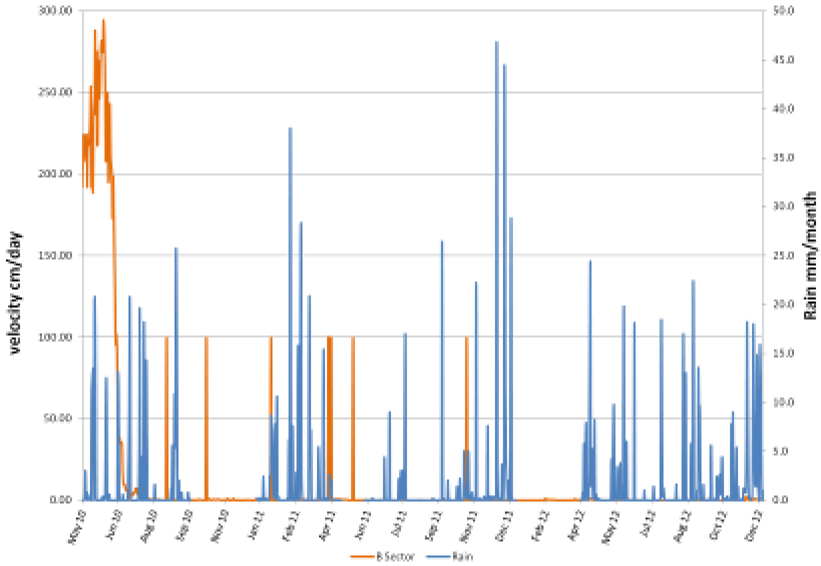

Figure 61 - Graph of the "B Sector" velocity and daily rainfall.

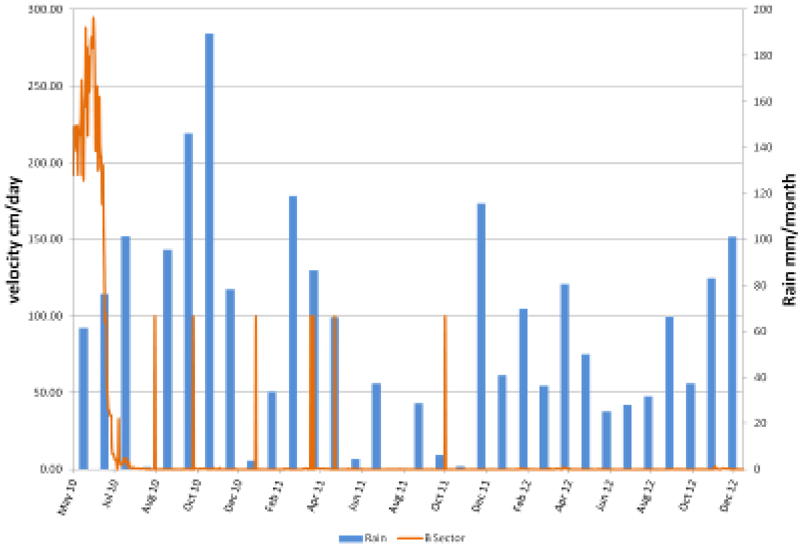

Figure 62 - Graph of the "B Sector" velocity and monthly rainfall.

Comparing the DTM of April 2010 and the DSM of June 2011 (Figure 63) changes in "B Sector" consist of the visible slope reprofiling. In this area, because of the invasive work performed is not possible to extrapolate the natural modifications that may have occurred. Compared to 2010, the surface topography had a general decrease, probably due to both the down slip of the material and the engineering works.

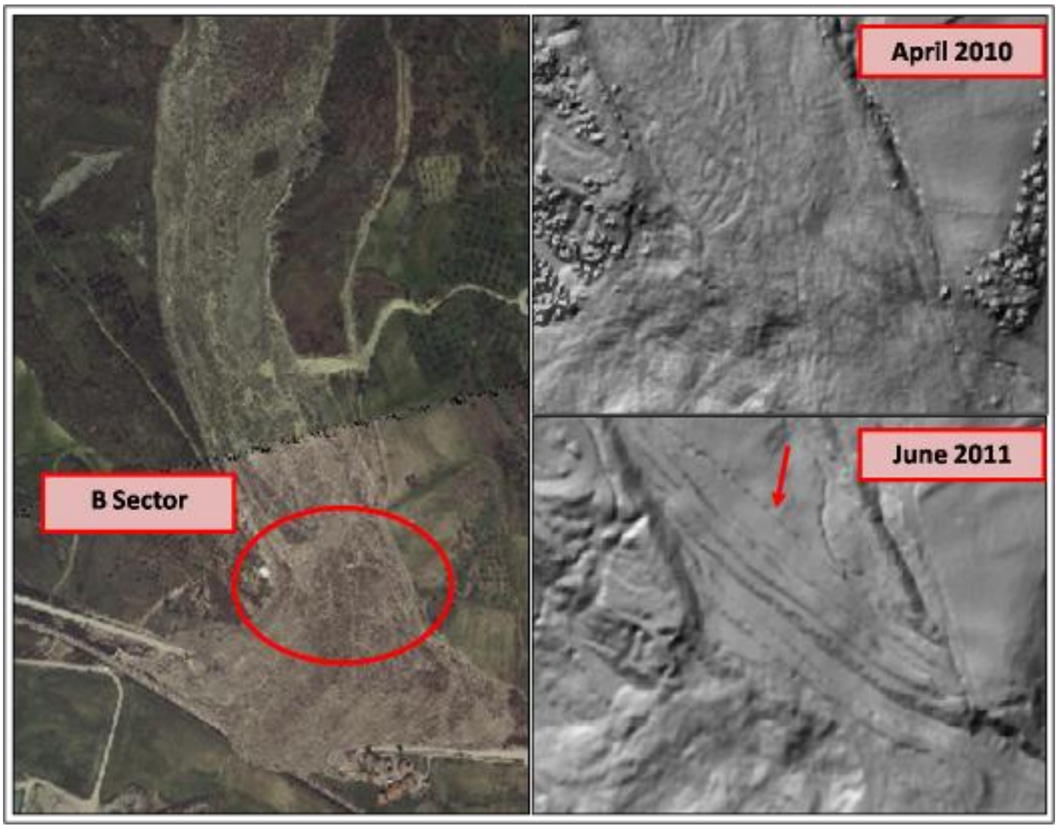

Figure 63 - Comparison between the DTM and DSM of the "Sector B" and location of the area on orthophotos (left).

Figure 64 shows the comparison between the first monthly cumulated displacement map available (July 2010), and the following month in which the deformation decreases sharply and those of December 2012: taking into account the differences in scale, it is clear as the area is almost stabilized.

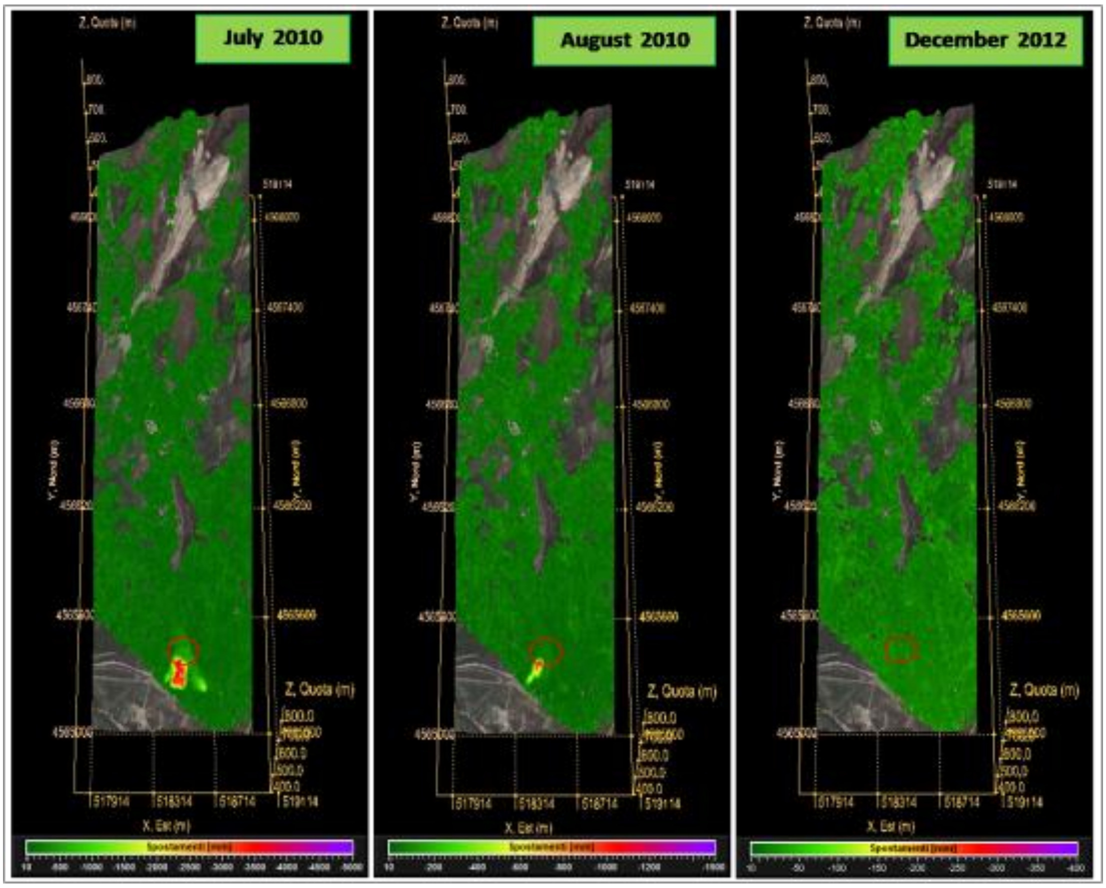

Figure 64 - Cumulated displacement map of July 2010, August 2010 and December 2012 (note the differences in scale) and location of the " B Sector ".

4.2.3 C Sector

The maximum deformation occurred on May, 29th 2010, Figure 67 shows the interferogram on the short-term: the highest apparent displacement reached was equal to 6.2 mm in 4 minutes, corresponding to 1.98 m/day.

Figure 65 shows the relationship between the daily deformation and the daily cumulated rainfall: as for the previous deformation fields, the zone was subjected to decrease from July 2010. Considering Figure 66, which relates the monthly cumulated rainfall with the apparent velocity, even in this case the deformation decrease is directly correlated with the beginning of the stabilization work. However, unlike the previous cases, the changes in the following months had some velocity peaks, it can be concluded that in the considered area the deformations do not become lower until May 2012, when the works at the landslide foot were finalized. Latter have had a significant impact on the landslide deposit and morphology, because they protect the road infrastructure, presumably part of the deformation recorded is probably due to the works activity.

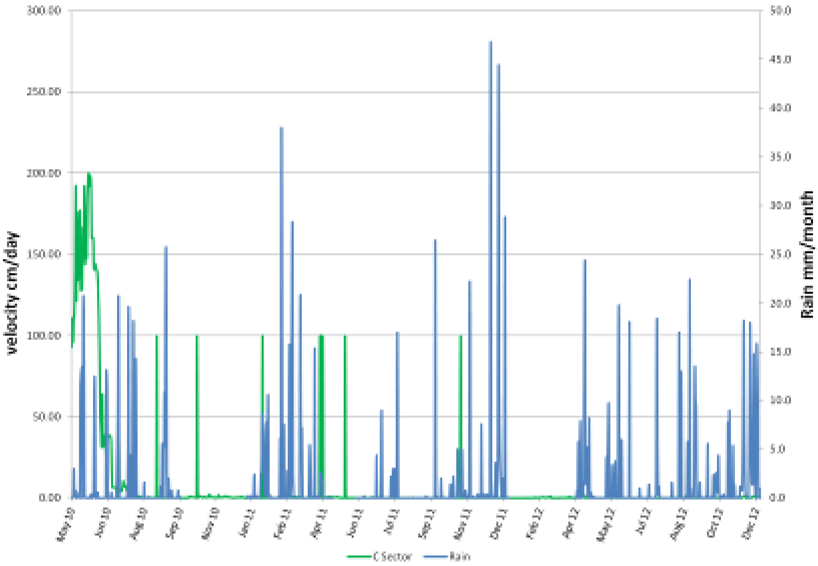

Figure 65 – Graph of the "C Sector" velocity and daily rainfall.

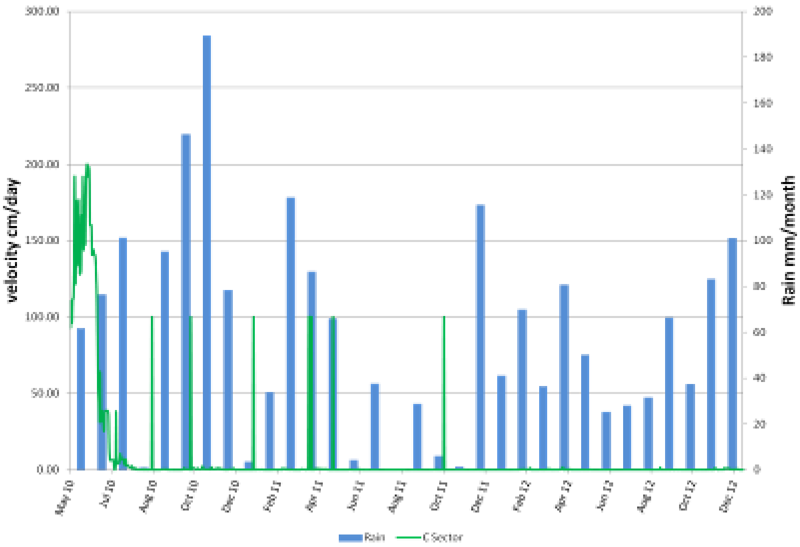

Figure 66 - Graph of the "C Sector" velocity and monthly rainfall.

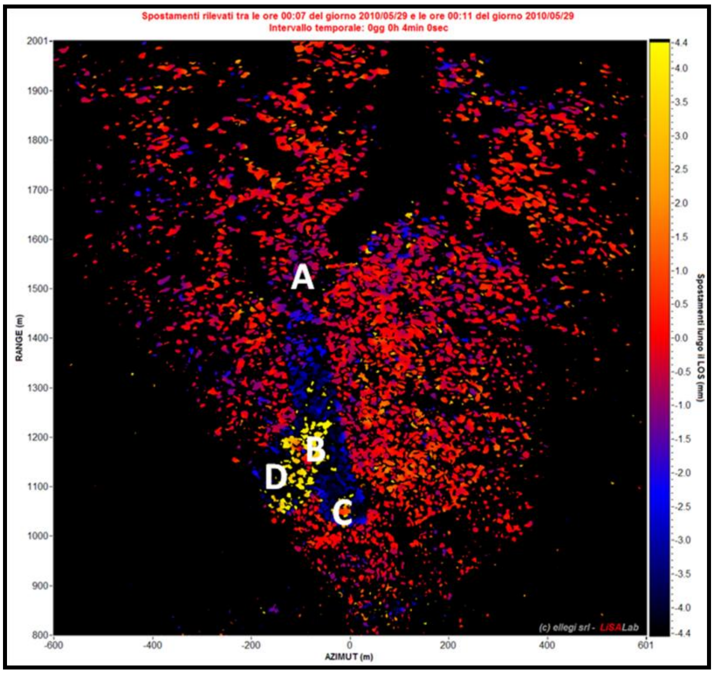

Figure 67 - Interferogram (time interval of 4 minutes) of May, 29th 2010. The time shown is GMT (-2h compared to local time). The deformation rate of the "C Sector" was about equal to 6.2 mm.

The comparison of the surface topography between 2010 and 2011 (Figure 68) shows the total reshaping of the slope, as for the previous sector it is not possible to distinguish the natural slope variation. A general lowering of the topography, due both to the downstream slipping of the material and the material removal, is however detected.

Figure 69 shows the comparison between the first monthly cumulated map available (July 2010), that in May 2012 (the month in which the landslide foot works ended) and that of December 2012: taking into account the differences in scale, it is clear as the area is almost stabilized.

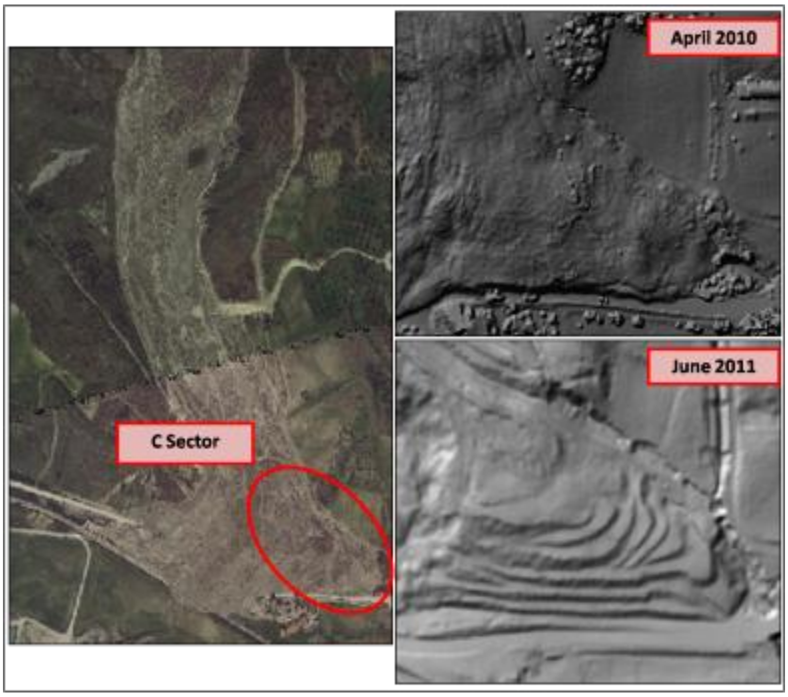

Figure 68 - Comparison between the DTM and DSM of the "Sector C" and location of the area on orthophotos (left).

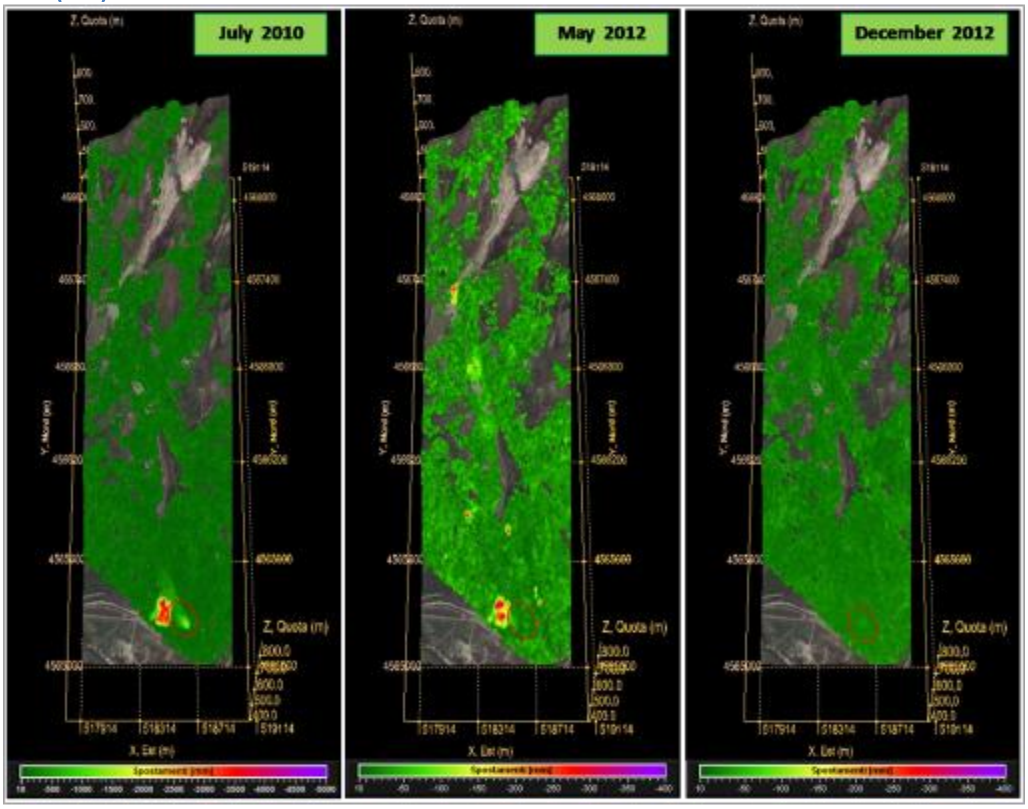

Figure 69 – Monthly cumulated displacement map of July 2010, May 2012 and December 2012 (note the differences in scale) and location of the " C Sector ".

4.2.4 D Sector

There were been several days in which the maximum velocity speed recoded was of the same magnitude: June, 16th- 17th – 18th and 21st, 2010 , with displacement greater than 7.6 mm in about 4 minutes, corresponding to 2.43 m/day; related interferograms are shown in Figure 72. The "D Sector" was then second sector in terms of deformation rate after the "B Sector".

Comparing the daily deformations and the daily cumulated rainfall (Figure 70 and Figure 71), this area behaves different from the previous. Despite the deformations were subjected to a decrease from July 2010 as in other cases, the values variations recorded in the following months are higher compared to the preceding areas: the causes of this behaviour can be many. Firstly, the need to restore the fully functional of the road and railway network in a short time made it necessary the removal of the landslide deposit from the bottom, an unusual practice for the restoration of a landslide, since it causes a constant material supply from the upper side.

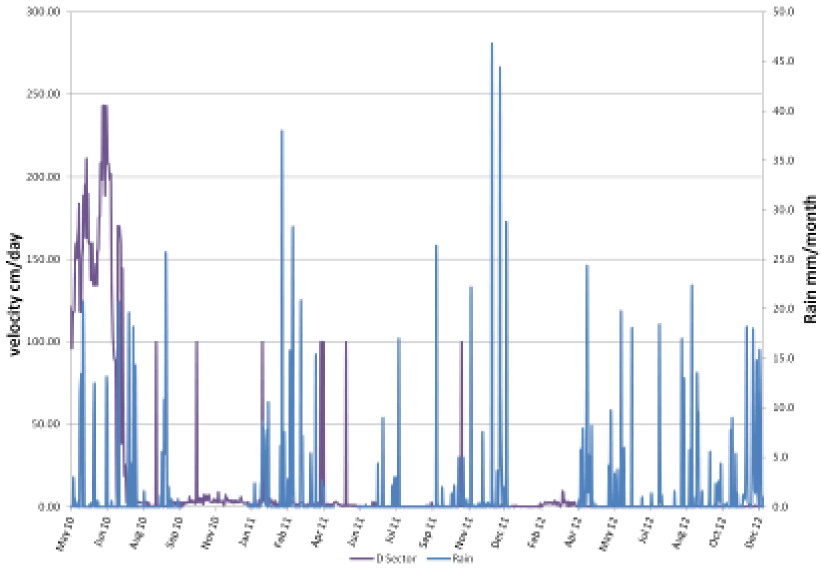

Figure 70 – Graph of the "D Sector" velocity and daily rainfall

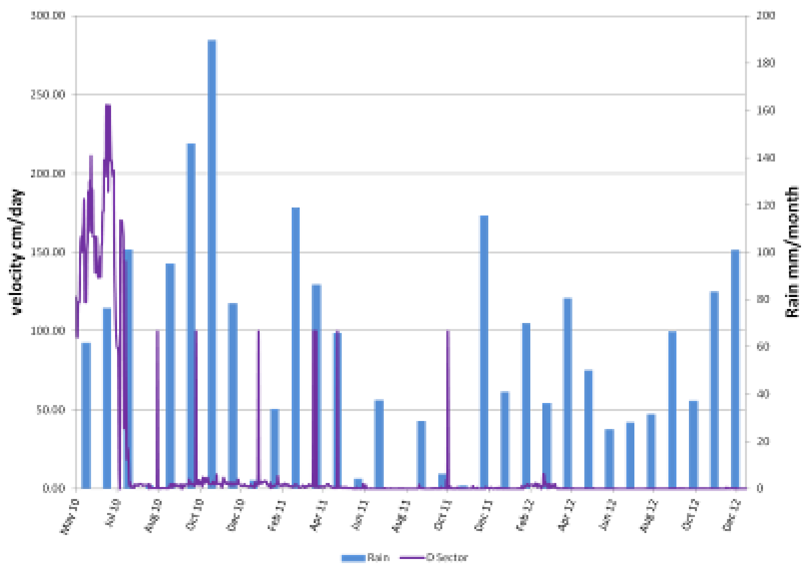

Figure 71 - Graph of the "D Sector" velocity and monthly rainfall.

In addition, the implementation of the engineering works have been continuing over the time, the deformation rate reach a more marked decrease since May 2012, when the works at the landslide foot were finalized.

Comparing the topographic surface corresponding to the "D Sector" between 2010 and 2011 (Figure 73) is immediately evident the deposit removal from the road and railway. Indicated by the red arrow instead, significant increase of surface runoff in the most central area can be distinguished, probably caused by the material removal at the foot bottom. The evolution of this movement is shown in

Figure 74, the comparison between the contour obtained from the raster of the monthly cumulated displacement maps, provides the representation of the contour lines of equal deformation. In April 2010, in the concerned area (indicated by arrow), there is a limited apparent shift, while in November 2010 the variation is much greater and the movement border seems backward. In May 2011, the deformation is decreased but the movement is further backward. The contour maps point out that the "D Sector" was subjected to high strain values and for a large area. In general, the surface topography of 2011 is located at a lower level compared to 2010, especially in the most central part where, the variation reaches up to 7 - 8 m.

In Figure 75the comparison between the first monthly cumulated displacement map available (July 2010), that in May 2012 (the last month in which there is an appreciably shift) and that in December; shows the zone is almost stabilize.

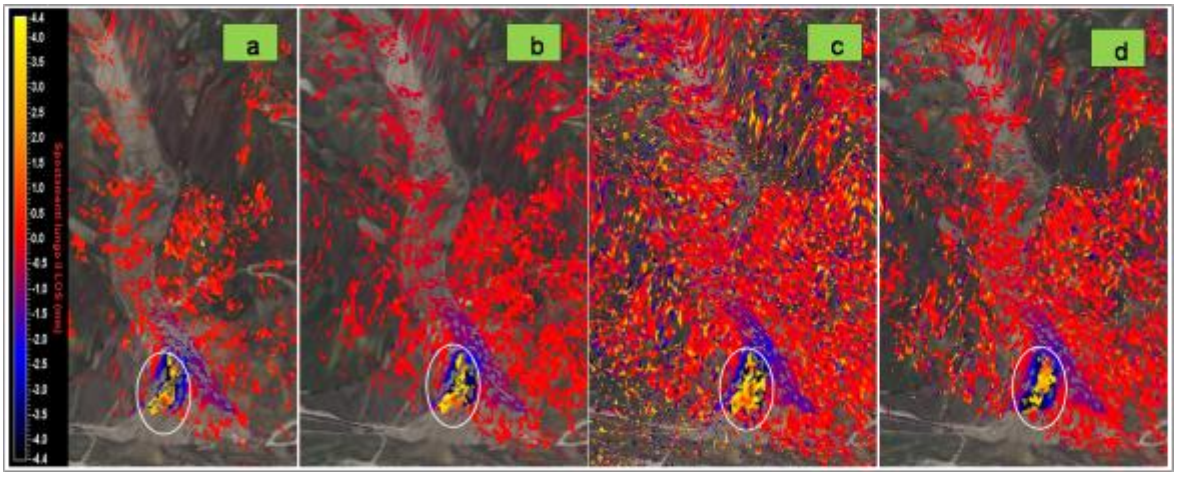

Figure 72 - Interferograms (time interval of 4 minutes) referred to the days: a) 16 b) 17 c) 18 d) 21 (June 2010). The time shown is GMT (-2h compared to local time). The larger deformation of the "D Sector" was equal to 7.6 mm.

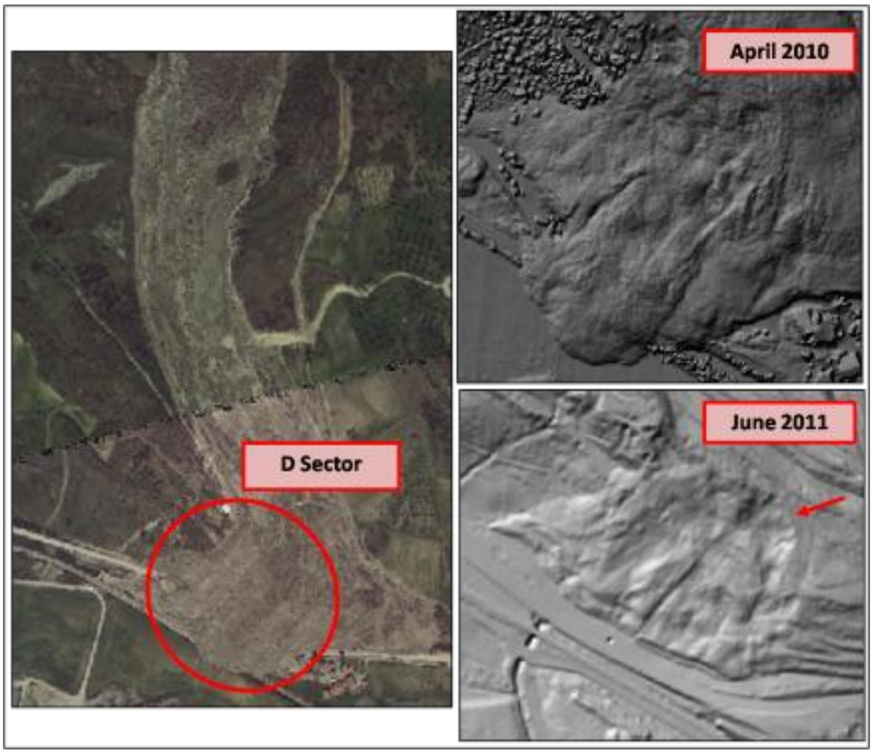

Figure 73 - Comparison between the DTM and DSM of the "D Sector" and location of the area on orthophotos (left)

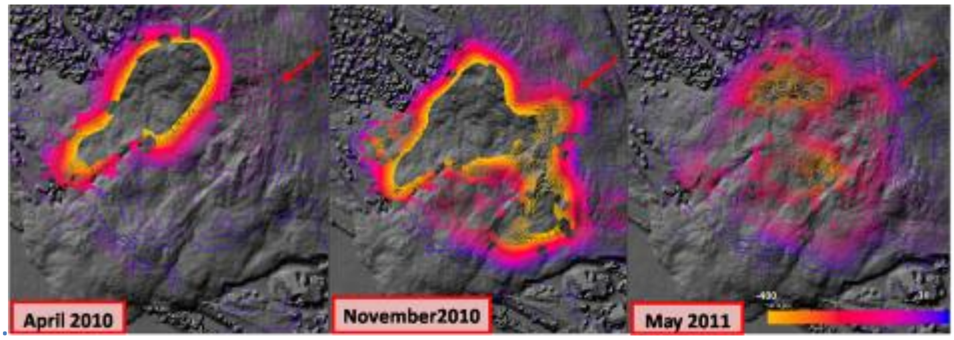

Figure 74 - Comparison of the contour maps extrapolated from the monthly cumulated displacement maps, relative to “D Sector”.

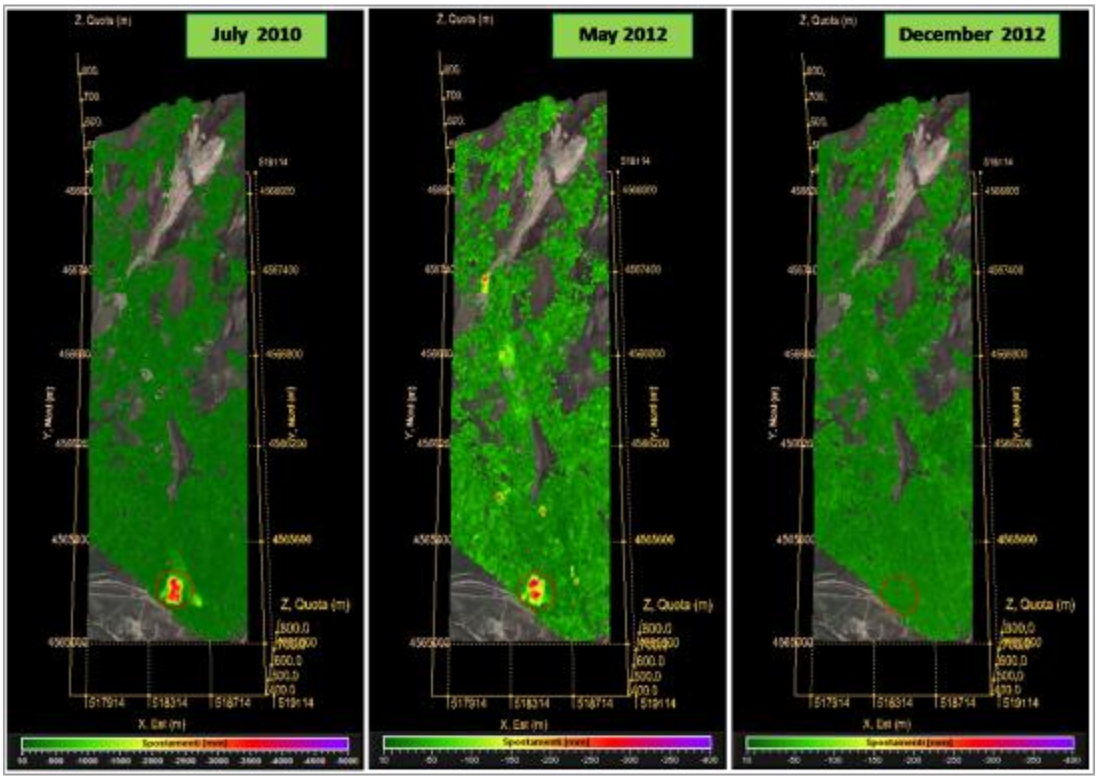

Figure 75 - Monthly cumulated displacement map of July 2010, May 2012 and December 2012 (note the differences in scale) and location of the " D Sector ".

4.2.5 E Sector

During July 2011 specifically analysis dedicated to the detection and interpretation of some new areas subjected to landslide deformation, were carried out. The monitoring results analysis, led to the identification of an area located upstream of the sector A Sector called then E (Figure 76).

Figure 76 – E sector limits and location.

This sector is located between the "elbow" of the landslide and the Sector A and corresponds approximately to the lower part of the area called "quota 700".

Basing on the monitoring radar evidences, a review of all the interferograms produced from the beginning (2 May 2010) was realized, with particular reference to the interferometric images on the interval of 4 hours, considered the most appropriate in relation to the possible movement rate of the E Sector (up to a few cm/day).

In this area the deformation was clearly detectable only in November 2010, while the highest velocity occurred in 2012, in particular on March, 16th and in April, 20th – 27th (71 mm/day).

As examples of interferogram of 4 hours in which the Sector E deformation is easily identifiable, are shown in Figure 77 those dating back to November, 24th 2010 and July, 28th 2011, from which we see the area is largely unchanged in its breadth and location.

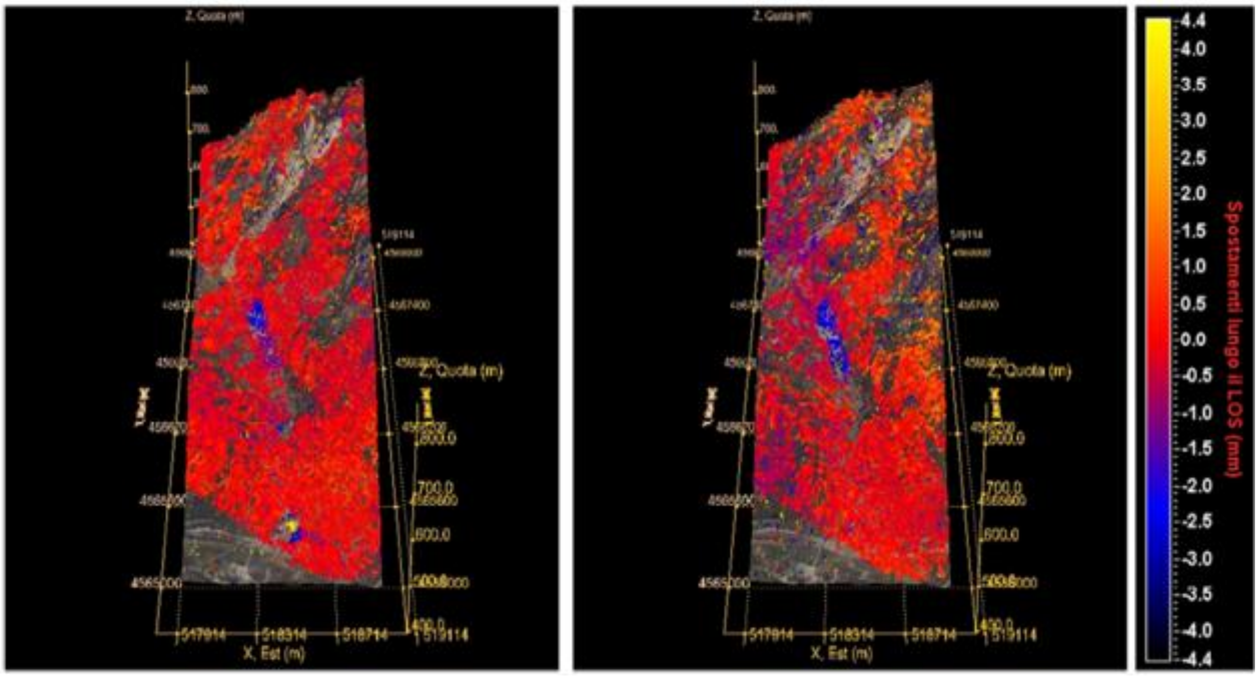

Figure 77 – Interferograms of 4 hours referred to November, 24th 2010 (left) and del July, 28th 2011 (right).

Daily speed data based on monthly or weekly can cumulated maps allow the assessment of a valid displacement values. In particular, weekly cumulated displacement maps relative to the period July 11th - August 7th, are reported in Figure 78 and Figure 79.

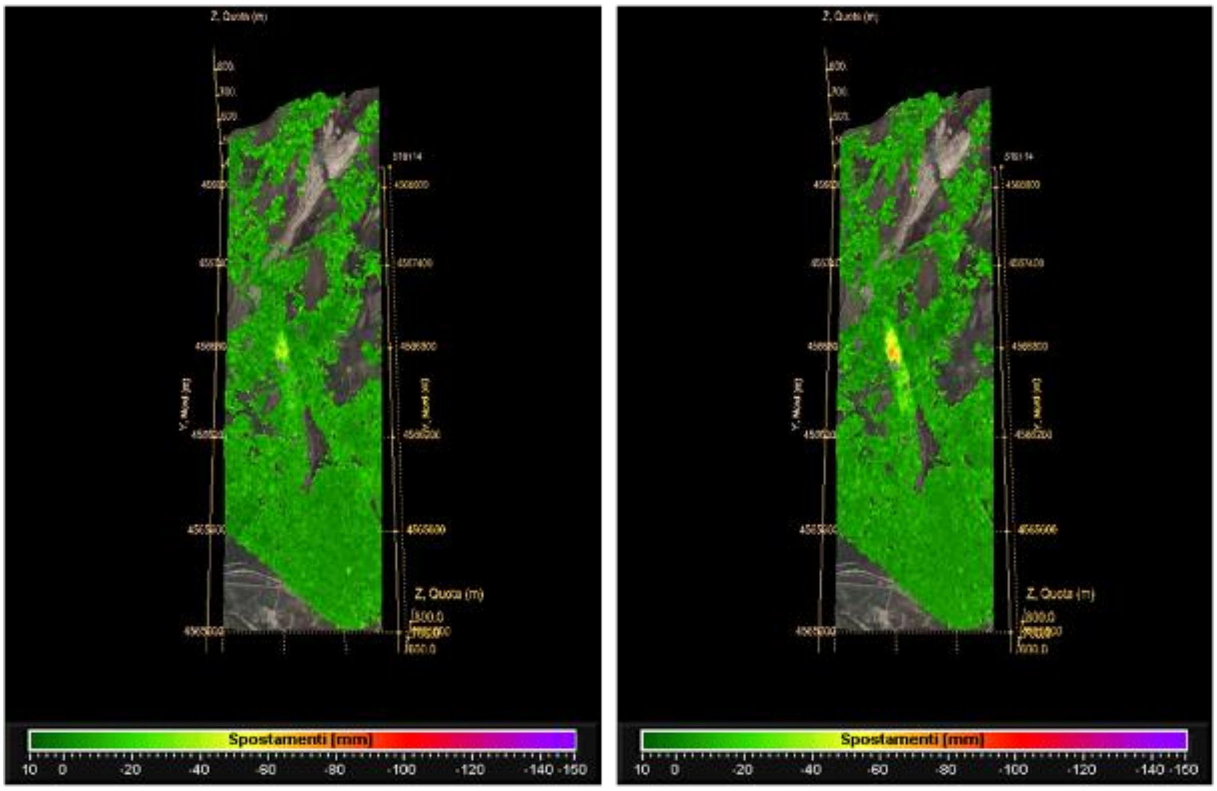

Figure 78 – July 2011, weekly cumulated displacement maps (11th - 17th and 18th - 24th).

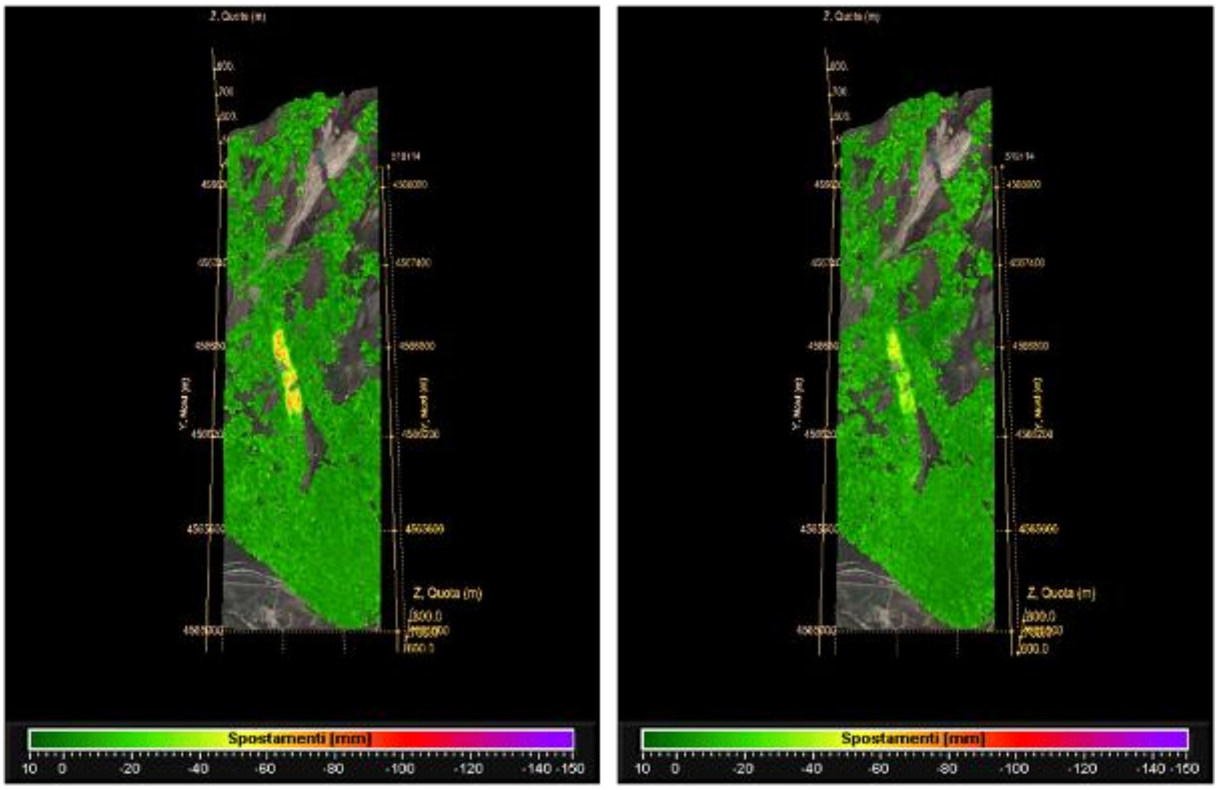

Figure 79 –July/August2011, weekly cumulated displacement maps (July, 25th – 31st and August, 1st - 7th).

Was observed that, although the E Sector is substantially unchanged in its geometry, highest displacements are usually located in the upper portion. The area so appears divided in three sectors, but two narrow transverse bands of separation are due to the shadow effects of the radar signal and therefore this division is considered mainly due to this phenomenon.

Figure 80 and Figure 81 show the relationship between the daily deformation rate and the monthly rainfall: a the considered scale, an abrupt decrease of velocity speed is not detectable (during the period from May to July 2010 there is lack of data), but from January 2012 the displacement rate keep its value under 1cm/day.

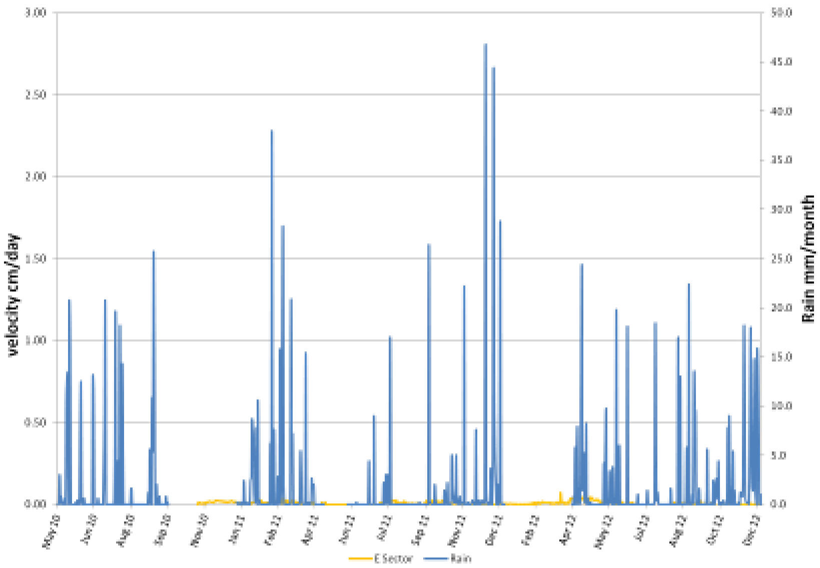

Figure 80 - Graph of the "E Sector" velocity and daily rainfall.

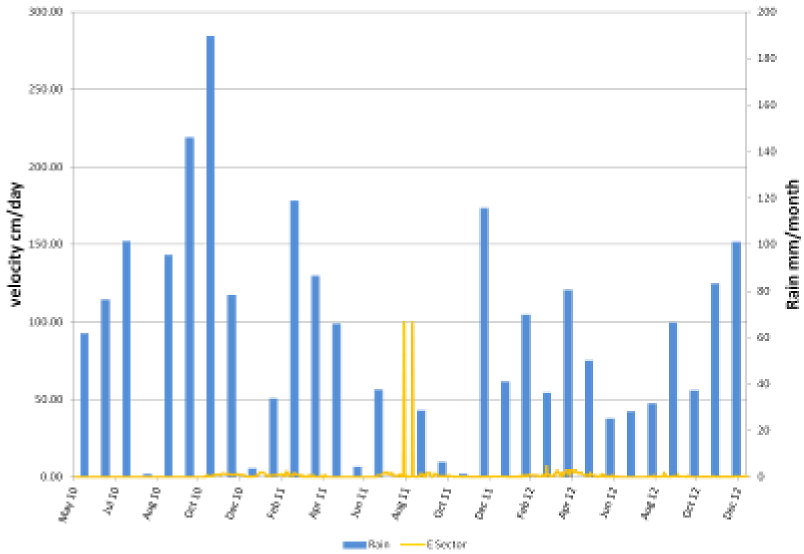

Figure 81 - Graph of the "E Sector" velocity and monthly rainfall.

Comparing the DTM (April 2010) and DSM (June 2011) in Figure 82, the more visible changes occurred are indicated by arrows. Corresponding to the number 1 a more pronounced slope is shown in the DSM 2011, while the arrow number 2 highlights a slight advance of the landslide deposit. Although these two aspects, the landslide morphology, unlike other sectors, has not undergone major changes, even the height difference was minimal. These evolution can also be observed in

Figure 83 where a contour comparison is shown. From November 2010 to March 2012 the scarp retrogression increasing is observable, which is subject to an even greater deformation in April 2012 and the landslide deposit downstream occurred.

Figure 84 illustrates the comparison between the monthly cumulated displacement maps of November 2010, March 2012 and December 2012: taking into account the differences in scale, the zone is almost stabilized.

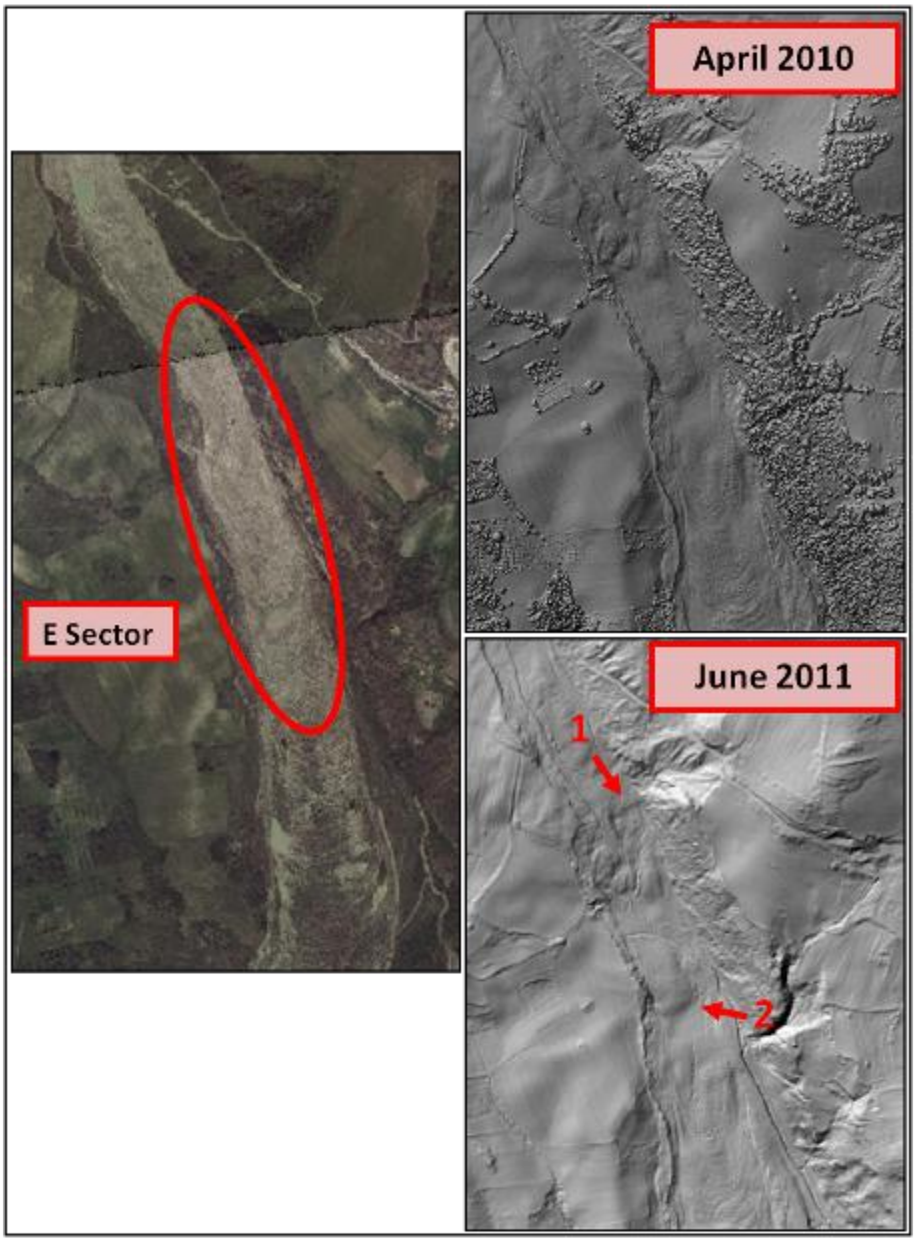

Figure 82 - Comparison between the DTM and DSM of the "E Sector" and location of the area on orthophotos (left).

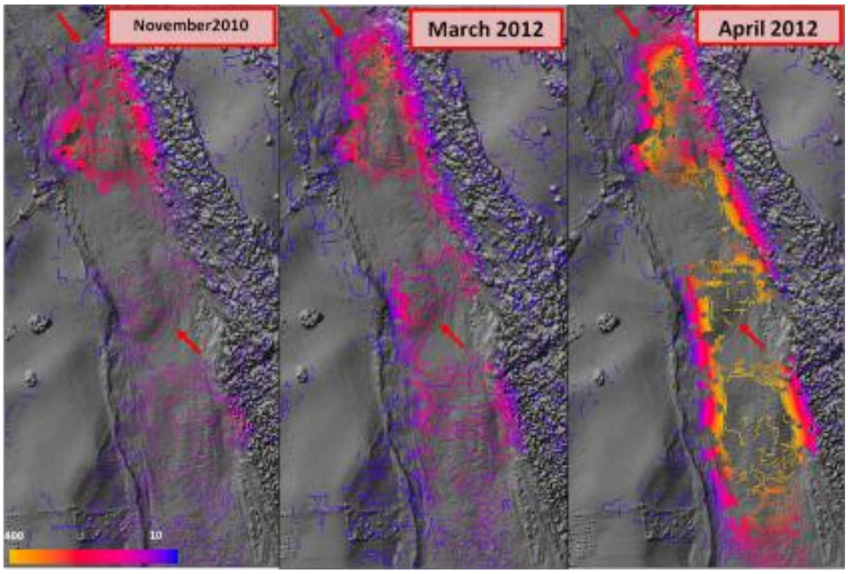

Figure 83 - Comparison of the contour maps extrapolated from the monthly cumulated displacement maps, relative to “E Sector”.

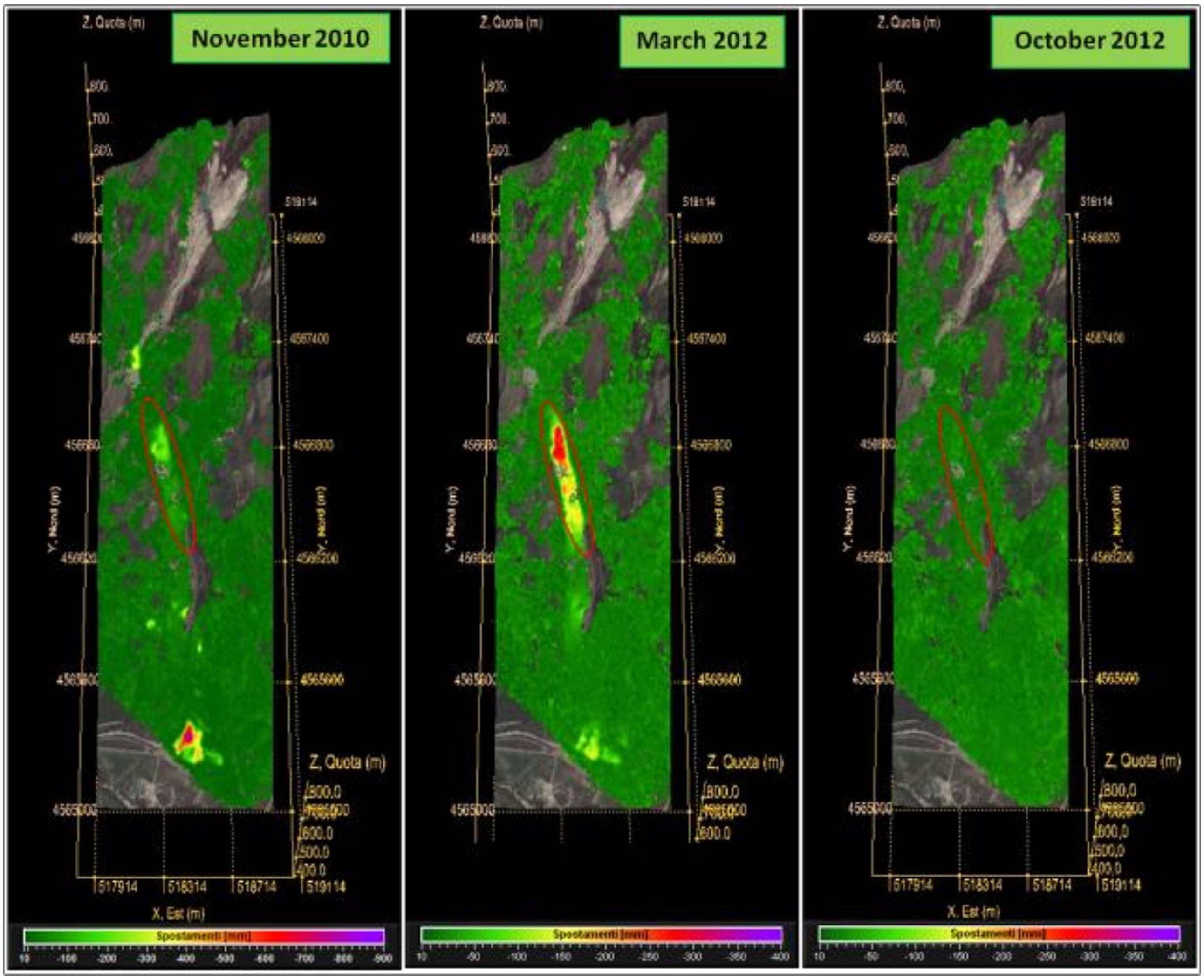

Figure 84 - Monthly cumulated displacement map of November 2010, March 2012 and December 2012 (note the differences in scale) and location of the "E Sector ".

4.3 The observational method as a support in stabilization works

In addition to the landslide monitoring activities, the DST-UNIFI, in collaboration with INGEO S.r.l., has provided the preliminary and detailed design as well as the works management that have been carried out, and the works to guarantee the security and landslide stabilization.

The Montaguto earthflow represents a really interesting case study in which the relation between the monitoring activities and the works design is closely linked to the Observational Method application.

Usually the monitoring has the aim to verifier the conformity between the design plan and the observed behaviours, and to check the works fully functionality over the time. When it is coupled with the observational method, its goal is also to validate the adopted design solution, otherwise, to identify the most appropriate design solution among the planned ones.

4.3.1 The Observational Method

The development and the using of the Observational Method started from the 40's, its historical evolution can be listed as follow:

- 40 to 60's - *Terzaghi and Peck*
- 1969 - *Peck's Rankine Lecture*
- Early 90's - *Channel Tunnel, Limehouse Link*
- 1994 - *Geotechnique Symposium in Print*
- 1995 - *EC7 OM Clause*
- 1996 - *ICE and HSE NATM publications*
- 1999 - *CIRIA OM Report No 185*
- 2001 - Managing Geotechnical Risk
- 2003 - Ciria C580 – Embedded Walls.
- 2004 – EC7 updated.

The two main ground-breaking were Terzaghi and Peck with their most important theories:

- “Every job is a large scale experiment. The information obtained from such experiments cannot be secured by any other means. It is of inestimable value in connection with future construction work of similar nature, provided the observations were reliable and complete enough to permit fairly definite and complete enough to permit fairly definite interpretation”(Karl Terzaghi);
- “*Peck’s observational method involves developing an initial design based on most probable conditions, together with predictions of behavior. Calculations are made and this are used to identify contingency plans and trigger values for the monitoring system. Peck proposed that construction work should be started using the most probable design. If the monitoring records exceeded the predicted behavior, then the predefined contingency plans would be triggered. The response time for monitoring and implementation of the contingency plan must be appropriate to control the work”*

The observational method facilitates design changes during stabilization works and establishes a framework for risk management.

It is not surprising that proposing changes tends to create concerns regarding safety and certainty. However, it is unfortunate that the method may be inappropriately associated with uncomfortably low safety margins coupled with the potential cost and delay of contingency measures.

Peck set out the Observational Method in his 1969 Rankine lecture and defined two OM approaches:

a) “*Ab Initio”* approach, adopted from inception of the project;

b) “*Best Way Out”* approach, adopted after the project has commenced and some unexpected
event has occurred that is different to the predefined design or failure occurs, and where OM is required to establish a way of getting out of a difficulty.

Predefined Design Process	**The OM Process**
Permanent works	Temporary works
One set of parameters	Two sets of parameters
One design / predictions	Two designs and predictions

Outline of construction method	Integrated design and construction methods
Contractors temporary works design/method statement	Methods relate to triggers
Monitoring checks predictions not exceeded	Comprehensive and robust monitoring system
If checks are exceeded, consider (a) Best Way out approach to design; or (b) redefine the predefined design approach reassessing the geotechnical uncertainties in the ground	Review and modify process – Contingency plan – Improvement plan
Emergency plan	Emergency plan

4.3.2 The coupled actions: OM and GBInSAR monitoring and stabilization works efficiency

The GBInSAR system became a key element in the work planning, reporting on a daily basis interferometric data that drove the interventions, and also suggesting when to stop in case of abrupt accelerations.

As described before, this first emergency phase ended in July 2010, when the displacement rate decreased.

After the analysis of all available data in terms of previous studies, results of recent surveys and direct observation of the area, was established a design line, to be updated "in progress" according to the responses of the landslide complex interventions in progress . This methodology has been placed at the base of all activities carried out up to now on the landslide led to indisputable results, although it cannot certify, at least at present, the definitive stabilization of the landslide.

The analysis activity starts from the preliminary definition of the works criteria and traces the subsequent phases of design and construction.

Since water was the main engine of the landslide, the primary objective of the undertaken actions was to remove it, both from the surface and from the deep layers. The restoration of an effective surface circulation has thus been planned, coupled with drainage trenches, able to collect deep circulation water.

The area affected by the landslide is very large, therefore it has been zoned into 3 different parts, to better plan and carry out the required interventions.

The upper part was characterized by the presence of a system of lakes, whose water, collected into a well by the drainage trenches and superficial channels, is delivered into a watershed located outside the landslide.

Superficial channels with bottom hydraulic jumps are currently carried out in the middle part of the landslide. Furthermore, deep drainage trenches have been dug, allowing deep water to spring at the hydraulic bottom jumps of the channels.

The system of superficial channels coupled with drainage trenches was also repeated at the lower part of the landslide. The water from the lower part and from lateral channel system are conveyed towards a natural watercourse that flows beyond the landslide foot.

In this way all the abundant stagnant water within the depressions created by the ground movements has been eliminated, thus reducing water infiltration and contributing to slow the landslide velocity down.

A pilot well has been also drilled upstream the landslide, to intercept the water flowing towards the main scarp; the promising results in terms of water amount and quality suggest a possible acqueductistic employment.

Finally, stabilization works were performed starting from the foot, once the interventions for water reduction was completed with the aim of protecting the main elements at risk. At first, steel reinforced gabions were installed to build a draining tied wall of considerable size, then the landslide has been reshaped in accordance with the drainage works already carried out.

A very interesting example of coupled action, is the analysis of the behaviour of the mid-sector of the landslide, the so-called ‘elbow’ (sector E): the movement of this sector became very relevant during November 2011 – May 2012 and its evolution was highlighted by GBInSAR data. This information was very useful in planning the working activities, primarily in the design of the drainage system, which was modified in progress.

The E Sector area still represents the most critical landslide portion, that’s why a design variation in terms of drainage elements addition in the two main channels realization, Figure 85 Figure 85 –illustrates the interferometric evidence of the deformation phenomena affecting the E Sector and the sub sequential design variant. The monthly displacement cumulated maps are referred to the two highest deformation rates time (March – April 2012), in which the velocity reached values equal to about 1 cm/day.

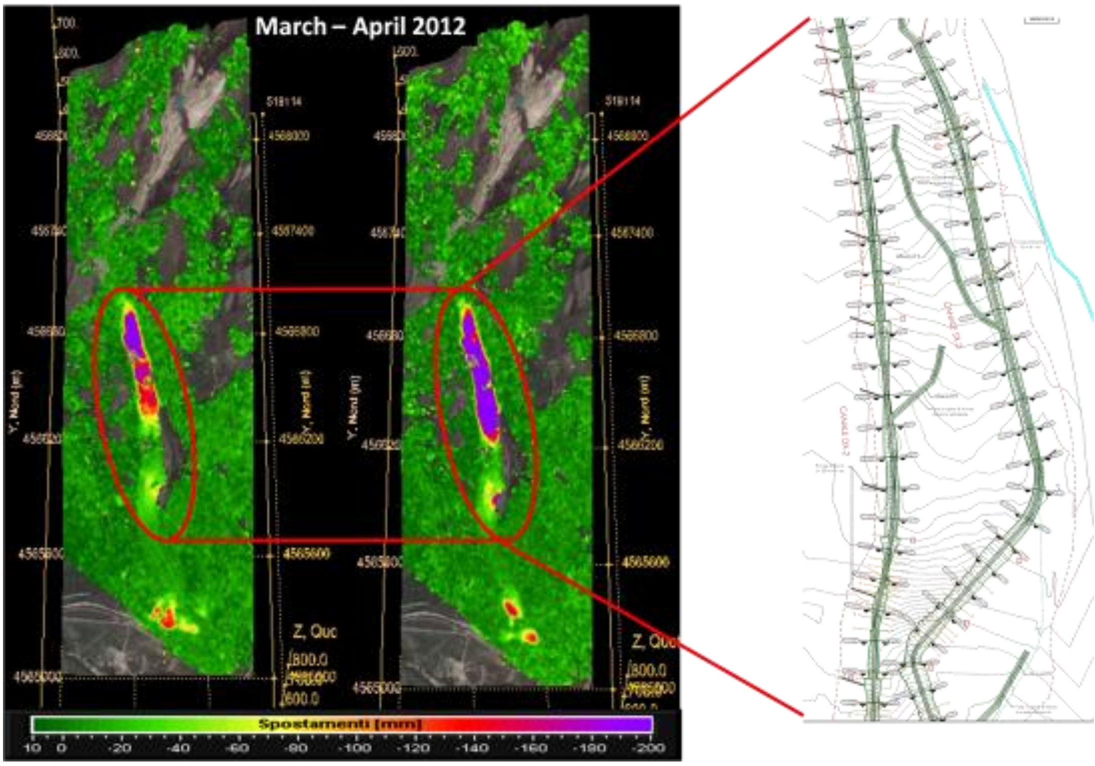

Figure 85 – Monthly cumulated displacement map with deformation area location and relative variant design of the area.

4.3.3 The stabilization works

The first works phases are practically completed, with exception of the important realization of the so-called "well field" at the head of the landslide, the only work, not ratified yet. It will then reference to the necessary works to achieve a degree of stability useful to consider the phenomenon “solved”.

Based on the landslide morphological characteristics, the lines of action, divided into three sectors are illustrated in Figure 86 .

In September 2010 work phases were outlined, and are here descried in Table 7.

In May 2012 the stabilization works ended improving on the landslide evolution in terms of deformations; in the same time the GBInSAR approach has been proved to be very useful during the emergency, for the support in the quick definition of the stabilization work plan, and to guarantee the safety of the involved personnel, as well.

The efficiency of the undertaken activities can be evaluated by observing the time history of the velocity recorded at critical points and the works phases distribution among the time, Figure 87.

The velocity graph reported has the vertical axes expressed in log scale, so its interesting to note the real gap in terms of order of magnitude.

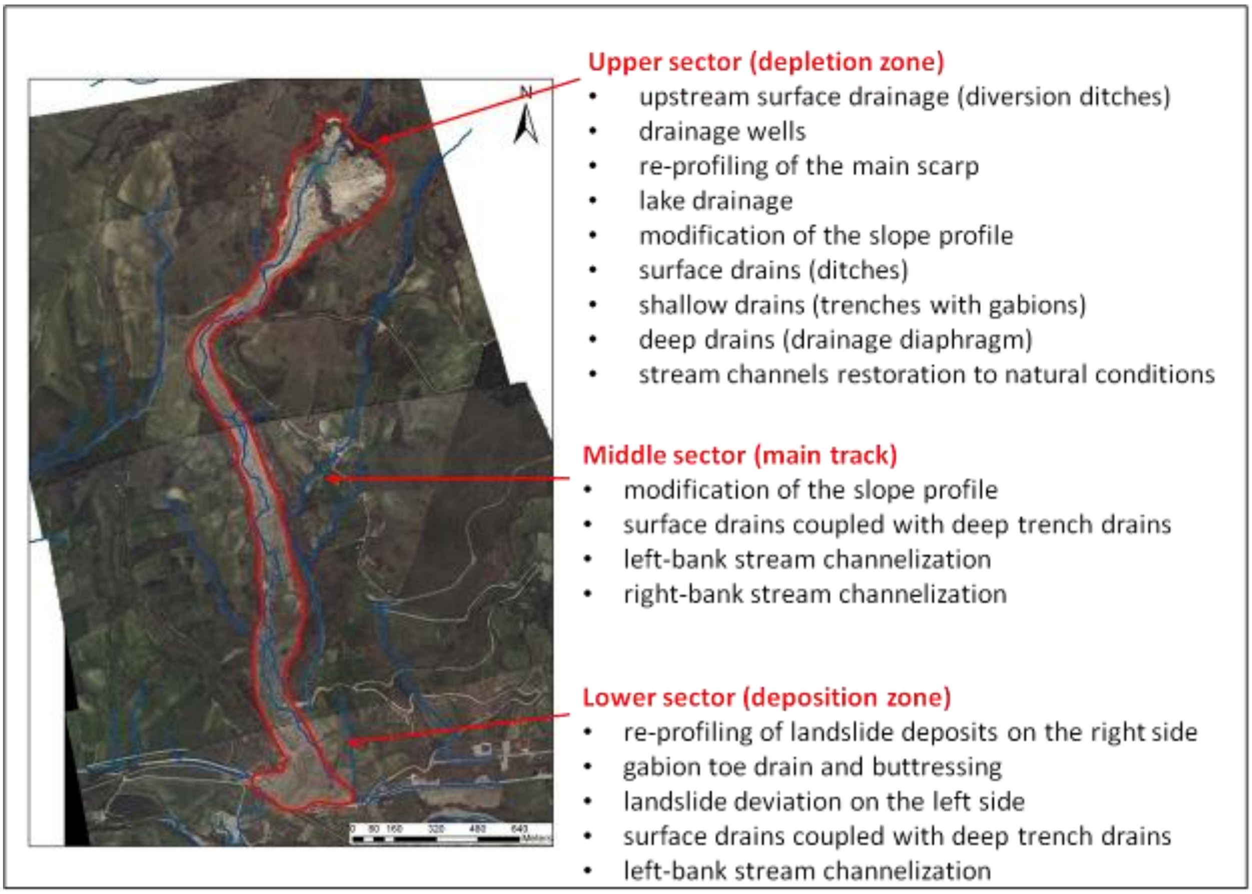

Figure 86 – Landslide morphological characteristics and relative stabilization works description.

Table 7 – Work phases outline.

PHASES	OBJECTIVE
Phase 1 Provisional restoration to working order of infrastructure by removing the soil and the reshaping of the foot of the landslide.	Restoration of rail traffic on the Rome - Bari; restoration of traffic on the SS. 90

Phase 2a Interventions for the reduction of water in the landslide body	Limiting the speed of the moving masses and the reactivation of the landslide in the autumn winter season
Phase 2b Interventions for the conservation of the foot of the landslide in the transitional period	Ensure the functionality of the infrastructure during the implementation of structural
Phase 3 Programming and planning of the final settlement in accordance with the configuration of the infrastructure project	Definitive restoration and safety of the infrastructure concerned by the failure.

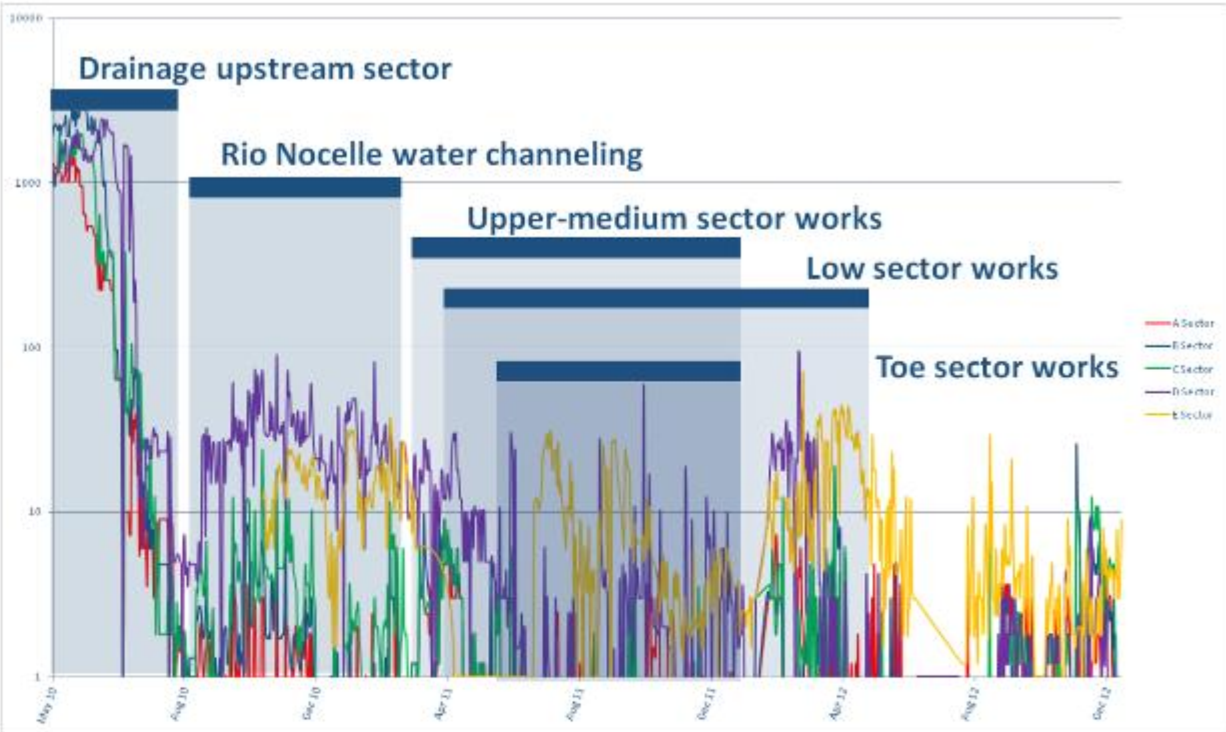

Figure 87 – Graph reporting the stabilization works evolution and the displacement velocity decrease from the emergency phase beginning and the end of the considered study period.

5. Hydrological and stability modelling of Montaguto landslide

5.1 Introduction

In order to simulate the hydraulic response of a landslide over relatively short, it was necessary to represent the physical nature of component hydrological processes in a relatively simple manner; in the model the vertical soil profile is represented by just three layers: root zone, colluviums, and underlying impermeable layer; and a suitably scaled digital elevation model (DEM) is used to apportion the landslide laterally. For each cell then, processes of infiltration, unsaturated and saturated flow, and through flow, are represented using a simple 'non-linear tank model' approach (Suawara, 1995). Gravity driven vertical moisture movement is simulated at a rate limited by soil conductivity and the capacity of the underlying layer to receive moisture. Horizontal movement is modeled in the direction of neighboring cell of lowest moisture content, and at a rate determined by a derivative of Darcy's Law. For each time step, moisture movement is therefore modeled vertically between layers for each cell; and then horizontally, between cells of the same layer.

Physically based models are favoured since they are capable of predicting alterations in the hydrological behaviour by means of the constituent equations for the incorporated processes (Grayson *et al.*, 1992). The applicability of these models for future scenarios is, however, limited. Practical limitations are the related problems of spatial and temporal resolution, numerical stability and computation time. A further limitation is the large dataset that the more complex models require. Even if all model parameters can be acquired, it remains doubtful whether the changes in model output are discernible against the ensuing uncertainty (Nandakumar & Mein, 1997).

The uncertainty in parameter values derives from the natural variability and the discrepancy model-, process- and sample scale. Because of the use of the constituent physical relations, the model scale is inseparably bound to the scale at which the material properties have been sampled and at which the formulae have been defined. It coincides usually with a point scale and the support of the retrieved data is seldom larger than volumes of 1 dm^3 or 1 m^3 for soil properties that are taken constant over time. For soil properties, sampled over time by automated equipment, this support may even be smaller. This support may differ from the relevant process scale, often referred to as the representative elementary area or volume (REA, REV), that determines the observed behaviour (Bear, 1972; Wood, 1995).

Partly because of the spatial resolution of the data, partly because of the natural variability of the incorporated processes, the temporal scale of most models lies in the range from seconds to days. In contrast, the scale of interest is usually defined by larger natural or administrative entities (e.g. catchments and provinces) and by periods covering many years. The tendency of reducing the model resolution to cover these larger scales of interest leads to uncertainty in the estimation of parameter values (Heuvelink & Pebesma, 1999).

5.2 Climatic and hydrographical characteristic of the study area

Drainage

The study area is drained by 4.34 km^2 of streams. The area has been divided in 6 hydrographic basins and sub basins; the basin B06, so identified, surrounds the entire toe landslide zone.

Based on the Digital Terrain Model (DTM) with 5m cells, the main physiographic characteristic were calculated, as shown the Table 8.

Due to the widespread presence of wooded areas constituted by very permeable bedrock and the total urbanized areas absence, A_2= 10% A was assumed.

Table 8: Main physiographic parameters of the examined basins.

BASIN	A (km^2)	A_1 (km^2)	A_2 (km^2)	H max (m a.s.l.)	H med (m a.s.l.)	H min (m a.s.l.)	Length (km)	Medium slope *i*
B01	0.417	0.38	0.04	921.15	856.08	709.00	0.95	0.223
B02	0.332	0.30	0.03	835.00	730.66	623.96	0.89	0.237
B03	0.409	0.37	0.04	777.00	622.50	497.60	1.23	0.226
B04	0.290	0.26	0.03	635.16	570.90	485.99	0.96	0.155
B05	0.970	0.87	0.10	920.67	753.36	525.00	2.44	0.162
B06	2.661	2.39	0.27	921.15	703.45	415.00	3.45	0.147

The values obtained by the method VA.PI. have been used, with The empirical formulas application for calculating the time of concentration, which for the main basin and a return period of 100 years provide a peak flow approximately equal to 10 m^3/s.

Since a detailed investigation with direct measurements was not possible at that time, however a conservatively estimation of the water runoff during a critical event was determinate, Table 9.

Table 9: estimable runoff volumes (m^3) at a given period T for floods events

Basin	Return periods T (years)						
	2	5	10	20	50	100	200
B01	2.201	3.264	4.124	5.137	6.604	7.768	8.932
B02	1.622	2.405	3.039	3.785	4.866	5.724	6.582
B03	2.141	3.175	4.012	4.996	6.423	7.556	8.688

B04	1.499	2.222	2.808	3.497	4.496	5.289	6.081
B05	6.773	10.042	12.689	15.803	20.318	23.899	27.480
B06	21.465	31.827	40.216	50.085	64.395	75.745	87.094

Climate and Ordinary hydrologic condition

Based on the meteorological measurements in the study area (*www.campaniameteo.it*), seems it hasn't the same general rainfall pattern of the Campania region. The study area is one of the zone of where the minors precipitation events.

The nearest meteorological station to the study area located at 700m (a.s.l.), on the opposite side slope of the landslide is Savignano Irpino, which is about 5km distance to the South – West of the study area (Figure 88).

Figure 88: location of the meteorological station and of the unstable slope.

The nearest possible measurement of other climatic variables are available from this meteorological station. The area experiences temperate temperature conditions, with high relative humidity. Table 10 compiles the average values of various available climatic variables for the study region.

Table 10: Available meteorological parameters for the Savignano Irpino meteorological station

Variable	Average
Temperature max	12°C
Temperature min	6°C
Relative Humidity	75%
Wind Speed	16 km/hr

The meteorological station is on working from 2002, so seem to give an average representative sample of the rainfall trend of the unstable study zone; it was possible to investigate the inflow average trend of 11 years. The Figure 89 shows the monthly rainfall patterns relative to eleven years data, from 2002 to 2012. The yearly inflow value is about equal to 800 mm, the main amount of precipitation is concentrated during the winter time, while throughout the months between June and August minimum precipitations values occurred, this trend has been observed during the entire analysed time interval.

For this basin the contribution of precipitation would therefore results in an average supply equal to about 1.91 mm^3.

Since the landslide main activation occurred on March 10th, 2010, the meteorological data used during the modelling phase concern the time interval from the 2009 (pre-event) to the 2012 (event and post-event). With the exception of this climate section, the next, more detailed observation and analysis, will concern the shorter four years time lapse.

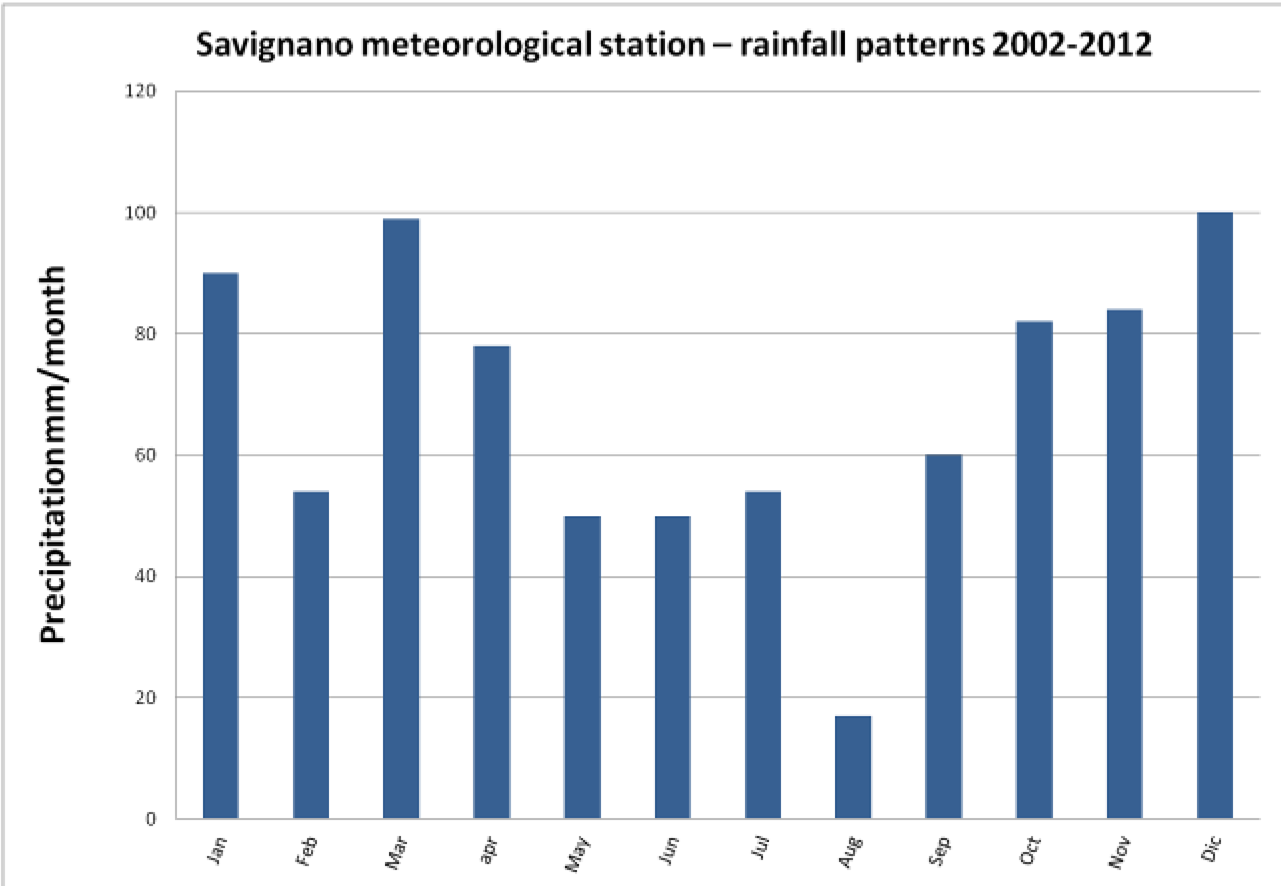

Figure 89: monthly average rainfall patterns relative to the years 2002-2012.

For this reason a monthly average rainfall patterns comparison, between the two set of years, was carried out and is shown in Figure 90. The graph exhibits a moderate difference in terms of water supply, the average yearly amount for the 2002-2008 interval is equal to 716 mm while the 2009-2012 one is equal to 780 mm. The extra 64 mm are limited to the wet season.

The Figure 91 points out that 2009 and 2010 were the rainiest years among those reported, with 1059 and 110 mm/year respectively.

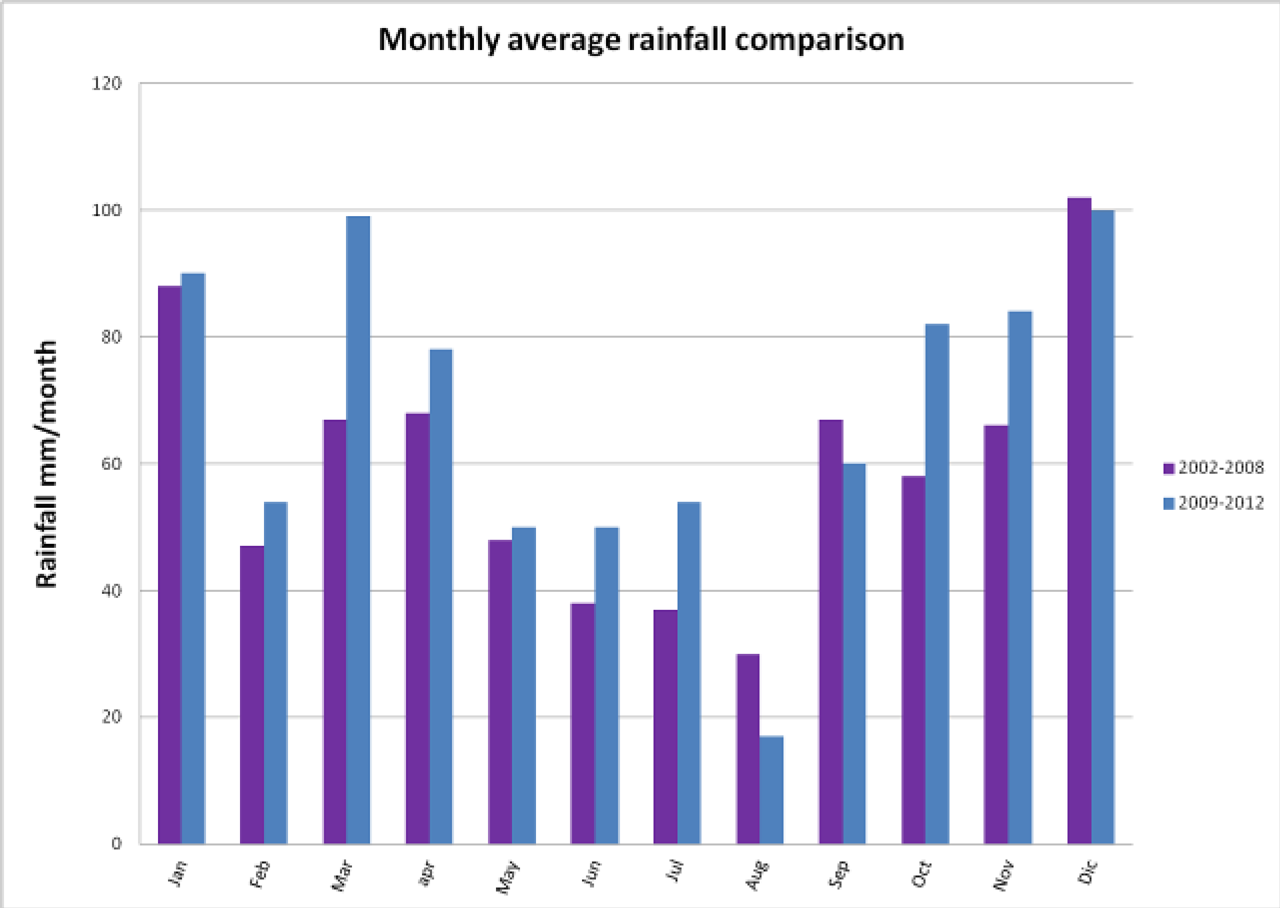

Figure 90: monthly average rainfall patterns comparison between the previous years (2002-2008) and last analysed four years (2009-2012).

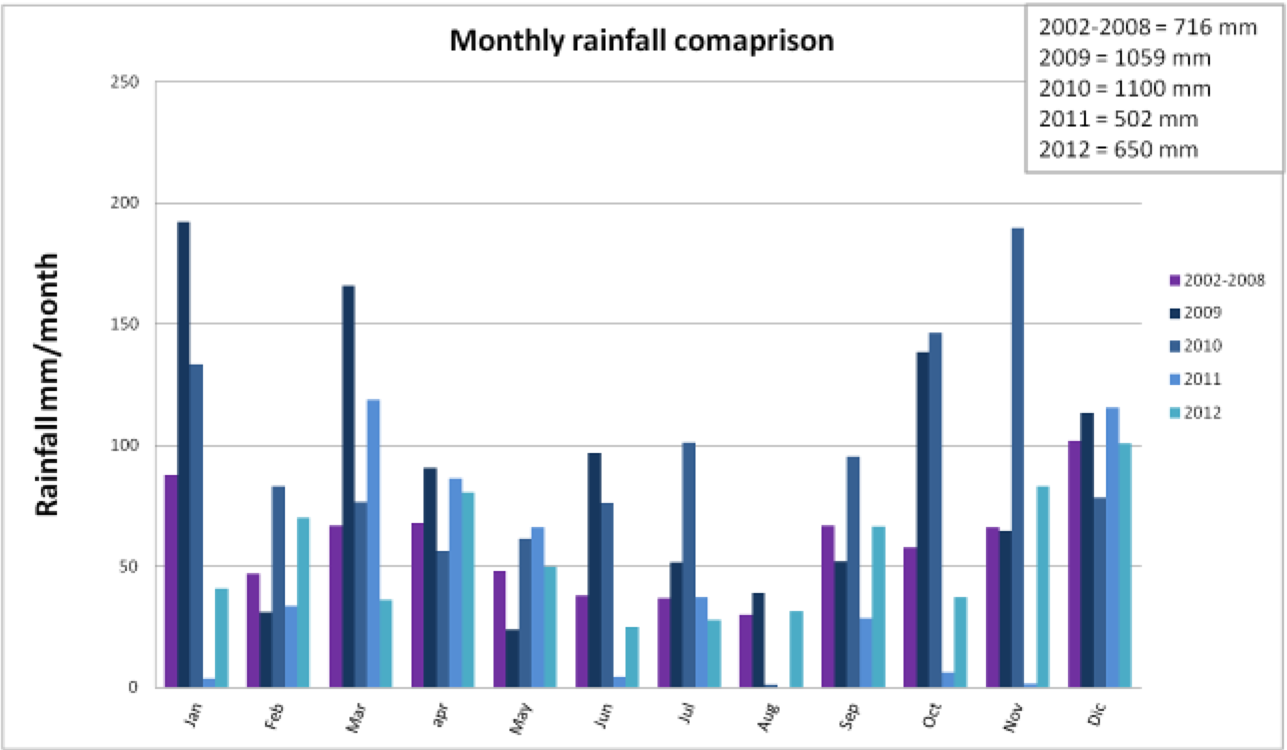

Figure 91 - Monthly rainfall patterns comparison between the last analysed four years (2009-2012) the monthly average of the previous years (2002-2008).

Potential Evapotranspiration and Net Rainfall

In the precipitation data shown in the previous section the evapotransipiration effect was not considered, the rainfall patterns so obtained refer only to the gross rainfall values.

Since to achieve a more realistic water balance the potential evapotransipiration and the net rainfalls were necessary, the subsequent calculation step was to obtain these data.

The data necessary for computing the potential evapotransipiration (Pet) were collected from the Savignano Irpino meteorological station as well. The computation was made using the daily average values of temperature minima and maxima for the years from 2009 to 2012.

Extraterrestrial Solar Radiation was computed using the Equation 1 (Allen *et al.*, 1998)

$$R_a = \frac{24(60)}{\pi} G_{sc} d_r [\omega_s \sin(\varphi)\sin(\delta) + \cos(\varphi)\cos(\delta)\sin(\omega_s)]$$

Equation 1: Extraterrestrial Solar Radiation

Where R_a extraterrestrial solar radiation in MJ m^{-2} day^{-1}, G_{sc} solar constant = 0.0820 MJ m-2 min-1, *dr* inverse relative distance Earth-Sun, *ωs* sunset hour angle, ϕ latitude, δ solar decimation.

The calculated R_a, the mean daily temperature and the mean daily Δ_T (Temperature Difference) was used to compute daily PE for the study area using Hargreaves Equation, Equation 2.

$$Pet = 0.0023 * S_0 * \sqrt{\Delta T} * (T + 17.8)$$

Equation 2: Hargreaves Equation for Evapotransipiration

Where, S_0 is the water equivalent of extraterrestrial radiation in mm/day, T the temperature in °C and Δ_T is the difference between maximum and minimum temperatures.

Once obtained the Pet values the subsequent calculations had the aim to determinate the net rainfall amount using first the Equation 3:

$$S_m = S_m - 1 \exp\left[\frac{Pet - W}{Smax}\right]$$

Equation 3: Soil Moisture Storage equation.

Where, S_m is soil moisture storage, S_m -1 is the initial soil moisture storage, Pet is the potential evapotransipiration, W are the precipitation and S_{max} is the maximum soil moisture storage possible assumed equal to 100, these parameters are expressed in mm/month.

Sub sequentially, to obtain the effective Evapotransipiration (ET) the follow function was applied:

$$\begin{cases} W - Pet > 0; & ET = Pet \\ W - Pet < 0; & ET = W + S_{m-1} - S_m \end{cases}$$

The *Appendix 2* shows the table with the detailed values for each month, relative to the water balance calculation.

The Figure 92 shows the calculated actual evapotransipiration for the four investigated years, it's evident from the graph that the general trend is represented by highest ET values during the dry season (from April to September) and lowest values in the wet season (from October to March).

The resulting ET averages relative to the dry and the wet season are shown below :

- 2009 = 2,2 mm/day (dry season) and 0,7 mm/day (wet season);
- 2010 = 2,3 mm/day (dry season) and 0,5 mm/day (wet season);
- 2011 = 1,5 mm/day (dry season) and 0,4 mm/day (wet season);
- 2012 = 1,7 mm/day (dry season) and 1,4 mm/day (wet season).

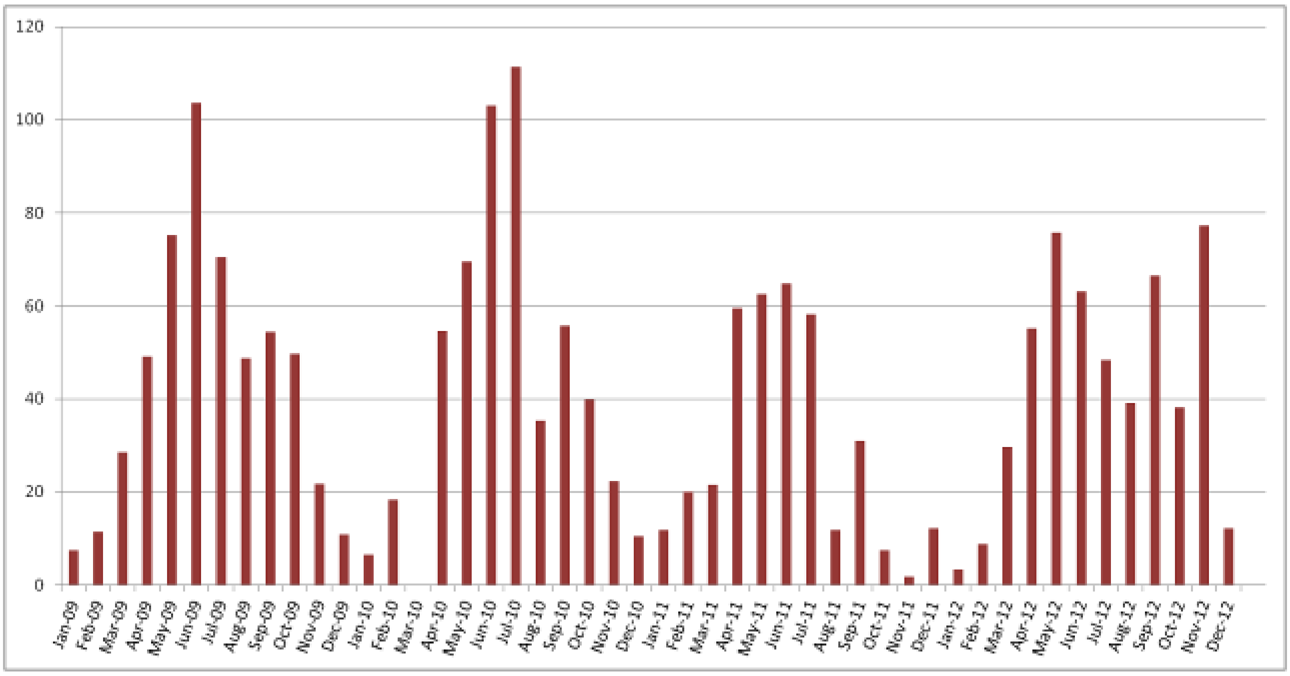

Figure 92: graph of the monthly average evapotransipiration from 2009 to 2012.

As the graph and the ET daily values highlight, while during the first three years the differences in terms of mm/day of evapotransipiration between the dry and wet season are quite evident with summer values up to 3 times the winter ones. This trend goes to change during the 2012, where the monthly average ET reach almost the same quantity in the both period (dry and wet) equal respectively to 1,7 and 1,4 mm/day.

Indeed, as is shown subsequently, the 2012 was the least rainy year among the considered period. The final significant results concern the net rainfalls values extracted from the Equation 4:

$$P_{net} = \frac{(W - P_{et})^2}{W - P_{et} + S_m}$$

Equation 4: Net precipitation equation.

In the Figure 93 the graph represents the comparison between the monthly precipitation, the potential evapotransipiration and the net rainfalls.

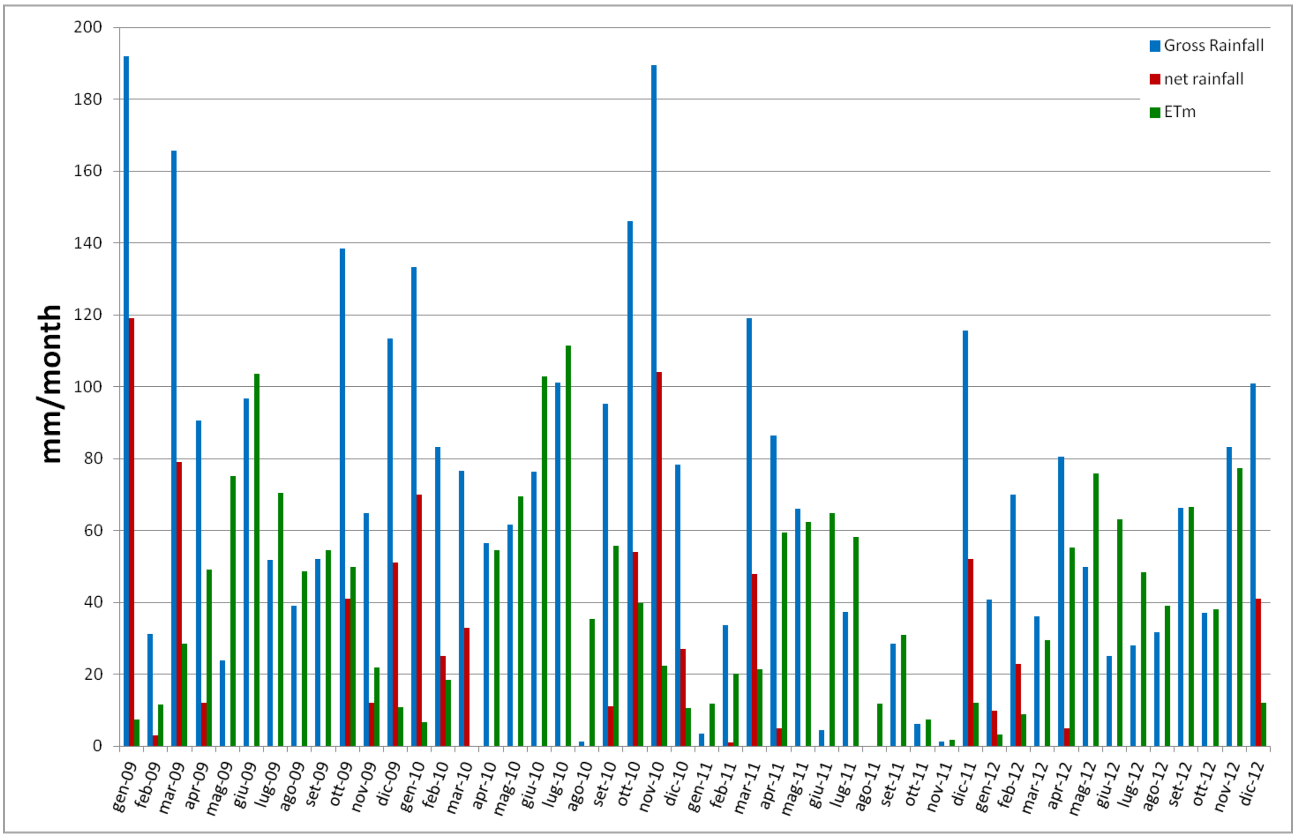

Figure 93: comparison between the most relevant meteorological parameters (in blue the gross rainfalls, in red the net rainfalls and in green the evapotransipiration), all expressed in mm per month.

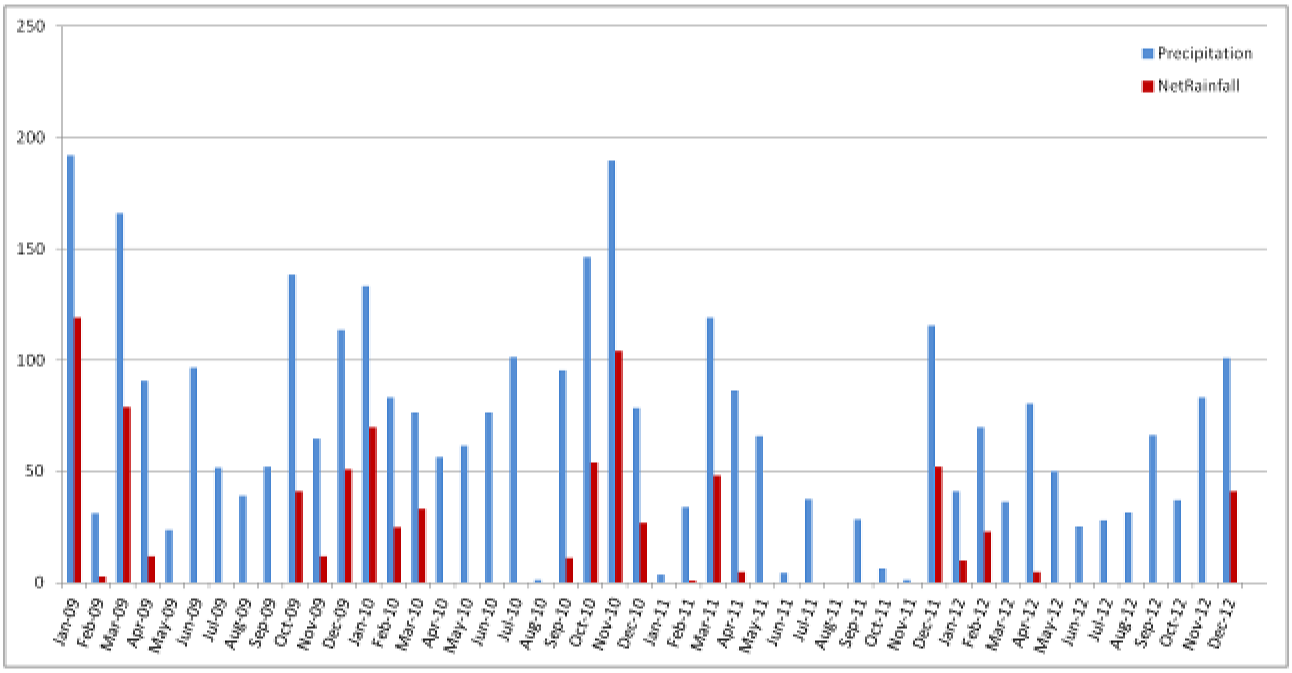

Figure 94: net and gross rainfall comparison

5.3 The model

The model chosen for conducting the study of the landslide evolution is physically based and is named as STARWARS + PROBSTAB (van Beek, 2002). The model was chosen, as it is needs the meteorological and geotechnical parameters as required for the objectives set out by this research, it allows land use and vegetation dependent parameterisation as well; in the case of the study area those parameters are not influential variables. Il the following section a brief synthesis of the PCRaster® Software is provided; a more detailed description of the slope hydrolology (STARWARS) and the slope stability model (PROBSTAB) devised by Dr. van Beek is furnished as well. Only few important assumptions and mathematical equations that relevant to the present study are clarified here.

5.4 PCRaster® Software

A brief description about the used software characteristics and use mode are described in this section. This software is a package of powerful set of command lines directly applicable in environmental studies. It is a Geographical Information System, which consist of a set of computer tools for storing, manipulating, analysing and retrieving geographic information, in which data type information in added to all spatial data (Karssenberg, 2002).

A first step to start using the all set of command and tools is the creation of a properly database.

Four kinds of data are used in the PCRaster database. Data from 2D areas are represented by raster maps. These PCRaster maps have a special PCRaster format that enables simple and structured manipulation of spatial data in the package. It is the most important kind of data in the database: almost any PCRaster operation uses and/or generates a PCRaster map. For analysis of PCRaster maps with other software packages, conversion to ascii format is needed. The remaining three kinds of data (tables, time series and point data column files) represent relations between PCRaster maps, temporal data and data from points respectively. These kinds of data are in ASCII format; as a result these can also be analyzed with other software packages, without conversion.

PCRaster maps describes the format of maps, including the location attributes, data types and legends in detail.

Relations between PCRaster maps can be defined by tables , which is the second kind of data used in PCRaster, see A table defining relations between PCRaster map layers; using these conditions a NewMap is generated, on a cell by cell basis, Figure 95. In a table, map layers are combined by specifying keys. Each key gives a certain combination of cell values of the map layers 1,2,3,... A key may be for instance: the cell of map 1 must have a value 6, the cell of map 2 a value larger than 200 and the cell of map 3 must contain a negative value. Using the keys in a table a new map layer can be generated which contains information taken from several layers. For instance a soil map, vegetation map and a slope map can be combined using keys in a table containing the classes of these maps, generating a new map with landscape classes. Also a table can be used for determining the number of cells that match the conditions given in the keys.

Table format describes the format of tables. The third kind of data used in PCRaster is the time series.

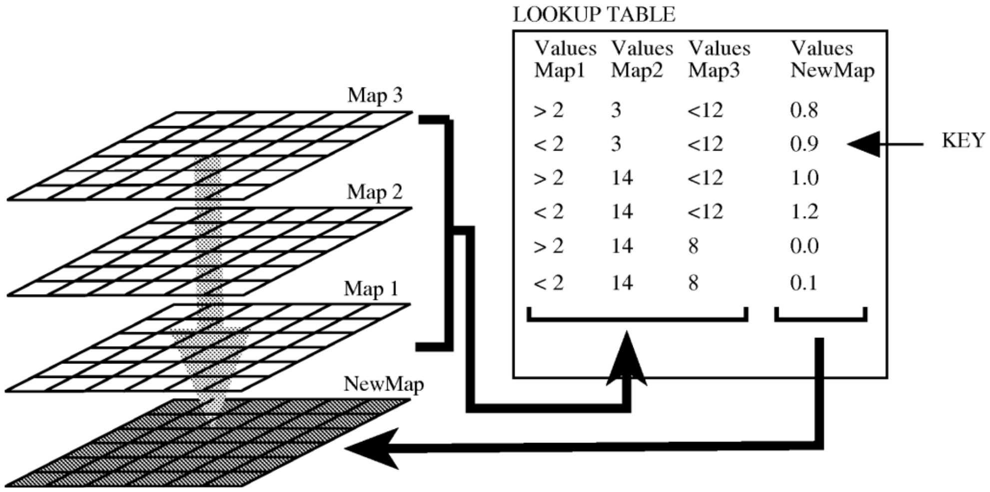

Figure 95 - A table defining relations between PCRaster map layers; using these conditions a NewMap is generated, on a cell by cell basis.

When you start a project, and want to import data to the PCRaster package in PCRaster map format it is wise first to make a map containing the header with the correct location attributes and the data type of the first data set you want to import.

How this is done is described in PCRaster maps: database management. This section also describes other aspects of database management with a map.

The location attributes projection , xUL,yUL, cell length, number of rows, number of columns and angle are used to define the position of the map with respect to a real world coordinate system and the shape and resolution of the map.

The Figure 96 shows schematically a PCRaster map of a study area and the location attributes used. As shown, the location attributes define the map with respect to the real world coordinate system (an ordinary x,y coordinate system). The choice of the location attributes must be based upon the shape of the study area and the data set you want to store in the map. PCRaster maps always have a rectangular shape, but the shape and size of the map does not need to correspond exactly with the shape of the area studied, as shown in the figure above: during data import to the

PCRaster map the cells in the map outside the study area are assigned missing values. A missing valued cell is a cell which contains no attribute value. Missing valued cells are considered not to be included in the study area: PCRaster GIS and Cartographic or Dynamic Modeling operators ignore the missing valued cells. In general, cells that have a missing value on an input map of an operation are assigned a missing value on the resulting output map(s) also.

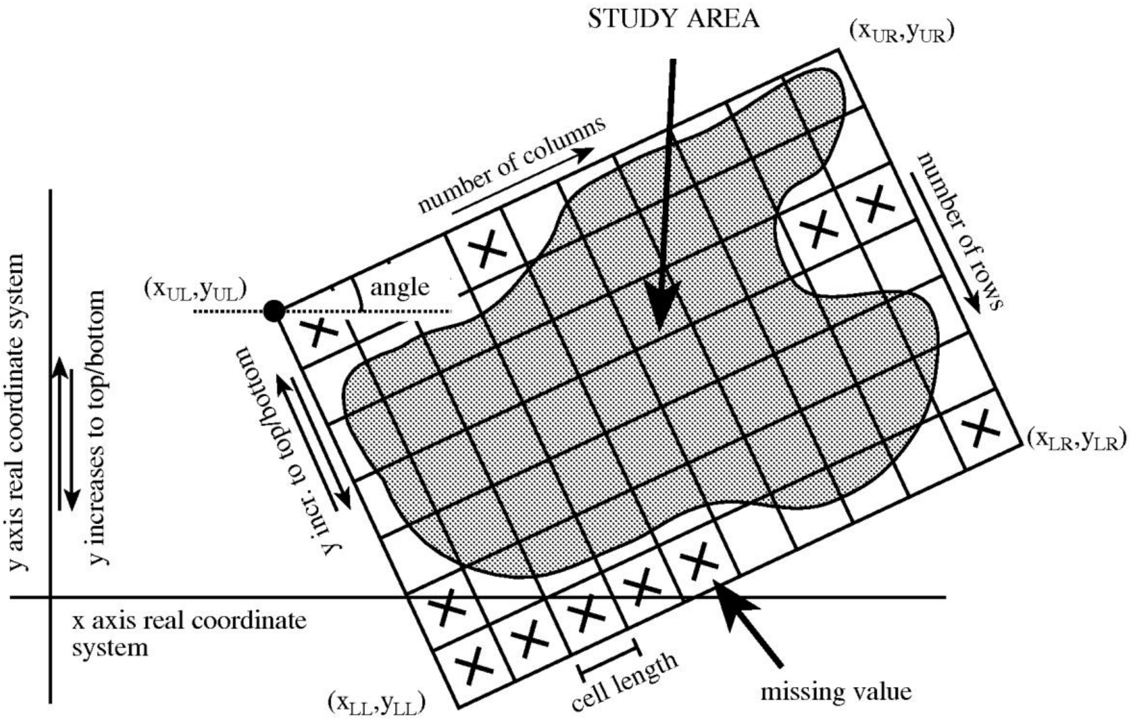

Figure 96 - Location attributes used to define the spatial characteristics of a PCRaster map.

Example of a time series file with a header, giving the temperature at three weather stations, meant for input or the output of a model with starttime 1, endtime 8 and timeslice 1.

Temp., three stations

4

time

station 1

station 2

station 3

1 23.6 28 23.9

2 23.7 22 24.8

3 23.7 22 25.8

4 21.0 24 21.1

5 19.0 24 17.2

6 18.9 22 17.9

7 16.2 22 15.9

8 16.8 24 14.9

A timeseries file with a header has the following format:

line 1: header, description

line 2: header, number of columns in the file

line 3: header, time column description

line 4 up to and including line n + 3: header, the names of the n identifiers to which the second and following columns in the time series are linked.

subsequent lines: data formatted in rows and columns, where columns are separated by one or more spaces or tabs.

Each row represents one timestep I at time t(I) in the model for which the time series is used or from which the time series is a report; the first row contains data for timestep I = 1, the second row for timestep I =2, etc. The first column contains the time t at the time steps. At the first row which contains data for the first time step (I = 1) it is always the start time t(1). For the following consecutive rows, the time in the first column increments each row with the time slice dt of the model: in the Ith row (Ith time step) the time is t(1) + (I-1) x dt. The remaining columns (column number 2 up to and including number N+1) contain values related to the N identifiers, where column number I is linked to the unique identifier value I-1. So, the second column contains values related to a unique identifier of 1, the third column contains values related to a unique identifier of 2 etc.

projection The projection of the real coordinate system which will also be assignednto the PCRaster map, is assumed to be a simple x,y field (also used innbasic mathematics). The x coordinates increase from left to right. The yn coordinates increase from top to bottom or from bottom to top. This can be chosen; from top to bottom is default.

xUL,yUL The xUL, yUL are the real world coordinates of the upper left corner of the PCRaster map. The location of the PCRaster map with respect to the real world coordinate system is given by this corner: if a rotated map is used (an angle not equal to zero), it is rotated around this point (so rotation over 90 degrees will result in a xUL, yUL that is at the bottom left side in Location attributes used to define the spatial characteristics of a PCRaster map.). Other PCRaster map corners are xLL, yLL ; xUR, yUR ; xLR , yLR .

cell length The cell length is the length of the cells in horizontal and vertical direction. This implies that cells in a PCRaster map are all of the same size and always square. The cell length is measured in the distance unit of the real world coordinate system.

number of rows, number of columns The number of rows and the number of columns are the number of rows and columns of the PCRaster map respectively. The cell length multiplied by the number of rows and number of columns is the height and width of then PCRaster map, respectively (in distance units of the real world coordinate system).

angle The angle is the angle between the horizontal direction on the PCRaster map and the x axis of the real world coordinate system. It must be between -90 and 90 degrees; a map with a positive angle has been rotated counter clockwise with respect to the real coordinate system, a map with a negative angle has been rotated clockwise.

In most cases an unrotated map will be sufficient (angle = 0 degrees).

Every time a new project starts and new maps and data input are set up, for each domain a data type need to be assigned, the Table 11 shows their characteristics.

Table 11: List of data types, domains for default cell representation, without legends.

Data	Type	Description attributes	Domain example
boolean	boolean	0 (false), 1 (true)	suitable/unsuitable,
nominal	classified, no order	$-2^{31} \ldots 2^{31}$, whole values	visible/non visible
ordinal	classified, order	$-2^{31} \ldots 2^{31}$, whole values	administrative regions
scalar	continuous, linear	$10^{37} \ldots 10^{37}$, real values	income groups
directional	continuous, directional	0 to 2 pi (radians), or to 360 (degrees), and -1 (no direction), real values	Temperature aspect
ldd	local drain direction to neighbour cell	1...9 (codes of drain directions)	drainage networks, wind directions

5.5 The Slope hydrology model: STARWARS

In the coupled model used here, the slope hydrological model STARWARS is complementary to the stability model and is used to investigate the spatial and temporal occurrence of critical pore pressures, VMC (Volumetric Moister Content) and the water level fluctuations; which are the most crucial component controlling slope stability of steep slope with poor quality geo-mechanical properties.

STARWARS simulates the spatial and temporal dynamics of moisture content and water levels in response to gross rainfall and evapotransipiration. Percolation through the unsaturated zone attenuates the response of the groundwater level to a large rainfall event. The importance of the antecedent net precipitation increases when the rainfall distribution becomes more erratic in time, as is the case in Mediterranean areas, (van Beek, 2002), as the case study.

The aim of the hydrological model , simulating the spatial and temporal occurrence of critical pore pressures, stipulates that the delay and loss of percolation in the unsaturated zone are included in the model. Therefore, the saturated and the unsaturated zone are considered freely draining and the groundwater levels unconfined.

In the model here, the response of the groundwater to the net rainfall is direct, the vegetation canopy of the landslide area is not enough to intercept the inflow water. Meanwhile, a rainfall fraction can be lost to the potential evapotransipiration.

The response of the groundwater is imposed on a constant groundwater level or generated over a semi-impervious lithological boundary that restricts the direct loss of soil moisture into the deeper strata. In the latter case, the resulting groundwater is a perched level, for example over the underlying bedrock. Although in theory the model is capable of simulating the response of deeper groundwater, only the latter case of perched groundwater layers is considered here. In this case, vertical flow is stagnating over the lithic contact between soil and bedrock.

As a consequence, percolation is limited to gravitational vertical flow only. Over the saturated zone, the piezometric head defines the lateral flow.

The soil profile is subdivided into three layers to best represent the variations in the soil properties with depth. In the model infiltration is added to the upper most unsaturated layer or in the case of full saturation to the saturated zone directly.

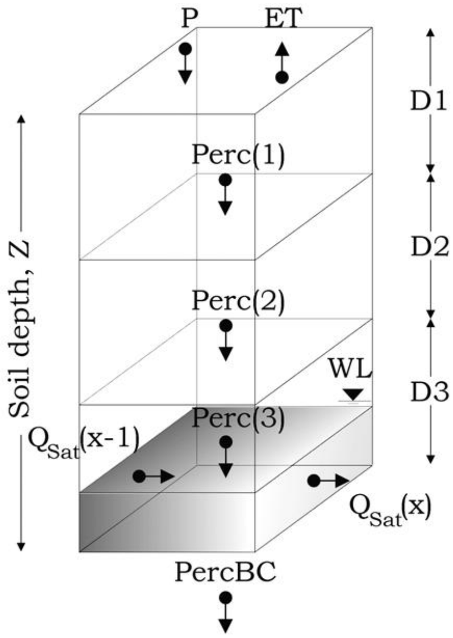

Figure 97: Schematic representation of the model concept of the hydrological component STARWARS. The Perc(z)fluxes are defined by $\theta_E(z)$, the saturated lateral flow Q_{sat} from the gradient *i* of the water level.

The utility of this method is that it supports computation as it can be converted by means of the maximum storage into the relative degree of saturation. The use of the relative degree of saturation has the advantage that it is the basis for the calculation of the percolation in the unsaturated zone. By definition, the relative degree of saturation, θ_E, is:

$$\theta_E = \frac{\theta - \theta_{res}}{\theta_{sat} - \theta_{res}}$$

where, θ is volumetric moisture content (VMC), θ_{sat} the saturated moisture content which is set to porosity and θ_{res} the residual moisture content.

The unsaturated hydraulic conductivity determines the travel time to pass each unsaturated layer and the percolation is directly proportional to the fraction of moisture that could pass the contact within one timestep. With ground water levels increase, the travel times reduce and to guarantee numerical stability the actual flux is calculated using a central finite difference solution including the additional changes in the unsaturated storage that arise from transpiration and infiltration/percolation. After obtaining the maximum transpiration as the product of the remaining potential evapotransipiration and the crop factor (van Beek, 2002), the actual evapotransipiration, therefore, is proportional to the available storage relative to the total storage of the soil profile. The actual evapotransipiration is distributed over the saturated and unsaturated zones according to the available storage. The procedure provides robust estimates of sustainable percolation and evapotransipiration rates in the soil.

Evapotransipiration and percolation lead to a change in the saturated storage that translates into a rise of the water table depends on the available unsaturated pore space. However, some leakage at the base of the soil column can occur and this can lower the water table or prevent its formation altogether as long as the percolation rate from the unsaturated zone is insufficient.

After evaluation of the vertical changes in water height for the current timestep, saturated lateral flow is considered. The elevation of the water table is used as the total head to calculate the gradient of the saturated flow in X- and Y-directions of the grid using a simple explicit, forward finite difference solution. The resulting lateral flow leads to a new water level and change in the depth of the unsaturated zone. The effective degree of saturation of the overlying unsaturated layer is used if water a fully saturated layer cavitates, if the soil becomes fully saturated any water in excess of the available storage exfiltrates as return flow to the surface.

5.6 The Slope hydrology model: PROBSTAB

The slope stability model is based on the infinite slope form of the Mohr-Coulomb failure law as expressed by the ratio of stabilizing forces (shear strength) to destabilizing forces (shear stress) on a failure plane parallel to the ground surface. The equation used is:

$$F=\frac{c'+\Delta c'+[(Z-WL)\cdot\gamma+WL\cdot\gamma']\cos 2\ \beta\tan\varphi'}{[(Z-WL)\cdot\gamma+WL\cdot\gamma_s]\sin\beta\cos\beta}$$

Equation 5: Safety Factor

Where, c' and Δc' are respectively the true and the apparent cohesion, ϕ' is the angle of internal friction, Z is the depth to the potential shear plane, β is the slope angle, WL is the water level above this plane and γ, γs and γ' are respectively the moist, saturated and buoyant bulk densities.

The slope stability assessment is deterministic and requires the input of the soil depth, Z, and the other parameters. The model has the option to calculate the critical depth, at which

F= 1, but for the present case the depth has been fixed to that of the third layer and the lithic contact is taken as the potential shear plane which is at the depth equal to 20m. The hydrologic input consists of the absolute matric suction, |h|, and the groundwater height, WL, which stem from the hydrological model component STARWARS.

Original PROBSTAB treats the variability of the shear strength rigorously, since a less computationally demanding method would be preferred the simpler First Order Second Moment (FOMS) approach has been adopted, in terms that the model provides an average, first negative and first positive standard deviation conditions of the safety factor based on the average and standard deviation inputs of the actual slope stability influencing parameters. The slope hydrology parameters are avoided for computing the FOMS based Probability of Failure. The original and more exhaustive PROBSTAB used by the model designer, is also computationally more expensive than the adopted FOMS approach, however its script allow to provide an estimation of the model sensitivity to the defined set of slope stability parameters excluding the slope hydrology parameters. It is assumed that arise from natural variability and sampling errors. The mathematics involved in the computation of Probability of Failure using FOSM is given below.

Foms assumes that the performance of a variable Y, such as Factor of Safety is a function G of random input variables $X_1, X_2, X_3 \ldots X_n$ (Equation 6 and Equation 7):

FS = G($X_1, X_2, X_3 \ldots X_n$)

Equation 6: Variable Performance

M(FS) = G($\overline{X_1}, \overline{X_2}, \overline{X_3} \ldots \overline{X_n}$)

Equation 7: Mean Factor Safety

where, M(FS) is the factor of safety computed with the mean values of all the input variables and function G is the infinite slope model. Cumulative Variance of FS based on each parameter is obtained based on the first negative and positive standard deviations. (Equation 8)

$$Var(FS) = \left(\frac{\Delta F}{\Delta X_1}\right)^2 \sigma^2(X_1) + \left(\frac{\Delta F}{\Delta X_2}\right)^2 \sigma^2(X_2) + \ldots + \left(\frac{\Delta F}{\Delta X_n}\right)^2 \sigma^2(X_n)$$

$$Var(FS) = \left(\frac{\Delta F_1}{2}\right)^2 + \left(\frac{\Delta F_2}{2}\right)^2 + \ldots + \left(\frac{\Delta F_N}{2}\right)^2$$

Equation 8: Cumulative Variance of Safety Factor

Assuming probability of failure normally distributed, the Z scores are obtained (Equation 9):

$$Z = \frac{FS - M(FS)}{\sqrt{Var(FS)}}$$

Equation 9: Z score assuming normal distribution

where, FS is the value of the factor of safety for which the probability of failure is determined, i.e. FS=1. This can be range between -∞ < F ≤ 1.

In the process the script as well computes that the factor of safety has with the change in each input parameter to the negative and positive standard deviations. These maps are a pragmatic estimate of the sensitivity that the safety factor has to each of the input parameters.

5.7 Model implementation

The coupled hillslope model is embedded in a dynamic GIS software package, PCRaster®, in this software the calculations take place on the level of the individual cells, therefore all parameters must be specified at the level of the individual cell. Since it is not feasible to specify the input for the individual cell, some form of generalization or interpolation is required. PCRaster supports different options, parameters can be entered as constants in the model script or included in tables, which relate the parameter value to a spatial attribute (van Beek, 2002). If a parameter is dynamic, it has to be specified for every moment in time. Spatially distributed parameters have to be provided as stacks of maps, with one map for every timestep. If the spatially distribution can be ignored or simplified to several units, timeseries can be used to enter dynamic model input.

Model output can also be generated in the form of maps and timeseries. Spatial information is well represented by maps, but often difficult to analyze over a longer period. For this purpose, the condensed information of timeseries, which give the temporal information for a limited number of points, is more suited.

The hydrological model component precedes the stability assessment, so the input of the first will be represented by the precipitation and the reference potential evapotransipiration over time, meanwhile its output will take part of the stability component input.

The hydrological model component also requires initial values for some of its state variables. These state variables are subsequently changed dynamically in the simulation of the hydrological processes. The Figure 98 shows what the input data included and the model performed steps to achieve the output data in the hydrological model component. The Figure 99 shows the stability model component structure; note that the dynamic output of the first model component are part of the input of the subsequent stability model component.

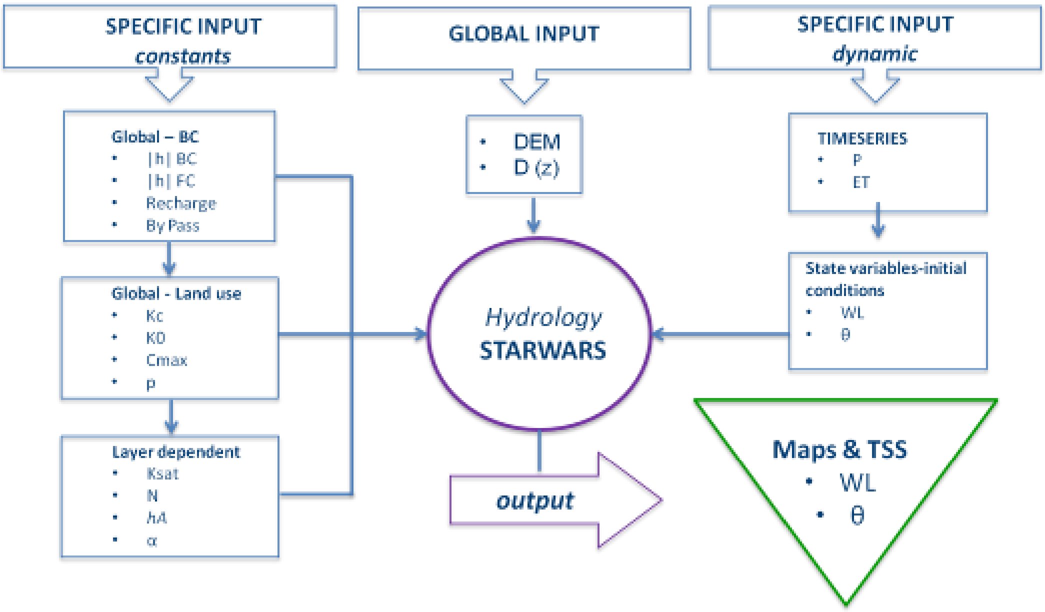

Figure 98: hydrological model component structure (after van Beek, 2002).

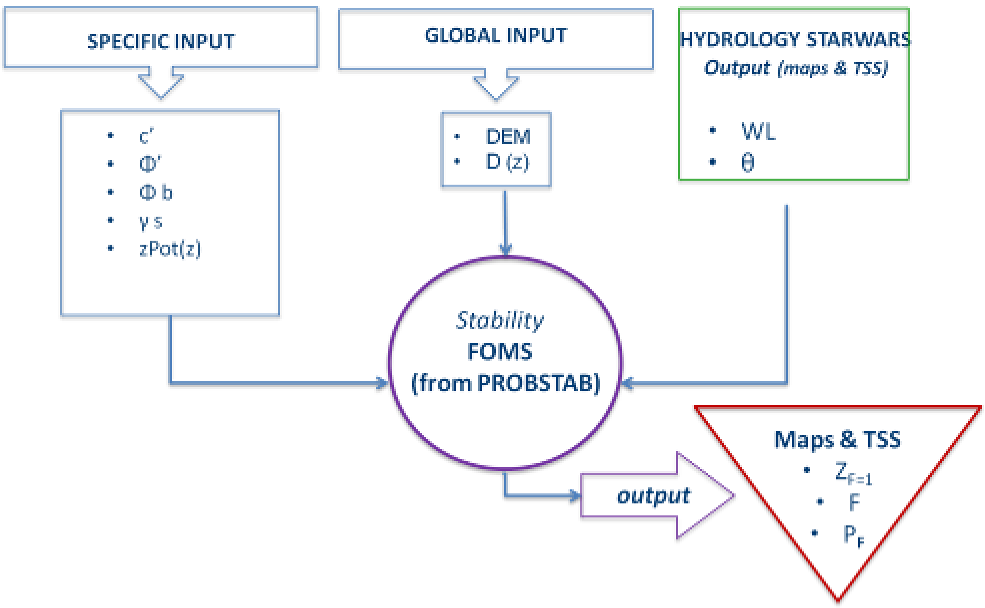

Figure 99 –Stability model component structure (after van Beek, 2002).

The schematization of the topography is based on the DEM, and the depth of the different layers above the semi-impervious lithic contact. This schematization is identical for the hydrological and the slope stability model component and has been used to specify the input for these modules.

The probabilistic stability component, is less demanding and requires the specific input of the shear strength parameters and of the dry bulk density.

The output of the stability assessment typically consists of the degree of safety, in this case of the safety factor, and the probability of failure over time. Together with the preceding output of the hydrological model component, the output of the coupled model comprises

• Groundwater levels;

• Soil moisture content for z layers;

• Average or expected factor of safety at specified locations, E[F], for example the base of z layers;

• Probability of failure at the above specified locations;

• The critical soil depth for which F= 1 ($Z_{F=1}$).

All output is basically composed of stacks of maps, reported at each timestep; in this case, the temporal scales of both components coincide.

In the Table 12 the model input and output are in detail described.

Table 12: Model input and output of the coupled hillslope model for hydrology (STARWARS) and stability (PROBSTAB) [based on: van Beek, 2002]

Model component	**Hydrology** **STARWARS**	**Stability** **PROBSTAB (FOMS)**
Model input		
Schematization	• High resolution **DEM (m)** • Layer depth **D(z) (m)**	
Constant parameter values	*Global boundary conditions* • Matric suction for lower boundary condition, **|h|BC (m)** • Matric suction at field capacity, 1st layer, **|h|FC (m)** • Residence* of surface detention, **Recharge (-)** • Fraction of bypass flow*, **ByPass (-)**	*Layer-dependent* • Cohesion **c' (kPa)** • Internal friction angle **ϕ' (°)** • angle of unsaturated shear strength contribution **ϕb (°)** • Dry bulk density of the soil **γs (kN·m-3)** • Depth of potential shear plane*** **zPot(z) (m)**
	Global – land use dependent *Evapotranspiration* • Crop factor **kc (-)** *Infiltration* • Infiltration constant **k_0 (-)** *Interception* • Max. storage capacity **Cmax (m)** • Direct throughfall ratio **p (-)**	

	*Layer depended*** • Saturated hydraulic conductivity** ksat (m·d-1) • Porosity n (m3·m-3) • Air entry value** hA (m) • SWRC slope** α (-)	*All parameters can be considered as layer and land use dependent*
	All parameters of the top layer can be considered as land use dependent	
Dynamic input – All timesteps	• Reference potential evapotransipiration **ET0 (m·d-1)** • Precipitation **P (m·d-1)**	• Groundwater level **WL (m)** • Volumetric soil moisture content **θ (m3·m-3)**
Initial conditions - state variables	• Groundwater level **WL (m)** • Volumetric soil moisture content **θ (m3·m-3)**	
	Model output	
Maps and Timeseries	• Groundwater level **WL (m)** • Volumetric soil moisture content **θ (m3·m-3)**	• Factor of safety F (-) • Probability of failure PF (-) • Critical depth ZF =1 (m)

*: not considered (by default all water is transferred over the LDD and no bypass flow occurs)
**: also required for lower boundary condition
***: optional if the potential shear planes do not coincide with the layer boundaries

Detailed data sets were required to parameterize the model on a daily timestep. Some kinds of parameters were not obtained from direct measurements but were estimated using established equations. Table 13 compiles various datasets used for parametrising the model with the respective use; all the vector layers were later converted to PCRaster .map files and ASCII format.

Table 13: Data, Type and Use

Data	Type	What for
Contour map (10m)	Vector layer	DTM, LDD and STREAM map generation
Sample location (GBInSAR monitoring sector)	Excel sheet (x,y points coordinates)	Controlpoints map generation
Geotechnical properties (cohesion, angle of internal friction, bulk density and degree of saturation)	Vector layer (points)	Calculation of Safety Factor
Rainfall (mm)	Excel sheet (daily rainfall from 2009-2012)	Effective rainfall reaching the ground
Temperature (°C) [min, max and average]	Excel sheet (1 location, daily from 2009-2012)	Reference evapotransipiration

Given the fact that DTM generated from 1m contour interval is the best available for the area constrains the best possible modeling resolution to 1m.
Daily meteorological data from 2009 to 2012, the examined period, were available for a point location close to the study area (see Section 5.2)

5.8 The model run

The slope hydrology model was run for 4 years (2009-2012), the required time-series files were derived from the climatic data available. The .txt files relative to the each investigated year were provided as inputs to the STARWARS script (*see Appendix 3*). The STARWARS was set to run on a quarter, an half and on a full day time step, and were made to report end time step of every day. This allowed to achieve water level and volumetric moisture content (VMC) acceptable trends. The PROBSTAB model was run in a batch file mode in order to arrive at the FOSM based probabilities of failure. The maps obtained were the Minimum Safety Factor and the unstable time steps.
It was set to run on a quarter, an half and on a full day time step in a first phase. Progressively the run mode was set on a spin-up time, which represents the time during which the information on the boundary is spread into the model and reaches the dynamic balance with the physical processes in the model. The length of spin-up time is dependent on model domain, season, and so on (Giorgi and Linda, 1999). During this period, some error information from the initial condition could also be left in the model, because of the balance between boundary forcing and dynamic processes in the model. Consequently, the simulated results could not completely reproduce the climate characteristics in the model. Therefore, the simulated results in the spin-up time are usually dismissed in the analysis of the results. No final conclusion has yet been reached on how to determine the spin-up time concretely. It has been found that the spin-up time for soil moisture and temperature in the upper soil layer is not too long. Generally, it will reach a balance with other variables in the model after weeks. However, a spin-up time of at least or more than 2 years is required for soil moisture in the depth of 1 m (Giorgi and Linda, 1999).
Basing on this considerations, the spin up time chosen was referred to every couple go years and/or more (2009-2011; 2010-2012; 2009-2012).

6. Discussion

The GBInSAR monitoring system results, discussed in Chapter 5, and the hydrological and stability model outcomes (Chapter 6) allow to draw general conclusions about the Montaguto earthflow evolution. In the following sections the comparison between the interferometric data analysis and the modelling results will be performed in relation to each monitored sector or landslide portion.

6.1 GBInSAR data results (Sectors A, B, C and D)

The behaviour of the sectors located in the lower area of the landslide can be equated. Although the velocity decrease occurred in different times, their variation as a function of the landslide works and drainage operation have been shown. In all four areas the apparent displacement is decreased after the works beginning and a further decline after the works achievement recurred. The deformations of both the lower transport part and the landslide foot are therefore not only caused by natural alterations but also by anthropic works, the same conclusion is reached in a recent paper by Giordan *et al.* , 2013.

In Figure 100 compares three optical images, illustrating the landslide view shot from the are compared GBInSAR location. The first (Figure 100a), shot on May, 18th 2010, about a month after the LiDAR flight, represents the landslide deposit still largely spread along the road and the railway: only in the C and D sectors, already show evidences of the slope remodelling. Despite the material removal from the foot doesn't represent the best practice in landslide areas, in this case it was necessary in order to reactivate the road and railway. However, a consequently and higher deformation condition, due to the progressive deposits was established. Figure 100b refers to June, 15th 2011, corresponding approximately to the second flight LiDAR, represents the four sectors considered partially improved compared to the previous situation: In "A Sector" you can see very well the drainage on the left border, while landslide debris has been removed from sectors C and D. It is also evident the drainage channel, designed to deflect the Rio Nocella waters, placed easterly direction with respect to the landslide. Especially in the central part of the image is notably as the landslide deposits is subject to revegetation, supporting the deformation reduction. In the last image (Figure 100c) is represented on the surface of the September 18th 2012: all the works have been accomplished, so in the middle-lower part notice the achievement of the drainage channels corresponding to the A sector, and the reshaping and works in the areas C and D.

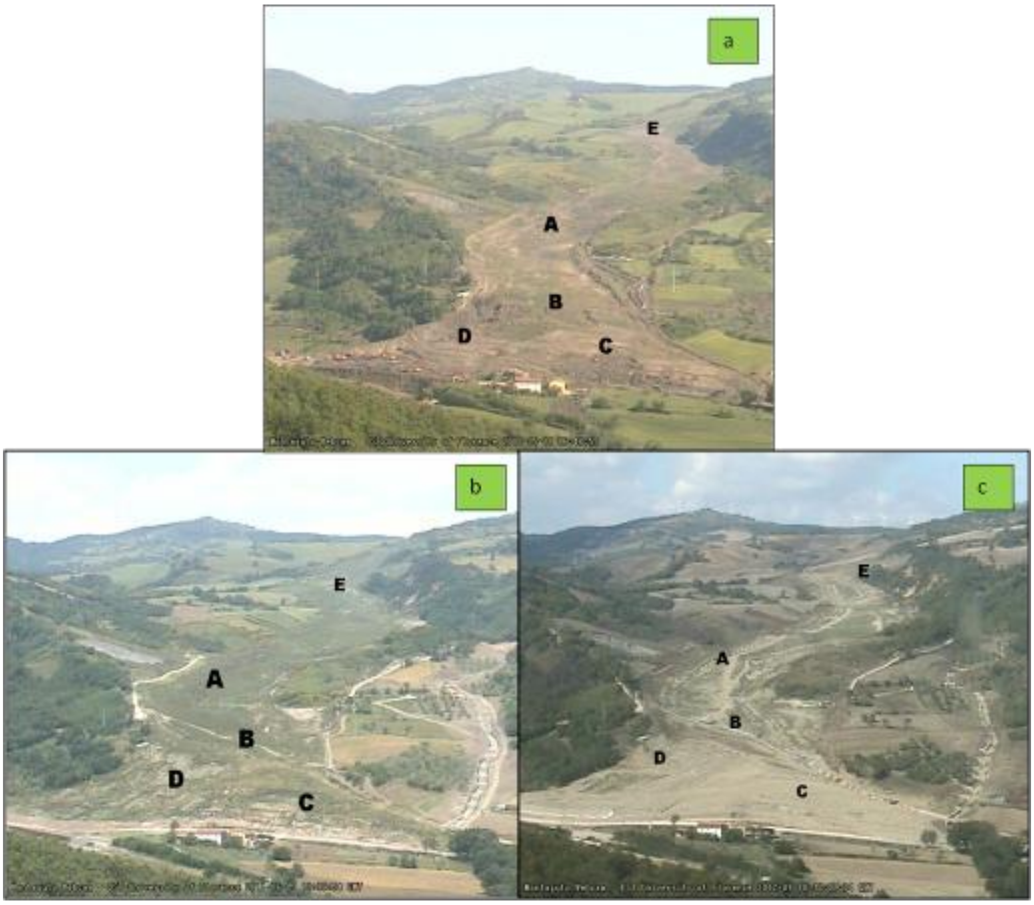

Figure 100 – Comparison between three optical images of the landslide medium-low part. a) May, 18th 2010; b) June, 15th 2011; c) September, 18th 2012.

The engineering works were carried out improving the landslide activity setting, with respect to the displacement speed: with the decrease of the displacement velocity the works have not been damaged and therefore they can be considered suitable for the aims. However, it must be reminded the work were intended to remove the shallow water: to have more certainty in keeping the landslide stabilized would be necessary also to plan works to allow ground water drainages.

Concerning the comparisons carried out thanks to the DSM and DTM obtained from LiDAR flights, it appears that the topographic surface in 2011 is generally located at a lower level than in 2010, proving a decline in the volume of involved material: the variation of volumetric changes from June 2005 to June 2011 comparing six different DEM (Digital Elevation Model) was calculated (Giordan *et al.*, 2013). Figure 101 shows the examined areas: the indicated area A corresponds to the upper and medium-upper landslide portion, the area B1 and B2 correspond approximately to the "E Sector", while Area C is located in the landslide foot, (A, B , C and D sectors). From the figure it can be seen during the period (April 2010 , green bar - June 2011 purple bar) the volume of the bottom areas has decreased, especially in the period April-June 2010.

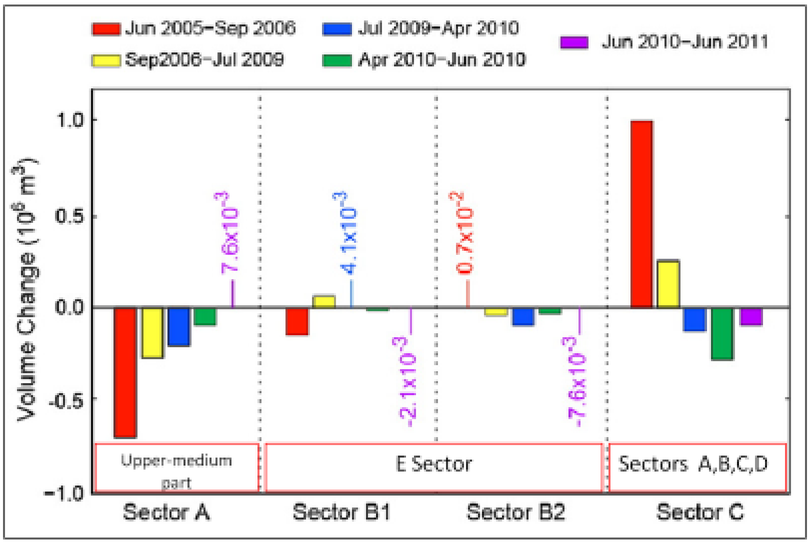

Figure 101 - Histogram of landslide volumetric changes for different sectors. Negative values indicate erosion, positive values indicate deposition (modified from: Giordan *et al.*, 2013).

6.2 GBInSAR data results (E Sector)

Since the E Sector showed a deformation behaviour different from the others, it is described in this separate section.

The works were carried between 2011 and 2012 (Figure 100), but unlike the previous cases, these have suffered considerable damage due to continuous deformation of the area. Some examples are shown in Figure 102: Photos A and B depict the dike deformed by the ground force, while C and D illustrate the deformation occurred to the geotextiles placed along the drainage channels.

A possible cause of the continued instability of the sector may lie in the fact that the engineering works carried out were not sufficient to guarantee the necessary water drainage in fact, as is represented in Figure 103 A and B, from a dig execution carried out in May 2012, the water outcrop was at few decimetres from the ground level. The ground water level reached a so much more superficial level compared to surveys conducted in 2006 and 2010: the level increase, could be a possible explanation for the fact that the deformations of this sector are significantly increased only since November 2010, the month in which however, the monthly cumulated rainfall (166 mm) reached its highest value among the analyzed time interval. The water flow in this landslide portion is definitely due to the drainage coming from the areas morphologically located on the upper external side of the landslide limit (Figure 103 C and D), where no retaining water flows works were carried out. Further movement evidence was the presence of fractures in the ground, as indicated by the red arrows in Figure 103 E.

Regarding instead the volumetric sector changes, the masses involved haven't subjected any net volumetric variations, (Figure 101) referring to the period April 2010 (green bar) - June 2011 (purple bar). Based on this evidence, supported by LiDAR and GBInSAR data, and through the model application a global data validation and comparison will be performed in the next sections.

Figure 102 – Examples of damaged works, due to the E Sector deformation.

Figure 103 - Photos of some E Sector criticality: A and B) groundwater level rising in a dike test; C and D) streams and pools of water present landslide limit, E) fractures.

6.3 Model results

Much effort was required to covert the accumulated data into the necessary parameters of the model as explained in *Chapter 6.* Results of this conversion from raw to model parameters are discussed below.

The relationships between the rainfall and the area of simulated failure stem from the hydrological response by which the net rainfall is transformed into pore pressure at the potential slip plane. The hydrological response is determined by the soil moisture deficit that must be replenished before percolation becomes significant. Over summer, the soil moisture deficit increases due to evapotransipiration. Because of this dependence, land use and climate control the soil moisture deficit. The resulting soil moisture deficit forms the initial setting at the start of the hydrological year.

In Figure 104 the hydrological response is given for two different model running mode. These represent differences in computation times and results, the STARWARS was set to run on a quarter day time step thus for a year the number of time steps were 1460 much more than the spin-up mode used for the PROBSTAB running.

The hydrological response is show through the illustration of the change in the volumetric moisture content (VMC), compared with the monthly total rainfall.

The differences in the hydrological response that arise are discussed here.

The larger evapotransipiration results in a constant moisture deficit that recurs every hydrological year, irrespective of the land use conditions.

The variations in VMC for the two types of model running mode seem deviate each other only during the beginning of the considered year, with an overestimated VMC values corresponding to the STARWARS results reported.

The disconnection for the STARWARS series is probably due to the restriction given by the restricted considered soil thickness, which is the direct result of the hydrological effects of soil type; during the PROBSTAB running the soil depth was set at 20 m. the differences in the percolation of water to the deeper layers can be attributed to the actual evapotransipiration, infiltration, drainage and the available storage, which are all higher for soils with few vegetation as a landslide debris. For this type of vegetation, the response in the topsoil is more accentuated and the response in the deeper layers is earlier and more pronounced.

2009

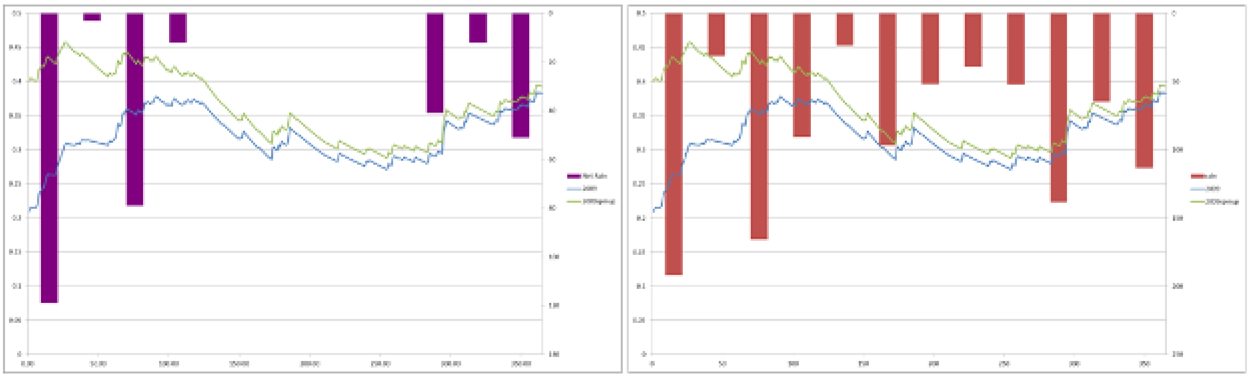

2010

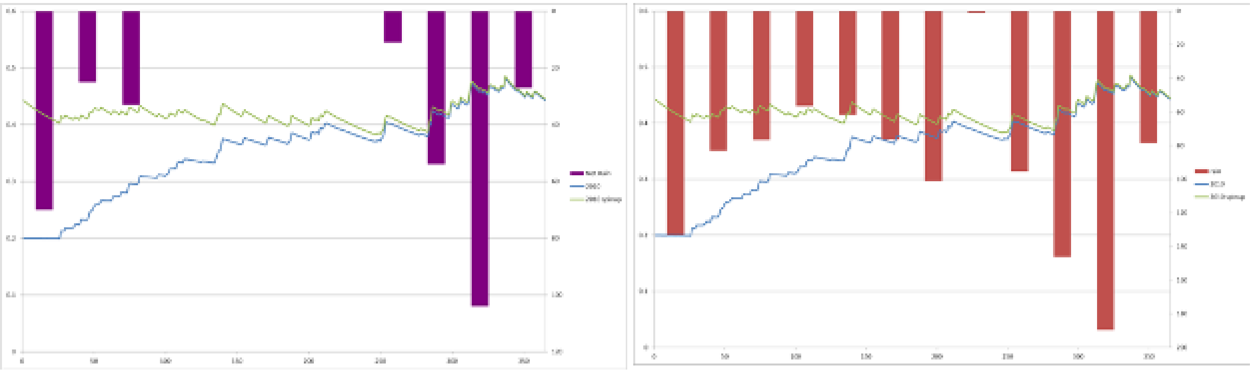

2011

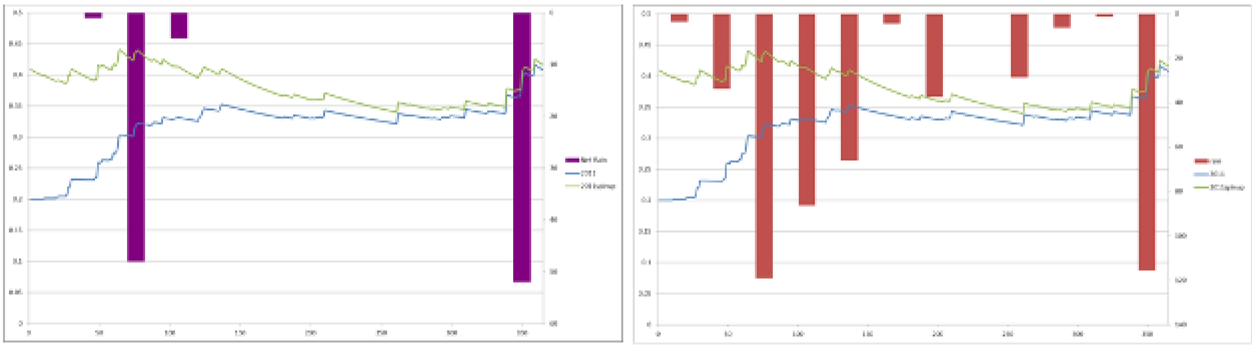

2012

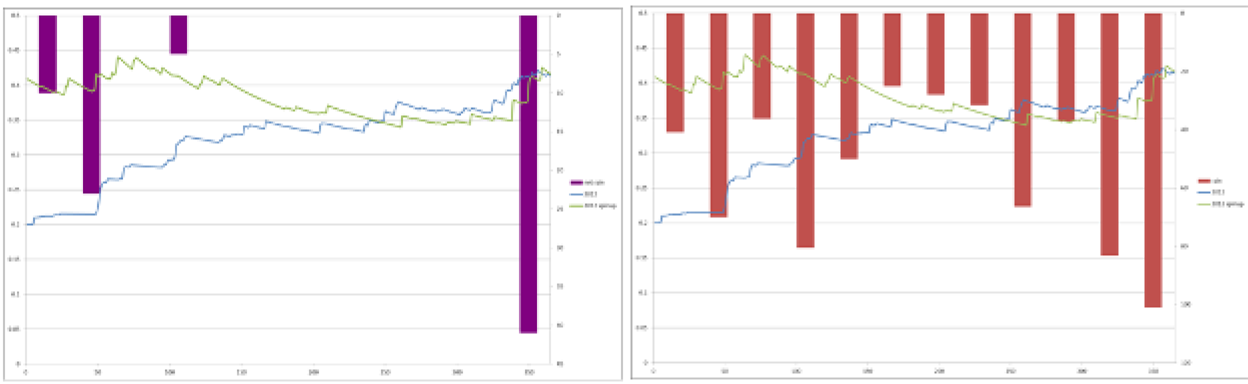

Figure 104 - Changes in the volumetric moisture content (VMC), for a quarter daily time steps (blue line) and a spin-up year (green line); compared with net monthly rainfall (violet bar) and total monthly rainfall (red bar) for each considered year.

In this layer, also the cumulative percolation along the slopes becomes apparent for the location under semi-natural vegetation as saturated conditions, i.e. perched water tables, occur in some years. This cumulative effect also explains the differences for the deeper layers for the various running mode.

The PROBSTAB run, as for the STARWARS, was carried out without hydrological and mechanical effects of vegetation. The results was interesting, the landslide area predicted as unstable (FS ≤ 1) was relatively more extended, involving the even the opposite slope Figure 105. As said in the geological setting section, the region is widely affected by hydrological instability, this results is consistent with the general area condition. The overall stability of the area is shown, based on the minimum safety factors scored on each pixel for the respective years; unstable area are those with FS ≤ 1.

Also the daily changes in slope instability are represented by means of the unstable time steps maps (Figure 106) for each modelled year.

In theory, a deterministic model for debris flow initiation can be said to perfectly predicting the temporal occurrence on an event when the first day of predicted instability matches with the day of occurrence of slides, this was not the case. The pre-event (Jan – March 2010) minimum safety factor map doesn’t show a satisfying match, given the fact that the region experiences shorts periods of high waterlevels the maximum pore pressure conditions are reached quite often.

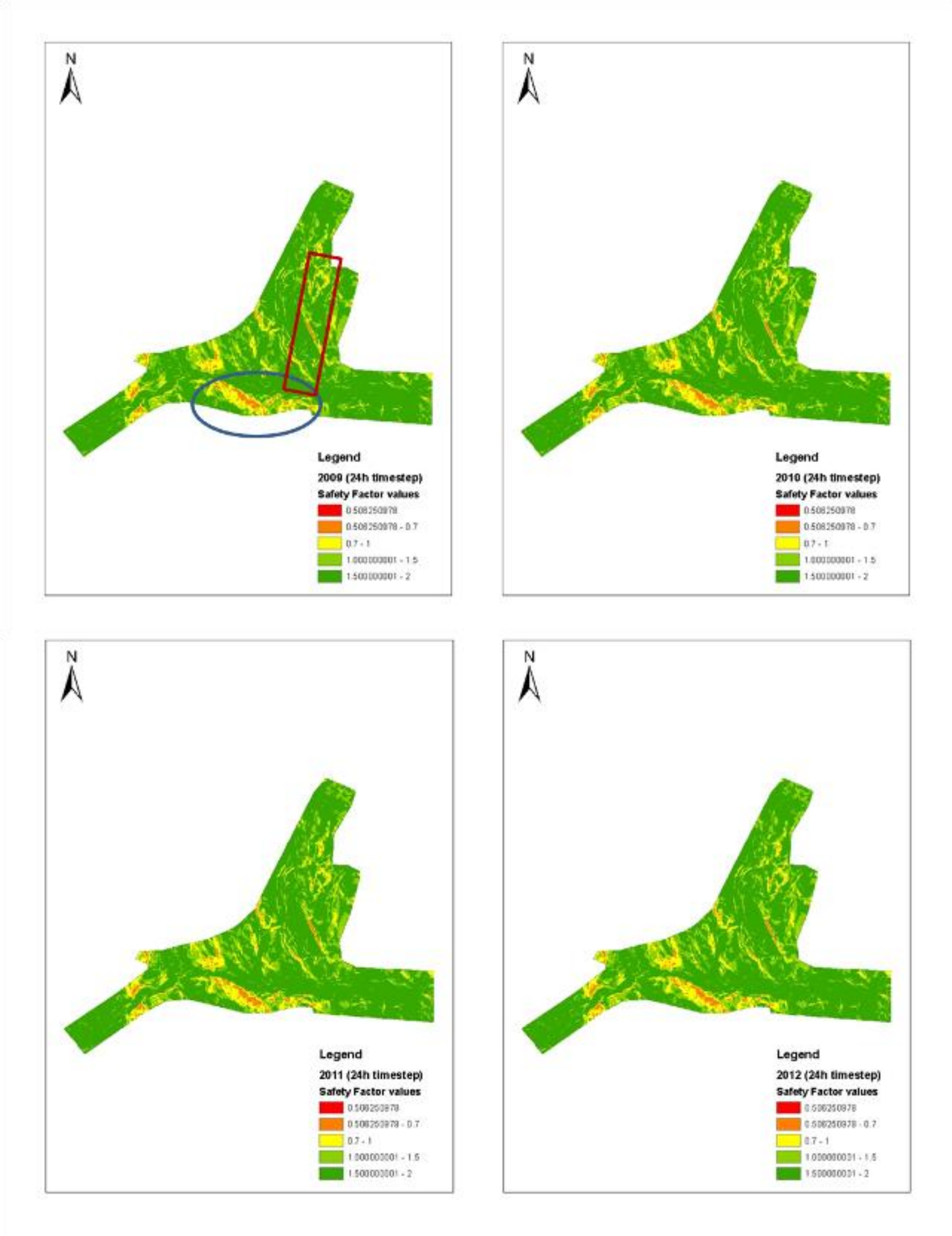

Figure 105 – Overall yearly variation of the minimum safety factor. Location of an unstable area (blue circle) out of the landslide body (red square). The maps are obtained from daily time steps.

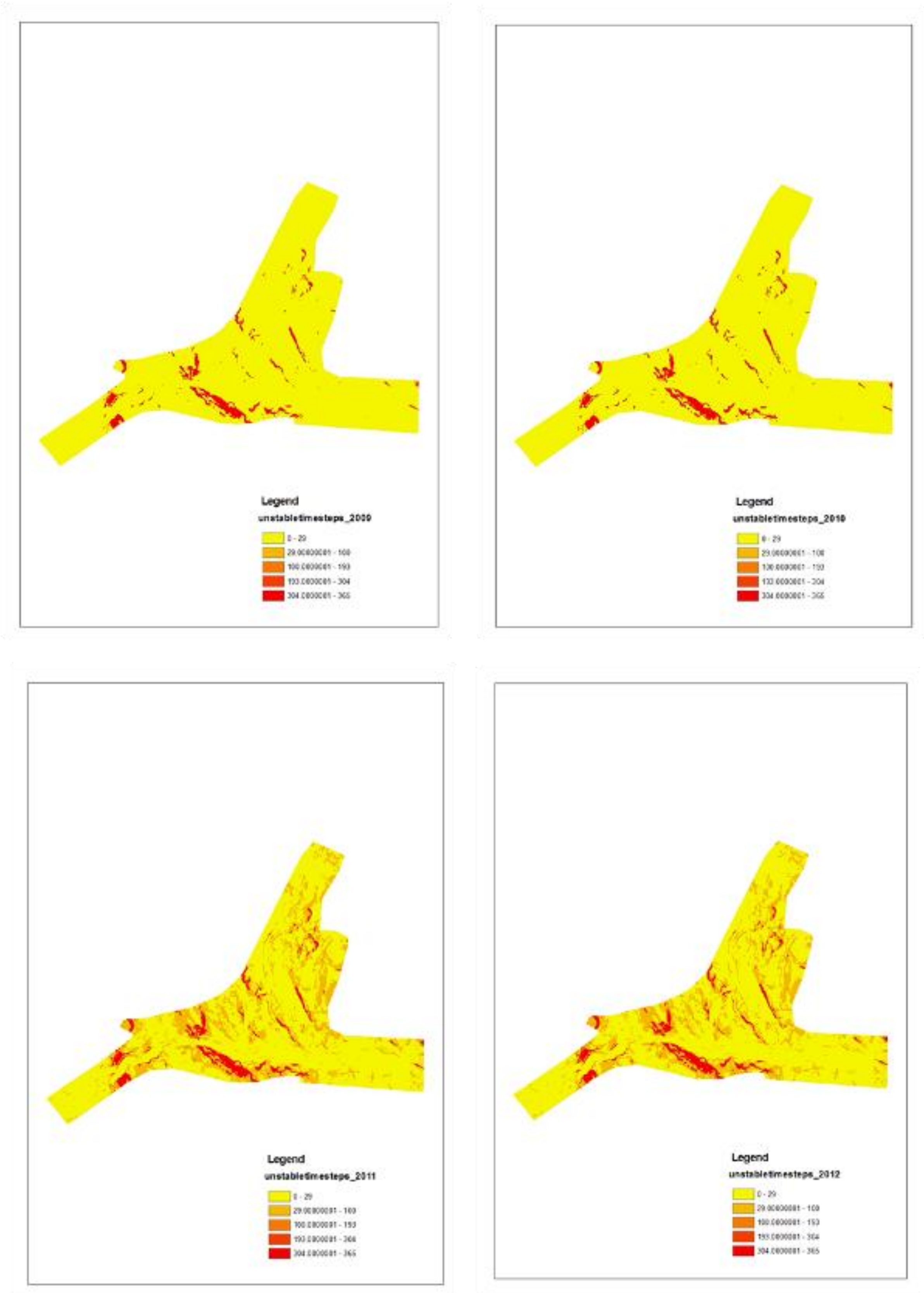

Figure 106 - Unstable time steps maps illustrating daily variations in slope stability. From yellow to red in shown the amount of unstable day.

Figure 107 - Minimum safety factor map relative to the pre-event time lapse, from January to March 2010.

From the variations in the spatial distribution of simulated failure, it emerges that landslide activity decrease or increase with a distribution in according with the GBInSAR critical monitored sectors. The evolution is the clearer for the distribution than for the persistence. Relative to the present situation, the alteration in land use results in a stronger decrease in landslide activity than those in climate conditions alone.

This is consistent with the changes in the area observed from the interferometric data analysis.

Though the model could not provide an exact match of the date of occurrence, it could still provide an understanding of the cumulative effect of persistence of critical condition.

In the year 2009, corresponding to the period preceding the main 2010 event, the safety factor trend along the landslide profile, already shown the well known unstable areas (Figure 108).

The results examination, concerning the safety factor values, were focused on their distribution along the landslide, in order to define an unambiguous landslide evolution behavior.

Which marks the main aim of this study, a suitable integration between two efficient landslide study methods.

Accordingly, the preceding step, before the overall data integration phase, was to obtain a spatial minimum safety factor distribution; consisting in the realization of a landslide profile from which the safety factor trend can be extrapolated, (Figure 108 -Figure 108). This first profile is referred to the year 2009, when no sizeable instability events occurred. The landslide aspect highlights a main scarp and the area corresponding to the E Sector, with medium instability evidences.

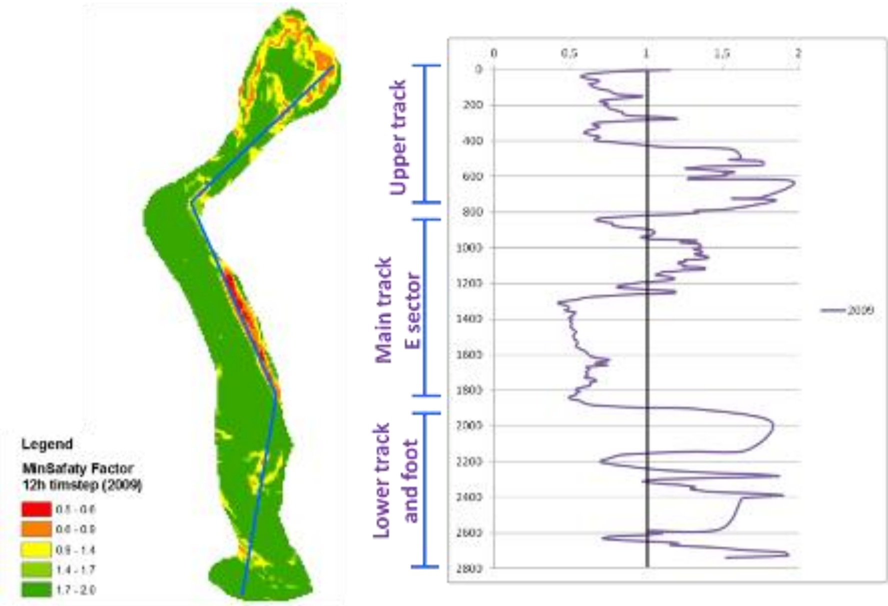

Figure 108 - Landslide minimum safety factor map (2009) and safety factor values graph, corresponding to each pixel crossed from the line section.

The safety factor trend relative to the year 2010 (Figure 109), compared with the 2009 below, shows a decrease of its values for the most in the landslide main track and foot, corresponding to the instability increase.

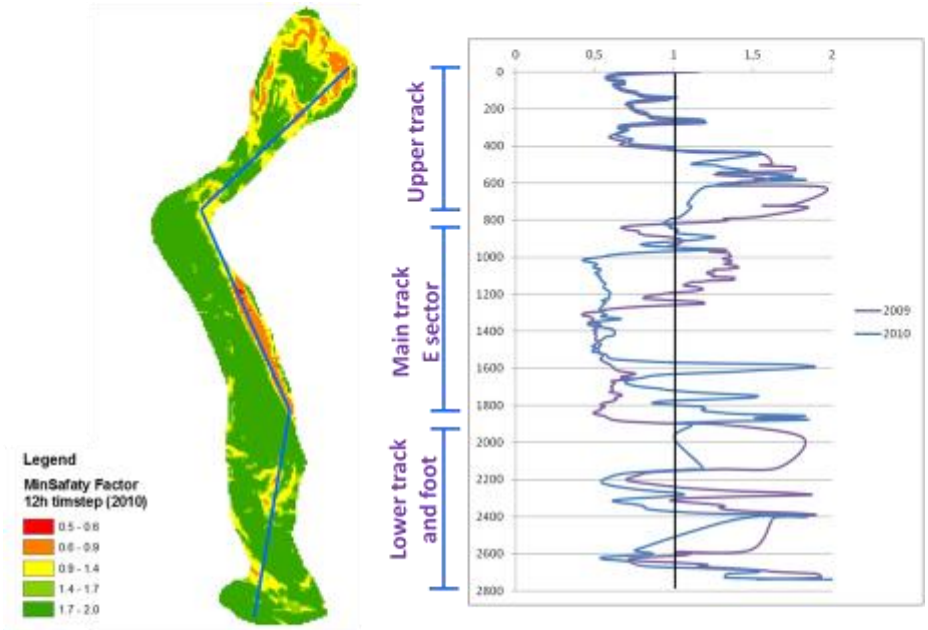

Figure 109 – Landslide minimum safety factor map (2010) and safety factor values graph, corresponding to each pixel crossed from the line section. The graph also shows the overlying with the previous trend (2009).

Concurring with the occurred phenomena in March 2010; even if the alimentation area located in the main scarp of the landslide seems keep a constant trend.

The trends obtained for the two next years (Figure 110 and Figure 111), show an always more intense decrease in safety factor values. Given the idea of a continuous unstable condition. It can been seen that the area computed as unstable is quite more than that in Figure 108 and Figure 109. If the revegetation was already present, in ca be deduced that the mechanical effect of vegetation and especially the root-induced cohesion added significantly support to the landslide stability. However, the environmental engineering works allowed to let the involved soil to start the natural slope environment restoration, meanwhile is still not possible to model with vegetation parameters. This letter induced the instability condition obtained.

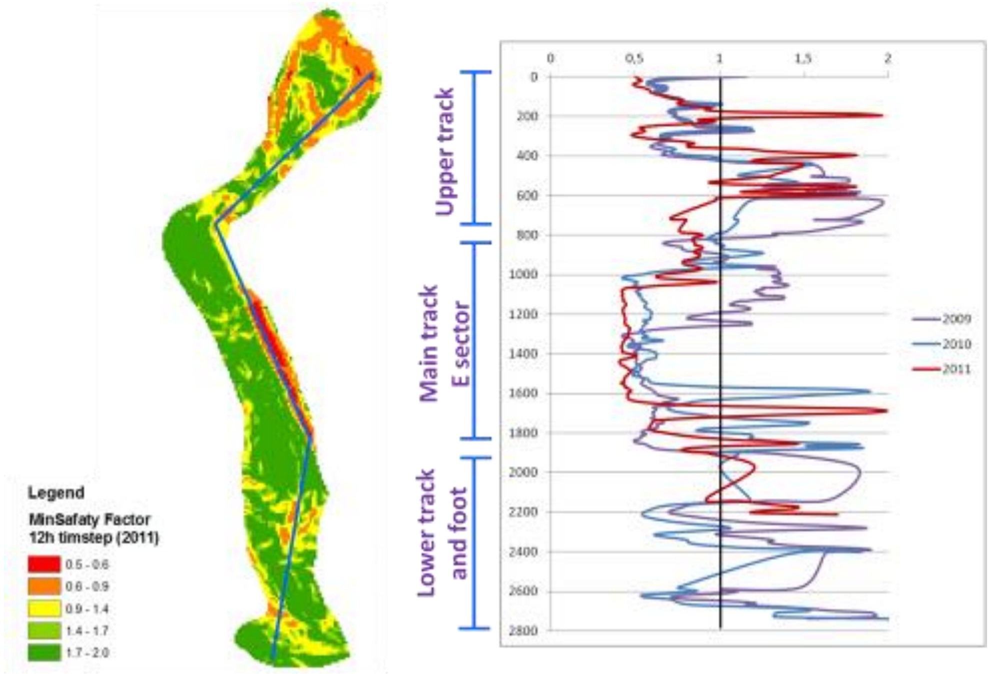

Figure 110 – Landslide minimum safety factor map (2011) and safety factor values graph, corresponding to each pixel crossed from the line section. The graph also shows the overlying with the previous trends (2009 and 2010).

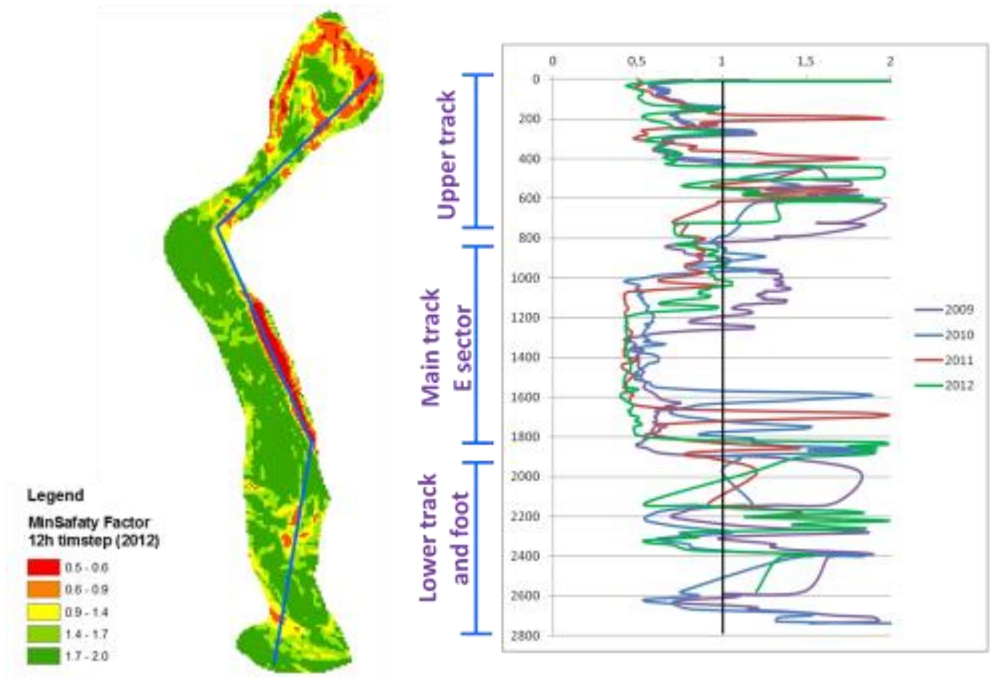

Figure 111 – Landslide minimum safety factor map (2011) and safety factor values graph, corresponding to each pixel crossed from the line section. The graph also shows the overlying with the previous trends (2009, 2010 and 2011).

6.4 Integration results

The results integration constitutes the final discussion phase; this section provides an overall view on the different type of results obtained from the as two used method.

The main interesting and important point to highlight concerns that the GBInSAR monitoring system data, expressed in terms of displacement rate and velocity, had never took part in the model running as input data, tables or maps. This aspect allows us to give greater weight to the achieved correlations.

To better discuss the positive relation between the all data types, the results, concerning the two best representative years(2010-2011) among thus considered, are here reported.

For each GBInSAR monitored sector and for both 2010 and 2011, cumulated displacement maps, DTM images, minimum safety factor maps and displacement velocity graph are illustrated in the followings figures (Figure 112, Figure 113, Figure 114, Figure 115 and Figure 116).

The data comparison need a correction with regards to the upper part of the landslide, known as the main scarp and the landslide alimentation zone. Since it is located in a GBInSAR shadow zone, none relative interferometric data are available.

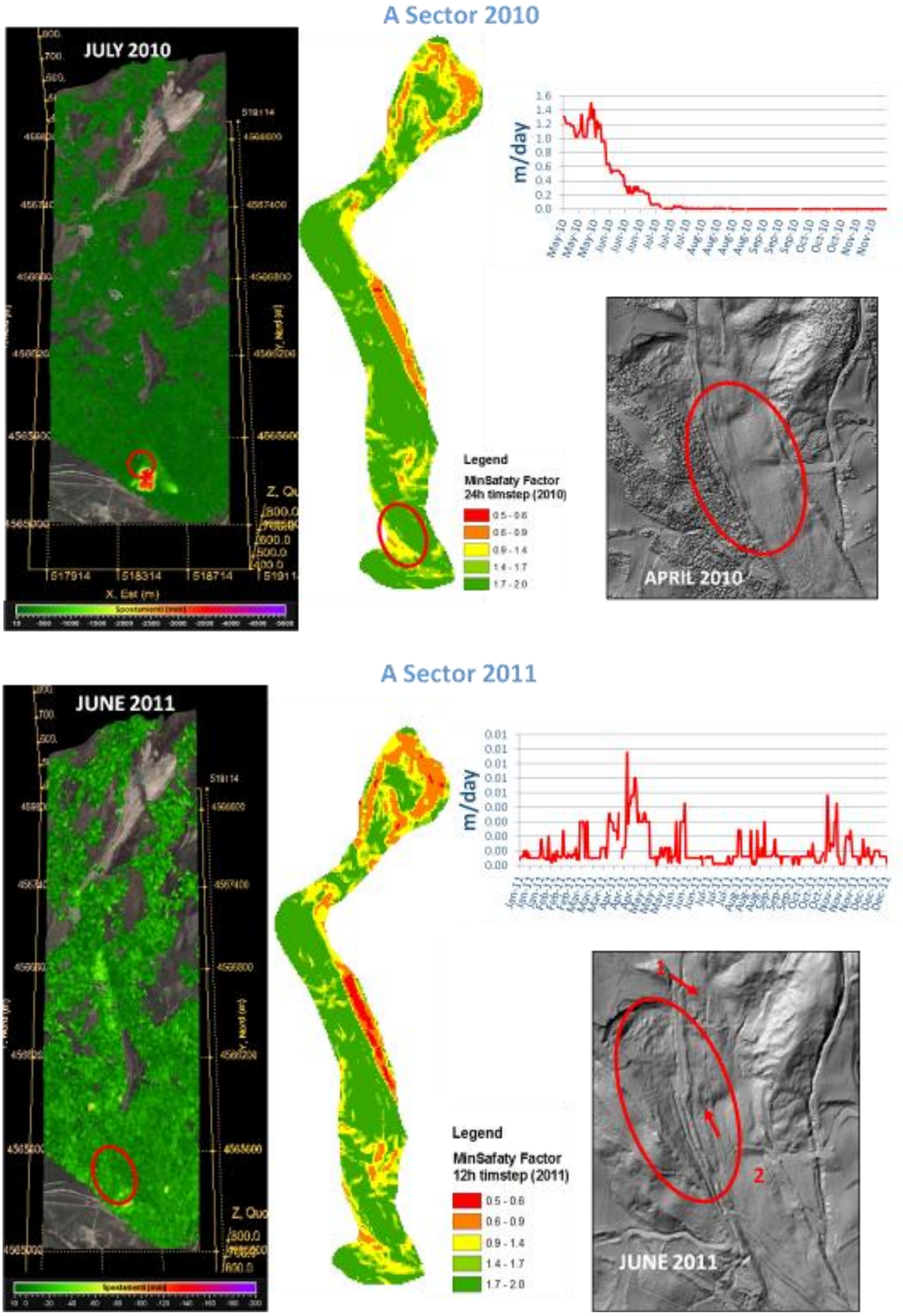

Figure 112 – Overall data results representation, relative to the A sector and for the years 2010 and 2011. Monthly cumulated displacement map on the left (July 2010 – June 2011), minimum safety factor map in the centre, upper right displacement velocity graph and at lower left sector location on DTM.

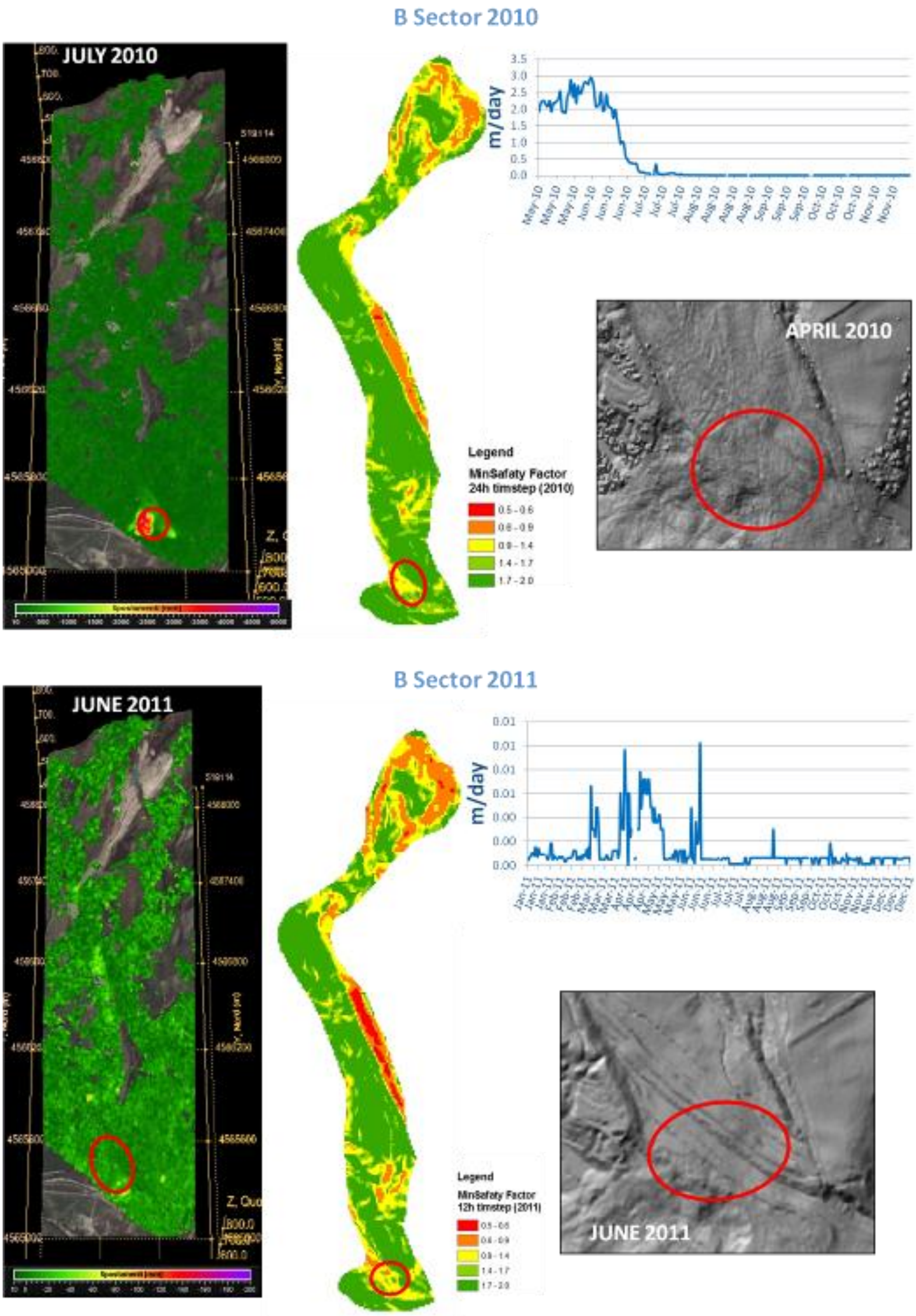

Figure 113 - Overall data results representation, relative to the B sector and for the years 2010 and 2011. Monthly cumulated displacement map on the left (July 2010 – June 2011), minimum safety factor map in the centre, upper right displacement velocity graph and at lower left sector location on DTM.

C Sector 2010

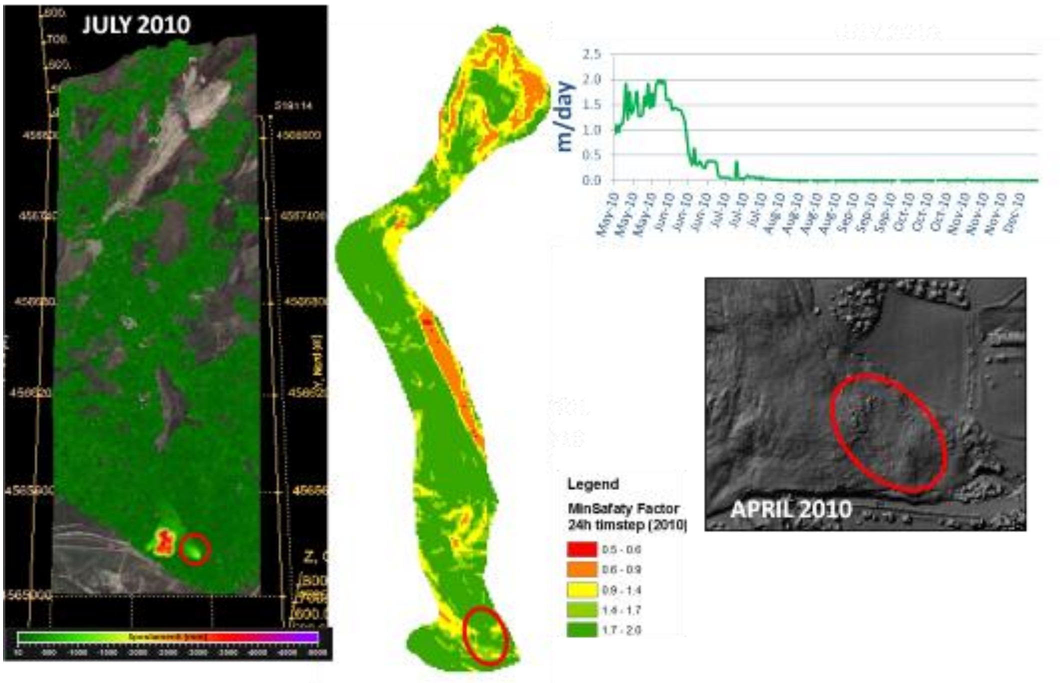

C Sector 2011

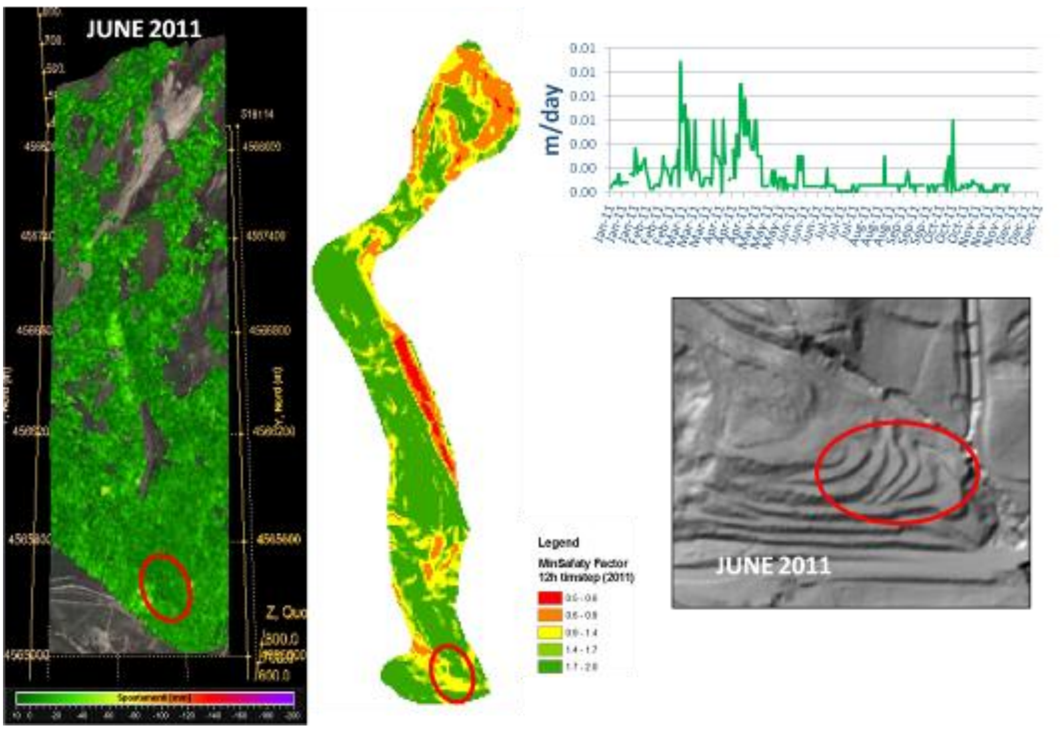

Figure 114 - Overall data results representation, relative to the C sector and for the years 2010 and 2011. Monthly cumulated displacement map on the left (July 2010 – June 2011), minimum safety factor map in the centre, upper right displacement velocity graph and at lower left sector location on DTM.

D Sector 2010

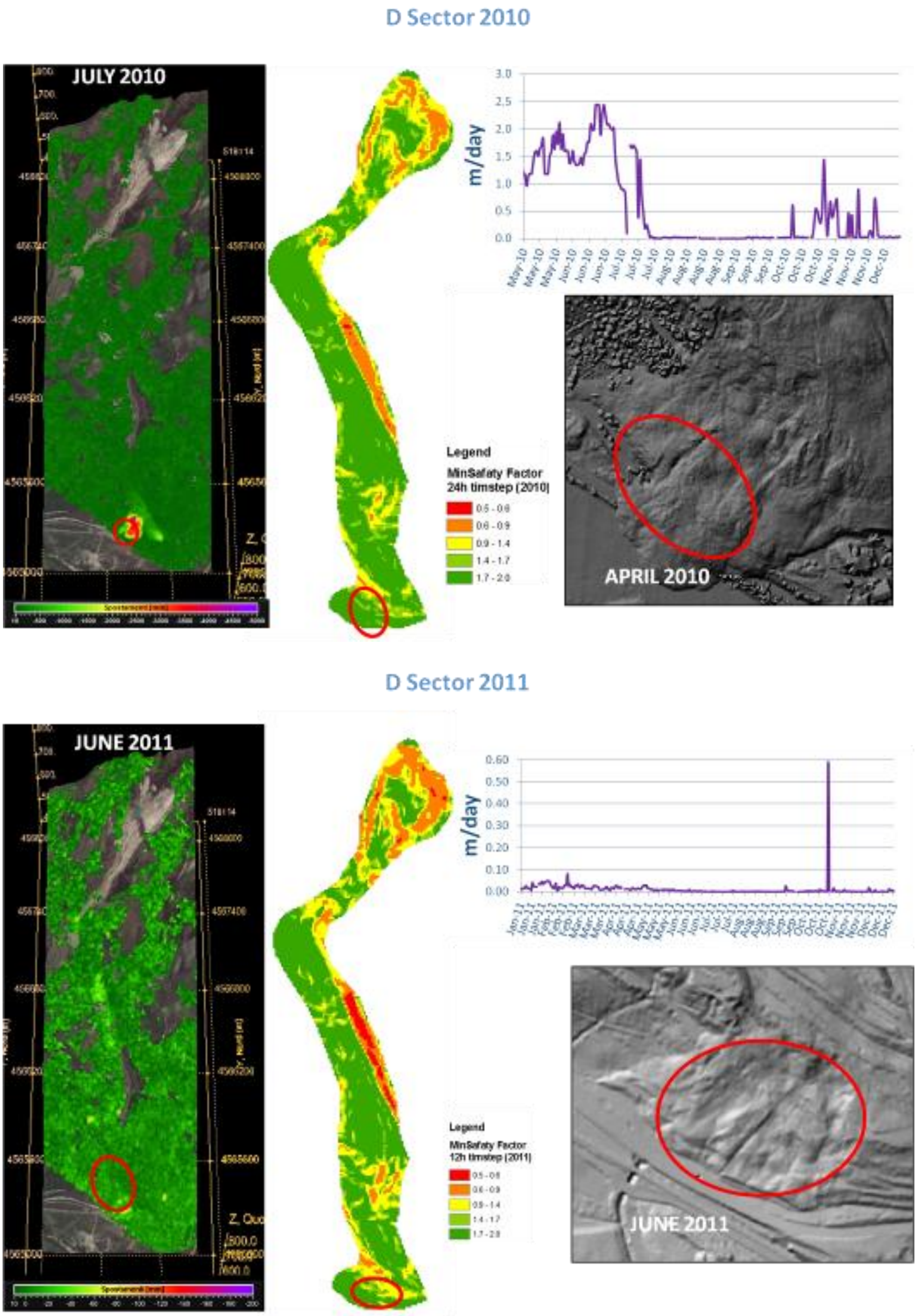

Figure 115 - Overall data results representation, relative to the D sector and for the years 2010 and 2011. Monthly cumulated displacement map on the left (July 2010 – June 2011), minimum safety factor map in the centre, upper right displacement velocity graph and at lower left sector location on DTM.

E Sector 2010

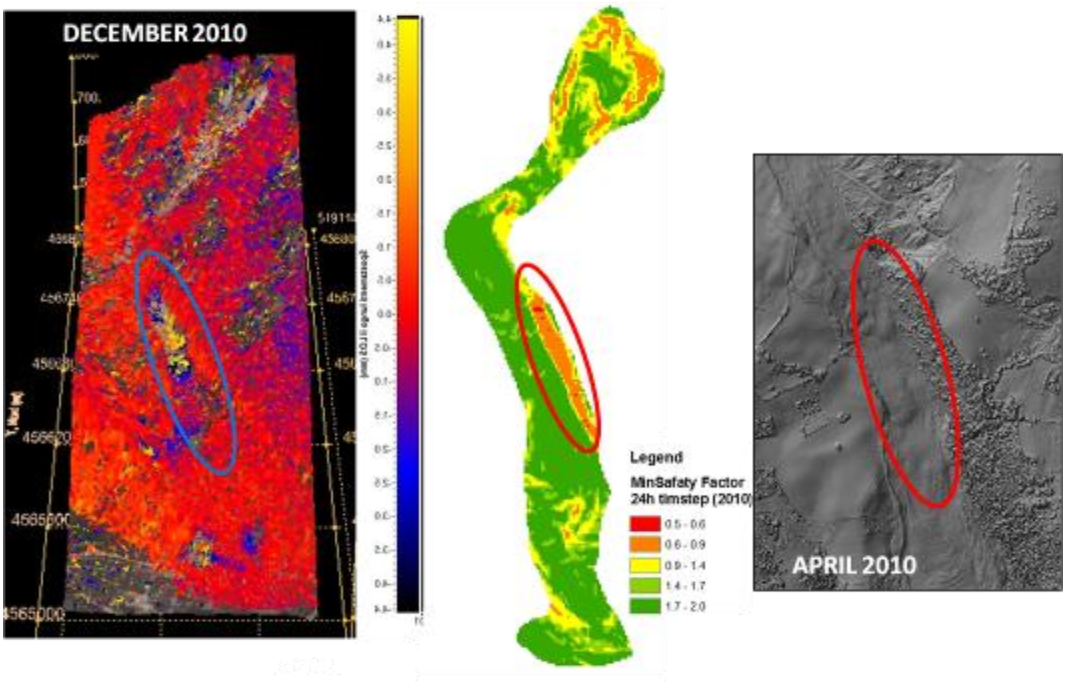

E Sector 2011

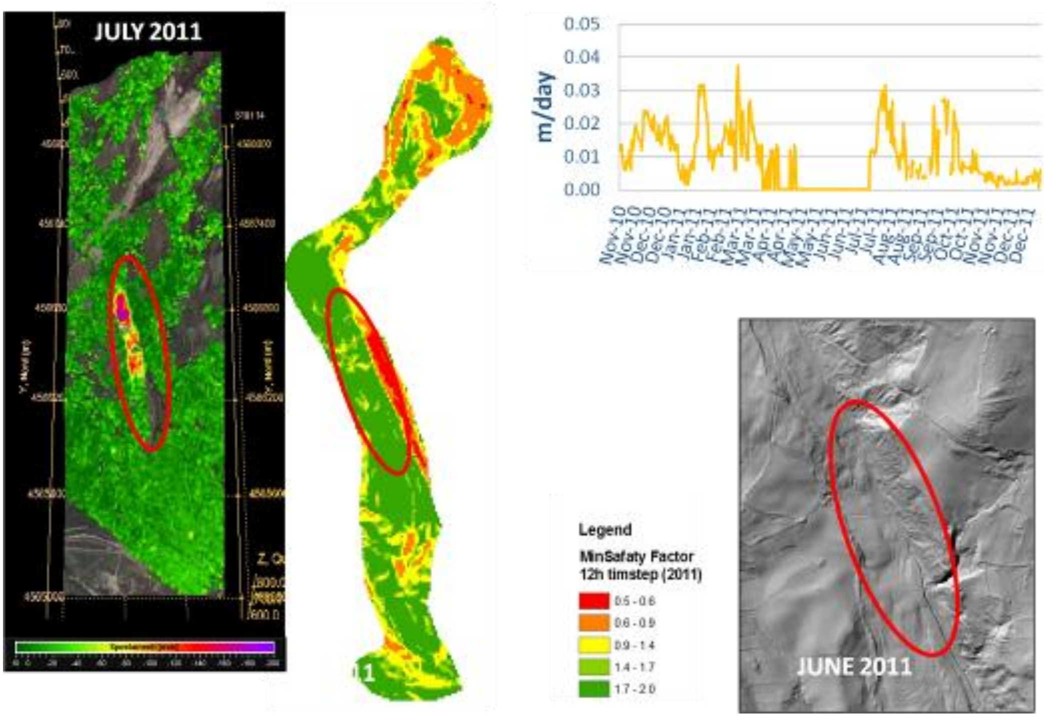

Figure 116 - Overall data results representation, relative to the E sector and for the years 2010 and 2011. Daily interferogram and monthly cumulated displacement map on the left (July 2010 – June 2011), minimum safety factor map in the centre, upper right displacement velocity graph and at lower left sector location on DTM.

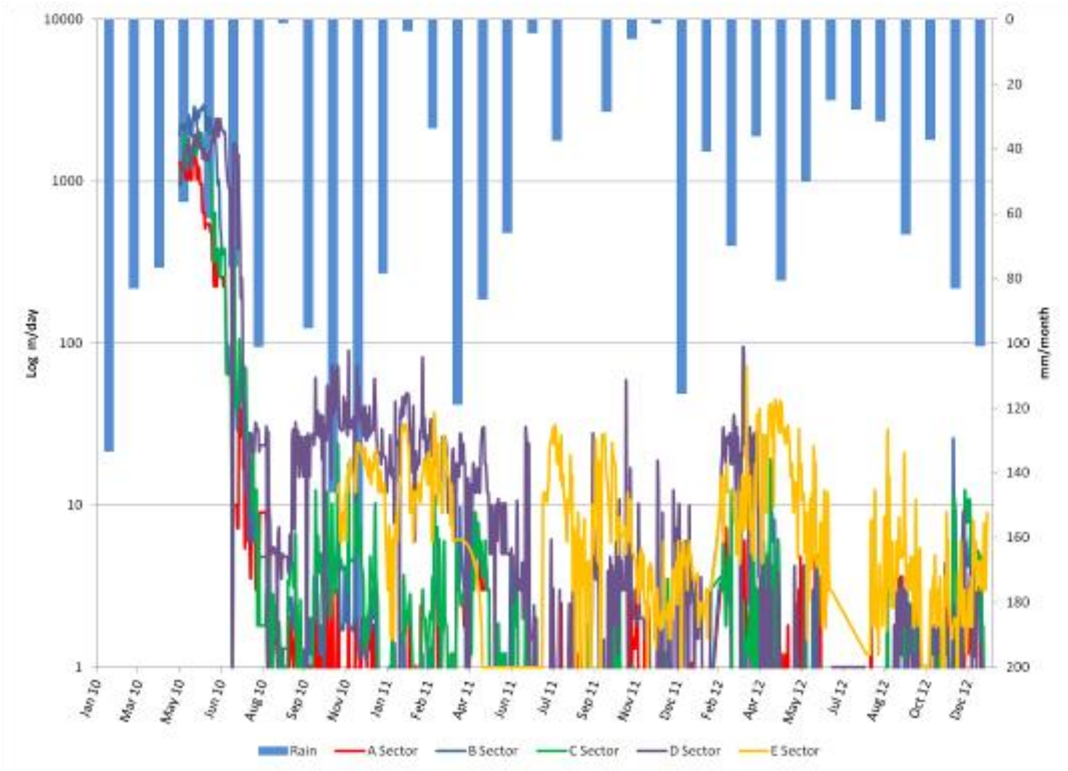

Figure 117 – Comparison between the monthly rainfall (expressed in mm) and the displacement velocity of the GBInSAR monitored sectors (in m/day and expressed in log scale).

The concluding remarks of the Montaguto landslide evolution and behavior is easily deducible observing the figure above:

- The interferograms exhibit a general decrease in terms of displacement trend, referable to the whole landslide system, even when the meteorological condition report substantial rain supply;
- The deepened interferometric data analysis reveals the presence of an unstable areas (sectors) spatial distribution that are concentrated in the most critical unstable slope portion; these areas match perfectly with those highlighted by the safety factor maps;
- Sectors and unstable zones are characterized by a strain that has both characteristics of persistence (the landslide is not inactive but stable) and discontinuity (some areas reach displacement speed increasing more often than others sectors or/and at different times), this is the case of the E Sector (Figure 116).
- The increase of the safety factor trend is due to both the peculiar landslide behavior characteristics just described and concurring to the settlement of the landslide debris exhibit through the DTM comparison.

7. Conclusions

Landslide activity analysis and data processing, together with those of surveying, monitoring and modelling processes, were performed to verify the effectiveness of an integrated use of different approaches.

Thanks to the effectiveness and versatility shown by the systems and the measuring instruments used, the possibilities of wider applications of monitoring tools and the integration of a coupled hillslope model providing complementary information, were outlined.

The application of GBInSAR technique for monitoring the Montaguto earthflow has demonstrated its capability to continuously acquire accurate displacement measurements over wide areas. Its high image acquisition rate and the capability to provide displacement maps with sub millimetre accuracy are specifically suited for assessing slope instability problems in emergency conditions. The areal mapping of displacements over the entire slope is very useful in the case of complex slopes characterized by different deformation patterns.

It revealed that the Montaguto earthflow behavior is characterized by a heterogeneous condition, with sectors with intermittent activity and other sectors mainly stable.

Indeed the landslide by characterized by complex morphology and different activation times. Accordingly, some areas with build up or with significant depletions, which cause an alteration of the morphology were detected.

The interferometric data analysis reveals the presence of an unstable areas (sectors) with spatial distribution that are concentrated in the most critical unstable slope portion; these areas match perfectly with those highlighted by the safety factor maps.

Sectors and unstable zones are characterized by a deformations having both characteristics of persistence (the landslide is not inactive but stable) and discontinuity (some areas reach displacement speed increasing more often than others sectors or/and at different times.

The results exhibit a general decrease in terms of displacement trend, referable to the whole landslide system, even when the meteorological condition report substantial rain supply.

Using of real time monitoring with new technologies allowed us to accomplish a 3 years of daily activity, which are still carrying out.

Meanwhile the GBInSAR approach has been proved to be very useful during the emergency phase supporting in the fast definition of the landslide toe excavation, and to guarantee the safety of the involved personnel, as well.
Through the daily monitoring activities was also possible to enrich the study using of the observational method. This phase allowed us to establish the efficiency of the works and to direct the possible project variations.
Finally, the efficiency of the undertaken activities can be evaluated by observing the time history of the velocity recorded at critical points.
The coupled hillslope model is physically based and is in principle capable to simulate the landslide activity under present and hypothetical environmental conditions. Changes in landslide activity, however, are only reflected in the temporal sensitivity as the susceptibility is not changed for the scenarios.

The model have reached a higher validation degree as the input data were acquired through measurements taken at sampling rates (meteorological, hydrological and geotechnical parameters). All output is basically composed of stacks of maps, reported at each timestep.
A clear model limitation is the static nature of the slope stability model. The model does not simulate changes in landslide susceptibility, which could arise from adaptations in the morphology and the soil properties of a slope. This simplification is valid under the assumption that changes in the temporal sensitivity precede those in the susceptibility. Because the scope of the model stretches beyond the event-scale, runoff cannot be included realistically in the model.
The model validity is affected by operational and model errors. Operational limitations concern rounding errors and data limitations that originate from the discretisation of the model.

Among the successes of this work certainly we highlight the effective integrated monitoring system, obtained by analyzing the results of the monitoring campaign, and by the comparison between the capabilities of the hydrological and stability model.
The awareness of having, at least in part, achieved the goal was represented by a clear correspondence in terms of temporal-space evolution and distribution of the most unstable areas, observed between the developed models and the measurements obtained through

monitoring campaigns, despite the presence of the stabilization works which have continuously disrupted the landslide environment.

8. References

ALLEN, R.G., PEREIRA, L.S., RAES, D., SMITH, M.*: Crop evapotranspiration: Guidelines for computing crop requirements*. Irrigation and Drainage Paper No. 56, FAO, Rome, Italy, 1998.

APIP TAKARA, K., YAMASHIKI, Y., SASSA, K., IBRAHIM, A.B., FUKUOKA, H.: *A distributed hydrological–geotechnical model using satellite-derived rainfall estimates for shallow landslide prediction system at a catchment scale*. Landslides, 7, 237–258, doi:10.100 7/s10346-010-0214-z, 2010.

ASKE, J.: *Remote Sensing Using Microwaves - does a Web-based Collaborative Course Serve a Purpose.* Proceedings of the 23rd EARSeL, Symposium on Remote Sensing in Transition, Millpress, Rotterdam, ed. R. Goassens, 527, 2003.

BAUM R.L., GODT J.W., SAVAGE, W.Z.: *Estimating the timing and location of shallow rainfall-induced landslides using a model for transient unsaturated infiltration*. Journal of Geophysical Research, 115, F03013, doi:10.1029/2009JF001321, 2010.

BAUM, R. L., SAVAGE, W. Z., GODT, J. W.: TRIGGERS – *A Fortran program for transient rainfall infiltration and grid based regional slope stability analysis, version 2.0*. US Geological Survey Open File Report, 1159, p. 74, 2008.

BAUM, R.L. and GODT, J.W.: *Early warning of rainfall-induced shallow landslides and debris flows in the USA*. Landslides, 7, 259-272, 2010.

BAUM, R.L., COE, J.A., GODT, J.W., HARP, E.L., REID, M.E., SAVAGE, W.Z., SCHULZ, W.H., BRIEN, D.L., CHLEBORAD, A.F., MCKENNA, J.P, MICHAEL, J.A.: *Regional landslide-hazard assessment for Seattle, Washington, USA*. Landslides, 2, 266–279, 2005.

BAUM, R.L., GODT, J.W., SAVAGE, W.Z.: Estimating the timing and location of shallow rainfall-induced landslides using a model for transient unsaturated infiltration, Journal of Geophysical Research, 115, F03013, doi:10.1029/2009JF001321, 2010.

BAUM, R.L., SAVAGE, W.Z., AND GODT, J.W.: TRIGRS: *A fortran program for transient rainfall infiltration and gridbased regional slopestability analysis*. Open-file Report, US Geological Survey, 2002.

BAUM, R.L., SAVAGE, W.Z., GODT, J.W.: *TRIGGERS A Fortran Program for Transient Rainfall Infiltration and Grid-Based Regional Slope-Stability Analysis*. U.S. Geological Survey Open-File Report 02-0424, p. 27, 2002.

BEAR, J.: *Dynamics of fluids in porous media*. New York: Elsevier, 1972.

BORGA, M., DALLA FONTANA, G., GREGORETTI, C., MARCHI, L.: *Assessment of shallow landsliding by using a physically based model of hillslope stability*. Hydrological Processes, 16, 2833–2851, 2002a.

BUTTLE, J.M., DILLON, P.J., EERKES, G.R.: *Hydrologic coupling of slopes, riparian zones and streams: an example from the Canadian Shield*. Journal of Hydrology, 287, 161–177, 2004.
by means of a ground-based SAR Interferometer. IEEE Transaction on Geoscience and Remote Sensing, 41, 4, Part 1, 745 – 752, 2003.

CANUTI, P., CASAGLI, N., FARINA, P., LEVA, D., TARCHI, D., NICO, G.: *Some examples of slope movements monitored by ground-based SAR interferometry*. In: Picarelli L (ed) Proceedings IC-FSM2003 International Conference on Fast Slope Movements: Prediction and Prevention for Risk Mitigation: 71–77. Sorrento (Italy), 11–13 May, 2003.

CASAGLI, N., CATANI, F., DEL VENTISETTE, C., LUZI, G.: *Monitoring, prediction, and early warning using ground-based radar interferometry*. Landslides, doi:10.1007/s10346-010-0215-y., 2010.

CASAGLI, N., TIBALDI, A., MERRI, A., DEL VENTISETTE C., APUANI, T., GUERRI, L., FORTUNY-GUASCH, J., TARCHI, D.: *Deformation of Stromboli Volcano (Italy) during the 2007 crisis by radar interferometry, numerical modeling and field structural data*. Journal of Volcanology and Geothermal Research, 182, 182–200, 2009.

COLESANTI, C., WASOWSKI, J.: *Investigating landslides with space-borne Synthetic Aperture Radar (SAR) interferometry*. Engineering Geology 88, 173–199, 2006.

CORDANO, E. and RIGON, R.: *A perturbative view on the subsurface water pressure response at hillslope scale*. Water Resources Research, 44, W05407–W05407, doi:10.1029/2006WR005740, 2008.

CROSETTO, M., CRIPPA, B., BIESCAS, E.: *Early detection and in depth analysis of deformation phenomena by radar interferometry*. Engineering Geology, 79, 81-91, 2005.

CROSTA, G.B. and FRATTINI P.: *Distributed modelling of shallow landslides triggered by intense rainfall*. Natural Hazards and Earth System Sciences, 3, 81–93, doi:10.5194/nhess-3-81-2003, 2003.

CROSTA, G.B. and FRATTINI, P.: *Distributed modelling of shallow landslides triggered by intense rainfall*. Natural Hazards and Earth System Sciences, 3, 81–93, doi:10.5194/nhess-3-81-2003, 2003.

CROSTELLA, A. and VEZZALI, L.: *La geologia dell'appennino toscano*. Bollettino Società Geologica Italiana, 83, 121-141, 1964.

FERRETTI, A., MONTI-GUARNERI, A., MASSONNET, D., PRATI, C., ROCCA, F.: *InSAR Principles: guidelines for SAR Interferometry Processing and Interpretation*. ESA Publications ESTEC Noordwijk NL; TM-19 February 2007, ed. K. Flecther ISBN 92-9092-233-8, 2007.

FERRETTI, A., PRATI, C., ROCCA, F.: *Permanent scatterers in SAR interferometry*. IEEE Transaction on Geoscience and Remote Sensing, 39 (1), 2001.

FREER, J., MCDONNELL, J.J, BEVEN, K.J., PETERS,N.E., BURNS, D., HOOPER, R.P., AULENBACH, B., KENDALL, C.: *The role of bedrock topography on subsurface storm flow.* Water Resources Research, 38, 1269, doi:10.1029/2001WR000872, 2002.

GEO-SLOPE: SEEP/W model and User manual 2000, Geo-Slope International, 2003a.

GEO-SLOPE: SEEP/W model and User manual 2000, Geo-Slope International, 2003b.

GIGLI, G., FANTI, R., CANUTI, P., CASAGLI, N.: *Integration of advanced monitoring and numerical modeling techniques for the complete risk scenario analysis of rockslides: The case of Mt. Beni (Florence, Italy)*. Engineering Geology, 120, 48–59, 2011.

GIORDAN, D., ALLASIA, P., MANCONI, A., BALDO, M., SANTANGELO, M., CARDINALI, M., CORAZZA, A., ALBANESE, V., LOLLINO, G., GUZZETTI, F.: *Morphological and kinematic evolution of a large earthflow: The Montaguto landslide, southern Italy*. Geomorphology, 187, 61–79, 2013.

GIORGI, F., AND LINDA O. MEARNS, 1999: *Introduction to special section: Regional climate modeling revisited*. Journal of Geophysical Research, 104, 6335-6352.

GOLDSTEIN, R.M., ENGELHARDT, H., KAMB, B., FROLICH, R.M.: *Satellite radar interferometry for monitoring ice sheet motion: application to an Antarctic ice stream*. Science, 262 (5139), 1525-1530, 1993.

GRAHAM, C.B., WOODS, R.A., MCDONNELL, J.J.: *Hillslope threshold response to rainfall: (1) A field based forensic approach*. Journal of Hydrology, 393, 65–76, 2010.

GRAYSON, R.B., MOORE, I.D., MCMAHON, T.A.: *Physically based modelling 2.: Is the concept realistic?* Water Resources Research 26, 2659-2666, 1992.

GRAYSON, R.B., WESTERN, A.W., CHIEW, F.H.S., BL"OSCHL, G.: *Preferred states in spatial soil moisture patterns: local and nonlocal controls*. Water Resources Research, 33, 2897–2908, 1997.

GUADAGNO, F.: *Perizia di somma urgenza. Relazione tecnica ed allegati. Dipartimento di Protezione Civile.* 2010

GUZZETTI, F., ARDIZZIONE, F., CARDINALI, M., GALLI, M., ROSSI, M., VALIGI, D.: *Landslide volumes and landslide mobilization rates in Umbria, central Italy*. Earth and Planetary Science Letters, 279, 222–229, doi:10.1016/j.epsl.2009.01.005, 2009.

GUZZETTI, F., CARDINALI, M., REICHENBACH, P., CARRARA, A.: *Comparing landslide maps: A case study in the upper Tiber River Basin, central Italy*. Environmental Management, 25, 3, 247–363, 2000.

GUZZETTI, F., GALLI, M., REICHENBACH, P., ARDIZZONE, F., CARDINALI, M.: *Landslide hazard assessment in the Collazzone area, Umbria, central Italy.* Natural Hazards and Earth System Sciences, 6, 115–131, 2006.

HEUVELINK, G. and PEBESMA, E.: *Spatial aggregation and process modelling*. Geoderma 89, 47-65, 1999.

HEWLETT, J.D. and HIBBERT, A.R.: *Factors affecting the response of small watersheds to precipitation in humid areas*. Forest Hydrology, edited by: Sopper, E. E. and Lull, H. W., Pergamon, 275–290, 1967.

HILBERTS, A., TROCH, P., PANICONI, C.: *Storage-dependent drainable porosity for complex hillslopes*. Water Resources Research, 41, W06001, doi:10.1029/2004WR003725, 2005.
HOPP., L. and MCDONNELL, J.J.: *Connectivity at the hillslope scale: Identifying interactions between storm size, bedrock permeability, slope angle and soil depth*. Journal of Hydrology, 376, 378–391, 2009.

IVERSON, R.: *Landslide triggering by rain infiltration*. Water Resources Research, 36 (7), 1897-1910, 2000.

JAKOB, M. and HUNGR, O.: *Introduction, in: Debris-flow Hazards and Related Phenomena*. Edited by: Jacob, M. and Hungr, O., Praxis Publishing House and Springer, Chichester, UK, 1–7, 2005

JAKOB, M., OWEN, T., SIMPSON T.: *A regional real-time debris-flow warning system for the District of North Vancouver*. Canada, Landslides, 9, 165–178, 2012.

KASSERBERG, D.: *Building dynamic spatial environmental models*. PhD Thesis, Utrecht University, Utrecht, 222 pp., 2002.

KEIJSERS, J.G.S., SCHOORL, J.M., CHANG, K.T., CHIANG, S.H., CLAESSENS, L., VELDKAMP, A.: *Calibration and resolution effects on model performance for predicting shallow landslide locations in Taiwan*. Geomorphology, 133, 168–177, 2011.

KENYI, L.W. and KAUFMANN, V.: *Estimation of rock glacier surface deformation using SAR intreferometry data*. IEEE Transaction on Geoscience and Remote Sensing, 41, 1512–1515, 2003.

KOJIMA, T. and TAKARA, K.: *A grid-cell based distributed flood runoff model and its performance, in Weather Radar Information and Distributed Hydrological Modelling*. Edited by: Tachikawa, Y., Vieux, B. E., Georgakakos, K. P., and Nakakita, E., IAHS, Publication no. 282, 234–240, 2003.

KRAHN, J.: *Seepage modeling with seep/w*. Alberta, Geoslope, 2004.

LANARI, R., LUNDGREN, P., MANZO, M., CASU, F.: *Satellite radar interferometry time series analysis of surface deformation for Los Angeles, California*. Geophysical Research Letters, 31, L23613, i:10.1029/2004GL021294, 2004.

LANNI, C., MCDONNELL, J.J., HOPP, L., RIGON, R.: *Simulated effect of soil depth and bedrock topography on near-surface hydrologic response and slope stability*. Earth Surface Processes and Landforms, online first: doi:10.1002/esp.3267, 2012.

LANNI, C., MCDONNELL, J.J., RIGON, R.: *On the relative role of upslope and downslope topography for describing water flowpath and storage dynamics: a theoretical analysis*. Hydrological Processes, 25, 3909–3923, doi:10.1002/hyp.8263, 2011.

LEVA, D., NICO, G., TARCHI, D., FORTUNY-GUASCH, J., SIEBER, A.J.: Temporal analysis of a landslide

LU, N., GODT, J., WU, D.: *A closed-form equation for effective stress in unsaturated soil*. Water Resources Research, 46, W05515, doi:10.1029/2009WR008646, 2010.

LUZI, G., MACALUSO, G., MECATTI, D., NOFERINI, L., PIERACCINI, M., ATZENI, C.: *Ground-based radar interferometry: results of experimental campaigns for landslides monitoring in Italy*. Proceedings of 24th EARSeL (European Advanced Remote Sensing Laboratoires) Symposium, Dubrovnik (Croatia), 25-27 May 2004.

LUZI, G., PIERACCINI, M., MECATTI, D., NOFERINI, L., MACALUSO, G., TAMBURINI, A., ATZENI C.: *Monitoring of an Alpine Glacier by Means of Ground-Based SAR Interferometry*. Geoscience and Remote Sensing Letters, 4 (3), 495-499, 2007.

LUZI, G., PIERACCINI, M., MECATTI,D., NOFERINI, L., GUIDI, G., MOIA, F., ATZENI, C.: Ground-Based Radar Interferometry for Landslides Monitoring: Atmospheric and Instrumental Decorrelation Sources on Experimental Data. IEEE Transaction on Geoscience and Remote Sensing, 42 (11), 2454 – 2466, 2004.

MALAMUD, B.D., TURCOTTE, D.L., GUZZETTI, F., REICHENBACH, P.: *Landslide inventories and their statistical properties*. Earth Surface Processes and Landforms, 29, 687–711, 2004

MASSONNET, D., VADON, H., ROSSI, M.: *Reduction of the need for the phase unwrapping in radar interferometry*. IEEE Transaction on Geoscience and Remote Sensing, 34, 489–497, 1996.

MASSONNET,D., ROSSI, M., CARMONA, C., ADRAGNA, F., PELTZER, G., FEIGL, K., RABAUTE, T.: *The displacement field of the Landers earthquake mapped by radar interferometry*. Nature 364, 138– 142, 1993b.

NANDAKUMAR, N. and MEIN, R.G.: *Uncertainty in rainfall-runoff model simulations and the implication of predicting the hydrologic effects of land use change*. Journal of Hydrology 192, 211-232, 1997.

PACK, R., TARBOTON, D., GOODWIN, C.: *The sinmap approach to terrain stability mapping*. 8th Congress of the International Association of Engineering Geology, Vancouver, British Columbia, Canada, 1998.

REICHENBACH, P., CARDINALI, M., DE VITA, P., GUZZETTI, F.: *Regional hydrological thresholds for landslides and floods in the Tiber River Basin (Central Italy)*. Environ. Geol. 35(2–3), 146–159, 1998.

REIGBER, A. and SCHEIBER, R.: *Airborne Differential SAR Interferometry: first results at L-Band*. IEEE Transaction on Geoscience and Remote Sensing, 41, (6), 1516-1520, 2003.

RIGON, R., BERTOLDI, G., OVER, T.: *Geotop: A distributed hydrological model with coupled water and energy budgets*. Journal of Hydrometeorology, 7, 371–388, 2006.

ROSEN, P.A., HENSLEY, S., JOUGHIN, I.R., LI, F.K., MADSEN, S.N., RODRIGUEZ, E., GOLDSTEIN, R.M.: *Synthetic aperture radar interferometry*. Proceedings of the IEEE 88 (3), 333–382, 2000.

ROSSI, G., CATANI, F., LEONI, L., SEGONI, S., TOFANI, V.: *HIRESSS: a physically based slope stability simulator for HPC applications*. Natural Hazards and Earth System Sciences, 13, 151–166, doi:10.5194/nhess-13-151-2013, 2013.

RUDOLF, H., LEVA, D., TARCHI, D., SIEBER, A.J.: *A mobile and versatile SAR system*. Proc. IGARSS'99, Hamburg, 592–594, 1999.
SANG-HO YUN: *Volcano Deformation Modeling Using Radar Inteferomery*. ed. VDM Verlag Dr. Muller, ISBN: 97-3-4-9-3, 2008.

SEGONI, S., ROSSI, G., CATANI, F.: .: *Improving basin scale shallow landslide modelling using reliable soil thickness maps*. Natural Hazards, 61, 85–101, 2012.

SIMONI S., ZANOTTI, F., BERTOLDI, G., RIGON, R.: *Modelling the probability of occurrence of shallow landslides and channelized debris flows using geotop-fs*. Hydrological Processes, 22, 532–545, 2008.

SIMONI, S., ZANOTTI, F., BERTOLDI, G., RIGON, R.: *Modelling the probability of occurrence of shallow landslides and channelized debris flows using geotop-fs*. Hydrological Processes, 22, 532–545, 2008.

SPENCE, C. and WOO, M.K.: *Hydrology of subarctic Canadian shield: soil-filled valleys*. Journal of Hydrology, 279, 151–166, doi: 10.1016/S0022-1694(03)00175-6, 2003.

SPENCE, C.: *A Paradigm Shift in Hydrology: Storage Thresholds Across Scales Influence Catchment Runoff Generation*. Geography Compass, 4, 819–833, doi:10.1111/j.1749-8198.2010.00341.x, 2010.

STIEGLITZ, M., SHAMAN, J., MCNAMARA, J. ENGEL, V., SHANLEY, J., KLING, G.W.: *An approach to understanding hydrologic connectivity on the hillslope and the implications for* *nutrient transport*. Global Biogeochemical Cycles, 17, 1105, doi:10.1029/2003GB002041, 2003.

STROZZI, T. and MATZLER, C.: *Backscattering Measurements of Alpine Snowcovers at 5.3 GHz and 35 GHz.* IEEE Transaction on Geoscience and Remote Sensing, 36 (3), 838-848, 1998.

SUGAWARA, M.: *Tank Model, in V.J. Singh*. Ed., Computer models of watershed hydrology, Water Resources Publications, CO, 1995.

TARCHI, D., CASAGLI, N., FANTI, R., LEVA, D., LUZI, G., PASUTO, A., PIERACCINI, M., SILVANO, S.: *Landside Monitoring by Using Ground-Based SAR Interferometry: an example of application to the Tessina landslide in Italy*. Engineering Geology 68, 15-30, 2003a.

TARCHI, D., CASAGLI, N., MORETTI, S., LEVA, D., SIEBER, A.J.: *Monitoring landslide displacements by using ground-based radar interferometry: Application to the Ruinon landslide in the Italian Alps*. Journal of Geophysical Research, 108, 10.1-10.14, 2003b.

TARCHI, D., OHLMER, E., SIEBER, A.J.: *Monitoring of structural changes by radar interferometry.* Research in Nondestructive Evaluation, 9, 213– 225, 1997.

TARCHI, D., RUDOLF, H., LUZI, G., CHIARANTINI, L., COPPO, P., SIEBER, A.J.: *SAR interferometry for structural changes detection: a demonstration test on a dam*. Proceedings IGARSS'99, Hamburg, 1522–1524, 1999.

TAROLLI, P. and TARBOTON, D.G.: *A new method for determination of most likely landslide initiation points and the evaluation of digital terrain model scale in terrain stability mapping*. Hydrology and Earth System Sciences, 10, 663–677, doi:10.5194/hess-10-663-2006, 2006.

TOFANI, V., DAPPORTO, S., VANNOCCI, P., CASAGLI, N.: *Infiltration, seepage and slope instability mechanisms during the 20–21 November 2000 rainstorm in Tuscany, central Italy*. Natural Hazards and Earth System Sciences, 6, 1025–1033, doi:10.5194/nhess-6-1025-2006, 2006.

TROMP-VAN MEERVELD, H.J. and MCDONNELL, J.J.: *Threshold relations in subsurface stormflow: 2. The fill and spill hypothesis*. Water Resources Research, 42, W02411, doi:10.1029/2004WR003800, 2006.

VAN BEEK, L.P.H. and VAN ASCH, TH.W.J.: *Quantification of diffuse landsliding by derivation of a general hydrological slope instability threshold*. In Moore, D.P. & O. Hungr (Eds.): 8th International Congress of the International Association of Engineering Geologists (IAEG, Vancouver), 896-906, 1998.

VAN BEEK, R.: *Assessment of the influence of changes in climate and land use on landslide activity in a Mediterranean environment*. Netherlands Geographical Studies no. 294, KNAG, Faculty of Geosciences, Utrecht University, p 366, 2002.

WOOD, E.F.: *Scaling behaviour of hydrological fluxes and variables: empirical studies using a hydrological model and remote sensing data*. In Kalma, J.D. & M. Sivapalan (Eds.): Scale issues in hydrological modelling. New York: Wiley, 1995.

ZEBKER, H.A. and GOLDSTEIN, R.M.: *Topographic mapping from interferometric synthetic aperture radar observations*. Journal of Geophysical Research, 91, 4993–4999, 1986.

ZEBKER, H.A., ROSEN, P.A., HENSLEY, S.: *Atmospheric effects in interferometric synthetic aperture radar surface deformation and topographic maps*. Journal of Geophysical Research - Solid Earth, 102, B4, 7547–7563, 1997.

ZEBKER, H.A., VILLASENOR, J.: *Decorrelation in interferometric radar echoes*. IEEE Transaction on Geoscience and Remote Sensing, 30, 950–959, 1992.

Acknowledgement

This thesis is the result of research at the Earth Science Department of Florence University that started in 2011. The contents of this thesis benefited from the contributions of many and I wish to thank the following persons in particular.

I would like to thank Prof. Nicola Casagli, my thesis tutor, for his precious advice and constructive suggestions, and above all for giving me this opportunity.

I am also grateful so much to Giovanni Gigli, for his constant support and guidance, and to Prof. Theo van Asch and Rens van Beek of the Utrecht University, for their time and willingness of sharing their knowledge and research team, giving me the chance to have a great experience.

I owe my deepest gratitude to all of my colleagues of the "Applied Geology Research Group",, for making my everyday work an interesting and pleasant experience.

Firenze, December 2013

Federica Ferrigno

Appendices

Appendix 1: Geo-technical Survey Sample Points and Results

Tipo di terreno	Sondaggio	Campione	Profondità m	LL %	LP %	IP %	CF %	γd g/cm3	γn g/cm3	w %	S	e	φ	c (Kg/cm2)
Depositi di Frana	S7	C1	4,00	69,75	38,03	31,72	64,69	1,24	1,76	42,45	0,96	1,25	17,05	0,18
	S7	C2	10,00	57,17	28,44	28,73		1,31	1,70	29,93	0,76	1,11		
	S7	C3	19,50	38,66	18,11	20,55	38,73	1,73	2,03	17,28	0,82	0,59		
Depositi alluvionali e/o eluvio colluviali	S9	C1	4,00	56,63	25,99	30,64	38,40	1,32	1,76	34,11	0,88	1,07		
Depositi dell'Unità di Villamaina - Parte alterata	S6	C1	4,00	34,19	18,94	15,25		1,88	2,16	15,07	0,90	0,60		
	S5	C1	4,00										21,12	0,16
Depositi dell'Unità di Villamaina - Substrato	S6	C2	9,00	45,82	24,32	21,5	37,41	1,48	1,86	25,49	0,82	0,85		
	S6	C3	15,00	38,21	21,37	16,84		1,68	2,03	21,22	0,89	0,66		
	S6	C4	23,00	41,43	21,94	19,49	27,27	1,72	2,05	19,25	0,88	0,60		
	S8	C1	18,00	37,53	20,03	17,5		1,74	2,10	20,48	0,96	0,59	21,49	0,23
	S8	C2	20,00	38,82	19,87	18,95	33,82	1,79	2,05	14,43	0,73	0,54		
	S9	C2	10,00	63,14	27,63	35,51		1,68	2,01	19,82	0,86	0,65		
	S9	C3	18,00	66,46	31,31	35,15	37,35	1,64	1,96	20,49	0,83	0,69		
	S9	C4	23,50	40,40	20,36	20,04		1,70	2,02	18,67	0,85	0,62		
	S8	C3	25,50	40,06	21,27	18,79		1,77	2,10	18,50	0,92	0,56		
Depositi del Flysch di Faeto	S2	C1	13,00	40,75	21,26	19,49	43,21	1,36	1,73	27,04	0,75	1,01		
	S2	C2	17,50	34,86	21,11	13,75		1,65	1,97	19,38	0,83	0,65		
	S2	C3	27,50	44,38	24,41	19,97	42,03	1,64	1,95	19,00	0,81	0,65		
	S2	C4	62,00	33,76	18,65	15,11		1,63	1,92	17,94	0,75	0,66		
Depositi di frana antichi	S5	C2	13,5	62,81	28,32	34,49		1,29	1,69	31,74	0,78	1,14		
	S5	C3	17,00	69,18	37,87	31,31	44,57	1,37	1,75	27,55	0,82	0,88		
	S5	C4	25,00	66,57	26,79	39,78		1,50	1,85	23,33	0,78	0,84		

(Guadagno *et al.*, 2010)

Appendix 2: Water balance calculation

Table with detailed values, for each considered month, relative to the water balance calculation using the follow function:

$$\begin{cases} W - Pet > 0; & ET = Pet \\ W - Pet < 0; & ET = W + S_{m-1} - S_m \end{cases}$$

Month	W mm	Pet	ET	Sm	Net Rainfall
Jan-09	192	7,5	7,5	100,00	119
Feb-09	31,2	11,5	11,5	100,00	3
Mar-09	165,8	28,6	28,6	100,00	79
Apr-09	90,6	49,1	49,1	100,00	12
May-09	23,8	95,9	75,2	48,61	0
Jun-09	96,8	111,9	103,6	41,80	0
Jul-09	51,8	111,4	70,6	23,05	0
Aug-09	39	93,9	48,7	13,30	0
Sep-09	52,2	70,9	54,5	11,04	0
Oct-09	138,4	49,8	49,8	100,00	41
Nov-09	64,8	21,8	21,8	100,00	12
Dec-09	113,4	10,9	10,9	100,00	51
Jan-10	133,4	6,6	6,6	100,00	70
Feb-10	83,2	18,4	18,4	100,00	25
Mar-10	76,6	0,0	0	100,00	33
Apr-10	56,4	54,6	54,6	100,00	0
May-10	61,6	69,8	69,5	92,13	0
Jun-10	76,4	110,4	103	65,57	0
Jul-10	101,2	118,1	111,4	55,39	0
Aug-10	1,2	96,9	35,3	21,27	0
Sep-10	95,4	55,7	55,7	100,00	11
Oct-10	146,2	39,9	39,9	100,00	54
Nov-10	189,6	22,3	22,3	100,00	104
Dec-10	78,4	10,5	10,5	100,00	27
Jan-11	3,6	12,2	11,9	91,72	0
Feb-11	33,8	20,1	20,1	100,00	1
Mar-11	119	21,5	21,5	100,00	48
Apr-11	86,4	59,5	59,5	100,00	5
May-11	66	62,5	62,5	100,00	0
Jun-11	4,4	96,9	64,8	39,64	0
Jul-11	37,4	112,3	58,3	18,75	0
Aug-11	0	99,1	11,8	6,96	0
Sep-11	28,6	71,2	31	4,55	0
Oct-11	6,2	40,0	7,5	3,24	0
Nov-11	1,4	19,6	1,9	2,70	0

Dec-11	115,6	12,2	12,2	100,00	52
Jan-12	40,9	3,3	3,3	100,00	10
Feb-12	70	8,9	8,9	100,00	23
Mar-12	36,2	29,6	29,6	100,00	0
Apr-12	80,6	55,2	55,2	100,00	5
May-12	50	79,9	75,8	74,19	0
Jun-12	25,1	97,2	63,2	36,08	0
Jul-12	28	111,1	48,4	15,71	0
Aug-12	31,6	96,0	39,1	8,25	0
Sep-12	66,4	68,6	66,6	8,06	0
Oct-12	37,2	49,2	38,1	7,15	0
Nov-12	83,2	22,9	77,3	13,07	0
Dec-12	101	12,2	12,2	100,00	41

Appendix 3: STARWARS PCRaster Script

```
#!--lddin –matrixtable
######################################################################
# Updated StarWars-script (V. 2.2)
# as standing per 16/11/2005
# - Flexible soil depth with BC fixed at lower layer
# - Three layers of variable thickness
# - Percolation proportional to travel time through unsaturated zone of each layer
# - ETA is dependent on the stored moisture in the soil column ETA= f((StorTot)^EFact)
# - Groundwater recharge is given by the current timestep Delta(Storsat)=Sum(Perc)-ETASat
# - Routing of groundwater is driven by the water table of the previous timestep (explicit)
# - Routing of groundwater is evaluated in X-,X+,Y- & Y+ directions (Finite Difference)
# - Groundwater flow is controlled by a lateral outflow BC set at LDD pits, no flow at all other
boundaries
######################################################################

########## Binding: variable & constant declaration ##########
binding

 #INPUT: Maps, Timeseries and Tables

 #General
 Duration=     scalar($3);                        #Length of timeslice in days
 WatSlice=     scalar(0.001);                     #1 unit of meteo input in m (i.e. 0.001= 1
mm)
 Area=         input\maps\combeloup_clone.map;         #Area of interest (boolean)
 DEM=          input\maps\combeloup_demrec.map;        #Digital terrain model (m)
 SampleLocs=   input\maps\combeloup_sample.map;        #Report: sample points (nominal)

 #Meteo read from timeseries specified
 #rainfall and reference potential evapotranspiration in units defined by WatSlice
 # 1: P, 2: E, 3: T
 METEOTSS= $1;                            #Rainfall per timestep
 EFact= scalar(1.0);                  #Power for ETP correction

 #Soil depth
 NOfLayers=    scalar(3);             #Number of layers (fixed to 3)
 Material=     nominal(1);            #Materials
 SDepth=       scalar(1.00);          #Soil depth (m)
 DF1=          scalar(0.20);          #Depth first soil layer (m)
 DF2=          scalar(0.30);          #Depth second soil layer (m)
                                      #Third layer set to remainder of soil depth
 Limfac=       scalar(0.95);          #Arbitrary fraction to restrict thin soil layers

 #Land cover
 LandCover=    nominal(1);            #Nominal map with land cover conditions
```

```
SMaxTBL=      input\tables\intmax.tbl;#Maximal canopy storage for interception (m)
CoverTBL=     input\tables\ftr.tbl;   #Cover of canopy (0-1)
CropTBL=      input\tables\ecrop.tbl;        #Crop factors for reducing ETo
KRel0TBL=     input\tables\krel0.tbl;        #Infiltration capacity (proportional to ksat first
layer)
#Hydrology
#-constants & general information
MQD=          scalar(4);              #Tortuosity parameter Millington & Quirk (MQD/MQN;-
)
MQN=          scalar(3);
Residual=     scalar(0.05);           #Fraction of VMC retained as residual soil moisture (-)
PsiFC=        scalar(1.0);            #Matric suction at field capacity (equilibrium conditions:
(m))
RapidFlow=    scalar(0.0);            #fraction of surface detention that replenishes
                                      #the groundwater table directly by bypass flow (-)
Redist=                 scalar(1.0);           #Redistribution of surface detention
(proportional 0-1)
PercMin=      scalar(0.0);            #Minimum Kr to ensure vertical connectivity

#snow routine parameters: constants
TT=    scalar(0.0);                          #threshold temperature for freezing/thawing (°C)
CFMAX=        scalar(0.0055);                            #degree-day factor (m·°C-1·d-1)
SFCF= scalar(1.00);                          #snowfall correction factor (-)
CWH= scalar(0.10);                           #water holding capacity snow cover (-)
CFR=  scalar(0.05);                          #refreezing coefficient (-)

#-initial conditions
IntIni= results\int00000.ini;   #amount of interception storage (m)
SCIni=        results\snowcov0.ini; #snow cover, water equivalent (m)
SCFIni=       results\snowliq0.ini;  #snow liquid storage, water equivalent (m)
SurfDetIni=   results\surfdet0.ini;  #amount of surface detention (m)
WatLevelIni=  results\watlev00.ini;  #waterlevel, WL, above lithological contact (m)
ThetaIni1=    results\theta1l0.ini;  #VMC (-), 1st layer
ThetaIni2=    results\theta2l0.ini;  #VMC (-), 2nd layer
ThetaIni3=    results\theta3l0.ini;  #VMC (-), 3rd layer

#-boundary conditions
Stream=       input\maps\combeloup_streams.map;              #Boolean map of stream
for LDD composition - BC for surface
PsiBC=        scalar(2.0);            #Matric suction of infinite store under lithological
contact (m)
                                      #BC at base of the soil
#-layer properties
MatPropTBL= input\tables\matprop.tbl;     #Matrix with material properties:
                                      #R(Mat#*LU#)xC(Prop#*Layer#)
                                      #Prop: Ks/ThetaSat/hA/alpha
                                      #Ks=  saturated hydraulic conductivity(m/d)
```

```
                                          #ThetaSat= porosity
                                          #hA= SWRC air entry value (m)
                                          #alpha= SWRC slope, alpha (-)

 #OUTPUT: Maps and TSS
 Int=           results\int;                    #Canopy interception
 SC=            results\snowcov;                #Snow cover
 SCF=           results\snowliq;                #Snow liquid storage
 SurfDet=       results\surfdet;                #Surface detention
 Theta1=        results\theta1l;                #VMC 1st layer
 Theta2=        results\theta2l;                #VMC 2nd layer
 Theta3=        results\theta3l;                #VMC 3rd layer
 WatLevel=      results\watlev;                 #waterlevel

 ETPSurf=       results\ETS;            #total evapotranspiration flux
 ETPSoil=       results\ETA;            #idem, of soil only

 Theta1TSS=     results\theta1.tss;             #VMC 1st layer
 Theta2TSS=     results\theta2.tss;             #VMC 2nd layer
 Theta3TSS=     results\theta3.tss;             #VMC 3rd layer
 WatLevelTSS=           results\watlevel.tss;   #Waterlevel
 OutflowTSS=    results\surfdet.tss;    #Surface detention
 QSatTSS=       results\qsat.tss;               #Saturated lateral flow

 SumStor0TSS=           results\sumstor0.tss;           #total storage in the saturated zone
 SumStor1TSS=           results\sumstor1.tss;           #after routing
 SumStor2TSS=           results\sumstor2.tss;           #& corrected

                                        #Budget check: maptotals (m)
 PRPTotTSS=     results\PRPtot.tss;     #total PRPipitation input
 IntTSS=        results\int.tss;        #total interception storage
 ETPTotTSS=     results\etptot.tss;             #total actual evapotranspiration loss
 StorTotTSS=    results\stortot.tss;            #total moisture stored in soil column
 SurfTotTSS=    results\surftot.tss;            #total surface detention & interception
 Perc4TSS=      results\Perc4.tss;      #total loss across lithic contact

############### Areamap: clone-map definition ################
areamap
 Area;
############ Timer: default time step set to days ############
timer
 1 $2 1;
 rep1= $4+$4..endtime;
 rep2= endtime;
 ######### Initial section:  definition of constants ##########
initial
```

```
#General
#DX= DY
DX= celllength();                    #pixelsize (m)
BaseLevel= DEM-SDepth;                        #bedrock surface
Mask = if(Area,
  BaseLevel/BaseLevel,scalar(0));             # Mask with value of 1

#topography of bedrock surface
DEMBase= DEM-SDepth;                                 #Surface 4th layer, infinite store
#ldd creation
LDDBase= lddcreate(DEMBase,1e31,1e31,1e31,1e31);
#setting up ldds in x- and y-directions
LDDXX= lddrepair(if(Area,ldd(6)));
LDDYY= lddrepair(if(Area,ldd(2)));
#boundary conditions
#locating no-flow boundaries
XXUpBC= if(upstream(LDDXX,scalar(1))== 0,boolean(1),boolean(0));
XXDownBC= if(LDDXX== ldd(5),boolean(1),boolean(0));
YYUpBC= if(upstream(LDDYY,scalar(1))== 0,boolean(1),boolean(0));
YYDownBC= if(LDDYY== ldd(5),boolean(1),boolean(0));
#locating head-controlled outlet
OutletBase= if(pit(LDDBase)== 0,boolean(0),boolean(1));
DEMBaseBCXX= if(OutletBase,
  if(XXUpBC,2*DEMBase-downstream(LDDXX,DEMBase),
   if(XXDownBC,2*DEMBase-upstream(LDDXX,DEMBase),DEMBase)),DEMBase);
DEMBaseBCYY= if(OutletBase,
  if(YYUpBC,2*DEMBase-downstream(LDDYY,DEMBase),
   if(YYDownBC,2*DEMBase-upstream(LDDYY,DEMBase),DEMBase)),DEMBase);

#Soil depth
D1= min(SDepth,DF1);                          #Depth of soil layers 1-3
D2= min(DF2,SDepth-D1);
D3= max(SDepth-(D1+D2),0);
D3= if(D3< (1-Limfac)*SDepth,0,D3);
D2= max(SDepth-(D1+D3),0);
UL2= D2+D3;                          #Surface layer 2

#LDD of topographical surface
LDDSurf= lddcreate(DEM-if(Stream,10,0),1e31,1e31,1e31,1e31);
#Outlet
Outlet= if(pit(LDDSurf)==0,boolean(0),boolean(1));
#OutXX= if(upstream(ldd(Mask*4),Mask)+downstream(ldd(Mask*4),Mask)==1,Outlet,0);
#OutYY= if(upstream(ldd(Mask*2),Mask)+downstream(ldd(Mask*2),Mask)==1,Outlet,0);

#Soil properties
Row= scalar(Material)*scalar(LandCover);
Col= 0;
```

```
KSat1= lookupscalar(MatPropTBL,Col*NOfLayers+1,Row);
KSat2= lookupscalar(MatPropTBL,Col*NOfLayers+2,Row);
KSat3= lookupscalar(MatPropTBL,Col*NOfLayers+3,Row);
Col= 1;
ThetaSat1= lookupscalar(MatPropTBL,Col*NOfLayers+1,Row);
ThetaSat2= lookupscalar(MatPropTBL,Col*NOfLayers+2,Row);
ThetaSat3= lookupscalar(MatPropTBL,Col*NOfLayers+3,Row);
Col= 2;
HA1= lookupscalar(MatPropTBL,Col*NOfLayers+1,Row);
HA2= lookupscalar(MatPropTBL,Col*NOfLayers+2,Row);
HA3= lookupscalar(MatPropTBL,Col*NOfLayers+3,Row);
Col= 3;
Alpha1= lookupscalar(MatPropTBL,Col*NOfLayers+1,Row);
Alpha2= lookupscalar(MatPropTBL,Col*NOfLayers+2,Row);
Alpha3= lookupscalar(MatPropTBL,Col*NOfLayers+3,Row);

#Land cover
#Infiltration capacity (m/timestep)
InflCap= KSat1*lookupscalar(KRel0TBL,LandCover)*Duration;
#Interception
IntMax= lookupscalar(SMaxTBL,LandCover);          #Maximum storage capacity
FTR= lookupscalar(CoverTBL,LandCover);        #free throughfall ratio
#Evapotranspiration
CropFactor= lookupscalar(CropTBL,LandCover);          #crop factor

#Hydrology
MQ= MQD/MQN;                                  #Constants of SWRC
MQAlpha1= 2*Alpha1;
MQAlpha2= 2*Alpha2;
MQAlpha3= 2*Alpha3;

KSatBC= KSat3;                                #Boundary condition at base - parameters
MQAlphaBC= MQAlpha3;
HABC= HA3;
#fluxes - ktheta at defined constant suction level
ThetaEffBC= if(PsiBC>HABC,1-ln(PsiBC/HABC)/(0.5*MQAlphaBC),1);
KrBC= if(ThetaEffBC>0,ThetaEffBC**MQ*
  (exp(MQAlphaBC*ThetaEffBC)-MQAlphaBC*ThetaEffBC-1)/
  (exp(MQAlphaBC)-MQAlphaBC-1),0);
PercBC= KrBC*KSatBC;

StreamAccu= accuflux(LDDSurf,scalar(Stream));     #BC for routing overlandflow
StreamAccu= StreamAccu/maptotal(StreamAccu);

                                            #effective degree of saturation in the first
                                            #layer for drainage after complete saturation
ThetaDrain1= if(PsiFC>HA1,1-ln(PsiFC/HA1)/Alpha1,0.99);
```

```
 ThetaDrain1= if(Duration>= 1,ThetaDrain1,(1+Duration*ThetaDrain1)/(1+Duration));

 ThetaRes1= Residual*ThetaSat1;                  #Inactive pore space (m3/m3)
 ThetaRes2= Residual*ThetaSat2;
 ThetaRes3= Residual*ThetaSat3;
 DegSat1= (1-Residual)*ThetaSat1;                #Active pore space per layer (m3/m3)
 DegSat2= (1-Residual)*ThetaSat2;
 DegSat3= (1-Residual)*ThetaSat3;
 StorMax1= DegSat1*D1;
 StorMax2= DegSat2*D2;
 StorMax3= DegSat3*D3;
 StorMax= StorMax1+StorMax2+StorMax3;            #Maximum available storage in the soil
column

 #Initial conditions
 Int= IntIni;                                #Canopy interception (m)
 SC= SCIni;                                  #Snow cover (m)
 SCF= SCFIni;                                #Snow liquid storage (m)
 SurfDet= SurfDetIni;                        #Surface detention  (m)
 WatLevel= WatLevelIni;                      #Groundwater conditions (m)
 H3= min(WatLevel,D3);
 H2= max(0,min(WatLevel-D3,D2));
 H1= max(0,min(WatLevel-(D3+D2),D1));
                                             #Theta(Eff) per layer (-)
 ThetaEff1= if(WatLevel<SDepth,(ThetaIni1-ThetaRes1)/DegSat1,scalar(1.0));
 ThetaEff2= if(D2>0,if(WatLevel<UL2,(ThetaIni2-ThetaRes2)/DegSat2,scalar(1.0)),
   (ThetaIni2-ThetaRes2)/DegSat2);
 ThetaEff3= if(D3>0,if(WatLevel<D3,(ThetaIni3-ThetaRes3)/DegSat3,scalar(1.0)),
   ThetaEffBC);
                                             #Groundwater level
 H1= if(ThetaEff1<1.0,H1,D1);
 H2= if(ThetaEff2<1.0,H2,D2);
 H3= if(ThetaEff3<1.0,H3,D3);
 WatLevel= H1+H2+H3;

########## Dynamic section: unsaturated and saturated flow ##########
dynamic

 #Surface fluxes
 #-initialising ETP fluxes
 ETPSurf= scalar(0);
 ETPSoil= scalar(0);
 #-bypass flow
 ByPass= RapidFlow*SurfDet;
 SurfDet= (1-RapidFlow)*SurfDet;
 #-meteo input
 PRP= if(Area,timeinputscalar(METEOTSS,1))*WatSlice*timeslice()*Duration;
```

```
ETP= if(Area,timeinputscalar(METEOTSS,2))*WatSlice*timeslice()*Duration;
TMP= if(Area,timeinputscalar(METEOTSS,3));
report (rep2) PRPTotTSS= maptotal(PRP);
#-interception
PRPGross= PRP;
PRP= FTR*PRPGross+max((1-FTR)*PRPGross+Int-IntMax,0);
Int= PRPGross+Int-PRP;
#-loss of interception to ETP
ETPLoss= min(ETP,Int);
report (rep2) Int= Int-ETPLoss;
ETP= ETP-ETPLoss;
ETPSurf= ETPSurf+ETPLoss;
#-snow accumulation and melt
DSC= if(TMP<=TT,CFR*SCF,-min(SC,max(TMP-TT,0)*CFMAX*Duration*timeslice()));
report (rep2) SC= SC+DSC+if(TMP<=TT,PRP,0);
SCF= SCF-min(0,DSC)+if(TMP>TT,PRP,0);
PRP= max(0,SCF-CWH*SC);
SCF= SCF-PRP;
ETPLoss= min(ETP,SCF);
report (rep2) SCF= SCF-ETPLoss;
ETP= ETP-ETPLoss;
ETPSurf= ETPSurf+ETPLoss;
report results\prp.tss= timeoutput(SampleLocs,PRP);
report results\sc.tss= timeoutput(SampleLocs,SC);
report results\scf.tss= timeoutput(SampleLocs,SCF);
#-loss of surface detention to ETP
ETPLoss= min(SurfDet,ETP);
ETPSurf= ETPSurf+ETPLoss;
SurfDet= SurfDet-ETPLoss;
ETP= ETP-ETPLoss;

#Storage based on state variables of previous timestep
#Unsaturated zone
#-depth of unsaturated zone (m)
DUnsat1= max(D1-H1,0);
DUnsat1= min(DUnsat1,D1);
DUnsat2= max(D2-H2,0);
DUnsat2= min(DUnsat2,D2);
DUnsat3= max(D3-H3,0);
DUnsat3= min(DUnsat3,D3);
#-storage of pores left (-)
#  note: effective degree of saturation for overlying layer used for drainage.
ThetaEff1= if(ThetaEff1<1,ThetaEff1,ThetaDrain1);
ThetaEff2= if(D2>0,if(ThetaEff2<1,ThetaEff2,ThetaEff1),ThetaEff2);
ThetaEff3= if(D3>0,if(ThetaEff3<1,ThetaEff3,ThetaEff2),ThetaEff3);
DeltaThetaEff1= (1-ThetaEff1);
DeltaThetaEff2= (1-ThetaEff2);
```

```
DeltaThetaEff3= (1-ThetaEff3);
#-actual available storage in the unsaturated zone
StorCap1= DUnsat1*DegSat1;
StorCap2= DUnsat2*DegSat2;
StorCap3= DUnsat3*DegSat3;
#-unsaturated storage available for drainage (m waterslice)
StorMat1= StorCap1*ThetaEff1;
StorMat2= StorCap2*ThetaEff2;
StorMat3= StorCap3*ThetaEff3;
#Saturated zone
#-saturated storage available for drainage (m waterslice)
StorSat1= H1*DegSat1;
StorSat2= H2*DegSat2;
StorSat3= H3*DegSat3;
#Total storage
#- available for drainage
StorMat= StorMat1+StorMat2+StorMat3;   #in unsaturated zone
StorSat= StorSat1+StorSat2+StorSat3;        #in saturated zone
StorTot= max(0.001,StorMat+StorSat);                        #total storage in soil column

#Soil fluxes

#At surface
#-actual evapotranspiration
ETP= if(StorMax>0,CropFactor*ETP*(StorTot/StorMax)**EFact,0);
ETMat1= if(StorTot>0,StorMat1/StorTot*ETP,0);   #ETP loss from unsaturated zone
ETMat2= if(StorTot>0,StorMat2/StorTot*ETP,0);
ETMat3= if(StorTot>0,StorMat3/StorTot*ETP,0);
ETSat= if(StorTot>0,StorSat/StorTot*ETP,0);          #ETP lost from saturated zone
#-surface detention & infiltration
SurfDet= SurfDet+PRP;
Perc0= min(InflCap*timeslice(),SurfDet);
SurfDet= SurfDet-Perc0;
ByPass= ByPass+if(SDepth-WatLevel<0.001,Perc0,0);
Perc0= if(SDepth-WatLevel<0.001,0,Perc0);

#Unsaturated zone
#-relative saturated hydraulic conductivity (-) for ThetaEff(i)
#-transmission of storage [-], drainage and average sustained percolation
# through layer (i),
#-balance check on fluxes, returning the actual percolation in m per time step
#-layer 1
Kr1= if(ThetaEff1>0,ThetaEff1**MQ*
  (exp(MQAlpha1*ThetaEff1)-MQAlpha1*ThetaEff1-1)/
  (exp(MQAlpha1)-MQAlpha1-1),
  0);
Perc1= Kr1*KSat1;
```

```
Trans1= if(DUnsat1>0.0,
  min(1.0,Perc1*Duration*timeslice()/DUnsat1),0.0);
ThEffNew= if(DUnsat1>0.0,max(0.0,(1-Trans1)*StorMat1+Perc0-ETMat1)/StorCap1,1.0);
ThEffNew= min(1.0,ThEffNew);
Kr1= if(ThEffNew>0,ThEffNew**MQ*
  (exp(MQAlpha1*ThEffNew)-MQAlpha1*ThEffNew-1)/
  (exp(MQAlpha1)-MQAlpha1-1),
  0);
Perc1= max(Perc1*Kr1*KSat1,PercMin);
Perc1= sqrt(Perc1);
Trans1= if(DUnsat1>0.0,
 min(1.0,Perc1*Duration*timeslice()/DUnsat1),0.0);
Perc1= StorMat1*Trans1;
MBC= ETMat1+Perc1;
MBC= if(MBC>0,(StorMat1+Perc0)/MBC,1.0);
MBC= min(MBC,1.0);
ETMat1= MBC*ETMat1;
Perc1= MBC*Perc1;
#-layer 2
Kr2= if(ThetaEff2>0,ThetaEff2**MQ*
  (exp(MQAlpha2*ThetaEff2)-MQAlpha2*ThetaEff2-1)/
  (exp(MQAlpha2)-MQAlpha2-1),
  0);
Perc2= Kr2*KSat2;
Trans2= if(DUnsat2>0.0,
  min(1.0,Perc2*Duration*timeslice()/DUnsat2),0.0);
ThEffNew= if(DUnsat2>0.0,max(0.0,(1-Trans2)*StorMat2+Perc1-ETMat2)/StorCap2,1.0);
ThEffNew= min(1.0,ThEffNew);
Kr2= if(ThEffNew>0,ThEffNew**MQ*
  (exp(MQAlpha2*ThEffNew)-MQAlpha2*ThEffNew-1)/
  (exp(MQAlpha2)-MQAlpha2-1),
  0);
Perc2= max(Perc2*Kr2*KSat2,PercMin);
Perc2= sqrt(Perc2);
Trans2= if(DUnsat2>0.0,
  min(1.0,Perc2*Duration*timeslice()/DUnsat2),0.0);
Perc2= StorMat2*Trans2;
MBC= ETMat2+Perc2;
MBC= if(MBC>0,(StorMat2+Perc1)/MBC,1.0);
MBC= min(MBC,1.0);
ETMat2= MBC*ETMat2;
Perc2= MBC*Perc2;
#-layer 3
Kr3= if(ThetaEff3>0,ThetaEff3**MQ*
  (exp(MQAlpha3*ThetaEff3)-MQAlpha3*ThetaEff3-1)/
  (exp(MQAlpha3)-MQAlpha3-1),
  0);
```

```
Perc3= Kr3*KSat3;
Trans3= if(DUnsat3>0.0,
  min(1.0,Perc3*Duration*timeslice()/DUnsat3),0.0);
ThEffNew= if(DUnsat3>0.0,max(0.0,(1-Trans3)*StorMat3+Perc2-ETMat3)/StorCap3,1.0);
ThEffNew= min(1.0,ThEffNew);
Kr3= if(ThEffNew>0,ThEffNew**MQ*
  (exp(MQAlpha3*ThEffNew)-MQAlpha3*ThEffNew-1)/
  (exp(MQAlpha3)-MQAlpha3-1),
  0);
Perc3= max(Perc3*Kr3*KSat3,PercMin);
Perc3= sqrt(Perc3);
Trans3= if(DUnsat3>0.0,
  min(1.0,Perc3*Duration*timeslice()/DUnsat3),0.0);
Perc3= StorMat3*Trans3;
MBC= ETMat3+Perc3;
MBC= if(MBC>0,(StorMat3+Perc2)/MBC,1.0);
MBC= min(MBC,1.0);
ETMat3= MBC*ETMat3;
Perc3= MBC*Perc3;

#New state variables per layer as a result of the current matric fluxes
#-change in matrix storage and any resulting return flow working from the bottom upwards,
#  leading to changes in the height of the water table
#-layer 3
StorMat3= if(D3>0,
  if(DUnsat3>0,StorMat3+Perc2-(ETMat3+Perc3),StorMat3),StorMat3);
Perc2= Perc2-max(0,StorMat3-StorCap3);
ThetaEff3= if(D3>0,
  if(StorCap3>0,min(1.0,StorMat3/StorCap3),ThetaEff3),ThetaEffBC);
H3= if(ThetaEff3<1.0,H3,D3);
#-layer 2
StorMat2= if(D2>0,
  if(DUnsat2>0,StorMat2+Perc1-(ETMat2+Perc2),StorMat2),StorMat2);
Perc1= Perc1-max(0,StorMat2-StorCap2);
ThetaEff2= if(D2>0,
  if(StorCap2>0,min(1.0,StorMat2/StorCap2),ThetaEff2),ThetaEffBC);
H2= if(ThetaEff2<1.0,H2,D2);
#-layer 1
StorMat1=  if(DUnsat1>0, StorMat1+Perc0-(ETMat1+Perc1),StorMat1);
ThetaEff1=  if(StorCap1>0,min(1.0,StorMat1/StorCap1),ThetaEff1);
H1= if(ThetaEff1<1.0,H1,D1);
#-exfiltration when top layer becomes saturated
MBC= max(0,StorMat1-StorCap1);
#actual infiltration and surface detention
Perc0= Perc0-MBC;
SurfDet= SurfDet+MBC;
```

```
#Saturated zone
#-fluxes in the saturated zone based on state variables of previous timestep
#-vertical fluxes evaluated first, ETSat already known
#-determining source of recharge
RecLayer= if(D3>0,if(WatLevel<D3,3,0));
RecLayer= if(RecLayer>0,RecLayer,
  if(D2>0,if(WatLevel<UL2,2,0),0));
RecLayer= if(RecLayer>0,RecLayer,
  if(D1>0,if(WatLevel<SDepth,1,0),0));
Sz= if(RecLayer==3,Perc3,
  if(RecLayer==2,Perc2,
  if(RecLayer==1,Perc1,0)));
#-outflow over lithic contact, vertical loss in m
Perc4=
if(SDepth>0,sqrt(PercBC*max(PercBC,WatLevel/SDepth*KSatBC))*timeslice()*Duration,0);
#-lateral fluxes
#-H: total head for nodes - retained from previous timestep
TotHead= DEMBase+WatLevel;
GradXXUp=
if(XXUpBC,if(OutletBase,DEMBaseBCXX+WatLevel,downstream(LDDXX,TotHead)),upstream(
LDDXX,TotHead))-TotHead;
GradXXDown= TotHead-
if(XXDownBC,if(OutletBase,DEMBaseBCXX+WatLevel,upstream(LDDXX,TotHead)),downstrea
m(LDDXX,TotHead));
GradYYUp=
if(YYUpBC,if(OutletBase,DEMBaseBCYY+WatLevel,downstream(LDDYY,TotHead)),upstream(L
DDYY,TotHead))-TotHead;
GradYYDown= TotHead-
if(YYDownBC,if(OutletBase,DEMBaseBCYY+WatLevel,upstream(LDDYY,TotHead)),downstrea
m(LDDYY,TotHead));
#-TSat between nodes; transmissivity T= hw.KLat
KLat= if(WatLevel>0,(H1*KSat1+H2*KSat2+H3*KSat3)/WatLevel,0);
TSat= -KLat*WatLevel;
TSatXXUp= if(XXUpBC,if(OutletBase,TSat,downstream(LDDXX,TSat)),
  upstream(LDDXX,TSat));
TSatXXUp= 0.5*(TSat+TSatXXUp);
TSatXXDown= if(XXDownBC,if(OutletBase,TSat,upstream(LDDXX,TSat)),
  downstream(LDDXX,TSat));
TSatXXDown= 0.5*(TSat+TSatXXDown);
TSatYYUp= if(YYUpBC,if(OutletBase,TSat,downstream(LDDYY,TSat)),
  upstream(LDDYY,TSat));
TSatYYUp= 0.5*(TSat+TSatYYUp);
TSatYYDown= if(YYDownBC,if(OutletBase,TSat,upstream(LDDYY,TSat)),
  downstream(LDDYY,TSat));
TSatYYDown= 0.5*(TSat+TSatYYDown);
#-QSat (m3) over timestep: Q= T*DX*DH/DX
```

```
 QSat= (TSatXXUp*GradXXUp-TSatXXDown*GradXXDown+TSatYYUp*GradYYUp-
TSatYYDown*GradYYDown)*Duration*timeslice();
 QOut= if(OutletBase,TSat*((DEMBase-DEMBaseBCXX)+(DEMBase-
DEMBaseBCYY)),0)*Duration*timeslice();

 #storage and budget for the saturated zone
 #-water level as a result of moisture changes in unsaturated zone
 WatLevel= H1+H2+H3;
 #  note: effective degree of saturation for overlying layer used for drainage.
 ThetaEff1= if(D1>0,if(ThetaEff1<1,ThetaEff1,ThetaDrain1),ThetaEff1);
 ThetaEff2= if(D2>0,if(ThetaEff2<1,ThetaEff2,ThetaEff1),ThetaEff2);
 ThetaEff3= if(D3>0,if(ThetaEff3<1,ThetaEff3,ThetaEff2),ThetaEff3);
 DeltaThetaEff1= (1-ThetaEff1);
 DeltaThetaEff2= (1-ThetaEff2);
 DeltaThetaEff3= (1-ThetaEff3);
 StorSat1= H1*DegSat1*DeltaThetaEff1;
 StorSat2= H2*DegSat2*DeltaThetaEff2;
 StorSat3= H3*DegSat3*DeltaThetaEff3;
 StorSat=StorSat1+StorSat2+StorSat3;
 Sz= Sz+StorSat+ByPass;
 MBC= Perc4+ETSat;
 MBC= if(MBC>0,Sz/MBC,1.0);
 MBC= min(MBC,1.0);
 ETSat= MBC*ETSat;
 Perc4= MBC*Perc4;
 StorSat= max(Sz-(ETSat+Perc4),0);
 #-budget correction for lateral flow
 #-total gross saturated storage available for routing (m)
 report (rep2) SumStor0TSS= maptotal(StorSat+QOut/DX**2);
 #-change as a result of lateral drainage,
 StorSat= max(StorSat-QSat/DX**2,0);
 report (rep2) SumStor1TSS= maptotal(StorSat);
 #-corrected for mass balance error (m)
 StorSat= StorSat*if(SumStor1TSS>0,(1-(SumStor1TSS-SumStor0TSS)/SumStor1TSS),1);

 #New state variables per layer at end of current timestep
 #-layer 3
 StorSat3= min(DeltaThetaEff3*StorMax3,StorSat);
 StorSat= max(StorSat-StorSat3,0);
 H3= StorSat3/(DeltaThetaEff3*DegSat3);
 ThetaEff3= if(D3>0,
  if((D3-H3)> 0.001,ThetaEff3,1.0),ThetaEff3);
 #-layer 2
 StorSat2= min(DeltaThetaEff2*StorMax2,StorSat);
 StorSat= max(StorSat-StorSat2,0);
 H2= StorSat2/(DeltaThetaEff2*DegSat2);
 ThetaEff2= if(D2>0,
```

```
  if((D2-H2)> 0.001,ThetaEff2,1.0),ThetaEff2);
 #-layer 1
 StorSat1= min(DeltaThetaEff1*StorMax1,StorSat);
 StorSat= max(StorSat-StorSat1,0);
 H1= StorSat1/(DeltaThetaEff1*DegSat1);
 ThetaEff1= if(D1>0,
  if(D1-H1>0.001,ThetaEff1,1.0),ThetaEff1);
 #Exfiltration to surface
 SurfDet= SurfDet+StorSat;

 #Reporting map stacks and timeseries
#-interception storage
 report (rep2) IntTSS= timeoutput(SampleLocs,Int);
 #-Evapotranspiration
 ETPSoil= ETMat1+ETMat2+ETMat3+ETSat;
 ETPSurf= ETPSurf+ETPSoil;
 #-surface detention (m)
 #-exfiltration from remainder waterlevel and routing
 SurfDet= SurfDet+StorSat;
 report (rep2) OutflowTSS= timeoutput(Outlet,Redist*SurfDet);
 SurfDet= (1-Redist)*SurfDet+upstream(LDDSurf,Redist*SurfDet);
 Perc0= maptotal(scalar(Stream)*SurfDet);
 report (rep1) SurfDet= if(Stream,StreamAccu*Perc0,SurfDet);
 #-calculation of VMC(i) (-)
 report (rep1) Theta1= ThetaRes1+DegSat1*ThetaEff1;
 report (rep1) Theta2= ThetaRes2+DegSat2*ThetaEff2;
 report (rep1) Theta3= ThetaRes3+DegSat3*ThetaEff3;
 report (rep2) Theta1TSS= timeoutput(SampleLocs,Theta1);
 report (rep2) Theta2TSS= timeoutput(SampleLocs,Theta2);
 report (rep2) Theta3TSS= timeoutput(SampleLocs,Theta3);
 #-outflow BC from the saturated zone
 report (rep2) QSatTSS= timeoutput(Outlet,QOut);
 #-total water height (m)
 report (rep1) WatLevel= H1+H2+H3;
 report (rep2) WatLevelTSS= timeoutput(SampleLocs,WatLevel);

 #Budget check - maptotals in m
 report (rep2) StorTotTSS= maptotal(H1*DegSat1+(D1-H1)*DegSat1*ThetaEff1+
    H2*DegSat2+(D2-H2)*DegSat2*ThetaEff2+
    H3*DegSat3+(D3-H3)*DegSat3*ThetaEff3);
 report (rep2) SurfTotTSS= maptotal(SurfDet+Int);
 report (rep2) Perc4TSS= maptotal(Perc4);
 report (rep2) ETPTotTSS= maptotal(ETPSurf);
```

Appendix 4:

Rend. Online Soc. Geol. It., Vol. 24 (2013), pp. 125-127

GB-InSAR monitoring of the Montaguto earthflow

Appendix 5:

Bull Volcanol (2014) 76:786
DOI 10.1007/s00445-013-0786-2

The ground-based InSAR monitoring system at Stromboli volcano: linking changes in displacement rate and intensity of persistent volcanic activity

Received: 21 June 2013 /Accepted: 17 November 2013

Author’s Resume

Contacts:

Address(es)	Via Ponte alle Mosse, 1 Firenze 50144	
Telephone(s)	+39 055 0948508	Mobile: +39 335 6738180
Fax(es)		
E-mail(s)	federica.ferrigno@unifi.it	geol.federicaferrigno@gmail.com

Federica Ferrigno was born in Polla (SA) on December, 20th 1985.

In 2008 she pursued bachelor degree (103/110) in Earth Science at the University of Florence disserting a thesis with title "Survey to identify the source of hydrocarbons pollution in Viale Europa (Firenze)" under the supervision of Prof. Giovanni Pranzini.

In 2010 she pursued master degree (109/110) in Soil Defense at the University of Florence disserting a thesis with title "Detection and mapping of landslides and subsidence at the basin scale" with the supervision of Prof. Nicola Casagli. In 2011 she has begun her PhD under the supervision of Prof. Nicola Casagli; her studies involve development of technical and scientific support for civil protection activities, related to landslide risk, monitoring and evaluation of volcanic related risks, real time monitoring of landslides using interferometric data, numerical models and analysis of temporal series.

She took part at several emergency scenarios in the nationwide as member of a Centre of Competence for remote sensing and geohazards of the National Department of Civil Protection of the Italian Government.

She spent four months at the Utrecht University under the supervision of Rens van Beek and Theo van Ash, in order to improve her research project and have the scientific support of experts on hydrological modeling at the slope scale.